2009

Behavior of rectangular concrete walls subjected to simulated seismic loading

Sriram Aaleti
Iowa State University

Behavior of rectangular concrete walls subjected to simulated seismic loading

by

Sriram R. Aaleti

A dissertation submitted to the graduate faculty

in partial fulfillment of the requirements for the degree of

DOCTOR OF PHILOSOPHY

Major: Civil Engineering (Structural Engineering)

Program of Study Committee:

Sri Sritharan, Major Professor
Terry J. Wipf
Max L. Porter
Lester W. Schmerr
Loren Zachary

Iowa State University

Ames, Iowa

2009

TABLE OF CONTENTS

LIST OF FIGURES

ABSTRACT

Structural walls are frequently used in buildings to resist earthquake lateral loads because of their effectiveness in limiting the building drifts and minimizing damage to both structural and non-structural elements. In a collaborative effort, as part of a PreNEESR project, three ½ -scale reinforced concrete rectangular shear walls were subjected to cyclic loading at the Multi-Axial Subassemblage Testing facility (MAST) at University of Minnesota. Also, a ½-scale precast wall system was tested at National Center for Research on Earthquake Engineering (NCREE), Taiwan to validate PreWEC system concept.

Overall dimensions of all four rectangular walls were identical, except that four different approaches were used to anchor the wall into the foundation. In the first wall, RWN, the longitudinal reinforcement was anchored into the foundation with adequate anchorage length without using any splices, while the second and third walls used couplers and code-based conventional lap splices to connect the wall reinforcement with the starter bars placed in the foundation. The precast wall, referred as PreWEC-1, used unbonded post-tensioning to anchor the wall to the foundation. All three reinforced concrete walls had two different stiffness and strength in the two in-plane loading directions as they were modeled to represent the response of a T-shaped concrete wall tested as part of the same project. PreWEC-1 was designed to replicate the response of RWN in in-plane weaker direction.

The fiber-based nonlinear beam-column element available in OpenSees software was used to model all three reinforced concrete walls with adequate attention to capture the influence of different anchorage details. In addition to capturing the total global response, the accuracy of the analysis was also examined in terms of simulating the local response as well as various displacement components due to flexure, bond slip at the critical section resulting from strain penetration, and shear. A zero-length bond slip element was used to account for the strain penetration effects while a nonlinear spring element was used to account for the shear deformation. By comparing with the experimental results, it was found that the analytical models well simulated the force-displacement responses including the unloading and reloading stiffness. However, it was found that the pinching model available in OpenSEES, which has been used in the past to represent the shear deformation hysteresis,

was not capable of capturing all the critical points in the shear deformation response recorded during testing. Hence, a monotonic and hysteretic cyclic shear model was proposed using the strut-and-tie modeling technique. The proposed cyclic shear model captured the observed experimental shear response adequately.

As part of PreWEC-1, testing an innovative, economical mild steel connector was developed and its behavior under cyclic shear loading was characterized using experimental and analytical means. The PreWEC system performed exceptionally well with good energy dissipation, self-centering ability and had 15% higher capacity compared to the traditional reinforced concrete wall. Simplified analytical and design methods were proposed to characterize the behavior and designing of PreWEC systems. The simplified analysis captured overall force-displacement response, connector displacements and wall contact length accurately.

ACKNOWLEDGEMENTS

The research presented in this thesis was made possible by the National Science Foundation (NSF) Grant CMS-0324559 and a supplement grant from the International Research and Education in Engineering (IREE) program of NSF. The research on the precast wall system was also supported by the Precast/Prestressed Concrete Institute (PCI) through a 2008 Jenny Fellowship. The financial support of all funding agencies is greatly acknowledged.

For the course of my doctoral research, I would like to express my thanks:

to my advisor Dr. Sri Sritharan for his much valued input and guidance throughout my doctoral study;

to Dr. Wipf, Dr. Porter, Dr. Zachary and Dr. Schmerr for serving on my thesis committee;

to Dr. Catherine French at University of Minnesota for her words of encouragements and guidance during my stay at the MAST laboratory;

to Dr. K.C. Tsai and Dr. Kevin Liu of National Center for Research on Earthquake Engineering (NCREE), Taiwan, for their support, hospitality, guidance and the opportunity to conduct a large-scale test at their test facility;

to laboratory personnel of MAST laboratory at University of Minnesota, NCREE laboratory in Taiwan and Doug Wood, structural lab manager at Iowa State University, for their assistance in conducting the experimental research reported in this thesis;

to my fellow graduate students especially Rick Henry for reading and providing feedback on my thesis. I want to acknowledge all the help provided by Beth Brueggen, Benton Johnson, John Waugh and all the undergraduate research assistants especially Helen Marie Jarvis, Vanessa Storlie, Blake Remmick, Jacob Reneson and Abigail Szarkowski during the construction and testing of concrete shear walls.

to my parents and siblings for their support and understanding during this exciting time in my life.

CHAPTER 1

INTRODUCTION

1.1 Concrete Structural Walls

Concrete structural walls provide a cost effective way to resist lateral loads generated by wind and earthquakes and thus they are frequently incorporated as the primary lateral load resisting system in buildings. Structural walls have a high in-plane stiffness, which helps decreasing the structural damage by limiting the inter-story drift during seismic events. The superior performance of the buildings consisted of structural walls as the primary lateral loading system is well documented in the literature. For example, during the 1985 Chilean earthquake buildings in which lateral force resistance was provided by structural walls showed excellent performance (Wood et al. 1987). Also, during the 1988 Armenia earthquake, poorly designed and constructed buildings that incorporated concrete walls as the main lateral force resisting system performed substantially better than buildings built with other structural systems (Wyllie 1989). Even during the most damaging earthquakes of recent times (e.g., 1994 Northridge earthquake in California, the 1995 Kobe earthquake in Japan, and the 1999 Kocaeli earthquake in Turkey), which altered the engineering community's view towards the earthquake engineering, no building incorporating shear walls as lateral load resisting system, collapsed. A detailed literature review on previous performance of shear walls is presented in references (Fintel 2002, Holden et al 2003, and Thomas 2003).

Concrete walls can be constructed in different shapes, such as rectangular, T-, L- or C-shaped walls. However, the rectangular walls are more prevalent compared to other shaped walls due to ease of construction and ease of placement of walls along the perimeter of a building. Traditionally, concrete structural walls are constructed with cast-in-place (CIP) reinforced concrete. When built using cast-in-place concrete, it is a common practice to splice the longitudinal reinforcement of walls near the base using either lap splices or mechanical couplers to simplify the construction process. Though the CIP concrete walls are more common, with the added benefits of prefabrication and recent developments in concrete

technology, there has been an increased use of precast concrete walls that are designed to emulate behavior of cast-in-place concrete walls using the splicing provisions of ACI 318-05 building standard (ACI 318, 2005). With advances made over the past decade in utilizing precast concrete to improve seismic performance of structures, a new precast walls assembly has been developed, which are constructed by tying down precast walls to the foundation using unbonded post-tensioning tendons.

In seismic design of buildings, the life safety of the occupants is of vital importance. For loads representative of wind or small, frequent earthquakes, structural walls are typically designed to respond in an elastic manner. However, during larger, less frequent earthquakes, the concrete walls in seismic regions are required to resist lateral loads while deforming in a ductile manner (i.e., allowing the wall to deform beyond its yield limit without experiencing any significant reduction in strength), thereby dissipating seismic energy imparted by an earthquake and preventing structural collapse. This desired response can be achieved by carefully selecting the location of critical regions, termed as "plastic hinges", and suitably detailing these regions to accommodate large inelastic deformations. The ductile response of a structure can be ensured, by allowing it to response in a manner dominated by inelastic flexural yielding of carefully detailed plastic hinges and inhibiting other nonductile failure modes such as shear failure (i.e., diagonal tension or compression failure), sliding failure, and bond failure of reinforcement in lap splices. The ACI 318 design standard (ACI 318, 2005) provides recommendations for the design of structural walls with different anchorage conditions to ensure that the above mentioned seismic design requirements are met. The specifications include details for required confinement reinforcement, length and height of confinement, required shear reinforcement, types and requirements of mechanical couplers suitable for reinforcement splicing, the lap splice lengths, and the amount of longitudinal reinforcement.

Reinforced concrete structural walls dissipate seismic energy by subjecting the longitudinal reinforcement in plastic hinge regions to large inelastic strains, thus leading to significant damage to the plastic hinge regions as well as large residual drifts and wide residual cracks (see Figure 1.1). Consequently, the repair cost of the structure should be

expected to be high after a damaging seismic event. Excessive damage in plastic hinge region and permanent deformation of reinforced concrete walls can be mitigated by uncoupling the energy dissipation mechanism from the structural force resisting mechanism and achieving the energy dissipation through other means. Recent advancements in research of precast concrete structures have introduced such a concept and examples include the hybrid wall system (Holden et al 2003), the jointed wall system (Priestley et al 1999) and precast wall with end columns known as the PreWEC system (Aaleti and Sritharan 2007). These wall systems are considered to be superior to cast-in-place walls because they are capable of maintaining structural integrity as well as providing sufficient energy dissipation when subjected to seismic loads.

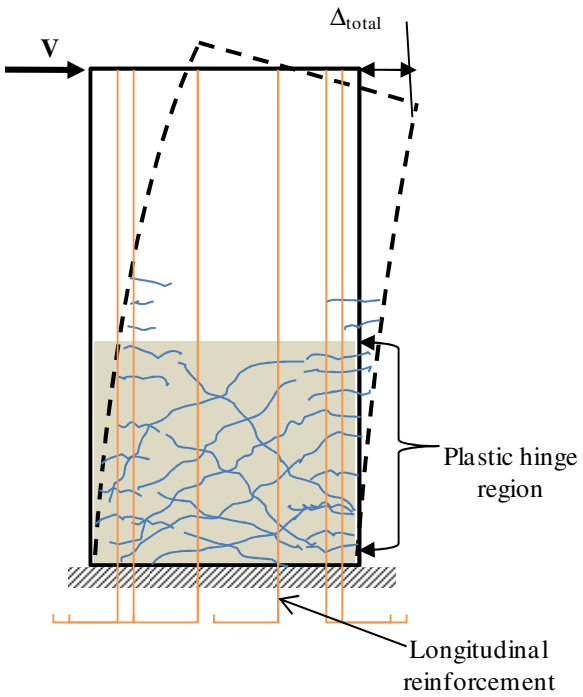

Figure 1.1 Plastic hinge region of a cast-in-place reinforced concrete wall

In precast wall systems, post-tensioning steel is typically designed to remain elastic up to the design-level earthquake loading. As a result, it will provide the necessary restoring force for the wall system to recenter when the applied lateral load is removed, thus minimizing the residual displacements associated with the earthquake input motion. The

behavior of a fully post-tensioned precast wall system without any energy dissipaters can be idealized to bilinear elastic behavior. In these systems damage is restricted to the bottom corners of the wall about which it rocks. By proper detailing, such damage can be minimized. The drawback with this system is that only a very small amount of seismic energy is dissipated by the system, which will lead the structure to experience a larger lateral displacement. The jointed wall and PreWEC systems address this concern by accommodating easily replaceable external energy dissipating elements.

In a jointed wall system, two or more precast walls, which are anchored individually to the foundation by unbonded post-tensioning, are connected to each other horizontally along the height, by energy dissipating shear connectors, as shown in Figure 1.2. The post-tensioning steel in the wall may be distributed evenly along the wall length or concentrated at the center of each wall. In a PreWEC system, a single precast wall is connected with two (steel or precast) end columns using special energy dissipating connectors, as shown in Figure 1.3. The wall and end columns are anchored to the foundation using unbonded post-tensioning. The post-tensioning steel in the wall may be distributed evenly along the wall length or concentrated at the center of the wall. The energy dissipating connectors are placed between the wall and end columns. More details of the PreWEC system is discussed Chapter 4 of this document.

In both the jointed wall and PreWEC systems, the special connectors help dissipating the seismic energy by undergoing inelastic deformations when subjected to moderate to large earthquake loads. Therefore, by proper detailing of the rocking corners of the walls and an appropriate amount of unbonded post-tensioning, these wall systems can provide additional benefits such as reduced damage, minimum residual displacements, and the ability to dissipate seismic energy when compared to the response of conventional cast-in-place concrete walls. Figure 1.4 schematically compares the response of a conventional reinforced concrete system with different unbonded precast wall systems.

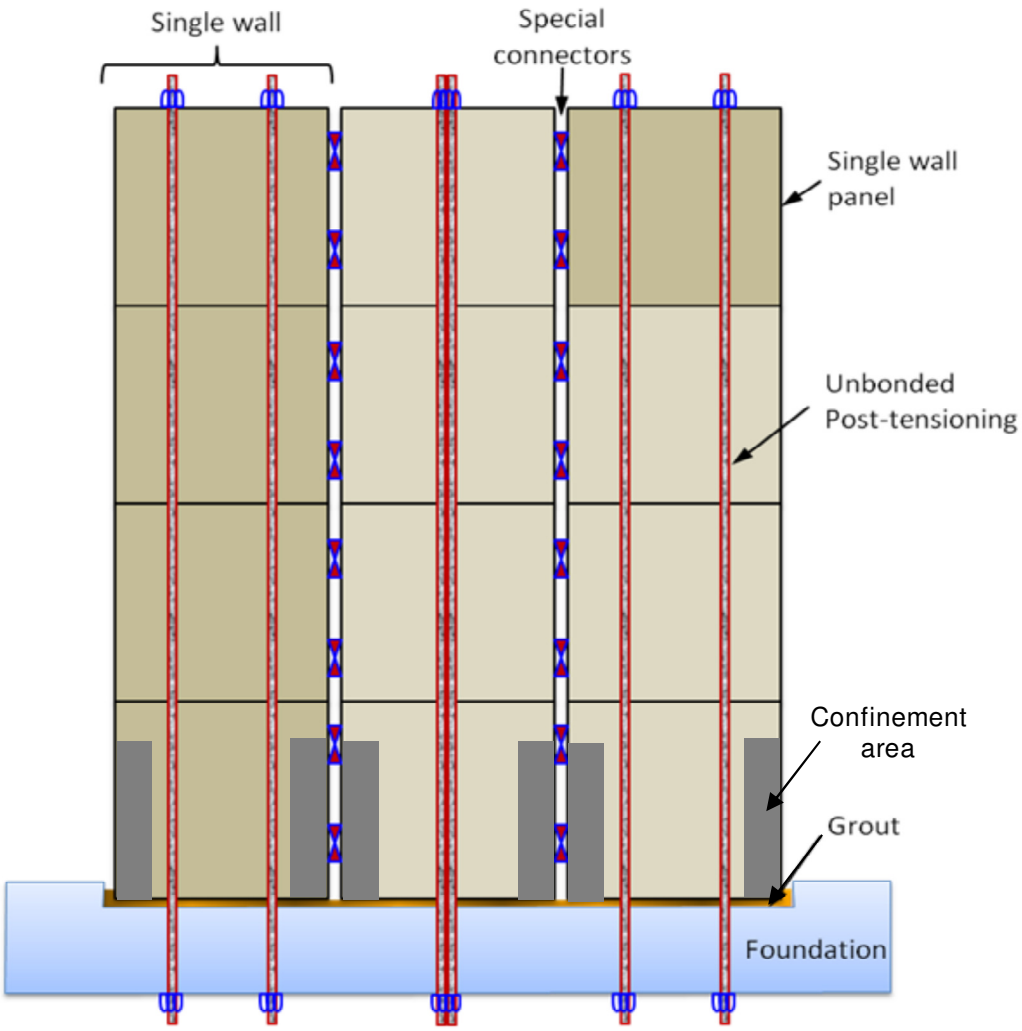

Figure 1.2 Typical details of a precast concrete jointed wall system

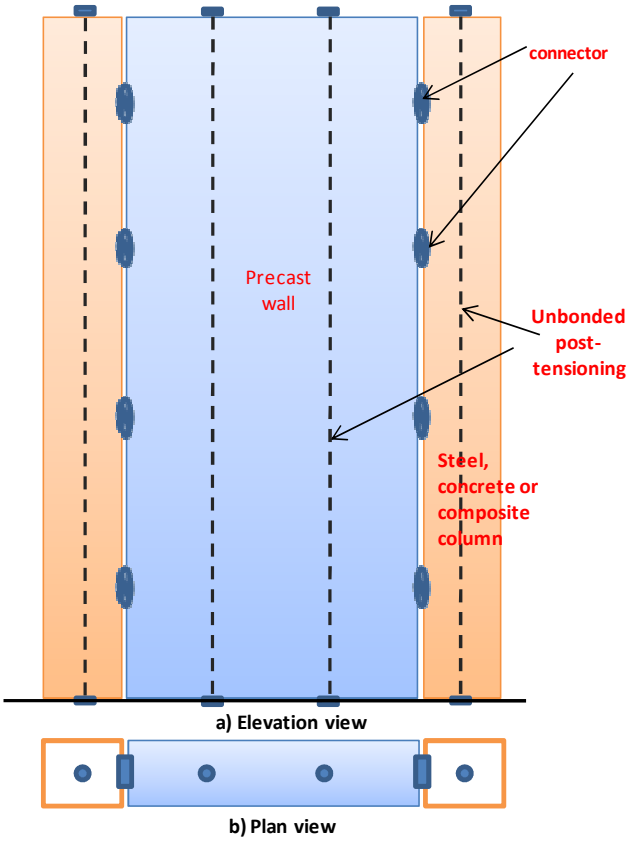

Figure 1.3 Typical Details of a precast wall with end columns (PreWEC) system

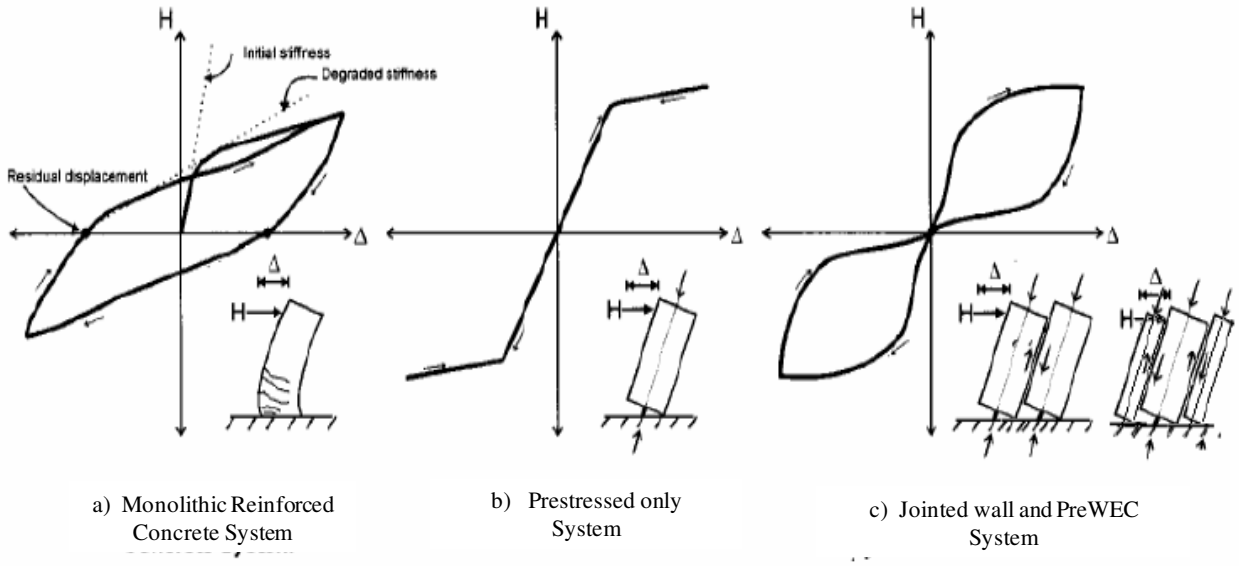

Figure 1.4 Schematic representation of cyclic responses of various structural wall systems (Holden et al. 2003)

The force-displacement behavior of a structural wall depends on the ratio of wall height to wall length, which defines the wall aspect ratio. When the aspect ratio is greater than 2.0, the walls are classified as "slender walls" and the flexural deformation is considered to be the prominent contributor to their lateral displacements. However, it is important to realize that, structural walls undergo several deformation modes when subjected to lateral loads, including flexural deformation mode, shear deformation mode, and deformation due to strain penetration in the form of rotation at the wall base, which are illustrated in Figure 1.5. In addition to the above deformation modes, the precast walls will also undergo a rotational deformation mode due to gap opening at the base of the wall (see Figure 1.6). Regardless of the aspect ratio, adequately capturing the individual contributions of different deformation modes is critical for understanding lateral load behavior of walls.

To achieve ductile behavior, cast-in-place wall should be designed such that it develops the full flexural moment capacity by allowing the longitudinal reinforcement to develop its full tensile strength under severe loading conditions. Thus, it is anticipated that longitudinal reinforcement anchorage and splicing details such as those used at the wall base should not have any negative impact on the plastic hinge formation, the lateral load behavior, the crack pattern and the overall deformation capacity of a structural wall. However, there are no experimental or analytical studies exist on this topic of research for structural walls in the literature. Developing rational analytical models to address anchorage and lap splice issues, quantify contribution of individual deformation components to the total lateral displacement and estimate the expected damage to the walls will help researchers and design engineers to understand and characterize overall behavior of the walls as a function of lateral displacement more accurately, which in turn will lead to better and economical buildings. These analytical models will also help with designing and evaluating structures under the performance-based engineering frame work.

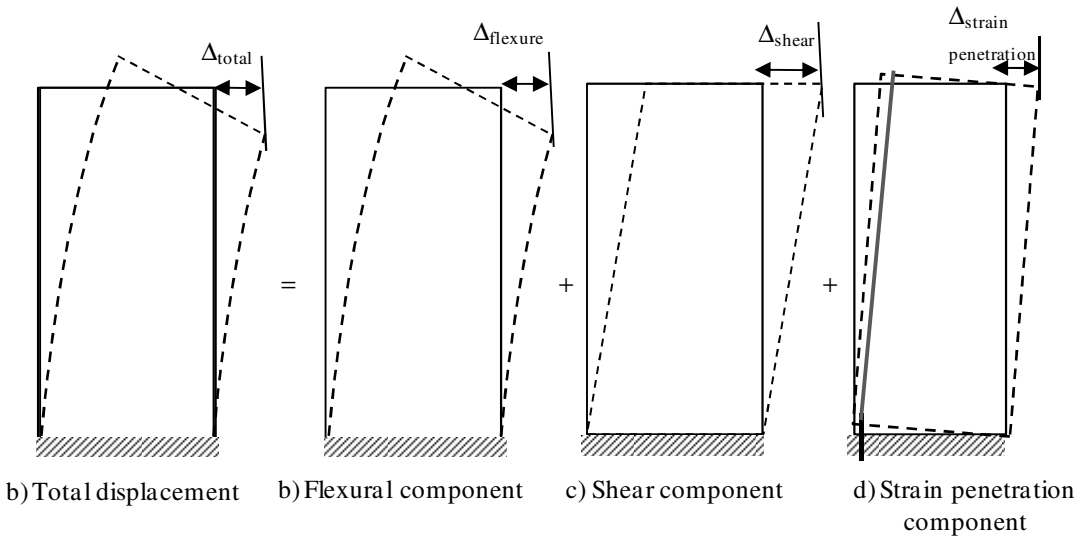

Figure 1.5 Deformation components expected in a reinforced concrete structural wall subjected to a lateral force

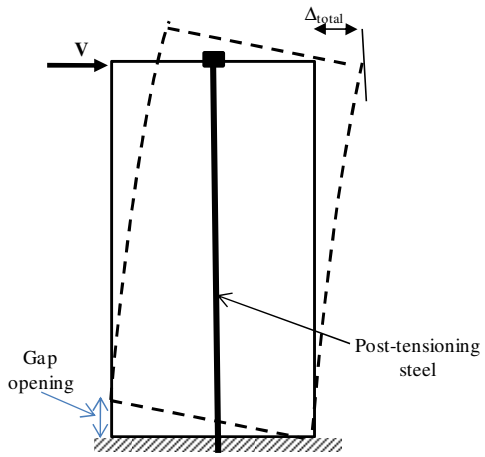

Figure 1.6 Gap opening at the base of the wall in unbonded post-tensioned precast wall systems

The superior seismic performance of the jointed wall system has been experimentally demonstrated (Priestley et al. 1999) and was further validated by analytical studies (Sritharan et al. 2007). However, it was shown that the jointed wall system is less efficient for resisting lateral loads when compared to a comparable cast-in-place structural wall. By addressing the shortcomings of this wall issue, the PreWEC system concept was developed (Aaleti and Sritharan 2007). However, the PreWEC concept has not been experimentally validated and thus needed data to develop the analysis and design tools of PreWEC was not available at the

beginning of this study. Such an experimental study will also elevate the confidence of practicing engineers in using this innovative and economical precast structural system in seismic regions.

1.2 Analytical Methods and Computer Software

Various analytical techniques have been used by researchers to predict the lateral load behavior of reinforced concrete structural walls under reversed cyclic loads. These methods have ranged from simple calculations based on moment-curvature relationships to general finite element analysis of the walls. More details of different analytical methods are presented later in this thesis as part of review of literature. For the study described in this thesis, a fiber-based finite element analysis approach was chosen to model and analyze the cast-in-place structural walls. The fiber concept represents a reinforced concrete section of a structural element with a group of uniaxial fibers and assigns the uniaxial concrete or steel behavior to these fibers. Three dimensional effects on material behavior are incorporated into the uniaxial behavior of the material in order to improve the accuracy of the analysis. Taucer et al. (1991) used this concept to develop a beam-column element for seismic response analysis of structural systems and demonstrated that it significantly improves the computational efficiency over the traditional finite element approaches. The main benefit of using a fiber-based element is that it allows the use of uniaxial stress-strain relationships that are well established, providing accurate force-displacement responses for structural members under lateral loads. An inherent assumption used in the fiber-based element is that plane sections remain plane after bending. The fiber-based analysis has typically ignored the effects of bond slip of longitudinal reinforcement resulting from strain penetration and shear deformations. Consequently, the analysis would lead to inaccurate estimate of damage and force-displacement responses as they are significantly dependent on local responses in the critical regions.

The open source finite element program OpenSees (Mazzoni et al., 2006) was used for the study in this thesis because it was capable of using a fiber section in conjunction with beam-column elements. Access to the source code of the program allowed new section

definitions and material models to be added to the program to overcome the challenges identified above and improve the simulation of the structural walls under cyclic loading.

1.3 Project Description

The study described in this thesis was a part of a larger collaborative project involving a team of researchers from the University of Minnesota (UMN), Iowa State University (ISU) and the University of Puerto Rico at Mayagüez. In parallel with establishment of the George E. Brown, Jr. Network for Earthquake Engineering Simulation (NEES) in October 2004, the National Science Foundation (NSF) funded an unsolicited collaborative research proposal to experimentally and analytically study the behavior of nonrectangular structural walls subjected to the effects of multi-directional loading.

In addition to addressing this fundamental problem, this project was aimed at examining the IT capability available for collaboration NEES research and verifying the capabilities of the Multi-Axial Subassemblage Testing (MAST) facility at UMN, which is one of 15 experimental facilities in the NSF's shared NEES network. This is one of three such projects to be awarded by NSF prior to establishing the NEES Research (NEESR) awards through a special solicitation for proposals that would utilize the unique capabilities of the NEES network. Consequently, these three projects funded through the unsolicited proposal scheme were referred to as the PreNEESR projects.

As part of this PreNEESR research project three rectangular and two T-shaped large-scale concrete walls were tested at the MAST facility at UMN. All researchers of the project participated locally or remotely in testing; researchers at ISU also remotely controlled some of the testing and examined the IT capabilities available through NEESit at the time of testing of each wall. The researchers at ISU also received supplementary funding from the NSF International Research and Education in Engineering (IREE) program, which enabled integration of international collaboration into the project through partnership with National Center for Research on Earthquake Engineering (NCREE) in Taiwan and introduction of a new precast wall system.

1.4 Scope and Objectives

The overall scope of the research presented in this thesis is to perform a comprehensive evaluation of reinforced concrete rectangular walls and unbonded post-tensioned precast walls under lateral loads to study the effects of anchorage details on the lateral load behavior. In the context of the above described project, current state of the knowledge and the shortcomings of fiber-based analytical software, OpenSees, the objectives of the study presented in this thesis are as follows:

1. Investigate the influence of different anchorage details for the longitudinal reinforcement (i.e., continuous, using mechanical couplers, and spliced reinforcement) on the cyclic lateral load behavior of reinforced concrete rectangular shear walls;
2. Using fiber based beam-column elements available in OpenSEES, study the analytical response of three rectangular concrete walls designed with different anchorage details and subjected to cyclic lateral loading. Experimentally quantify the deformation contributions due to flexure, shear, strain penetration (in case of reinforced concrete walls), the joint opening at the base (in case of unbonded post-tensioned precast wall systems) and comparing them with the respective components obtained from the analytical model. This investigation will be of greater interest for the development of performance-based engineering for structural systems incorporating structural walls;
3. Evaluate the existing analytical models in OpenSEES that are aimed to capture the shear deformation contribution and recommend any needed improvements. Develop a monotonic and hysteretic cyclic model addressing shear-flexure interaction and capable of to be implemented in macro models to capture the shear deformations of structural walls. Along with these analytical models, calibrate the existing strain-penetration models with the experimental data;
4. Experimentally investigate the lateral load behavior of Precast Wall with End Columns (PreWEC) system to validate the concept and its superior performance compared to traditional reinforced concrete walls. Develop a cost-effective energy dissipating connector and evaluate its performance with experimental testing.

Evaluate applicability of existing analytical procedures for predicting the lateral load behavior of PreWEC systems and recommend necessary improvements. Also, Develop a simplified design procedure to assist the designers to use the PreWEC system in real world applications;

1.5 Thesis Layout

This thesis consists of six chapters including the general introduction presented in this chapter. The following chapter reviews the available literature on previous experimental investigations relevant to the investigation of reinforced concrete rectangular walls and unbonded post-tensioned precast concrete wall systems. Various analysis techniques that have been used to analyze structural walls are also summarized in this chapter. Chapter 3 presents the post-test cyclic analysis of three rectangular walls using fiber based models developed in OpenSEES with comparisons to the recorded global and local responses. It also presents an analytical method to quantify the various deformations components contributing to the lateral displacement and the experimental contributions of flexure, shear and the strain penetration components in the top displacement of the three rectangular walls tested at the MAST laboratory Chapter 4 discusses the design and experimental testing of the PreWEC system and its components. This chapter also presents code validation of PreWEC system response, a simplified analytical procedure and its validation with the experimental data and a design procedure. Chapter 5 presents an analytical model capturing the monotonic and cyclic shear deformation behavior of structural walls. Chapter 6 presents conclusions from the study conducted on reinforced concrete walls and precast wall system and recommendations for future research.

CHAPTER 2

LITERATURE REVIEW

2.0 Introduction

Lateral load behavior of symmetric walls especially with rectangular cross section was extensively investigated experimentally and analytically in the literature. Experimental investigations were conducted to understand the effects of various design parameters on the lateral load behavior of these walls. Various analytical methods were used to predict the cyclic behavior of reinforced concrete walls. This chapter summarizes the existing knowledge from the past experimental research that has been performed on rectangular reinforced concrete structural walls, unbonded post-tensioned precast wall systems and nonlinear analysis techniques used for predicting the wall behavior.

2.1 Symmetric Wall Sections

Symmetric wall sections are walls that have typically either a rectangular or a barbell shaped cross section. These walls have been studied and the effects of various types and configurations have been investigated. Some of the types are briefly presented below, with references to these studies on this subject for those interested in exploring the specific research further.

2.1.1 Squat Shear Walls

As discussed earlier, the aspect ratio of the wall will determine if the wall behavior is dominated by flexure or shear. Squat walls are walls with an aspect ratio of 1 or less and their behavior is dominated by shear. Shear failures are typically brittle in nature, with decreased energy dissipating capacity and fail at small lateral displacements compared to flexural dominant walls. Most of the past research had significant focus on eliminating shear failures during lateral loading response of walls. Paulay et al. (1982) found that the effects of initiation of shear failure were early strength and stiffness degradation and increased

"pinching" in the hysteresis loops. However, if properly detailed, inelastic flexural response can develop (Paulay et al., 1982) in squat shear walls. Abrams (1991) and Ali and Wight (1990) give a list of references for previous research on squat reinforced concrete shear walls.

2.1.2 Slender Walls

Slender walls are walls that have an aspect ratio of greater than 2, and their behavior is dominated by flexure. Walls with an aspect ratio of less than 2 and greater than 1 are in the transition between flexure and shear dominated behavior, and both may have significant influence on the wall performance. The rectangular walls which were analyzed in this study are isolated slender walls. There are numerous references on the analysis, design and behavior of isolated slender walls and a few of the experimental studies conducted on slender walls focusing on the influence of various design parameters on lateral load behavior are summarized below.

2.1.2.1 Portland Cement Association (PCA)

The most extensive study on reinforced concrete walls was conducted at the Construction Technology Laboratories in Skokie, Illinois in the 1970s. The study consisted of three phases, and in the first two phases (Oesterle et al., 1976; Oesterle et al., 1979) sixteen 1/3-scale structural walls were constructed. These walls had rectangular, barbell, and flanged cross sections, and were designed in accordance to the 1971 ACI Building code (Oesterle et al., 1979). Each of these rectangular walls was 15 ft tall, 75 in. long and 4 in. thick. The flanged walls had 36 in. by 4 in. flanges on each end, while the barbell walls had 12 in. square boundary elements, see Figure 2.1. The concrete strength varied with each wall specimen from 3165 to 7775 psi, and the yield strength of the reinforcement varied from 59.5 to 74.2 ksi. The axial load applied to the walls ranged from zero to approximately 9% of $f_c^{'}$. The walls were loaded in the plane of the web under increasing reversed cyclical displacements.

Oesterle et al. (1979) found that the different cross section shapes led to different patterns of wall behavior. The rectangular wall had limited out-of-plane stiffness due to the small width of the wall, making it more susceptible to instability in the compression zone

under large load reversals resulting in out-of-plane buckling of the boundary element (Oesterle et al., 1979). This was observed in the failure of one rectangular test specimen subjected to in-plane lateral displacements. Oesterle et al. (1979) noted that rectangular walls exhibited lower flexural capacity compared to the barbell or flanged sections, of equal length and web thickness. The barbell shape prevented horizontal sliding shear failure by providing large dowel action in the boundary elements. The large boundary elements also provided high out-of-plane stiffness that minimized the wall instability. The large area of steel in the boundary element allows high flexural capacities to develop. Crushing of the web concrete was the primary failure mechanism observed in the tests because of the high strains that develop in the plastic region. The researchers recommended that barbell walls be designed for high shear stresses on the section. The flanged sections had a performance similar to the barbell shaped sections, with high flexural capacities developing and the requirement that high shear stresses must be designed for in the wall.

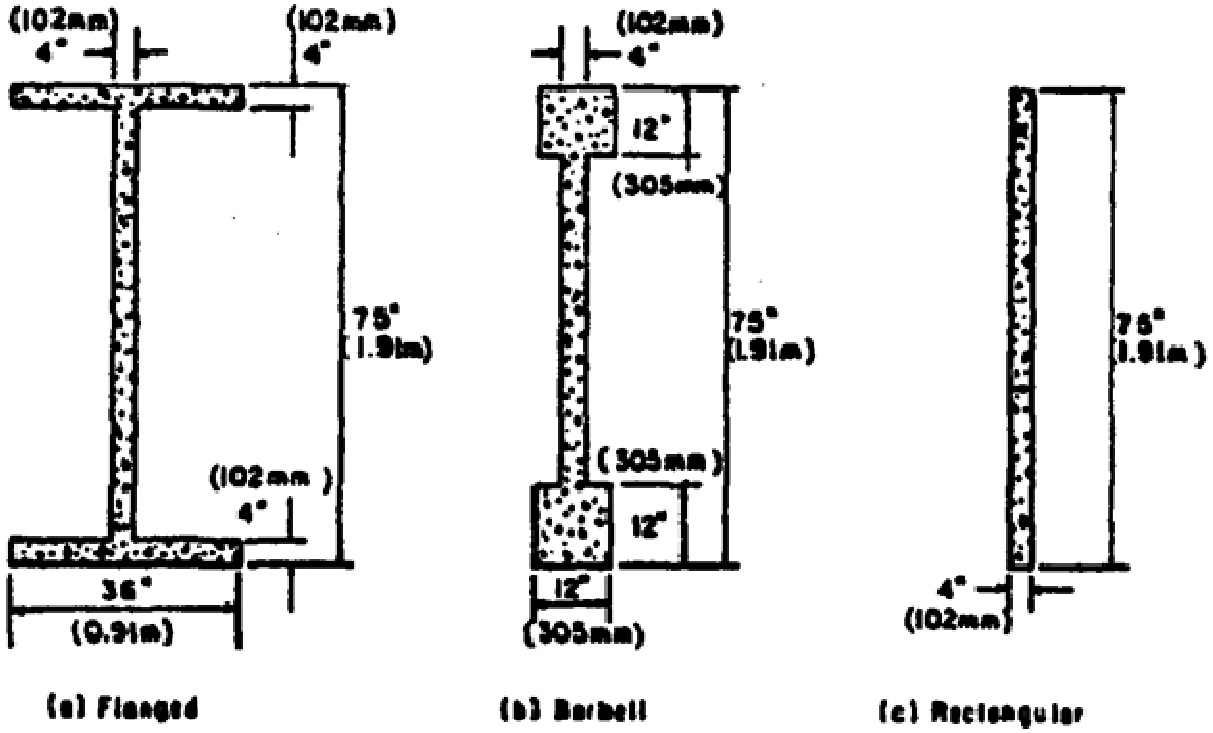

Figure 2.1 Wall sections tested by Oesterle et al. (1979)

Two failure mechanisms were generally observed in the walls tested corresponding to the level of shear stress on the wall. In walls with low maximum shear stress (i.e., $V < 3\sqrt{f_c'}$), the wall's displacement capacity was limited by buckling of the longitudinal reinforcement in the boundary elements and failure of the confined concrete. For walls with high maximum shear stress (i.e., $V > 7\sqrt{f_c'}$) the displacement capacity was limited by crushing of the web concrete. The ductility of a wall, determined from measured rotations, decreased with increased shear stress ranging from approximately 8 to 3. The researchers also noted that for walls subjected to high shear stress where crushing of the web concrete limited the performance, uniform axial load of $0.1\, f_c'$ increased the ductility of the section (Oesterle et al., 1979).

The third phase (Shiu et al., 1981) of the PCA research program consisted of testing of two 1/3-scale rectangular structural walls. The walls were 18 ft tall, 6.25 ft long, and had a uniform thickness of 4 in., simulating a six story shear wall, see Figure 2.2. With the exception of openings, the two walls were identical; one specimen had 12.5 in. by 18 in. openings cut into each story level simulating typical window openings. In the test, the wall without openings carried 14% more load; however, there were material property differences between the walls. In particular the yield strength of the primary reinforcement was different between the two walls. When the data for the two walls was normalized with respect to the reinforcing yield strength, the response is very similar leading the researchers to conclude that the presence of openings has little impact on the load versus deformation response of the walls. The primary effect of openings was that a diagonal compression strut could not form across the wall between the floor levels because of the interruption, reducing the initial shear stiffness of the wall with openings. These compression struts were observed in the wall without openings and helped resist the load. The failure to form the compression struts did not affect its lateral load or deformation capacity. Both walls experienced shear failures; the wall without openings failed due to horizontal sliding and the wall with openings failed due to shear compression failure of the boundary elements.

The researchers concluded that walls with openings should be designed as isolated walls without openings. Lintels should be then designed to fully couple the wall piers and

should not yield prior to developing yielding at the base of the wall. The design practice of placing interrupted steel evenly distributed along the opening performed well in the tests, and does not need to be changed.

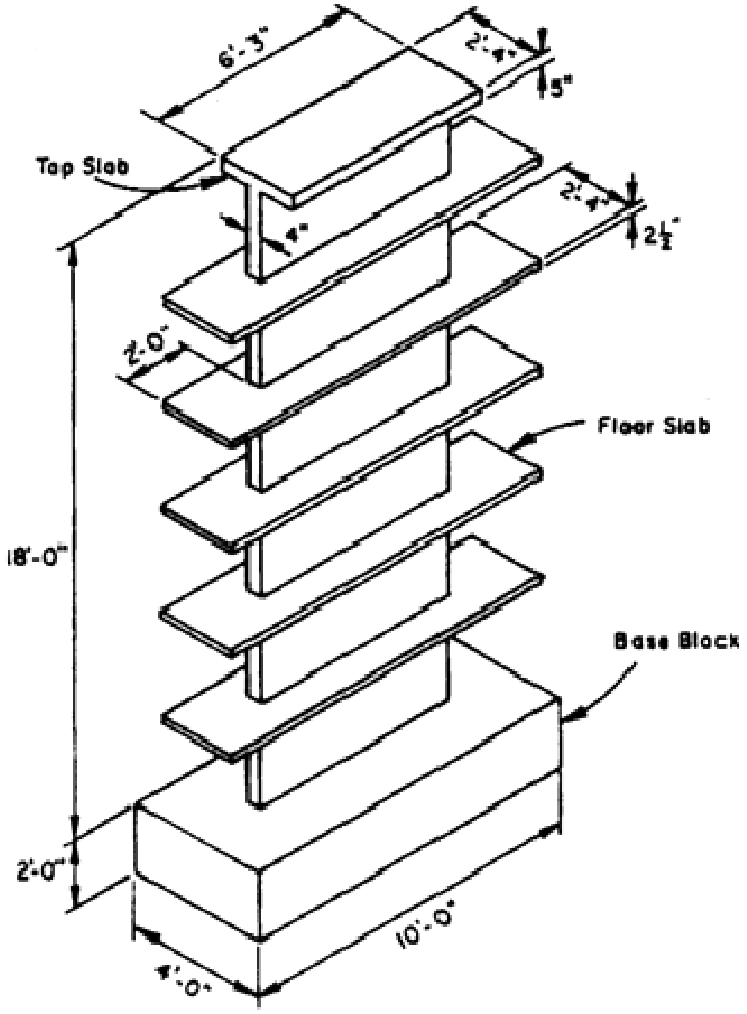

Figure 2.2 Wall specimen without openings tested by Shin et al. (1981).

2.1.2.2 Lefas and Kotsovos (1990)

The main focus of the study conducted by Lefas and Kotsovos (1990) was to investigate the effect of loading history and structural repair methods on the lateral load behavior of reinforced concrete walls. Four identical rectangular wall specimens (namely

SW30, SW31, SW32 and SW33) were tested as part of this study. The walls were 1/2.4-scale specimens with an aspect ratio of 2. The walls were 26 in. wide, 52 in. high and 2.6 in. thick. In all the specimens, the walls were monolithically constructed with the bottom and top beam. The longitudinal reinforcement was continuous across the wall-foundation interface and was properly anchored. All the four specimens were designed according to the ACI building code (ACI 318-86). The wall specimens were subjected to variable cyclic loading histories and were repaired after they experienced failure and retested under cyclic loading. From the experimental observations, it was concluded that the strength and deformational response of the walls were independent of the cyclic loading history. The walls also dissipated considerable amounts of energy before failure. It was also found that repairing only the damaged regions of the compressive zone was sufficient to fully restore wall strength, thus implying that the compressive zone was the main contributor to shear resistance.

2.1.2.3 Pilakoutas and Elnashai (1995)

Pilakoutas and Elnashai (1995) tested six 1/2.5-scale rectangular concrete walls with an aspect ratio of 2 to quantify the ductility and the energy dissipation potential of reinforced concrete walls. The test specimens namely SW4 to SW9 were 48 in. high, 23.6 in. wide and 2.4 in. thick. The walls were designed in three pairs; each pair had the same flexural reinforcement but different shear reinforcement. The flexural reinforcement was concentrated in the boundary elements to maximize the flexural capacity. The longitudinal reinforcement was continuous across the wall-foundation interface and was well anchored into the foundation block. All the test specimens were subjected to cyclic displacement with two full cycles at each peak displacement. The test setup and reinforcement details of the test specimens are shown in Figure 2.3 and Figure 2.4 respectively. It was observed that the cracks propagated from the wall boundaries toward centers and from the bottom upward. The cracks in the boundaries were horizontal, while they were inclined further away and the inclination increased along the height of the wall as shown in Figure 2.5. As the applied displacement increased, the crack density in the boundaries increased, while the main web cracks were limited to three to four on each side. All the specimens performed well with stable cyclic response. The observed force-displacement responses of the specimens are

presented in Figure 2.6. Based on the study, the researchers concluded that the strength and deformational characteristics of specimens were not affected significantly by shear reinforcement in excess of the amount needed to resist maximum applied load. It was also noted that the bulk of the energy dissipation was due to flexural action. Shear deformations, though significantly contributed to the total displacement of the wall, the authors concluded that it cannot be considered toward overall energy dissipation. It was also found by the authors that the longitudinal strains on the reinforcement near the top of the walls were found to be significantly higher than analytically expected, indicating the mobilization of possible arch and tie mechanism for shear resistance.

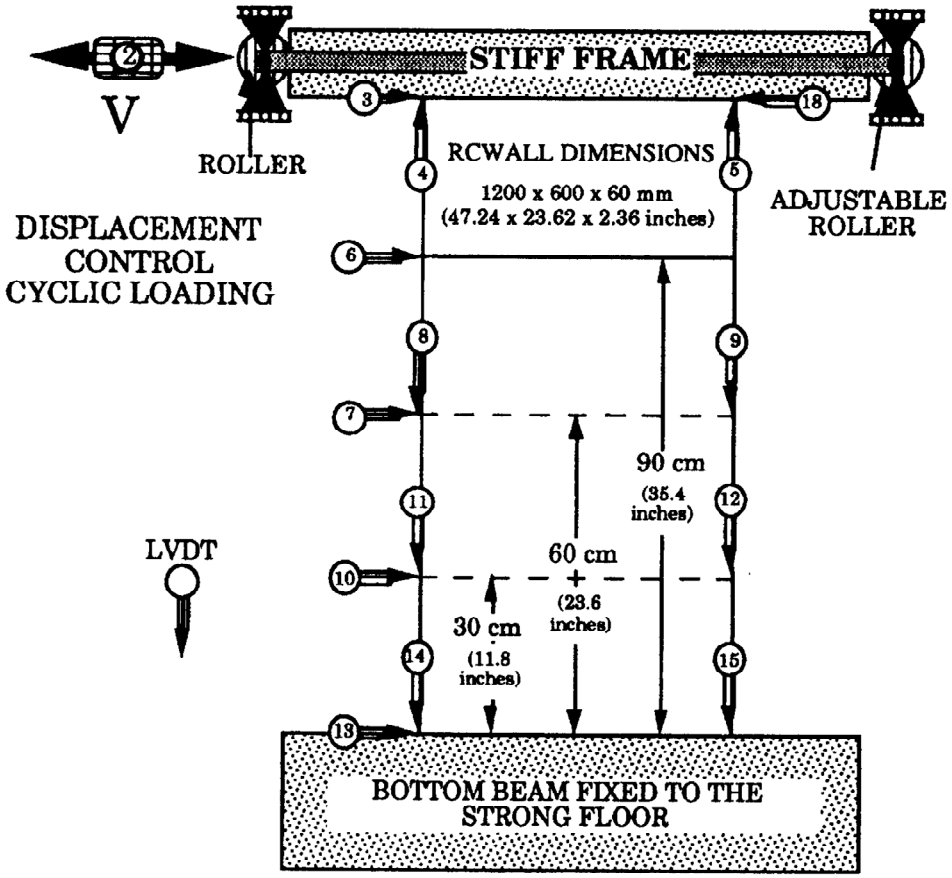

Figure 2.3 schematic of test setup used by Pilakoutas and Elnashai (1995)

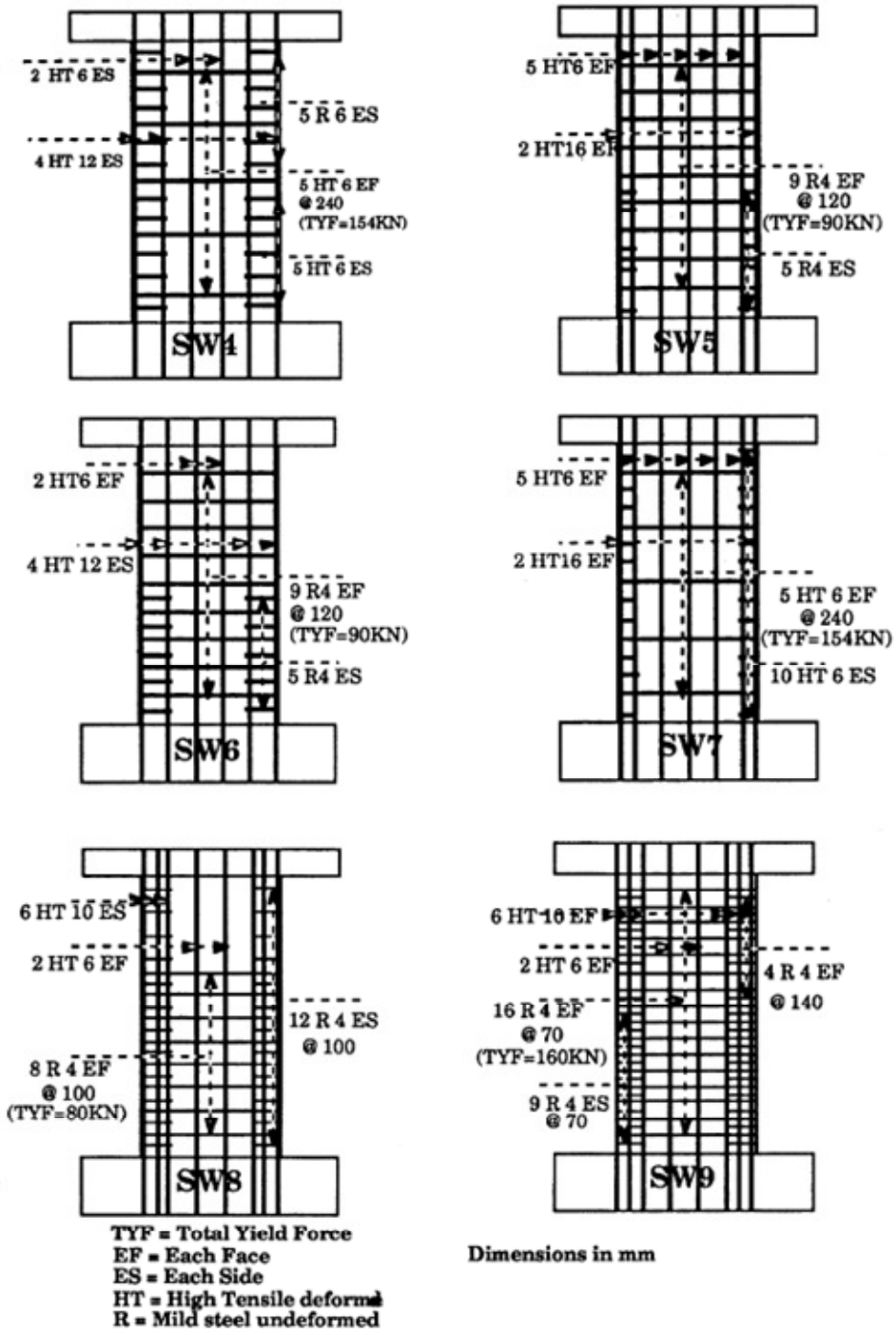

Figure 2.4 Reinforcement details of walls tested by Pilakoutas and Elnashai (1995)

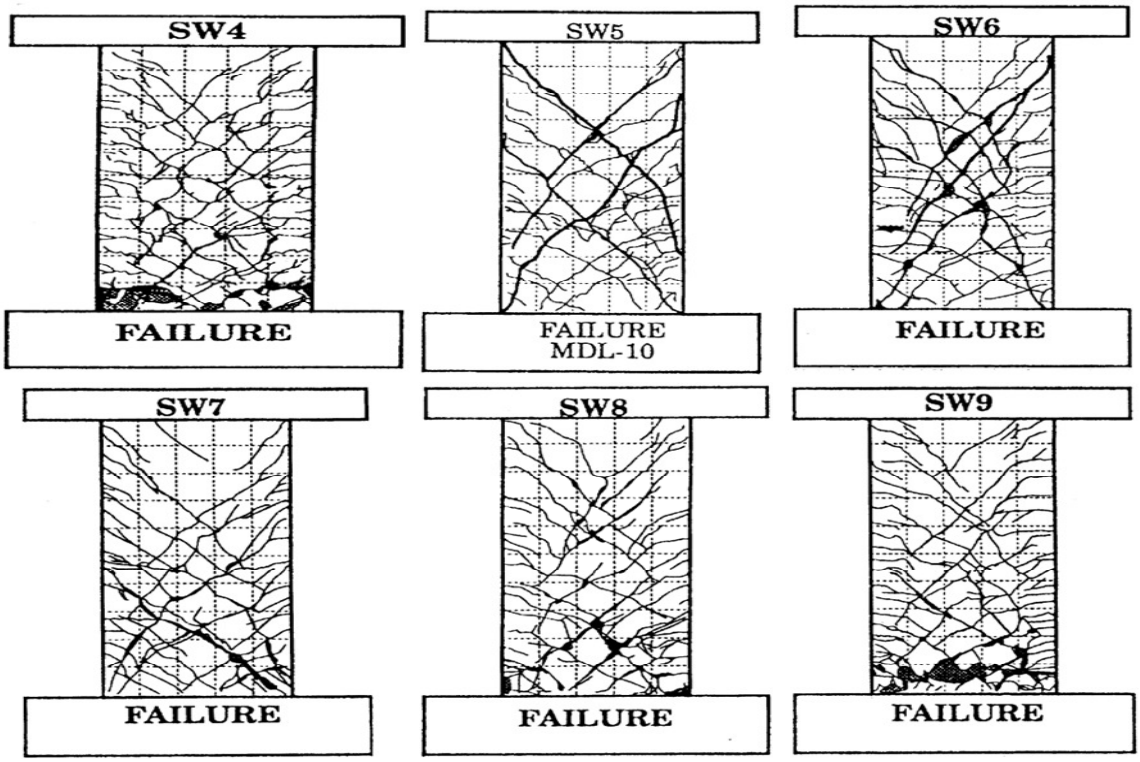

Figure 2.5 Experimentally observed crack patterns at failure in the walls tested by Pilakoutas and Elnashai (1995)

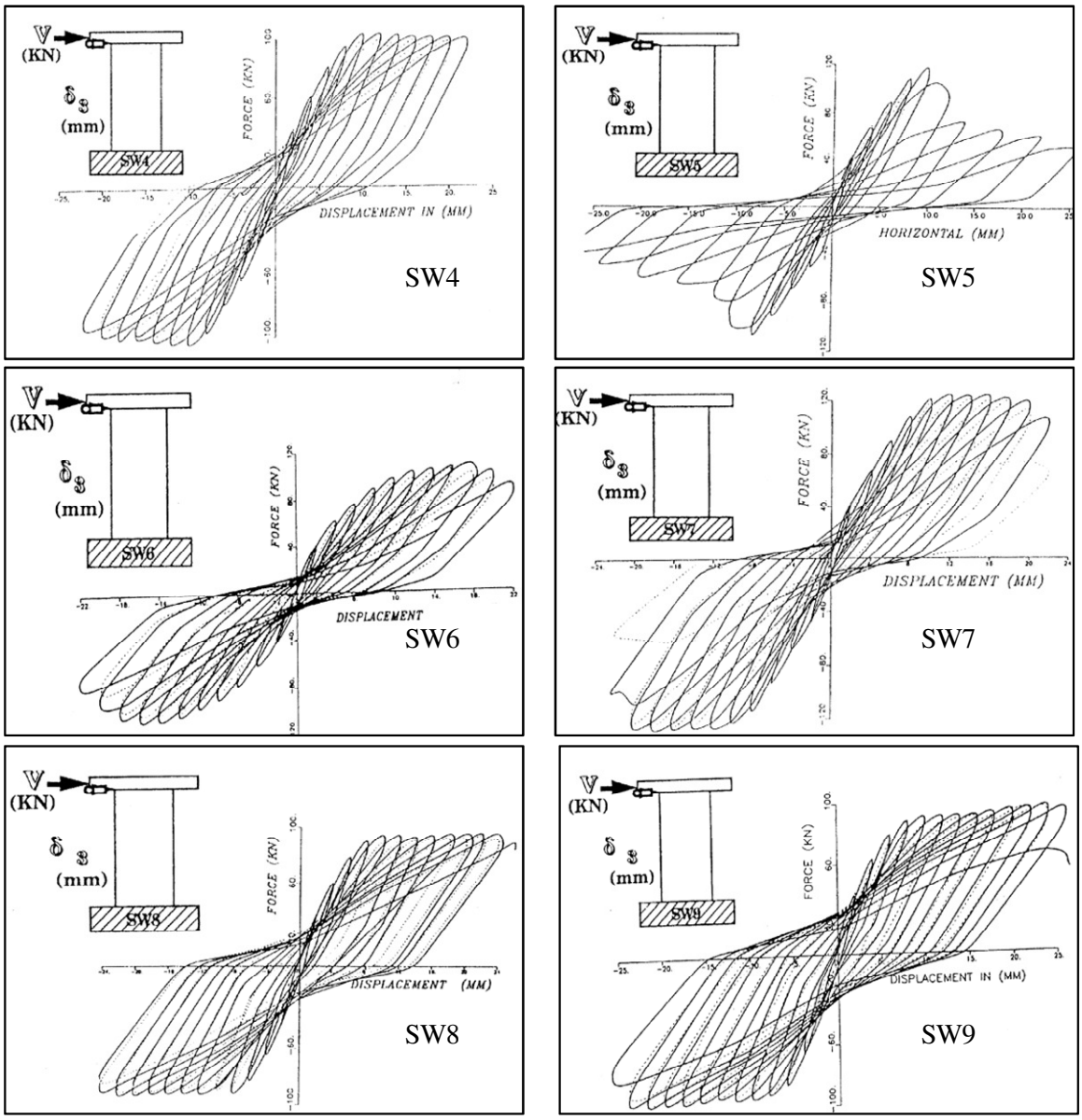

Figure 2.6 Experimental cyclic behavior of walls tested by Pilakoutas and Elnashai (1995)

2.1.2.4 Tasnimi (2000)

Tasnimi (2000) conducted an experimental investigation of rectangular concrete walls. The objective of the study was to experimentally investigate the lateral load behavior of structural walls used in mid-rise buildings, designed according to the Iranian seismic design code. As part of this study, four 1/8-scale rectangular wall specimens (i.e., SHW1,

SHW2, SHW3 and SHW4) with an aspect ratio of 3 were tested under cyclic loading. The walls were 60 in. tall, 20 in. long and 2 in. thick. All the four walls were constructed with identical dimensions and reinforcement details. The walls were monolithic; the longitudinal reinforcement was continuous across the wall-foundation interface and was well anchored into the foundation block. The specimens were subjected to cyclic displacements with increasing amplitude. The reinforcement details and the schematic of the test setup are shown in Figure 2.7 and Figure 2.8 respectively. All four specimens developed flexural cracks and inclined cracks in the critical region as expected for a flexural dominant walls. At failure, horizontal crack was formed near the wall-foundation interface, causing the lateral load carrying capacity of the specimens to drop abruptly, as shown in Figure 2.9.

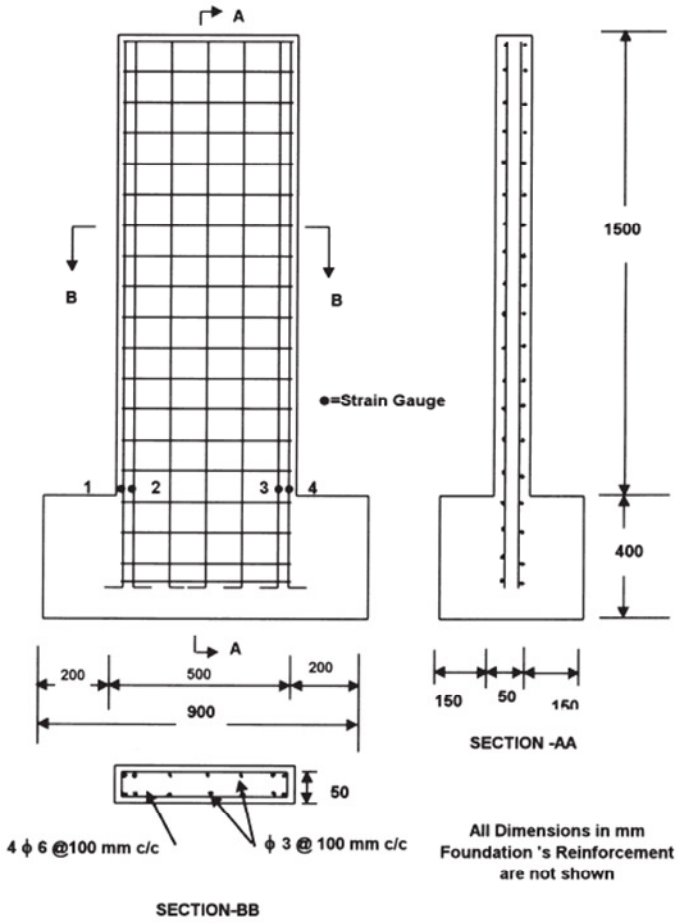

Figure 2.7 Reinforcement details of the wall specimens tested by Tasnimi (2000)

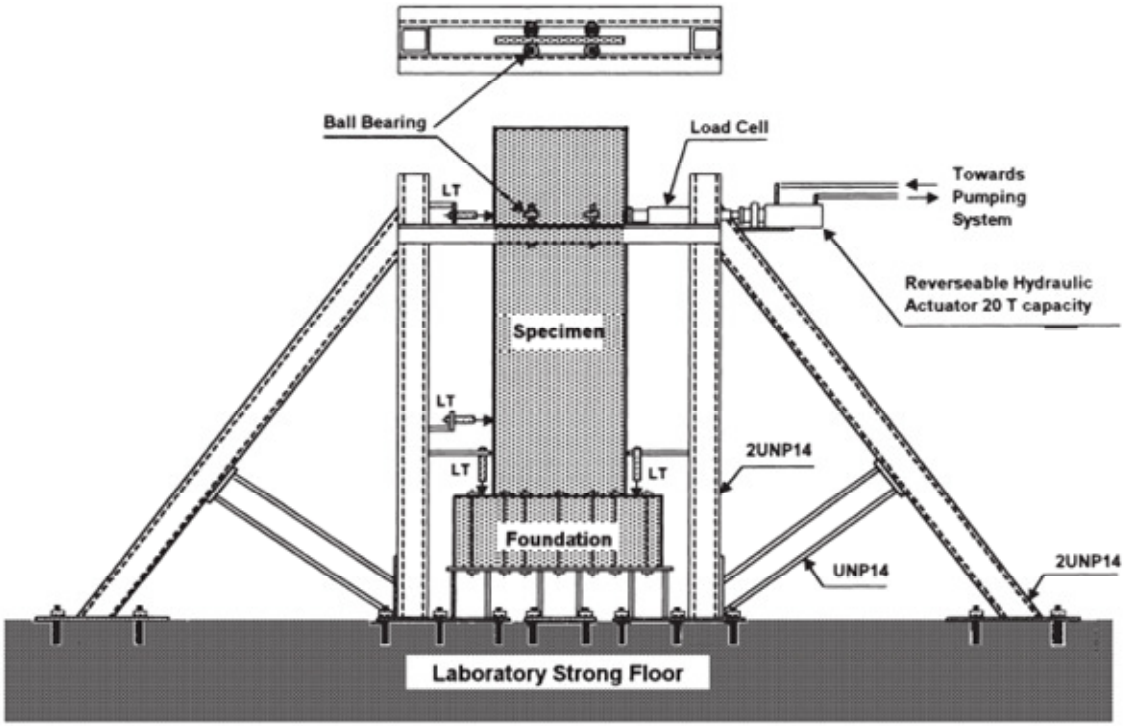

Figure 2.8 Test setup used for wall test by Tasnimi (2000)

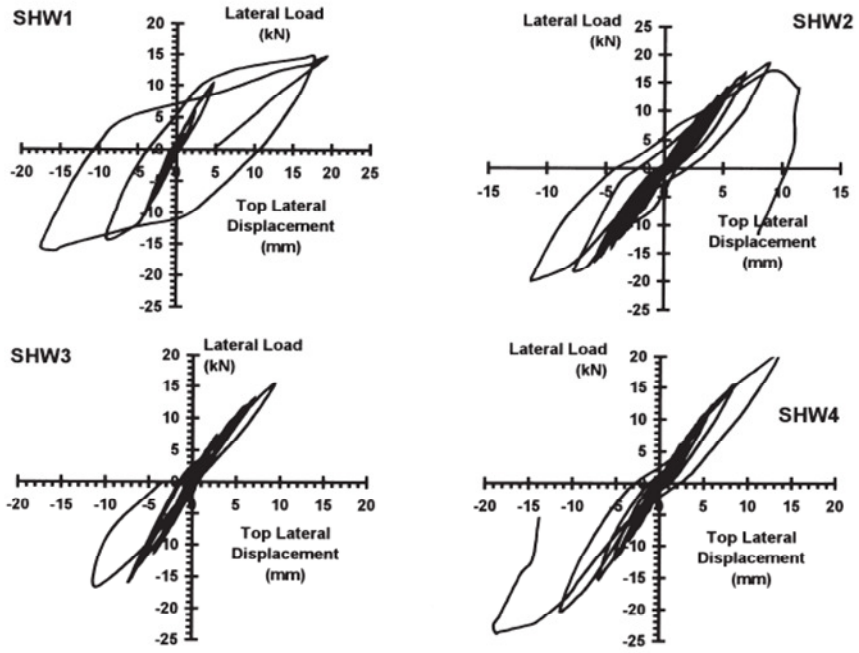

Figure 2.9 Lateral load versus top horizontal displacement loops obtained for the tested specimens (Tasnimi, 2000)

2.1.2.5 Zhang and Wang (2000)

Four rectangular walls (namely SW7, SW8, SW9 and SWCW12) were tested to understand the influence of high axial load ratio on the lateral load behavior of flexural dominant walls. Each specimen was tested under combined action of constant axial load and horizontal load reversals. Two parameters were considered and varied in the specimen design, that is, axial-load ratio and shear compression ratio. It was found from past experiments that the shear compression ratio is an important parameter that affects the post yielding behavior of shear walls. The specimens were designed to experience flexural failure mode. All the walls were 70 in. tall, 28 in. long and 4 in. thick. The longitudinal reinforcement was continuous across the wall-foundation interface and was well anchored into the foundation. The reinforcement details and the schematic of the test setup are shown in Figure 2.10.

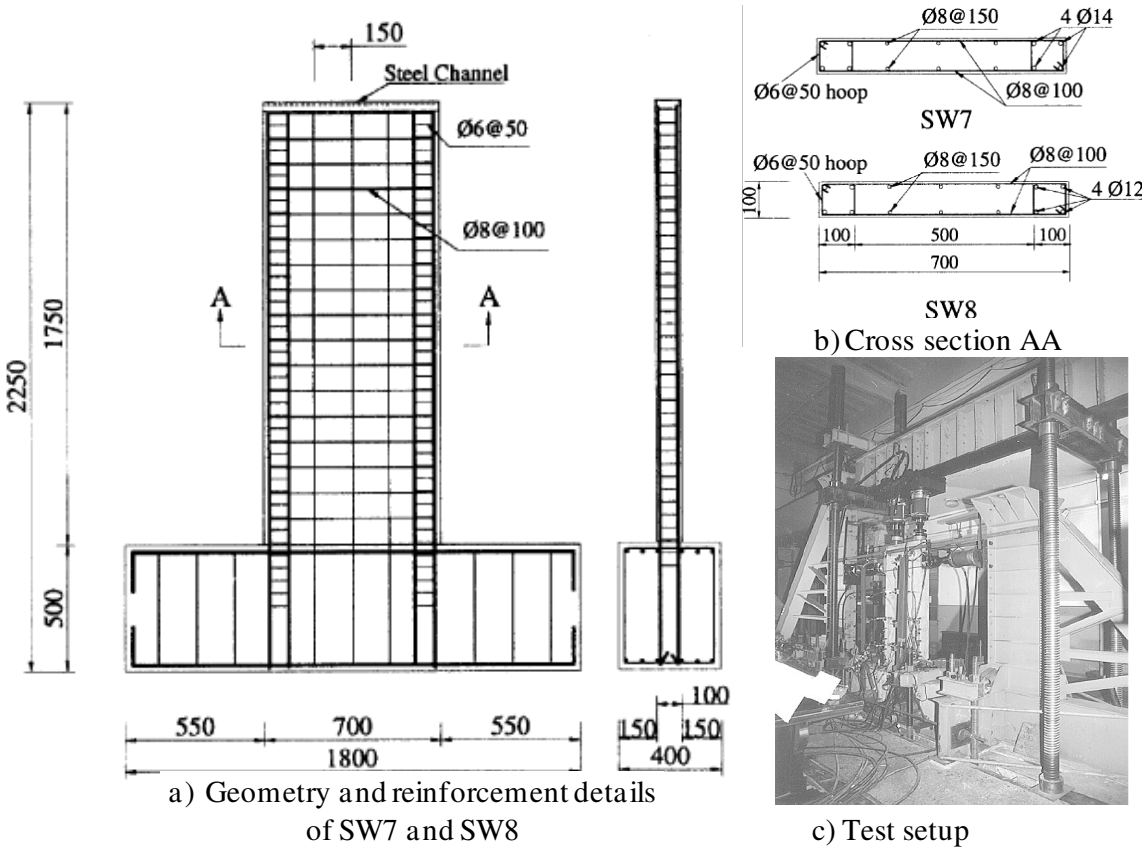

Figure 2.10 Reinforcement details of the SW7 and SW8 (Zhang and Wang, 2000)

All the four walls exhibited similar cyclic behavior and experienced a comparable crack pattern along the wall height, except that the load at which first crack was observed varied depending on the axial load ratio. The observed lateral load response of SW7 and SW8 is shown in Figure 2.11. Axial-load ratio had an important effect on the failure mode, stiffness, and ductility of the walls. In this study, the wall specimen subjected to a high axial-load ratio of 0.35 exhibited an undesirable out-of-plane buckling failure mode in the post yielding stage, whereas the wall specimen with an axial-load ratio of 0.25 and shear compression ratio of 0.11 exhibited a more favorable boundary element crushing failure mode with relatively high ductility. It was also found that the shear compression ratio affected the post yielding behavior of shear walls. Higher shear compression ratio resulted in development of extensive criss-crossing cracks (see Figure 2.12) in the web of the wall.

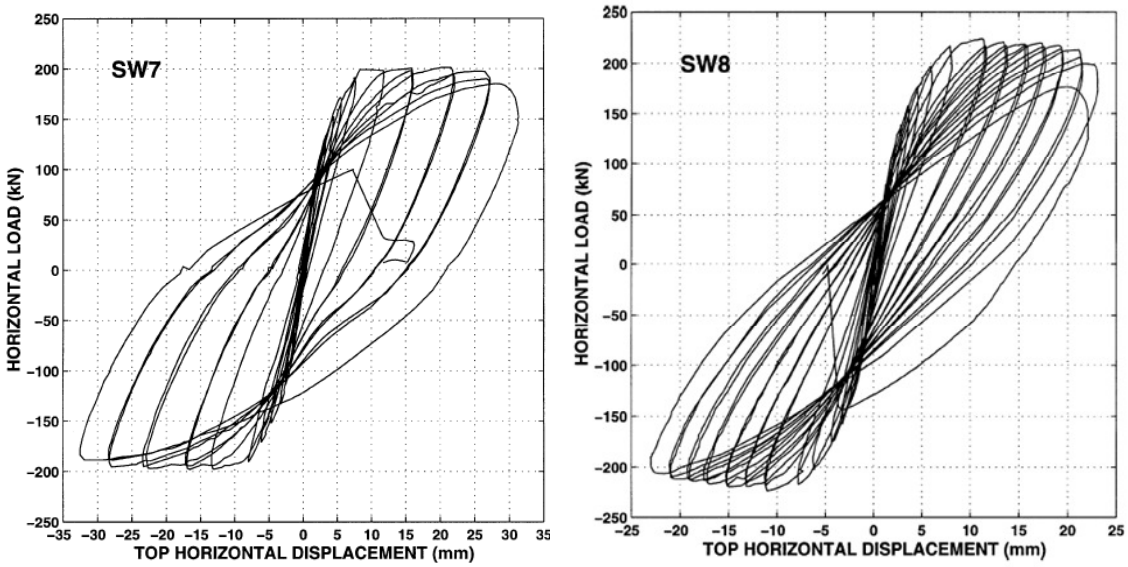

a) SW7 response b) SW8 response

Figure 2.11 Force-displacement hysteresis response of SW7 and SW8 (Zhang and Wang, 2000)

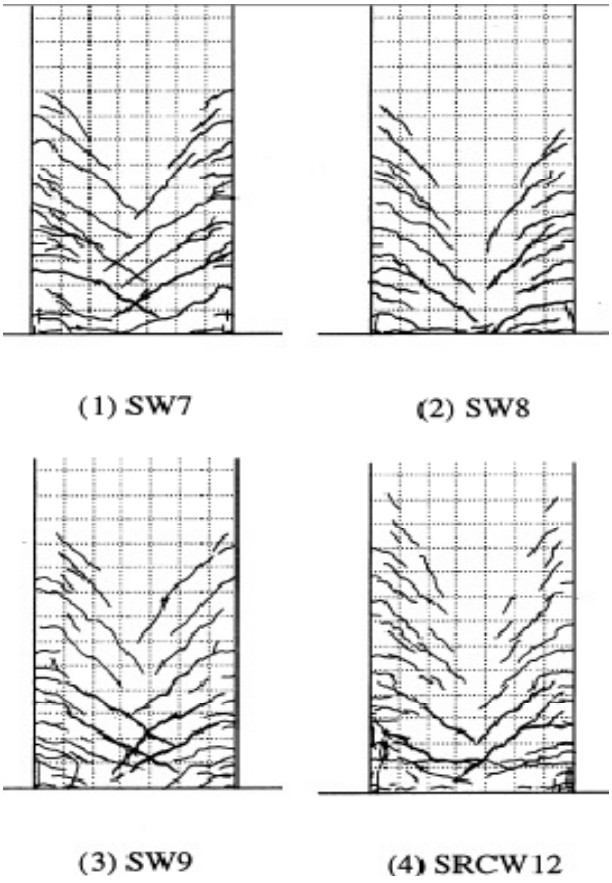

Figure 2.12 Cracking pattern at failure in walls tested by Zhang and Wang (2000)

2.1.2.6 Riva et al. (2003)

In this study, Riva et al. (2003) experimentally investigated the lateral load behavior of a full-scale rectangular concrete wall. The scope of their research was to partially fill the gap concerning full scale tests on slender walls, and also analyze the wall with a particular attention to the ductility, energy dissipation capability and the resisting mechanisms. The test specimen was representative of four storey shear building and was designed according to the Euro code 8 (EC8). The wall was 41.67 ft high, 9.33 ft wide and 12 in. thick. The longitudinal reinforcement was continuous across the wall-foundation interface. Due to the specimen size and readily available test setup shown in Figure 2.13, the wall specimen was tested horizontally by subjecting it to cyclic loads and displacements with increasing amplitudes, as shown in Figure 2.14. The lateral loads were applied at two points by means of hydraulic jacks. The position of the jacks were defined to obtain the same bending

moment and shear force around the critical section as the one resulting from the analysis of the four storey building.

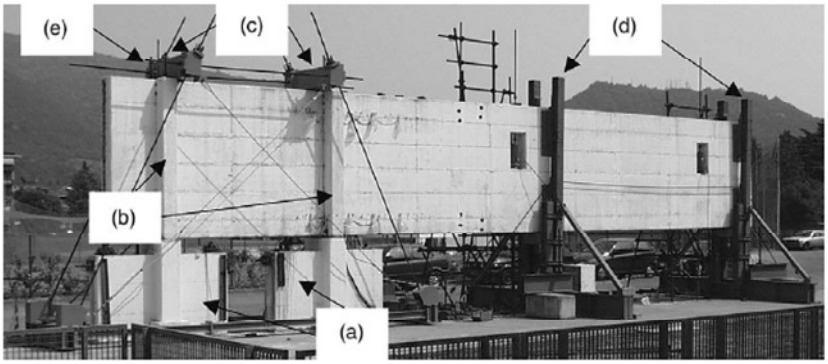

Test set-up: wall supports (a); ribs simulating the ground and basement floor diaphragms (b); post tensioned strands and bars (c); steel frame to avoid lateral instability (d); additional frames for improving safety in the test set-up (e).

Figure 2.13 Test setup used for the testing of a full-scale reinforced concrete wall by Riva et al. (2003)

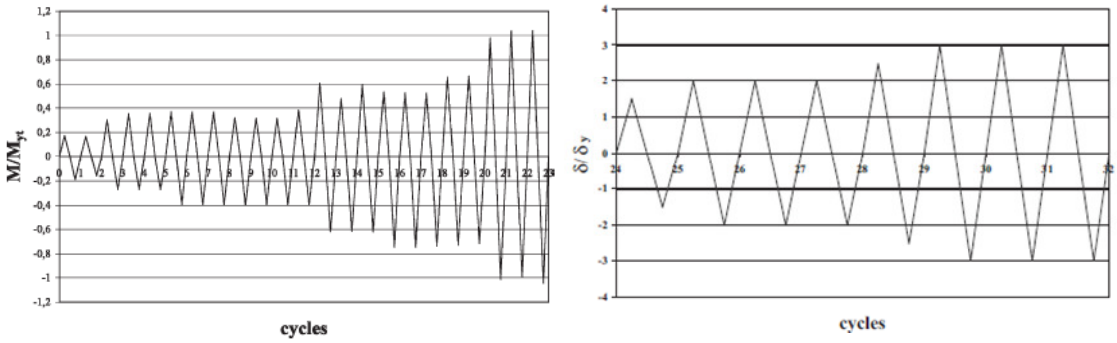

a) Loading history up to the theoretical yield load: *M/Myt versus* cycle number

b) Loading history after the structural yield load: δ/δ_y versus cycle number.

Figure 2.14 Applied cyclic force and displacement history for the wall specimen tested by Riva et al. (2003)

Prior to the yielding of the longitudinal reinforcement, the main cracks in the critical zone had limited inclination, proving that the behaviour was governed by bending due to high aspect ratio. The observed cyclic response is shown in Figure 2.15. The crack distance was close to the stirrup spacing in the external chords, where longitudinal reinforcement was concentrated, while in the middle part of the critical section the cracks were tend to merge into a lower number of cracks, characterized by larger opening and greater inclination, thus

showing the influence of shear stress. In the post-yield stage, a progressive damage with increased imposed displacement was observed. The damage was mainly localized at the critical section, with a wide crack (2 in. at mid depth of the wall) observed near the base of the wall. Concrete spalling, crushing of concrete, rebar yielding was observed in confined regions. At the end of the test, the wall specimen failed in shear along the wide crack. It was due to shear as a consequence of a lack of longitudinal reinforcement in the wall web (i.e., the wall between the boundary elements). It was concluded that the amount of web reinforcement provided in accordance to EC8 was not enough to limit the observed crack opening, and friction contribution to shear strength resulted in being much smaller than expected.

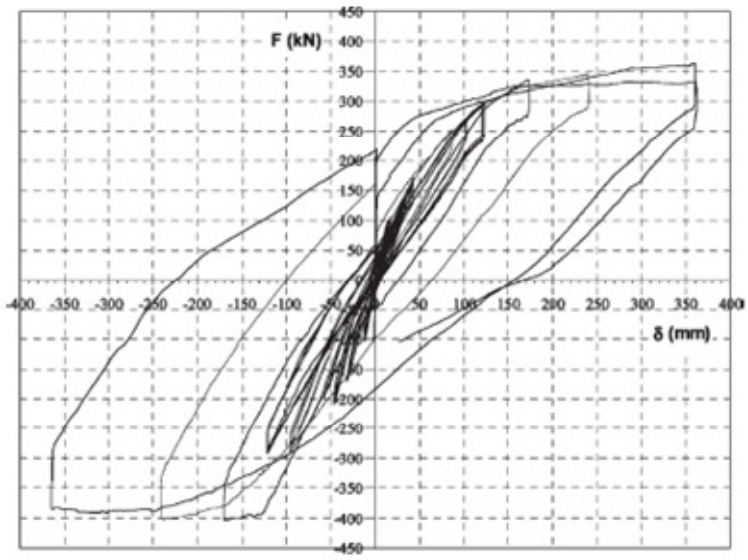

Figure 2.15 Measured cyclic response of the test specimen tested by Riva et al. (2003)

2.1.2.7 Dazio et al. (2009)

Dazio et al. tested six large-scale reinforced concrete cantilever walls under quasi-static cyclic loading to investigate the effects of different vertical reinforcement contents and different reinforcement ductility properties typical for the Central Europe on the deformation behavior of slender reinforced concrete walls. Various design variables such as, the longitudinal reinforcement layout and content, the ductility properties of the reinforcement, the confining reinforcement, and the applied axial load were varied among the specimens.

The geometry and reinforcement details of the test specimens are shown in Figure 2.16 and Figure 2.17.

The test specimens were half-scale models of the lower part of a reinforced concrete wall in a six-storey reference building. The six specimens were labeled WSH1 to WSH6 respectively. They were 6.56 ft long and 6 in. thick. The length of the shear span of the specimens was 14.96 ft for WSH1 to WSH5 and 14.83 ft for WSH6, corresponding t shear span ratios or the aspect ratios of 2.28 and 2.26, respectively.

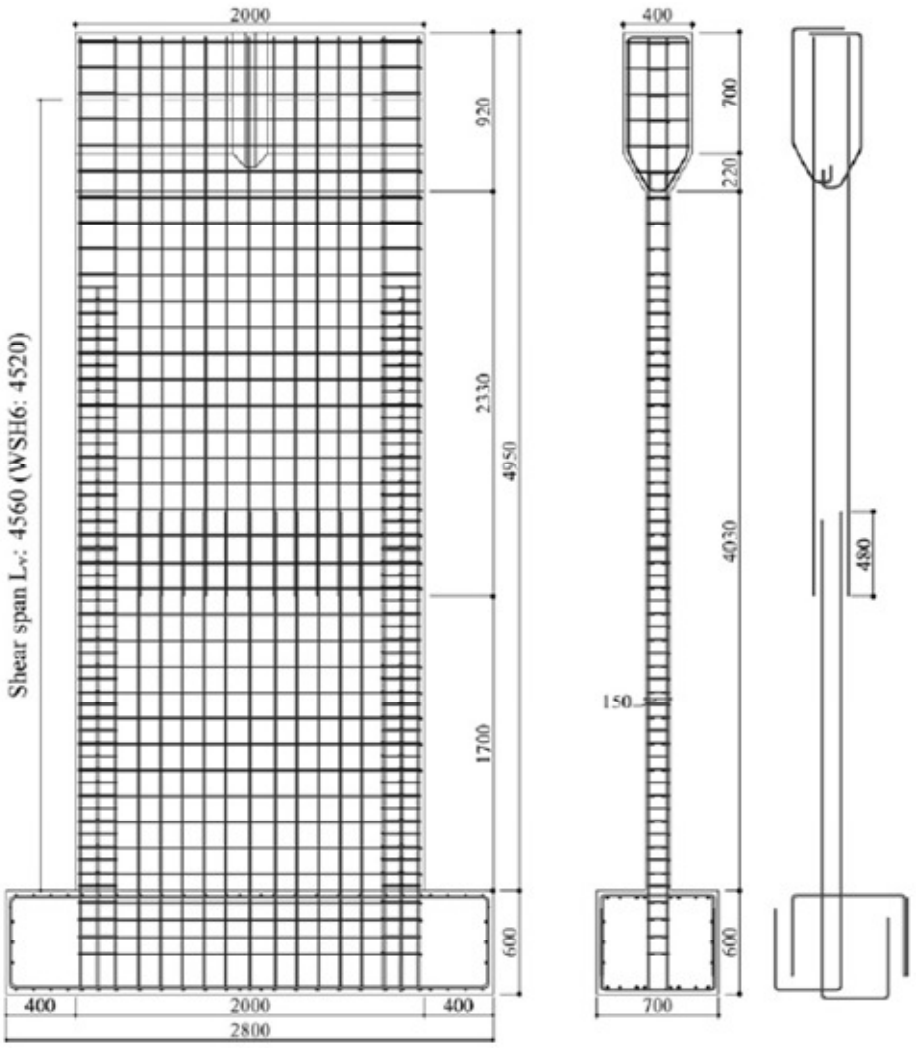

Figure 2.16 Vertical reinforcement layout of Test Unit WSH3 tested by Dazio et al (2009) (All dimensions in mm. 25 mm = 1 in.)

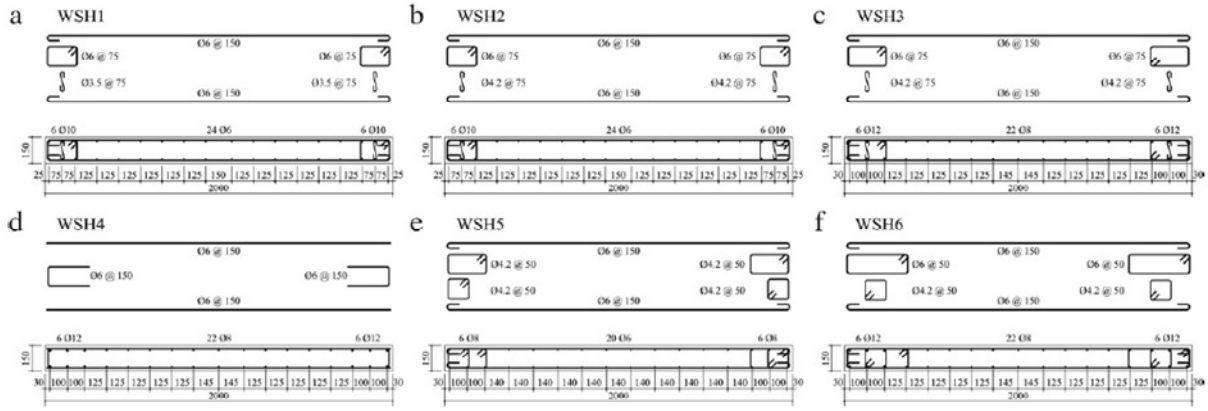

Figure 2.17 Reinforcement layout in the plastic zone of the test units (All dimensions in mm) (Dazio et al. (2009))

All the specimens were subjected to reverse cyclic loading with load applied at the top of the wall. The loading history corresponded to the standard protocol recommended by Park (1998). The first step of the testing protocol was the application of the axial load, which was kept constant throughout each test. Subsequently, the horizontal cyclic displacement history was applied to the top of wall by an actuator with two load cycles at each ductility level. The first two cycles of the loading protocol were force controlled while the rest of the test was performed under displacement-control.

All the wall specimens performed satisfactorily under cyclic loads with stable response, good ductility and energy dissipation capabilities. The observed hysteresis responses of the test specimens are shown in Figure 2.18. The experiments showed that the crack patterns of the six test units were not equally developed at yield capacity of the walls. For walls for which the axial load contributed significantly to the moment resistance (e.g., WSH5) the crack pattern was less developed than for walls with large flexural reinforcement ratios (e.g., WSH3) and therefore the estimates of the yield displacement of the walls differed considerably. All six specimens failed in a flexural mode and for all the specimens the flexural deformations were considerably larger than the shear deformations. At larger drifts, in WSH1, WSH2, and WSH5 flexural deformations were concentrated towards the base of the wall, while in WSH3, WSH4, and WSH6 the flexural deformations are distributed over a

larger portion of the wall.

The longitudinal web reinforcement in specimens WSH1, WSH2, and WSH5 fractured prematurely compared to the boundary element reinforcement. This was caused due to reduced spread of plasticity, smaller number of wider cracks in the web region due to the variation of the location and quantity of the vertical reinforcement, strain concentration at a crack due to the improved bond of the small diameter of the longitudinal web reinforcement when compared to the boundary region longitudinal reinforcement.

Based on the experimentally observed behavior of the six specimens, the authors concluded that walls with low longitudinal reinforcement ratios tend to have reduced flexure-shear cracking. Also, the smaller hardening ratio of the longitudinal reinforcement affected the spread of the plasticity causing the strain concentrations at the base of the wall and the reduced deformation capacity. It was also noted that the ductility properties of the longitudinal web reinforcement is as important as that of the boundary region reinforcement to achieve a good ductile response. In summary, the experiments showed the reduced deformation capacity of reinforced concrete structural walls with low longitudinal reinforcement content and this effect was further increased if reinforcing bars with low ductility properties were used.

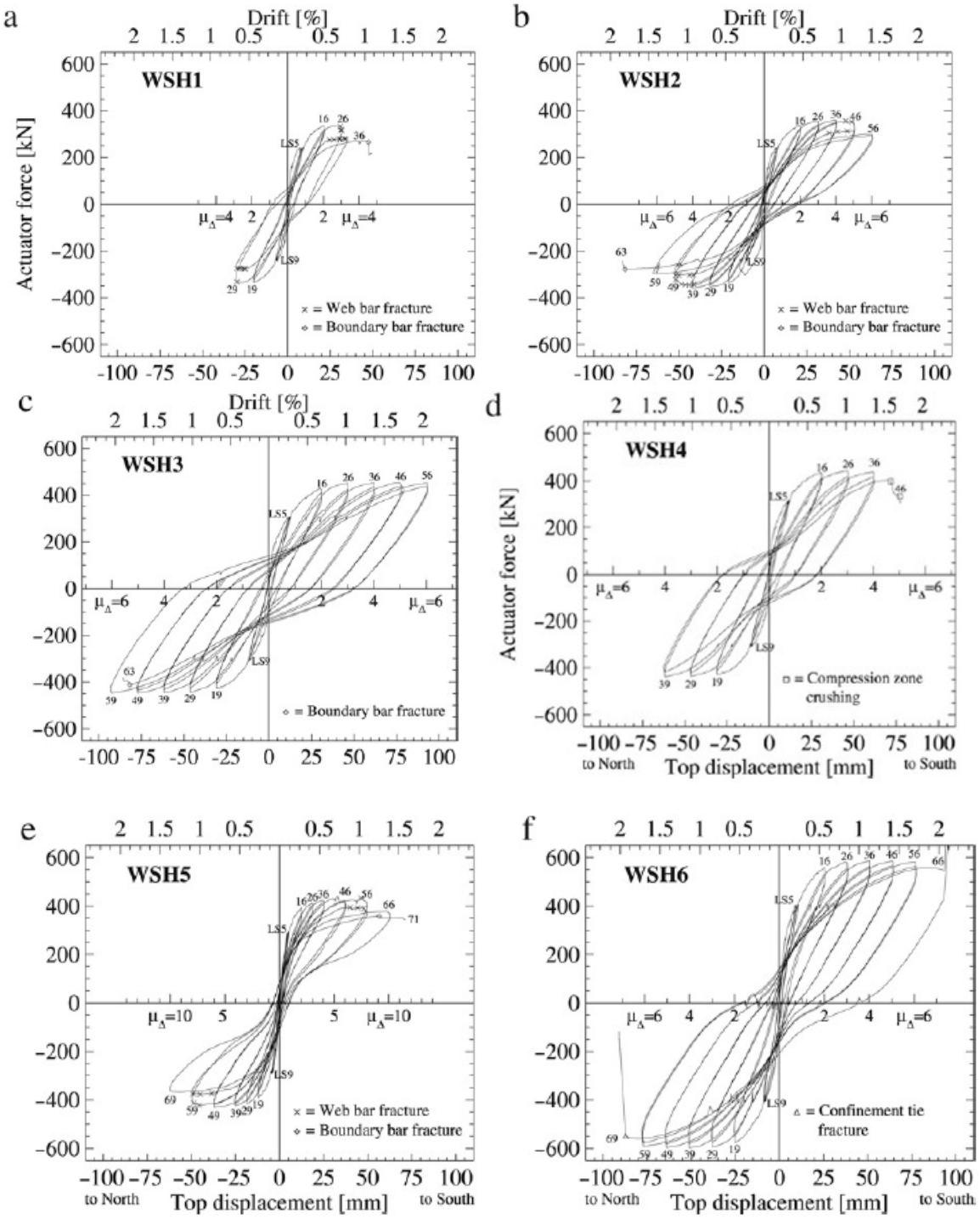

Figure 2.18 Measured force-displacement hysteresis response of the six wall units tested by Dazio et al. (2009)

2.1.2.8 Ghorbani-Renani et al. (2009)

The aim of this experimental study was to investigate the scaling effects on the inelastic behavior of ductile reinforced concrete shear walls designed and detailed according to seismic requirements of the National Building Code of Canada and CSA-A23.3-04 under monotonic and cyclic loading. The experimental program consisted of testing of four reinforced concrete walls; of which two of them were full scale specimens (Series A), while other two were of 1:2.37 reduced scale specimens (Series B). The test specimens were designed to reproduce the loading conditions and construction details of a typical shear wall used in a 10-story residential building located in Vancouver, BC, Canada. The full-scale test specimen was 4.26 ft long, 8.85 ft tall and 8 in. thick. The details of the reinforcement of the test specimens are shown in Figure 2.19. More details about reinforcement and material properties of the specimens are presented in Ghorbani-Renani et al. (2009).

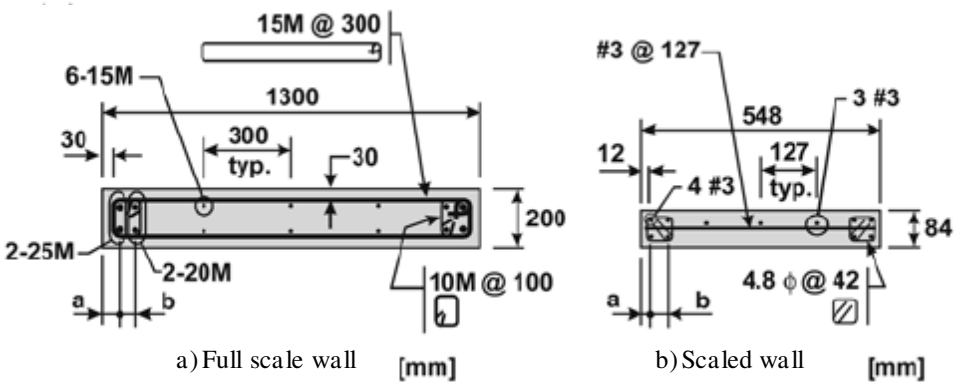

Figure 2.19 Reinforcement details of the full scale and 33% scaled wall specimens tested by Ghorbani-Renani et al. (2009)

One specimen pair was subjected to monotonic loading (A1M and B1M), whereas cyclic loading was applied to the other two walls (A2C and B2C). No axial load was applied on the wall specimens. In the cyclic tests, a displacement controlled loading history based on the ATC-24 protocol (ATC 1992) was adopted: three cycles at $\pm 0.33\Delta_y$, $\pm 0.66\Delta_y$, $\pm 1.0\Delta_y$, $\pm 2.0\Delta_y$, and $\pm 3.0\Delta y$, followed by two cycles at Δ_y, two cycles at $0.03h_w$, and two cycles at $0.04h_w$, where h_w is the height of the test specimen.

The normalized lateral load-lateral deformation response under monotonic loading for

Specimens A1M and B1M (see Figure 2.20) was nearly identical up to $\Delta/h_w = 0.0348$, where failure in tension of one of the longitudinal bars occurred in the model wall. Inspection after the test revealed that this bar suffered some damage during the installation of the instrumentation. In the cyclic tests, both the full-scale and reduced-scale wall specimens exhibited a stable hysteric response dominated by flexure up to a displacement ductility of 4.0. Upon flexural inelastic response, inelastic shear deformations progressively developed in the plastic hinge region of the wall reaching approximately 20% of the total wall deformations at ductility of 4.0. The shear deformations were linearly proportional to the measured flexural displacements. At a ductility of 4.0, shear sliding started to develop in both tests, which led to significant strength degradation of the wall specimens. For both full-scale and reduced-scale specimens, the monotonic response matched the envelope of the cyclic response before strength degradation occurred after ductility of 4. Based on these test observations, it was concluded that reduced scale models designed with a scaling factor of up to 2.4 and constructed with normal concrete mixtures and deformed bars for the main reinforcement could be used to examine the seismic response of ductile reinforced concrete walls, including inelastic flexural and shear deformation effects and shear sliding mechanisms.

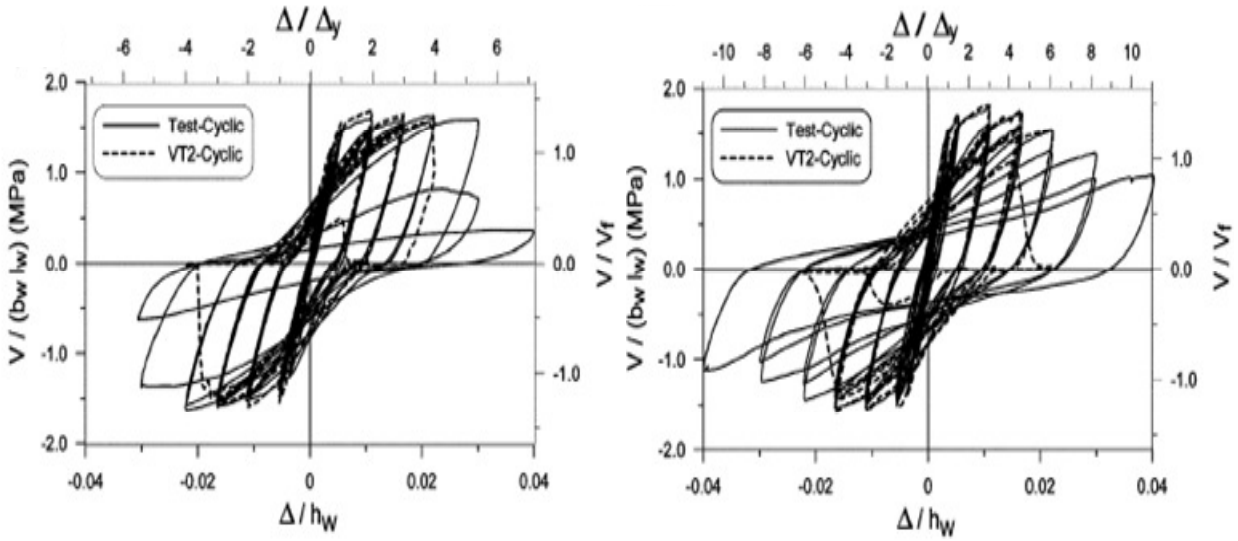

Figure 2.20 Measured normalized shear force vs. top drift response of test specimens tested by Ghorbani-Renani et al. (2009)

2.1.2.9 Shimazaki (2008)

Recent increased emphasis and interest on damage control design of structures, the focus of the Shimazaki (2008) experimental program was to examine the behavior of reinforced concrete shear walls with de-bonded diagonal reinforcements to reduce the expected damage to walls and improve repairability. As part of this experimental program, three rectangular wall specimens of 5.9 ft (1.8 m) height, 2.95 ft (0.9 m) width and 4.8 in. (120 mm) thickness were tested.

WP1 was a conventional reinforced concrete wall with vertical longitudinal reinforcement continuous across the wall-foundation interface. Specimen WX1 had de-bonded diagonal reinforcements arranged instead of the edge vertical reinforcing bars of six #4 (or D13) bars of WP1, and additional 6-D6 bars were arranged at that place for confining bars. The reinforcing bars were debonded using a de-bond tape (butyl type rubber, Saint Tuck Sheeler) and gummed tape. WSX1 and WSX2 were made from precast panels containing debonded edge vertical longitudinal bars tied together using fixing plates (see Figure 2.21) at the panel boundaries. The reinforcement details of the wall specimens WX1 and WSX2 are shown in Figure 2.22.

Figure 2.21 Fixing plates used by Shimazaki (2008) to tie the debonded vertical reinforcement together

The specimens were subjected to cyclic horizontal force applied at the top of the wall under constant axial compression load of 88 kips (392 kN). All the wall specimens performed well and produced stable cyclic responses. At 0.5% drift, the flexural shear cracks

were prominent for WP1, whereas for WX1, the horizontal crack region was wide and there were few diagonal shear cracks. Only a few diagonal cracks were observed in WSX1 and WSX2. At 1% drift, signs of concrete crushing were observed at the bottom corners of all specimens.

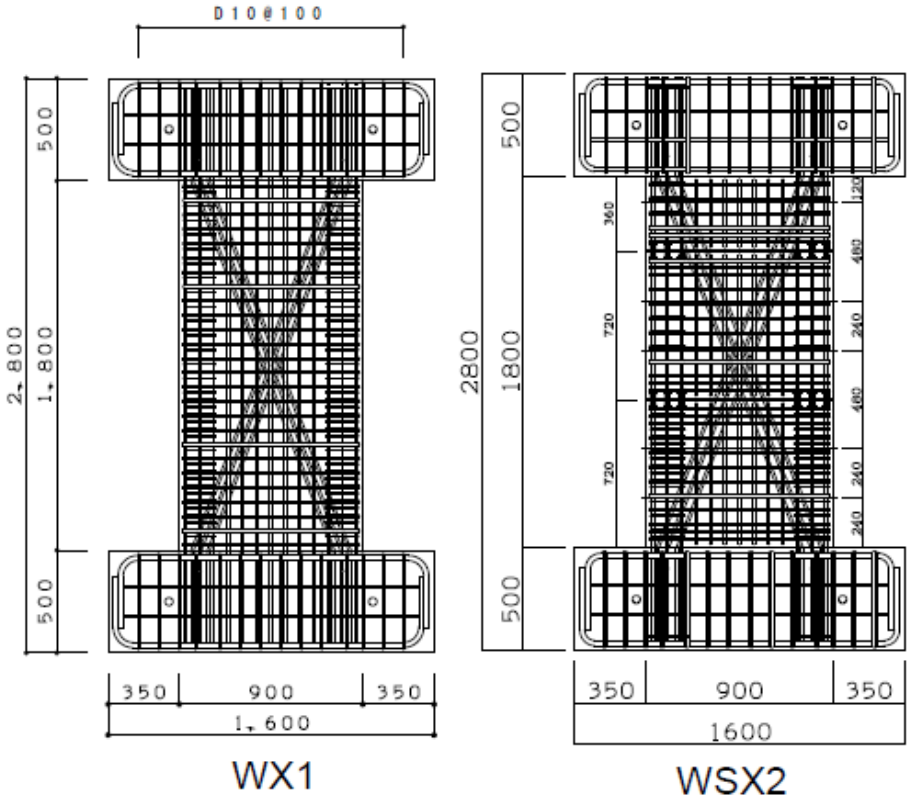

Figure 2.22 Reinforcement details of specimens WX1 and WSX2 tested by Shimazaki (2008) (all dimensions are in mm.)

The shear deformation accounted for over 50% of the total deformation for the common reinforced concrete wall WP1. However, wall WX1 with the de-bonded X type reinforcing bars, the shear deformation accounted for only 20% of the total measured top deformation. This is a direct result of decreased shear cracking of WX1. The flexural deformation accounted for over 85% in WSX1, for which the panel wall was divided at each story level, and 90% in WSX2 in which wall was divided in the horizontal direction into three parts. The energy dissipation capacity of WX1, WSX1 and WSX2 were nearly identical (see Figure 2.23), though the damage to WX1 was more than other two specimens.

Based on the observed lateral load behavior of the wall specimens, it was concluded that the debonded x-type reinforcement decreased the shear demand on the wall panels and resulted in decreased cracking and improved repairability.

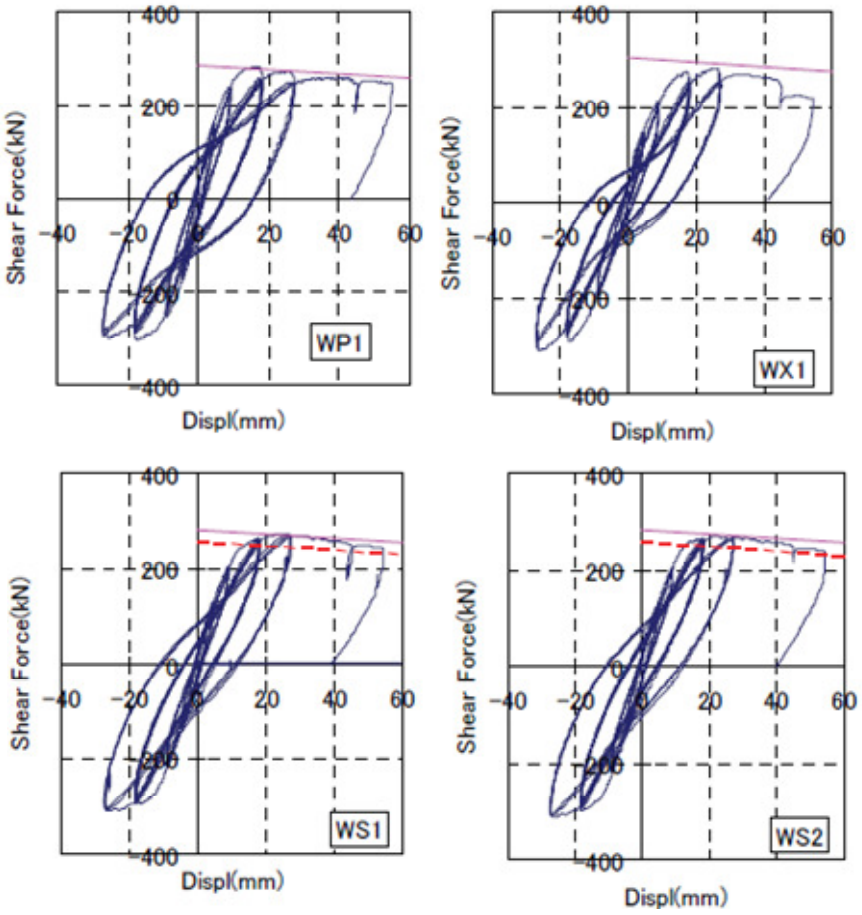

Figure 2.23 Measured cyclic response of test specimens WP1, WX1, WSX1 and WSX2 tested b Shimazaki (2008)

2.1.2.10 Thomsen and Wallace (1995)

Thomsen and Wallace conducted an investigation on the behavior of structural walls with rectangular and T-shaped cross-sections. The walls were selected based on a prototype building multi-story office building located in a high seismic region; see Figure 2.24 for the floor plan of the prototype building. The building was six stories tall, and incorporated both rectangular and T-shaped walls as well as moment resisting concrete frames to resist lateral and gravity loads.

Thomsen and Wallace used a displacement-based design procedure to determine estimates of the lateral roof displacement and story drifts of the prototype structure. In this procedure, individual walls were designed based on the required global deformations The section analysis program BIAX (Thomsen & Wallace, 1995) was used in the design procedure to determine the flexural strength of walls, transverse steel in the boundary elements, and the required shear strength of the wall. They wanted to show that their displacement-based design method effectively designed both rectangular and nonrectangular walls. The rectangular wall was designed considering the forces corresponding to the in-plane response, while the T-shaped wall was designed considering the forces in the plane of the flange and in the plane of the web.

The prototype rectangular wall was 192 in. long by 16 in. thick. The prototype T-wall was 192 in. wide at the flange and was 192 in. deep; both the flange and the web were 16 in. thick. The rectangular and T-walls were 864 in. tall in the prototype structure. Once the designs for the rectangular and T-shaped walls in the prototype structure were completed, four 1/4-scale test specimens were designed and constructed. They were identified as RW1, RW2, TW1, and TW2. The dimensions and reinforcement details of rectangular specimens RW1 and RW2 are shown in Figure 2.25 and Figure 2.26 respectively. RW2 differed from RW1 by using a closer spacing for the transverse reinforcing steel in the boundary elements to suppress buckling of the longitudinal reinforcement and allow the confined concrete to control the lateral load behavior of the wall. However, the diameter of the transverse reinforcement was not changed, increasing the volumetric ratio by 50% thereby greatly increasing the confinement effects to the concrete.

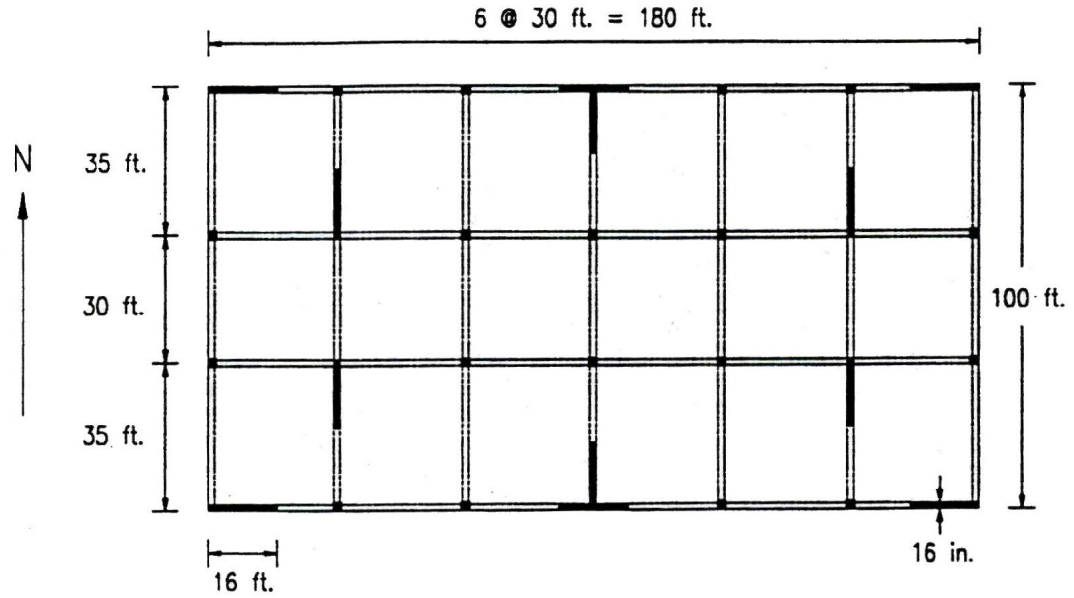

Figure 2.24 The floor plan of the prototype building chosen by Thomsen & Wallace (1995)

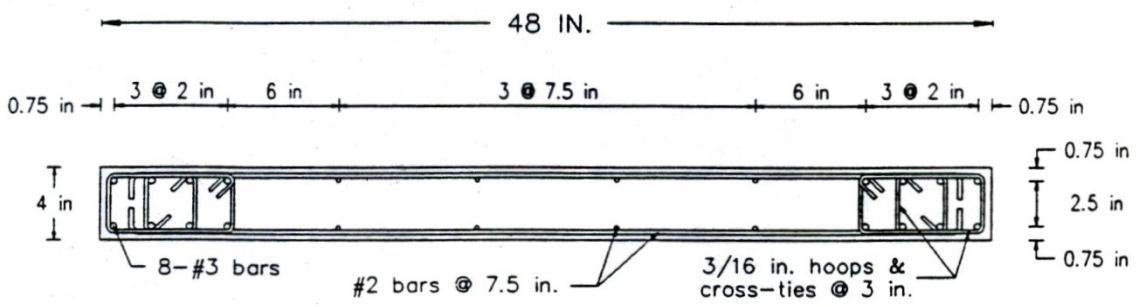

Figure 2.25 Section of Rectangular Wall RW1 Tested by Thomsen and Wallace (1995)

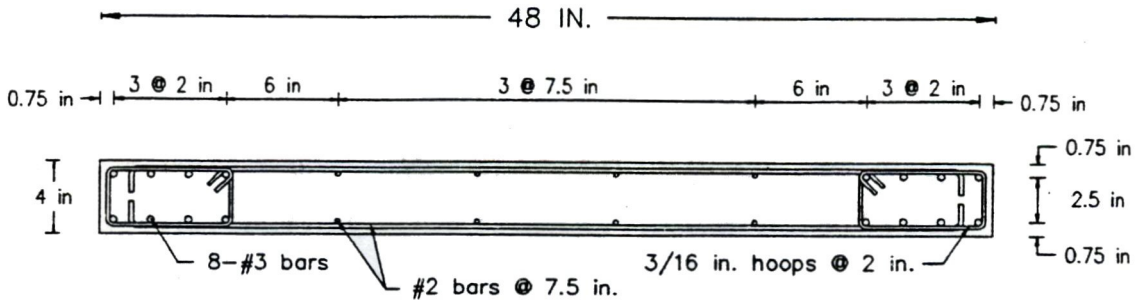

Figure 2.26 Section of Rectangular Wall RW2 Tested by Thomsen and Wallace (1995)

Prior to testing them lateral load, all walls were subjected to axial loads in the range of $0.07A_g f'_c$ to $0.1A_g f'_c$, where Ag is the gross cross-sectional area and f'_c is the measured concrete strength. The actual axial load ratio applied to each wall is noted in the force-displacement plots in Figure 2.27 and Figure 2.28, where f'_c values were 4.58 ksi, 6.33 ksi for RW1, RW2 respectively. The rectangular walls were loaded in the plane of the wall and cycled at least twice at each level of target story drift. The drift targets were 0.25%, 0.50%, 0.75%, 1.0%, 1.5%, 2.0%, and 2.5% drift. With good detailing, specimens RW1 and RW2 were expected to provide adequate ductility with no strength degradation. Figure 2.27 and Figure 2.28 show the response of rectangular walls, which experienced a symmetric response in terms of strength and ductility when loaded alternatively in the positive and negative directions. RW1 failed by buckling of all eight longitudinal bars in the boundary element between the transverse reinforcement at 1.5% drift. RW2 also failed due to buckling of the longitudinal reinforcement between the transverse reinforcement; however, the reduced spacing of the transverse reinforcement delayed buckling until 2.5% lateral drift.

Thomsen and Wallace compared the predicted force-displacement response of the wall based on the moment-curvature results of the section analysis program BIAX (Wallace and Moehle, 1989) with the response recorded during the experiment. BIAX has different material models that can be used to simulate the behavior of the concrete. Thomsen and Wallace ran two separate analyses of each wall one using a Modified Kent-Park (Park, Priestley and Gill, 1982) concrete model and the other using the Sastcioglu & Razvu (1992) concrete model. Figure 2.27 shows that the BIAX results showed a slightly stiffer response predicted than that was observed in the elastic region; however, the lateral capacity of the wall was well predicted for RW1. Figure 2.28 compares similar results for RW2, and it appears that BIAX predicted the stiffness adequately, but somewhat under predicted the lateral strength of the wall.

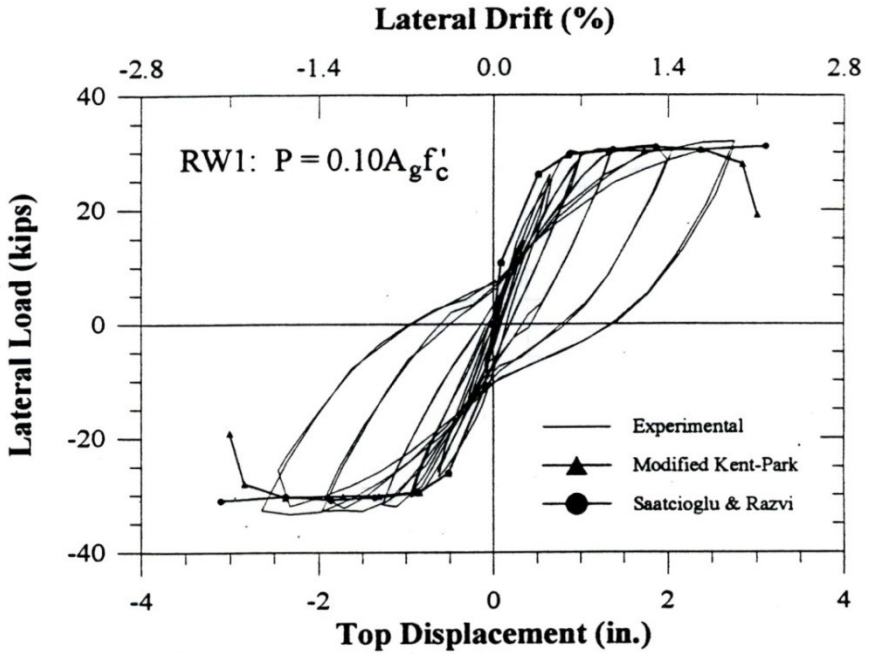

Figure 2.27 Measured and Analytical Response of RW1 (Thomsen & Wallace, 1995)

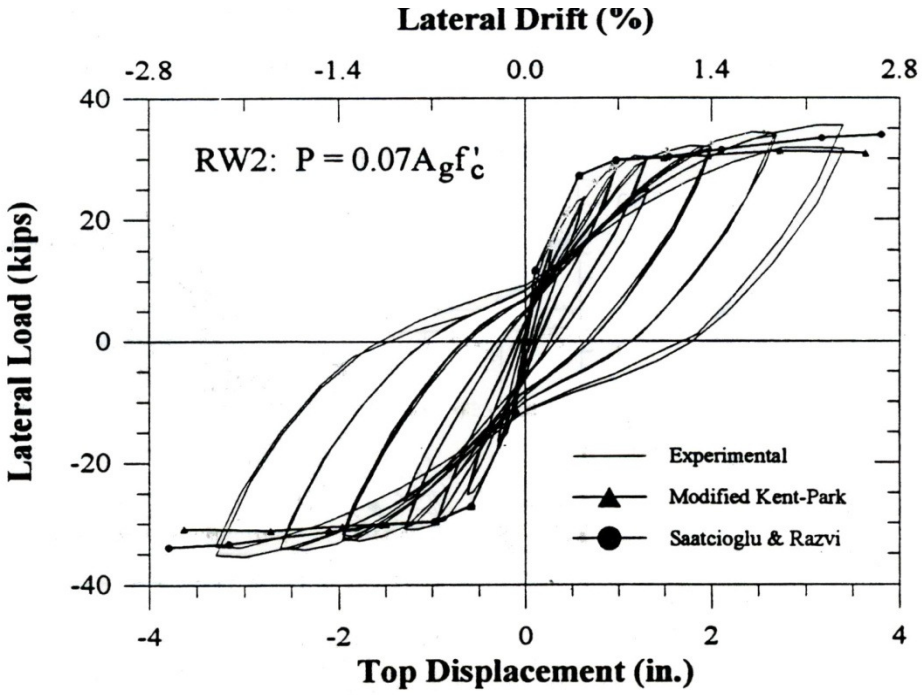

Figure 2.28 Measured and Analytical Response of RW2 (Thomsen & Wallace, 1995)

In summary, based on the observations from the experimental investigations presented herein, It can be deduced that the later load behavior and failure modes of slender walls depends on the axial load ratio, shear reinforcement distribution, confinement steel in boundary elements, shear compression ratio. It is important to notice that in all the experimental investigations, the longitudinal steel was continuous at the wall-foundation interface. However, in practice for ease of construction, it is common to splice the longitudinal reinforcement at the wall-foundation interface using either mechanical couplers or lap splices. It was noticed from the literature review that there are no studies done to understand the influence of splicing of reinforcement on the lateral load behavior of structural walls.

2.1.3 Unbonded Post-Tensioned Precast Wall Systems

This section presents an overview of previous research conducted on precast concrete walls for seismic application. In the section, large-scale tests conducted on unbonded precast walls by researchers at University of California at San Diego (UCSD) as part of the PRESSS program, by researchers at ATLSS Research center of Lehigh University, and by Rahman and Restrepo at the University of Canterbury, New Zealand are summarized.

In unbonded post-tensioned precast wall systems, the walls are tied to the foundation using unbonded post-tensioned steel distributed symmetrically about the center of each wall, providing yet another alternative to connect the wall to the foundation. The basic concept of these wall systems is that it allows the wall to rock individually at the base when subjected to lateral loads and return to its vertical position after the event has concluded (Priestley et al. 1999). The post-tensioned steel is typically designed to remain elastic under the design-level earthquake loading. As a result, the post tensioning steel provides the restoring force for the jointed wall when the applied lateral load is removed. The external energy dissipaters (special connectors or mild steel bars etc.) dissipate energy by experiencing inelastic deformations under the applied earthquake loads.

2.1.3.1 Jointed Wall System

In response to the recognized need to overcome the limitations for the use of precast concrete in seismic regions, the PRESSS (PREcast Seismic Structural Systems) program was

initiated in the early 1990's in the United States. The jointed wall system was developed and tested as part of the PRESSS program.

In a jointed wall system, two or more unbonded single precast walls are connected to each other with the help of special connectors along the vertical joints. As a part of the PRESSS program, a 60% scale model of a five story precast building with moment resisting frames in one direction and a precast jointed wall in the perpendicular direction was tested at UCSD. The main objectives of this large-scale testing were 1) to demonstrate the viability of precast concrete for seismic regions through experimental means, and 2) to develop seismic design guidelines for precast concrete systems, which can be incorporated into the model building codes.

The precast jointed wall used in the PRESSS building consisted of a total of four 8-in thick wall panels, each 2 ½ stories tall (18.75-ft) by 9-ft wide. The panels were joined vertically to form two walls separated by a small gap between them. Each wall was secured to the foundation using four unbonded post-tensioning bars. These two walls were connected horizontally by 20 U-shaped flexural plates (also referred to as U-plates or UFP connectors), which were placed in the gap between the walls in vertical direction. The U-plates were used as the connector because of their ability to maintain force resistance under large displacements and contribute to energy dissipation by flexural yielding of plates.

The test building was subjected to a series of simulated seismic tests, including the pseudo dynamic tests involving modified segments of recorded accelograms. Based on the observed response of the PRESSS building, it was concluded that the structural response of the wall system under different levels of seismic loading was excellent (see Figure 2.30) and damage to the precast jointed wall was noticeably negligible even when subjected to loads that were greater than the design-level earthquakes (see Figure 2.30).

Figure 2.29 The jointed precast wall included in the PRESSS test building (Priestley eta al. 1999)

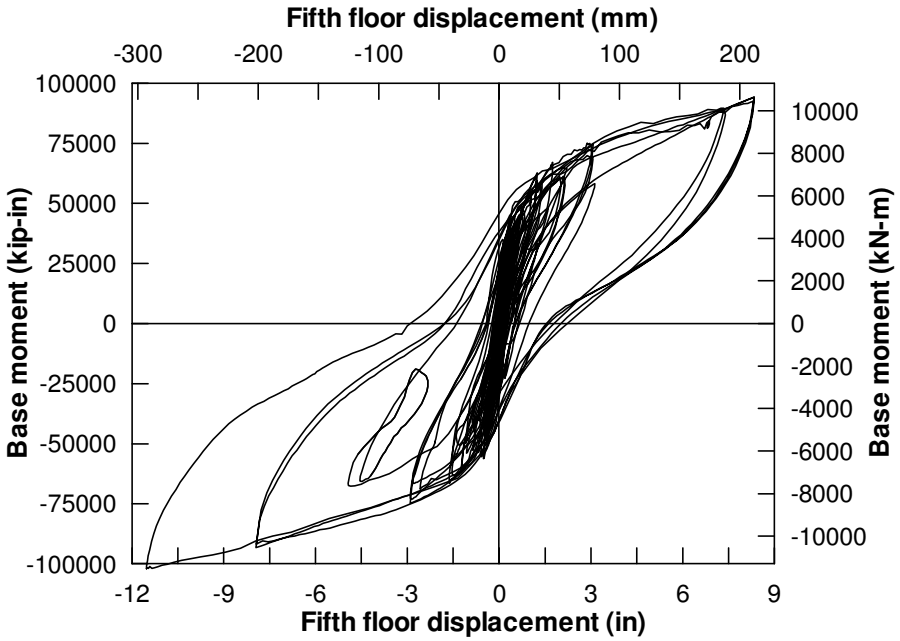

Figure 2.30 Overall response of wall direction test of the PRESSS building (Priestley et al., 1999)

2.1.3.2 Single Precast Wall Systems

A set of unbonded post-tensioned precast concrete single walls with the horizontal joints were tested under reversed cyclic loading at the ATLSS research center of Lehigh University to investigate the effect of total area of prestress steel, initial stress in post-tensioning steel, and confinement of concrete on the lateral load behavior of single precast walls with unbonded post-tensioning. The tests were conducted on 5/12 scaled models, which represented a prototype precast wall designed for a six-story office building. A total of five precast walls, designated as TW1, TW2, TW3, TW4 and TW5, were tested as part of this research. The specimens were 100 in. long, 284.75 in. height and 6 in. thick. The unbonded post-tensioning was distributed about the center of the wall. More details about the specimens can be found in Perez et al. (2004). Except TW1, all the test specimens were subjected to cyclic loading. The force-displacement responses of the test units observed under cyclic lateral loading are shown in Figure 2.31. The flexural cracking was concentrated at the base of the walls, significantly reducing the amount energy dissipation. Inelastic strains were developed in the prestressing steel at large drift ratios causing loss of prestress load upon unloading. Prestress losses in the range of 11-23 % were observed when walls were displaced to higher drift levels. The test specimens showed a small or no residual displacement upon removal of lateral loads, which was the result of having enough restoring force in the system that was provided by the unbonded prestressing steel. The observed largest residual displacement during the wall test before failure was 0.1%.

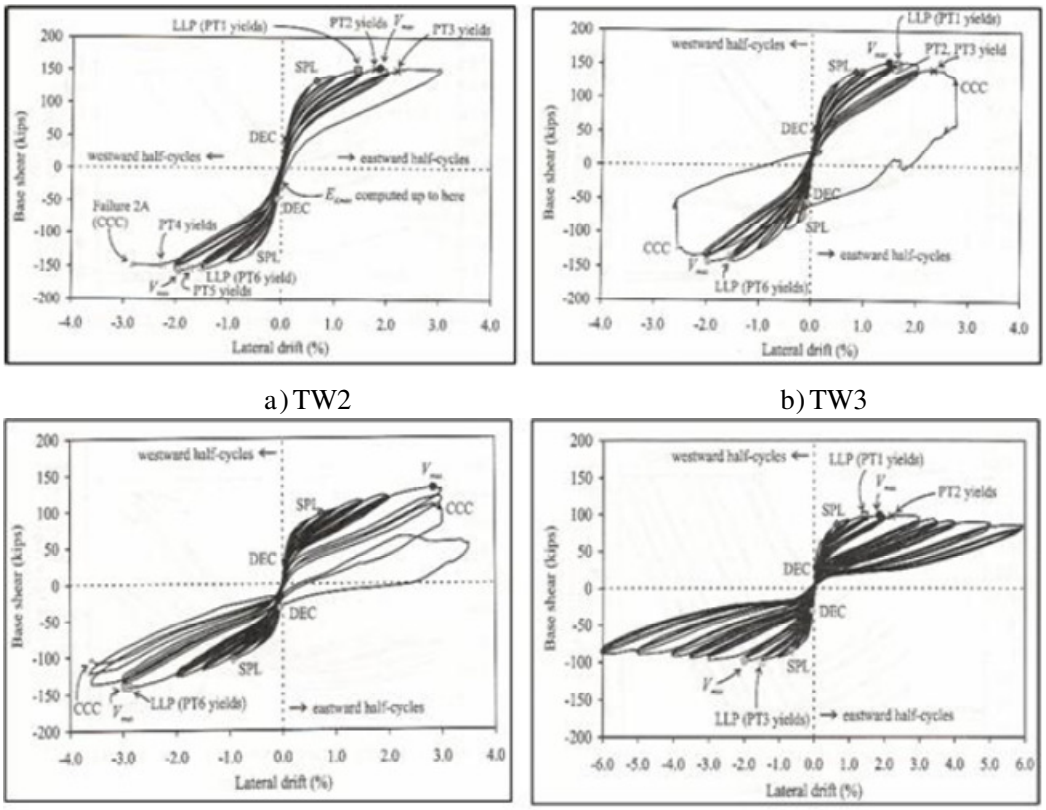

Figure 2.31 Experimental cyclic load response of walls TW2, TW3, TW4 and TW5 tested by Perez et al. (2004)

2.1.3.3 Hybrid Wall Systems (Rahman and Restrepo)

Hybrid precast walls utilize a combination of mild steel and high-strength unbonded post-tensioning steel for flexural resistance across horizontal joints. A schematic of typical hybrid wall system is shown in Figure 2.32. The mild steel reinforcement in the wall is typically designed to yield in tension and compression, providing energy dissipation. The unbonded post-tensioning steel provides self-centering capability, as with other wall systems, reducing the residual lateral displacements of the wall when subjected to a large earthquake. Both the PT steel and the mild steel contribute to the wall lateral strength, resulting in an efficient structure.

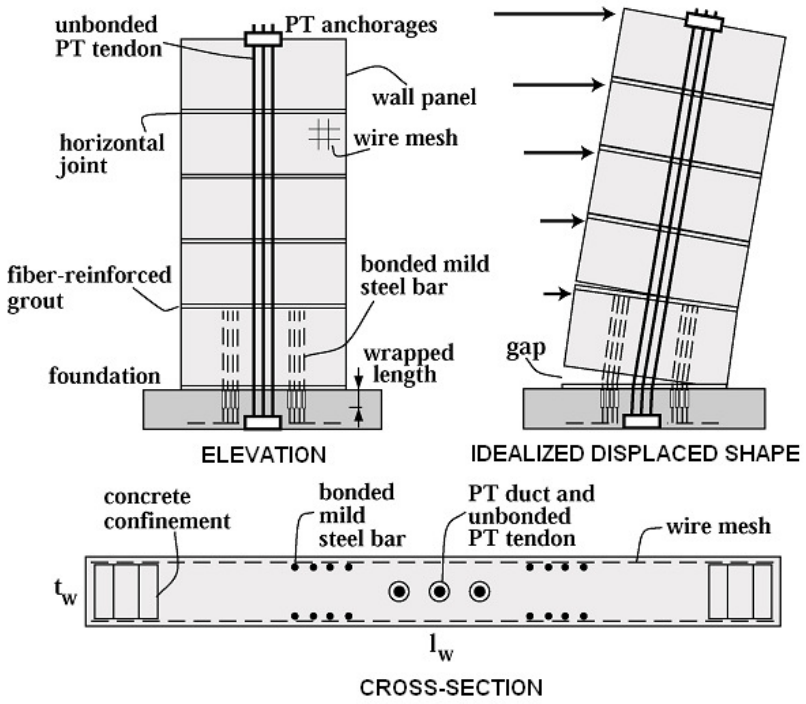

Figure 2.32 Schematic of typical hybrid wall system (Smith and Kurama, 2009)

Rahman and Restrepo tested three half-scale precast concrete wall units, representative of a four-storey building. The units were designed to ensure that yielding of the tendons would not take place below 2.5% drift. The wall specimens were 13.33 ft high by 4.5 ft long by 5 in. thick. Units 2 and 3 incorporated energy dissipation devices, whereas Unit 1 was post-tensioned only. Additional gravity load of 45 kips was applied in Unit 3. The geometry of the test specimens and the loading frame are shown in Figure 2.33.

Quasi-static reversed cyclic loading was applied to the specimens at the top using a horizontal actuator. The wall specimens were prestressed to a total prestressing force of 188 kN using 2-12.7 mm diameter low relaxation strands. A 20 mm diameter Grade 430 steel bar with a nominal strength of 430 MPa was used for the axial energy dissipation devices in Units 2 and 3. The Units 2 and 3 were identical, except for the confinement length, axial load and debonded length of the mild steel reinforcement. The two wall units performed satisfactorily under applied cyclic lateral loading and the measured cyclic response of these units are shown in Figure 2.34.

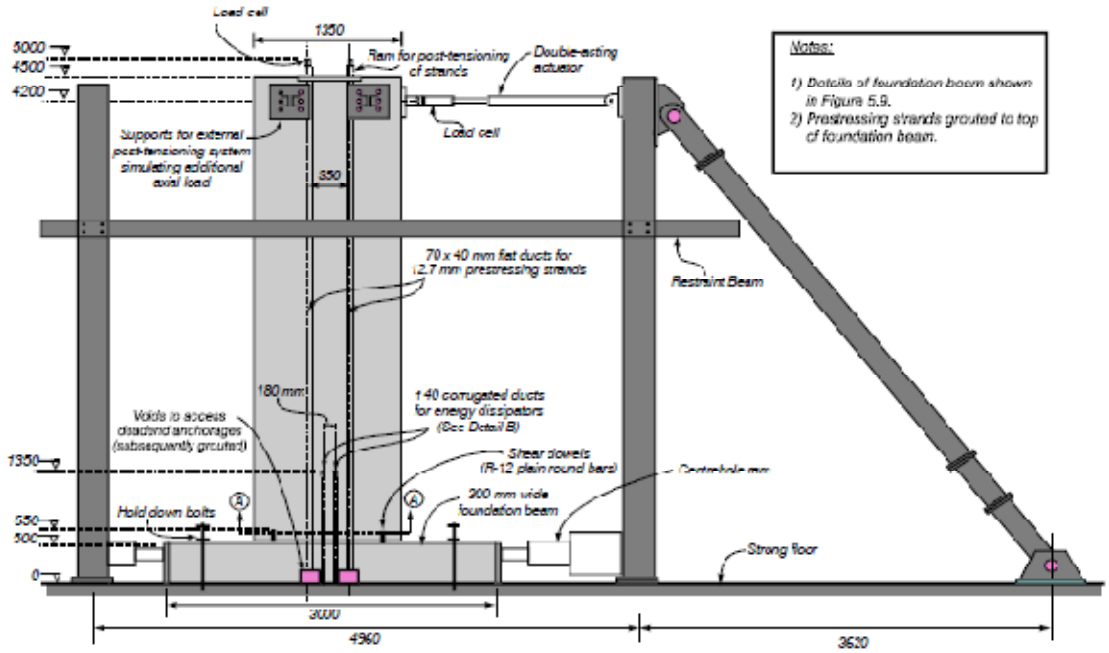

Figure 2.33 Schematic representation of loading frame in tests reported by Rahman and Restrepo (2000)

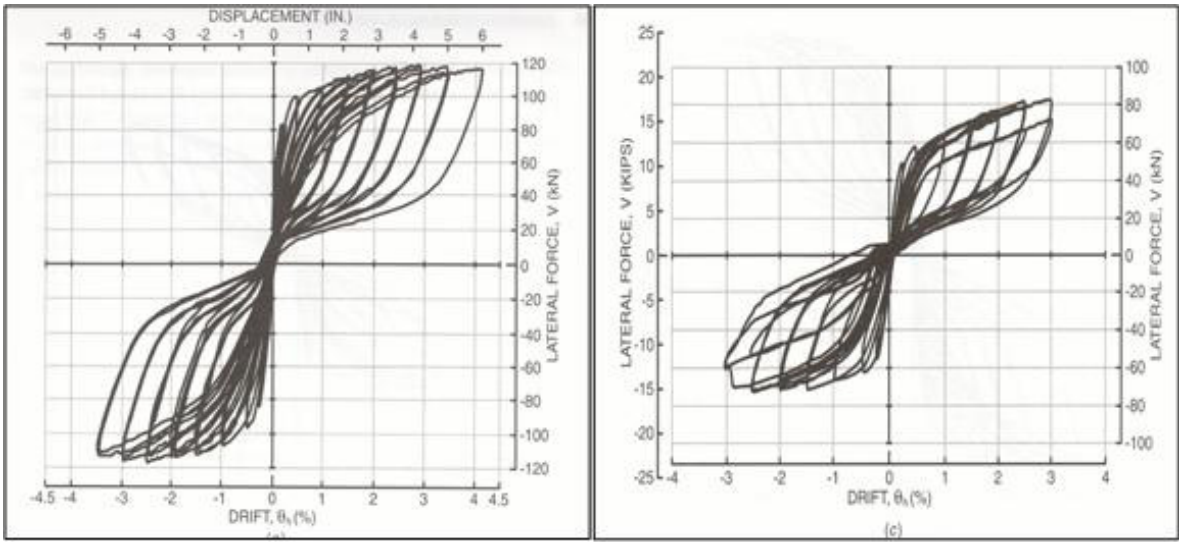

Figure 2.34 Cyclic load response of Units 2 and 3 tested by Rahman and Restrepo (2000)

2.2 Analytical Studies

This section presents various analytical approaches presented in literature for modeling the response of structural walls. Although not all studies investigated one specific wall shape, all of these techniques can be for analysis of reinforced concrete walls. Structural walls have been modeled and analyzed using a number of different approaches by researchers. Rather than making an extensive listing of all the analytical studies done on structural walls, a summary of various modeling approaches used for walls studies are presented, followed by a representative sample of analyses and commentary on the advantages and disadvantages of the different approaches.

2.2.1 Solid (Brick) Elements

The behavior of structural walls has been simulated using solid or brick elements. Solid elements have been used by a number of researchers [Deshmukh et al., 2006; Moaveni et al., 2006] to simulate the structural wall behavior under lateral loads. This modeling approach has the advantage of allowing the strain and corresponding stress to vary across the section without the user having to specify a particular distribution such as that based on the plane section remains plane assumption. Additionally the shear stiffness of the wall is determined for the individual elements. In this approach, the longitudinal and transverse reinforcement can be smeared across the solid element or modeled discretely using truss elements. The 3D nature of the model allows bi-directional lateral loads to be applied to the wall. However, solid elements have some significant disadvantages. These include incorporating an accurate 3D concrete material model that can accurately model the initiation, propagation, and orientation of cracks as they form in concrete elements as well as the loading and unloading paths. A large number of solid elements may be required to model the concrete and reinforcement of a wall accurately, which may require significant computational time to run the analysis. Including the effects of strain penetration is challenging and typically ignored in the analysis [e.g., Moaveni et al, 2006; Deshmukh, 2006].

2.2.2 Plane stress, Plane Strain, or Shell Elements

Plane stress, plane strain, and shell elements have also been used to simulate the response of structural walls in 2D. Studies conducted by Sittipunt and Wood [1993], Palermo and Vecchio [2004], and Kelly [2006, 2007] are good examples of this modeling approach. This approach has some of the same advantages and disadvantages as the solid element. A reliable 2D concrete model is required for the analysis that should include the effects of cracking and appropriate unloading/reloading rules. In addition to the concrete model, complexity and number of elements, these models are being limited to unidirectional loading only. Similar to solid elements, including the effects of strain penetration is difficult and commonly ignored [e.g., Sittipunt and Wood, 1993].

However, in recent times few researchers have addressed the short coming s by modeling the strain penetration effects by other means. Kelly [2006] modeled a 7-Story building slice consisting of web wall, flange wall, and post-tensioned column using nonlinear plane stress elements to predict the building behavior under dynamic loading. The effects of strain penetration were modeled using pairs of nonlinear gap-truss elements to model the reinforcement at the base of each wall. The gap truss elements allowed a large crack to form at the base of the wall, simulating the base rotation due to strain penetration. The model had 686 degrees-of-freedom which is relatively low. The comparison of the calculated and measured displacement profiles is shown in Figure 2.35, which that the model predicted the displacement response envelope for events EQ1 and EQ4. The relatively low number of degrees of freedom (DOF) makes this modeling approach well suited for the analysis of a complete building in a design office.

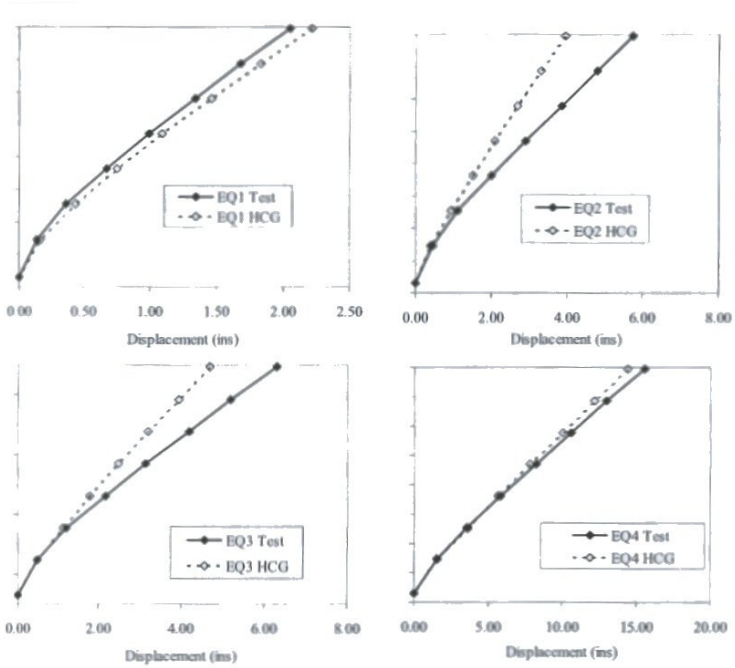

Figure 2.35 Displacement Profile Comparison [Kelly, 2006]

2.2.3 Macro Model Elements

Macro model elements are a type of element that instead of specifying microscopic behaviors, such as stress-strain relationships, global response parameters are specified directly. Typically, macro models lump various behaviors into one element to simplify the analysis and increase the computational efficiency of the analysis. Macro model elements are used to capture regions of nonlinear behavior, while linear elements are used for regions that will remain elastic during the analysis.

One example of a macro model element is the multiple-vertical-line-element-models (MVLEM) that have been shown to capture the response of structural walls [Fischinger and Isakovic, 2006; Orakcal et al., 2004]. This modeling approach simulates the behavior of rectangular walls using a series of vertical and shear springs connected by rigid beams at the top and bottom of the element. Figure 2.36 shows the MVLEM schematically. The force-displacement characteristics of the springs can be defined to incorporate the various response components of the structural walls.

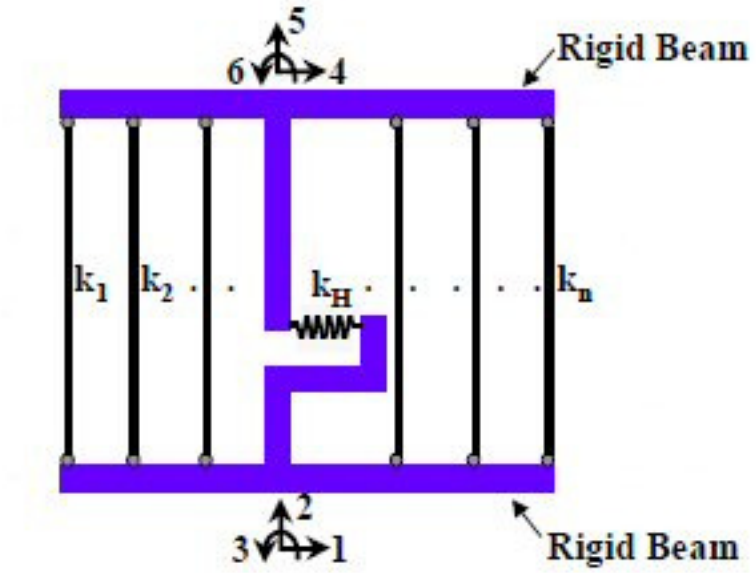

Figure 2.36 Multiple Vertical Line Element Model

A "beam with hinges" is another example of a macro model used to simulate structural walls [Bolander and Wright, 1991]. This model lumps all the nonlinear behavior at the ends through the use of axial and rotational springs. The spring behavior is then defined to give almost any type of response that is desired by the user.

Orakcal and Wallace [2006] presented an improved analysis model for predicting lateral load behavior of reinforced concrete structural walls. Using the data recorded in the experiment, they concluded that shear-flexure interaction had a significant impact on the response of the wall. Consequently, they created a special type of element called the "Multi-Component-in-Parallel Model" (MCPM) to capture the flexure-shear interaction. The MCPM model is similar to the multiple-vertical-line-element models (MVLEM) discussed above. The force-displacement response comparison between their analytical model and the experimental response shows an excellent match for RW2 seen in Figure 2.37. However, the data from RW2 was used to calibrate the parameters used in the MCPM model; a prediction of the response for a wall using the MCPM has not been presented.

The primary advantage of macro model elements is that they are very computationally efficient and provide good simulation of the global wall behavior. However, macro model elements require experience and knowledge to determine the force-displacement

relationships for the springs, rather than stress-strain relationships of the material that are more familiar to most engineers. Additionally, strain penetration and other behaviors are lumped together in the spring behavior, potentially leading to inaccurate simulation at the local level.

Fischinger and Isakovic [2006] successfully modeled the UCSD 7-Story Building slice using the MVLEM approach. The web wall was modeled using a stack of MVL elements, of which four of them were used in the first story and one element in all the other stories. Five vertical springs were used to simulate the entire cross section of the wall and the compressive strength of the vertical spring was based on the compressive strength of the confined concrete, neglecting the steel reinforcement in compression. Empirically verified values were used to define the hysteretic relations in the vertical springs. The shear behavior was assumed to remain elastic. Figure 2.38 shows the predicted and measured maximum displacement profiles.

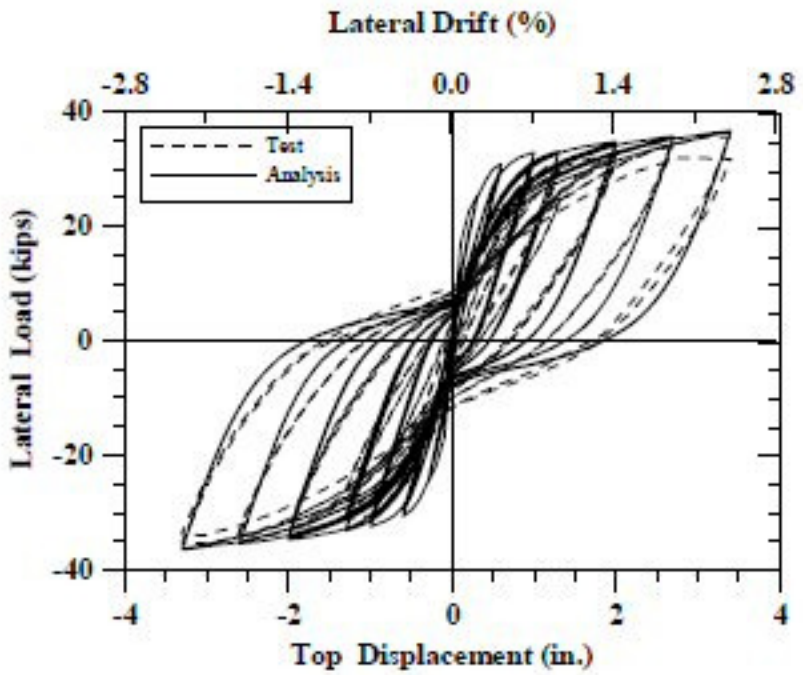

Figure 2.37 Comparison of results from the MCPM model of RW2 with the Measured Response (Orakcal and Wallace, 2004)

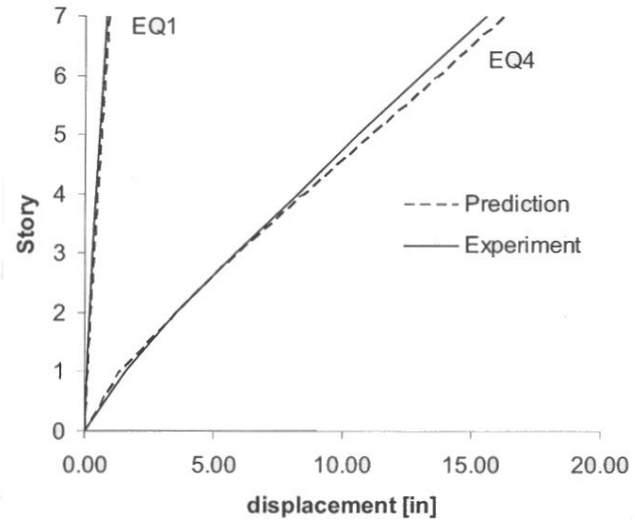

Figure 2.38 Predicted and Experimental Displacement Profiles

2.2.4 Beam-Column Elements

Beam-column elements with fiber sections have been used to simulate response of structural walls [e.g., Martinelli and Filippou, 2006; Grange et al., 2006; Dazio, 2006]. These models allow the user to specify uniaxial stress-strain behavior of longitudinal reinforcement as well as that of confined and unconfined concrete including the effects in the transverse direction. A large variety of models are available that can be used to characterize the behavior of different materials in order to capture the section and member responses accurately. Since the model is based on the uniaxial stress-strain behavior of groups of fibers, the models are easier to build and understand. The disadvantage of fiber beam-column elements is that the strain distribution at the section level is typically predefined. Additionally, some fiber based elements require the shear deformation to be handled separately. In this case, the beam-column element only considers the axial and bending deformations on the element, and no shear stiffness is included in the element stiffness. In order to include the effects of shear deformation, a separate material model must be used to define the global shear force-deformation relationship for the beam column element. The shear material model can be placed in parallel to the beam-column, thus including the shear stiffness in the global structural stiffness matrix.

CHAPTER 3

ANALYSIS OF RECTANGULAR CONCRETE WALLS

3.0 Introduction

As previously noted, the experimental part of this collaborative PreNEESR project included characterization of lateral load behavior of reinforced concrete structural walls at the MAST Laboratory of the University of Minnesota. As part of this collaborative effort, three structural walls with rectangular cross section and two walls with T-shaped cross section were tested. The rectangular walls were subjected to in-plane cyclic loads. Presented in this chapter are the theoretical characterizations of the rectangular walls using fiber-based beam-column elements. The three rectangular walls were identical, except for the fact that they used different anchorage details for the longitudinal reinforcement at the wall-to-foundation interface. These tests were conducted as part of the investigation of the behavior of T-shaped concrete walls and were motivated to understand the impact of different anchorage details on the response of the T-walls. In practice, concrete walls are designed with conventional lap splices at the base of the walls (ACI 318, 2002), whereas experimental research on walls has typically eliminated any splices as this detail often influences the response of concrete walls. Consequently, the rectangular walls were designed to examine the influence of following three different details at the base of the walls: 1) continuous longitudinal reinforcement without any splices 2) couplers and 3) code-based conventional lap splices. When detailing the walls, two different boundary elements were used such that the wall response in the two different in-plane directions would correspond to the flange in tension and flange in compression response of a T-wall loaded in the web direction (Johnson, 2007). All three rectangular walls were subjected to cyclic loading with full reversals. Analytical Investigation of all walls was conducted using the OpenSees software (OpenSees 2007). In addition to presenting a summary of the tests, this chapter presents the analytical responses of the rectangular walls with comparison to experimental results wherever possible. To ensure that the analytical model satisfactorily captures measured response, both

global and local parameters, as well as different displacement components are compared. Failure to do this may inadequately validate analytical model since compensation of error may lead to satisfactory structural response at global level as demonstrated by Sritharan et al. (2000)

3.1 Description of Test Walls

The rectangular concrete walls used in this study were designed to replicate the web direction response of a 50% scale prototype T-wall designed for a six story building located in Los Angeles, CA. The details of the prototype T-wall and the six-story prototype building are presented in Chapter 5. Details of the design computations of the prototype T-wall can be found in Narina (2007) and Johnson (2007).

The first wall specimen used continuous longitudinal reinforcement from the footing to the top of the wall, which was identified as RWN (where "RW" represents rectangular wall while "N" stands for no splicing). The second wall specimen used mechanical couplers to splice the longitudinal reinforcement near the wall-to-foundation interface; which was referred to as RWC (where "C" stands for coupler). The third wall specimen used conventional lap splices near the wall-to-foundation interface, which was identified as RWS (where "S" stands for splices). The dimensions and the reinforcement details of the rectangular walls were chosen to closely match the strength of the 50% scaled prototype T-wall in the web direction. The reinforcement in the rectangular walls was designed to ensure that the flexural strain gradient along the wall height and the inelastic curvature at the base will be comparable to that of the T-wall in the flange in tension and flange in compression under web direction loading. This design requirement caused the rectangular walls to have unsymmetrical amounts and distribution of longitudinal steel in the boundary elements. Complete details about the design considerations adopted for the rectangular walls can be found in Johnson (2007).

As shown in Figure 3.1 and Figure 3.2, all three rectangular concrete walls were 254 in. tall, 90 in. long and 6 in. thick. Since these walls were designed to match the moment resistance of a T-wall, they consisted of two different boundary elements: one with #6 (d_b = 0.75 in., where d_b is the bar diameter) and #5 (d_b = 0.625 in.) longitudinal bars, the other with

#9 (d_b = 1.125 in.) longitudinal bars. Consequently, the two boundary elements were referred to as No. 6 boundary element and No. 9 boundary element respectively. Between the boundary elements, #4 (d_b = 0.5 in.) longitudinal bars were distributed at 18 in. of spacing. The distributions of the longitudinal reinforcement for the three walls are seen in Figure 3.1 and Figure 3.2.

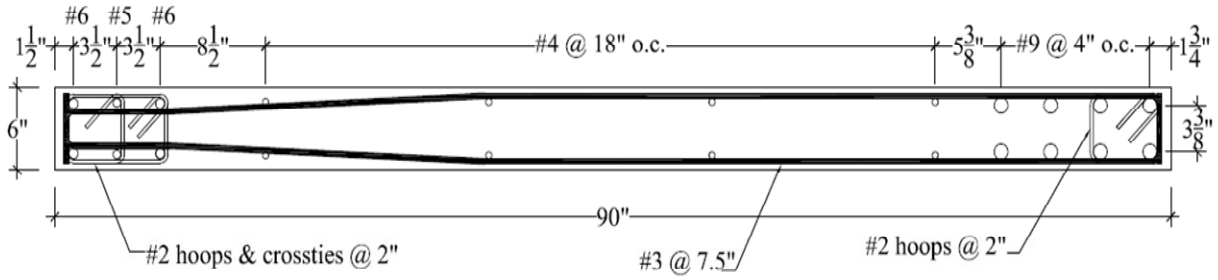

a) RWN with no splices in the longitudinal reinforcement

b) RWC with mechanical couplers at the foundation interface

c) RWS with traditional lap splices near the wall base

Figure 3.1 Reinforcement details of the three rectangular walls

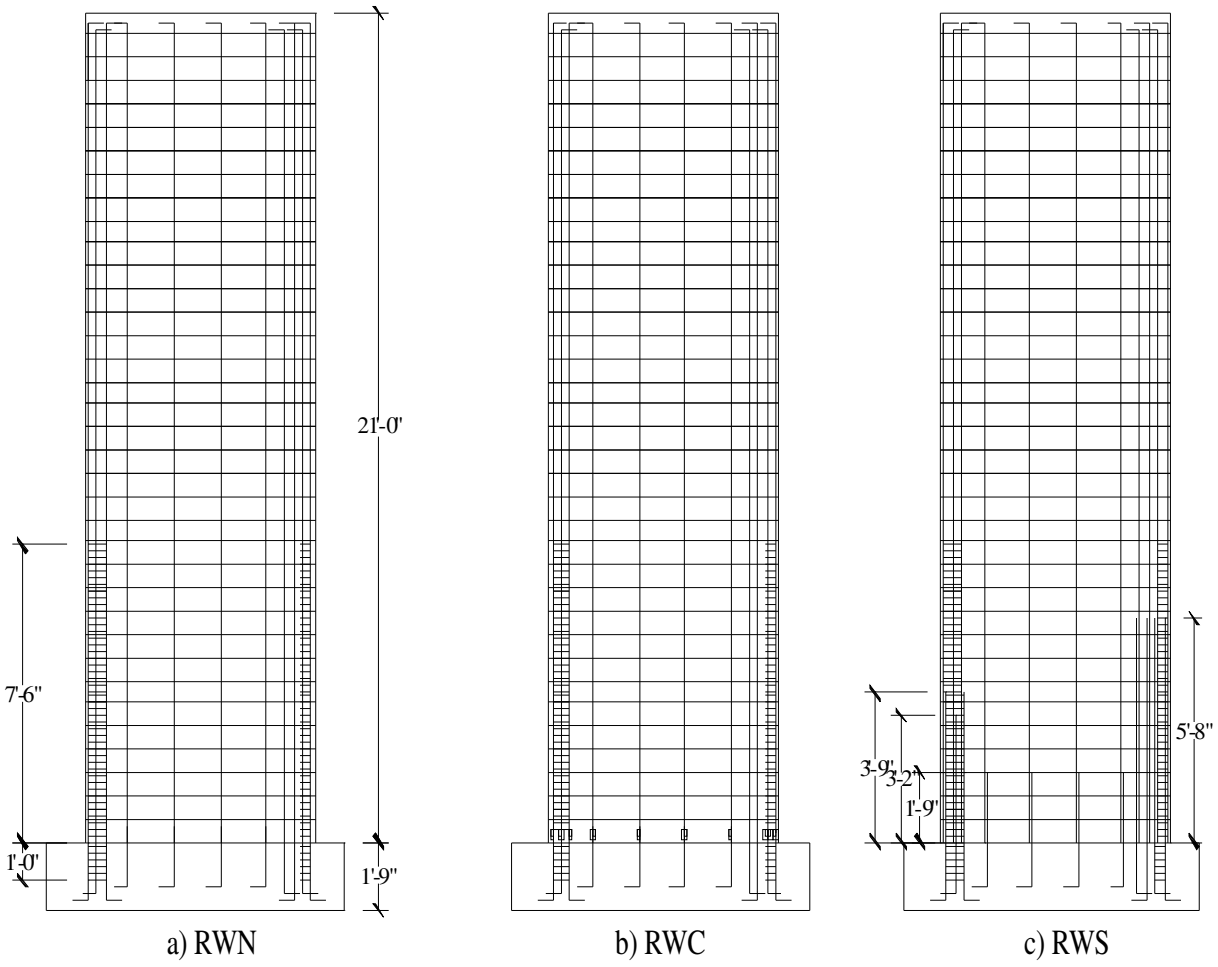

Figure 3.2 Reinforcement details along the wall height in the rectangular walls

Both boundary elements were also designed with #2 (d_b= 0.25 in.) hoops spaced at 2 in. over the bottom 90 in. of the wall as confinement reinforcement. Since, #2 bars were not readily available, the confinement hoops were made from ASTM A496 D-5 deformed wire. The boundary elements lengths were determined based on the ACI 318-02 requirements (2002). The potential for shear failure to occur in the rectangular walls prior to the development of full flexural moment resistance was avoided in design by adequately designing the shear reinforcement according to the requirements of ACI 38-02 design code, which led to #3 (d_b = 0.75 in.) horizontal bars in the walls spaced at 7.5 in. for the entire height. For splicing of longitudinal bars in RWC, type-2 mechanical couplers (as defined in

section 21.1.6 of ACI 318-02 code) manufactured by Headed Reinforcement Corporation (HRC) (http://www.hrc-usa.com) were used at the wall-to-foundation interface. All mechanical couplers in RWC were located just above the interface (see Figure 3.3). RWS used "Class B" lap splices (lap length is equal to 1.3 times the tensile development length calculated according to 12.2.2 or 12.2.3 of ACI 318-02 code), which were designed according to the ACI-318 (2002) at the interface. The foundation block of each wall was 21 in. tall and provided required anchorage depth for the longitudinal reinforcement. A strut and tie design method according to ACI 318-02 was used for the foundation design to reduce reinforcement congestion (Johnson 2007).

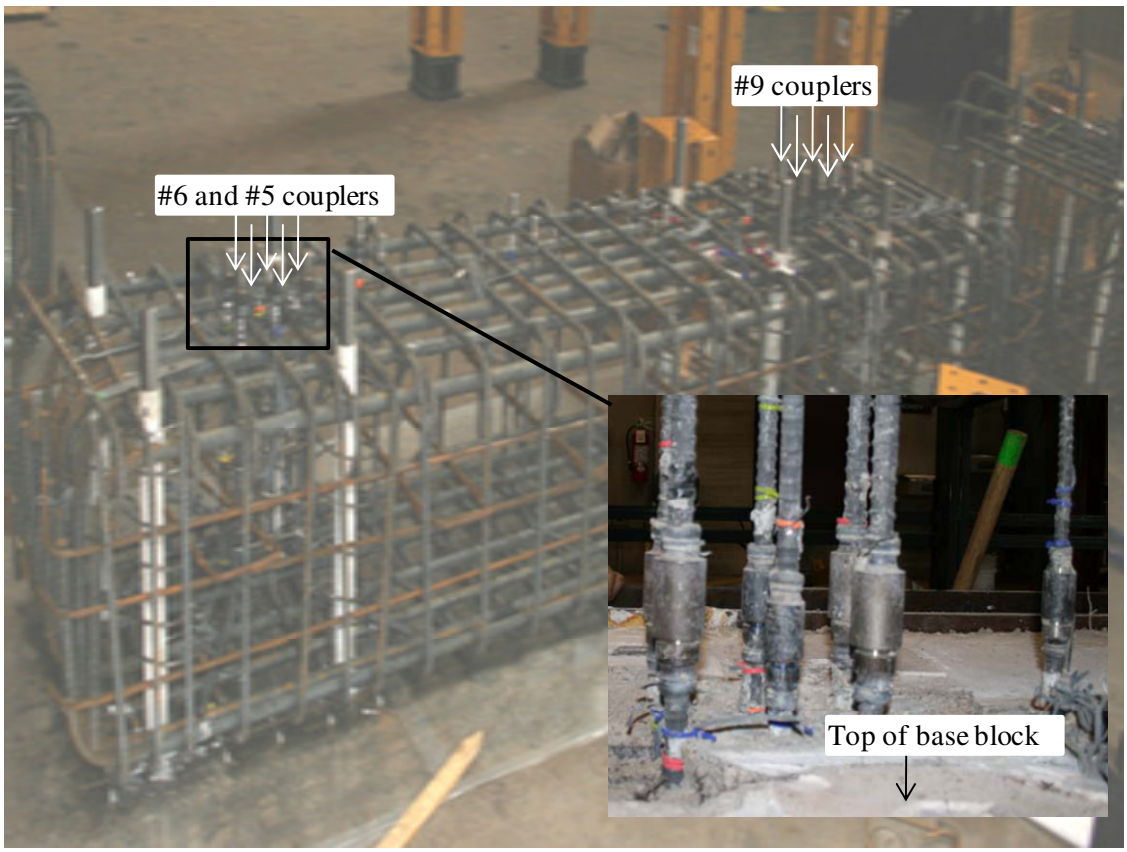

Figure 3.3 Location of the mechanical couplers in RWC

3.2 Experimental Test Setup, Loading Protocol and Test Observations

3.2.1 Test Setup and Loading Protocol

This section briefly discusses the test setup and the loading protocol used for the experimental investigation of rectangular walls. A schematic of the rectangular wall test setup is shown in Figure 3.4. The base block of each test wall was firmly post-tensioned to the strong floor using 10 three-inch diameter threaded bars. The rectangular walls were subjected to reverse cyclic loading using a ± 220 kip capacity hydraulic actuator mounted horizontally to the MAST reaction wall. In each case, predetermined reversed cyclic displacements were applied to the wall at 20 ft from the foundation-to-wall interface under displacement control. To distribute the applied forces over the entire horizontal length of the wall, the actuator was connected to a pair of steel channels that were clamped to the wall using five one-inch diameter pretensioned rods. The rods were distributed over the horizontal length of wall in a zigzag pattern (see Figure 3.4). A roller restraint was provided at the top of the wall to prevent any out-of-plane movement of wall during testing. The walls were not subjected to any external vertical load.

Ignoring the influence of anchorage details, the initial displacement targets for the testing were chosen based on a predicted force-displacement response of the walls that was obtained from a moment-curvature analysis of the wall section. All three walls were subjected to the same displacement history until initiation of failure. Three load cycles were used at each target displacement, to ensure the stability of the force-displacement response at that displacement. The applied displacement history for the three rectangular walls is shown in Figure 3.5. During testing, the applied lateral displacements to the walls were controlled using an external string potentiometer located at the loading height (i.e. 20 ft from base of the wall). The walls were divided into four panels along the height (see Figure 3.4) to monitor the deformation components and damage within each panel. In addition to recording the wall displacement at the loading height, the lateral displacement at each panel was monitored during testing. Complete details of the test setup can be found in Johnson (2007). All three walls experienced a global buckling failure in the No. 6 confined region during testing at 2% drift cycles as the No.9 confined region was subjected to tension. Consequently, the load histories beyond this point were varied for each wall due to the damage state of each wall at

the time of buckling. However, the loading history used after the buckling of the wall was not considered in the analytical investigation presented in this chapter, as this failure mode was not included in the model.

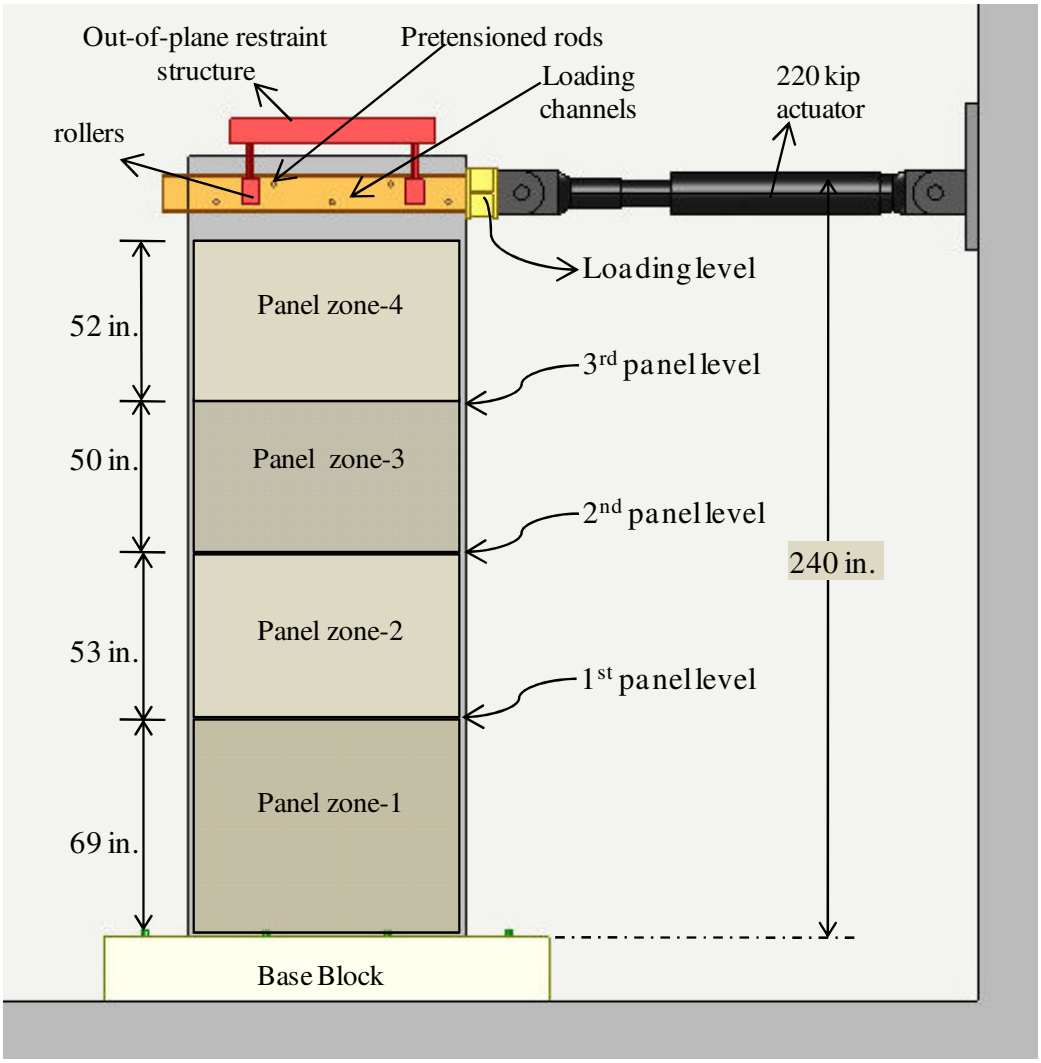

Figure 3.4 Schematic of the test setup used for the rectangular wall tests

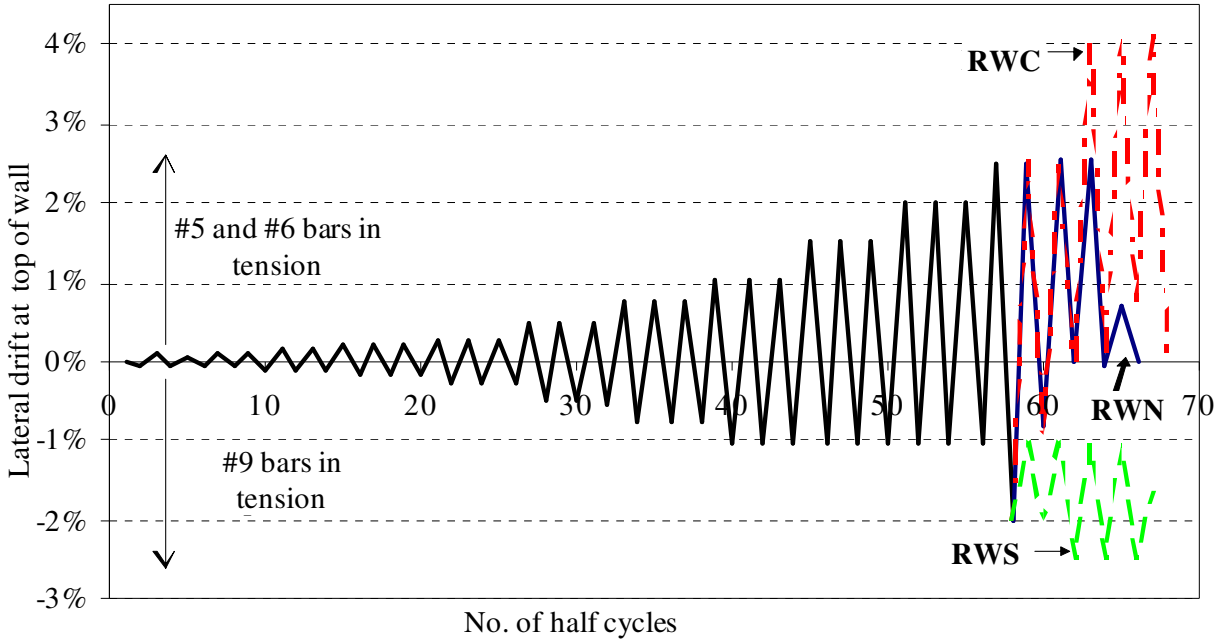

Figure 3.5 The displacement protocol used for testing of the three rectangular walls

3.2.2 Experimental Observations

The measured cyclic responses of the walls are shown later in section 4.4. All three rectangular walls performed satisfactorily up to 2% lateral drift, when the #5, #6 bars were in tension and up to 1% drift when the #9 bars were in tension. The longitudinal steel in all walls experienced yielding at a drift of about 0.4 %. The three walls also showed similar responses and crack patterns for drift levels below 1%. However, at larger drifts, the response of RWS was relatively stiff in comparison to other walls, which was expected due to the additional steel in the lap spliced region. Large number of closely spaced flexural cracks formed over the bottom 72 inches of the walls, some of which transitioned into inclined shear cracks outside the confined region (between the confined regions). The shear cracks were much wider when compared to the flexural cracks in the confined region. The crack at the wall-foundation interface was similar in size as the other cracks in the wall until 1% drift. However, in case of RWS the interface gap grew much wider (13 mm wide at 2 % drift), which was caused by the bond degradation in the splice region leading to the slippage of the bars. This large gap opening at the interface caused stress concentration in the bars, leading

to local buckling and fracture of longitudinal reinforcement in the No.6 boundary element. In RWS, The flexural cracks at the end of the splice region were much wider than the flexural cracks at other locations. An interesting phenomenon observed during the testing of the walls was shear sliding of the wall along horizontal cracks in the plastic hinge region. This was observed in all the three walls. However, the height of the cracks along which sliding took place were different. When compared to other walls, the sliding in RWS took place at a higher level and outside the spliced region, which is believed to be due to higher amounts of longitudinal steel reinforcement in the splice region.

In summary, the wall with the mechanical couplers performed comparable to that with the continuous reinforcement. The wall with lap splices was stiffer compared to the other two walls and the performance was not as good as the other two walls. The interface crack opening was observed in all the walls but at higher drifts, the interface crack in RWS was nearly 3 to 4 times wider than that was observed in RWN and RWC. In RWN and RWC, the damage was extended up to 65-70 inches from the base, whereas in RWS the damage was concentrated more at the base over a shorter distance, causing the local buckling of the longitudinal reinforcement and thus reducing the energy dissipation capability of RWS. Based on observed performance of RWS, while detailing the NTW2 reinforcement, the lap splice was moved to the first story level to prevent the local buckling of longitudinal reinforcement and the slip along the splice length. More details about the observed experimental behavior of rectangular walls can be found in Johnson (2007).

3.2.3 Estimation of deformation components

The displacement of a reinforced concrete wall is comprised of various deformation components due to flexure, shear and strain penetration effects. In order to quantify the each contribution towards total displacement an extensive instrumentation plan was used in testing of rectangular concrete walls conducted in this study. The details of the instrumentation plan can be found in Johnson (2007). Based on previous researchers experience and recommendations (Wallace 1995, Sritharan 1998), the rectangular wall was divided into four panels to separate the flexure and shear deformation contribution. String potentiometers along the four sides and the two diagonals of the panels were used to instrument the panel.

Flexural and Shear deformations estimation

The total deformation of a panel can represented by five different modes, namely pure shear, axial deformations in x and y directions, and flexural deformation in x and y directions. However, for a slender reinforced concrete shear wall, shear deformations and flexural deformation about the y-axis are predominant compared to other modes of deformations. Figure 3.6 shows the five independent modes of deformation and they can be calculated from the nodal displacements using Eqn.(3.1).

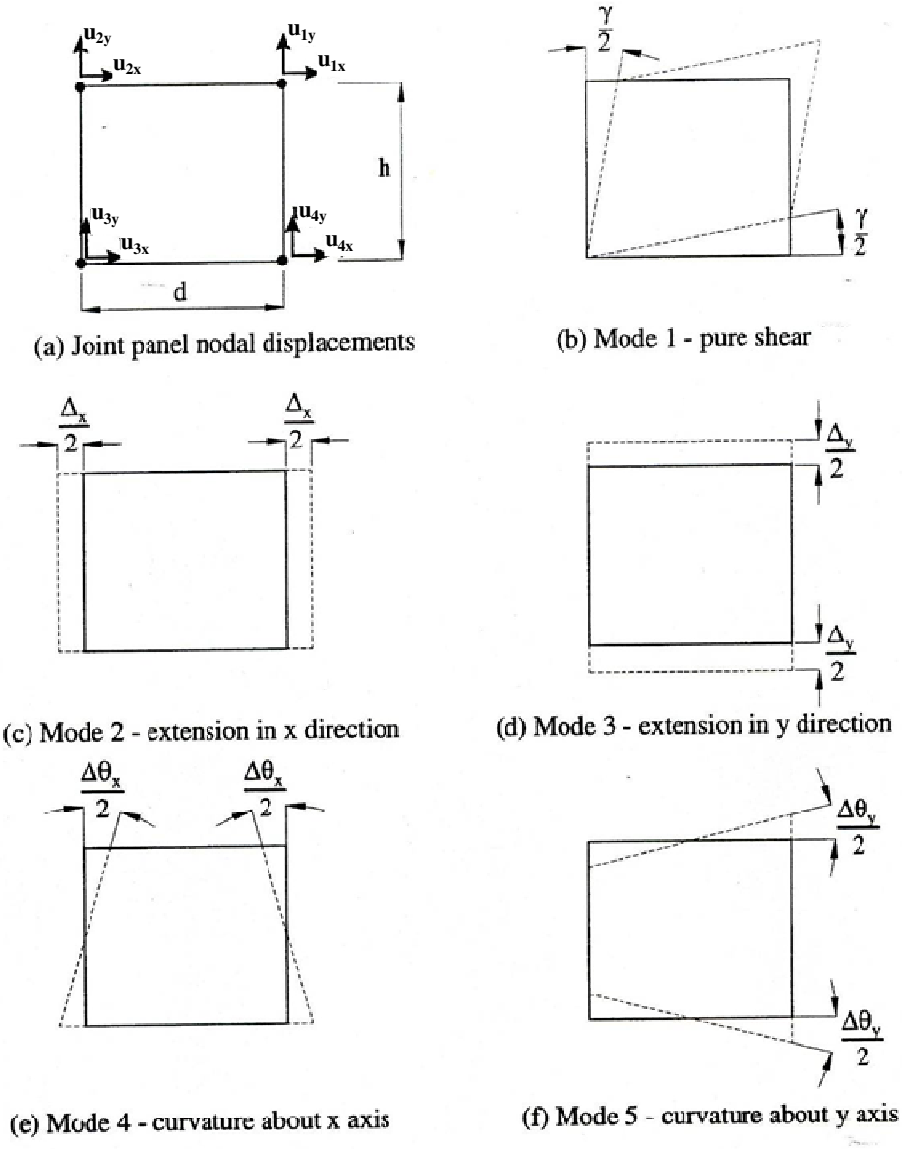

Figure 3.6 Deformation of joint panel deformation into five independent deformation modes

$$\begin{Bmatrix} \gamma \\ \Delta\theta_x \\ \Delta\theta_y \\ \Delta_x \\ \Delta_y \end{Bmatrix} = \begin{bmatrix} \frac{1}{2h} & \frac{1}{2b} & \frac{1}{2h} & -\frac{1}{2b} & -\frac{1}{2h} & -\frac{1}{2b} & -\frac{1}{2h} & \frac{1}{2b} \\ -\frac{1}{h} & 0 & \frac{1}{h} & 0 & -\frac{1}{h} & 0 & \frac{1}{h} & 0 \\ 0 & \frac{1}{b} & 0 & -\frac{1}{b} & 0 & \frac{1}{b} & 0 & -\frac{1}{b} \\ -\frac{1}{2} & 0 & \frac{1}{2} & 0 & -\frac{1}{2} & 0 & \frac{1}{2} & 0 \\ 0 & \frac{1}{2} & 0 & -\frac{1}{2} & 0 & \frac{1}{2} & 0 & -\frac{1}{2} \end{bmatrix} \begin{Bmatrix} u_{1x} \\ u_{1y} \\ u_{2x} \\ u_{2y} \\ u_{3x} \\ u_{3y} \\ u_{4x} \\ u_{4y} \end{Bmatrix} \tag{3.1}$$

For the panel configuration shown in Figure 3.7, let the initial lengths of the potentiometers be $\mathbf{B_0}$ (bottom), $\mathbf{T_0}$ (top), $\mathbf{N_0}$ (north), $\mathbf{S_0}$ (south), $\mathbf{D_{45,\,0}}$ (diagonal) and $\mathbf{D_{135,\,0}}$ (diagonal). Then the instrumentation lengths in the deformed mode can be estimated using simple geometric principles and are given below in Eqn.(3.2).

$$\begin{aligned} B &= B_0 + \Delta B = d + \Delta B \\ T &= T_0 + \Delta T = d + \Delta T \\ N &= N_0 + \Delta N = h + \Delta N \\ S &= S_0 + \Delta S = h + \Delta S \\ D_{45} &= D_{45,0} + \Delta D_{45} = \sqrt{h^2 + d^2} + \Delta D_{45} \\ D_{135} &= D_{135,0} + \Delta D_{135} = \sqrt{h^2 + d^2} + \Delta D_{135} \end{aligned} \tag{3.2}$$

By establishing the geometry of the panel from Eqns.(3.3)-(3.8) and assuming $u_{4y} = 0$, the remaining nodal displacements were calculated using Eqn.(3.9) and Eqn.(3.10) with respect to the reference node 3.

$$\theta_1 = \cos^{-1}\left(\frac{B^2 + S^2 - D_{45}^2}{2BS}\right) \tag{3.3}$$

$$\theta_2 = \cos^{-1}\left(\frac{B^2 - S^2 + D_{45}^2}{2BD_{45}}\right) \tag{3.4}$$

$$\theta_3 = \cos^{-1}\left(\frac{N^2 + D_{45}^2 - T^2}{2ND_{45}}\right) \tag{3.5}$$

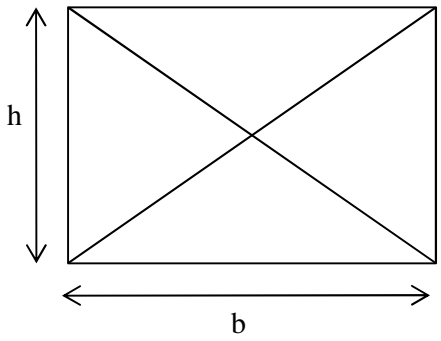

a) Undeformed shape

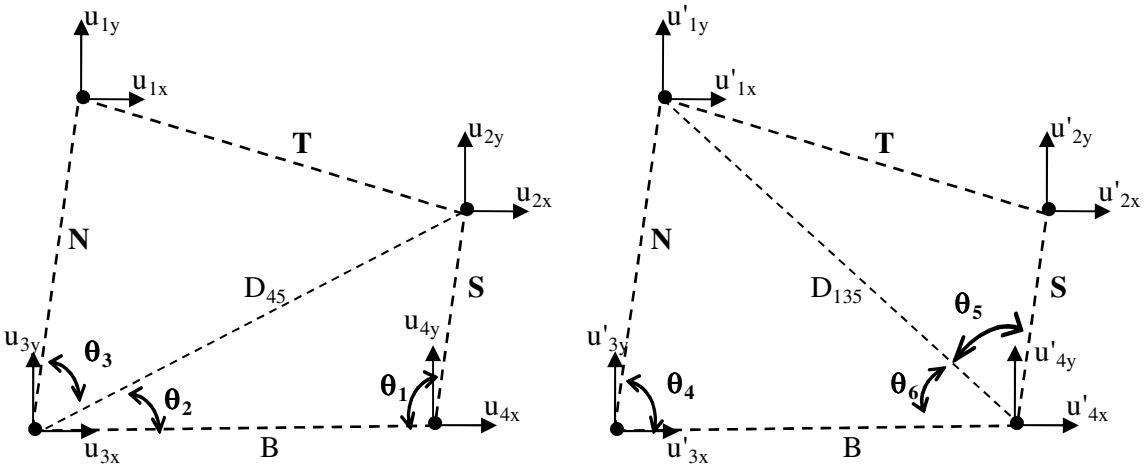

b) Deformed shape

Figure 3.7 Panel deformation

$$\theta_4 = \cos^{-1}\left(\frac{B^2 + N^2 - D_{135}^2}{2BN}\right) \tag{3.6}$$

$$\theta_5 = \cos^{-1}\left(\frac{D_{135}^2 + S^2 - T^2}{2SD_{135}}\right) \tag{3.7}$$

$$\theta_6 = \cos^{-1}\left(\frac{B^2 + D_{135}^2 - N^2}{2BD_{135}}\right) \tag{3.8}$$

$$\begin{aligned} u_{1x} &= D_{45}\cos(\theta_2) - b \\ u_{1y} &= D_{45}\sin(\theta_2) - h \\ u_{2x} &= N\cos(\theta_2 + \theta_3) \\ u_{2y} &= N\sin(\theta_2 + \theta_3) - h \\ u_{3x} &= u_{3y} = u_{4y} = 0 \\ u_{4x} &= B - b \end{aligned} \tag{3.9}$$

$$\begin{aligned} u'_{1x} &= u'_{4x} - S\cos(\theta_5 + \theta_6) \\ u'_{1y} &= S\sin(\theta_5 + \theta_6) - h \\ u'_{2x} &= N\cos(\theta_4) = B - D_{135}\cos(\theta_6) \\ u'_{2x} &= N\sin(\theta_4) - h = D_{135}\sin(\theta_6) - h \\ u'_{3x} &= u'_{3y} = u'_{3y} = 0 \\ u'_{4x} &= B - b \end{aligned} \tag{3.10}$$

The average of nodal displacements calculated from Eqn. 3.9 and Eqn. 3.10 were used to estimate the shear and flexural deformations of the panel using Eqn. 3.1.

Strain penetration deformation estimation

The approximation of deformations due to strain penetration is estimated by assuming that plane sections remain plane, so that the rigid body rotation of a wall due to strain penetration can be calculated based on the slip of the extreme tensile bars and the neutral axis location. This assumption leads to the expression

$$\theta_{sp} = \frac{\delta_{slip}}{d - c} \tag{3.11}$$

where, θ_{sp} is the rotation due to strain penetration, δ_{slip} is the slip of the extreme tensile bars in the anchorage zone, d is the distance from the extreme compression fiber to the extreme tensile bar, and c is the neutral axis depth as shown in Figure 3.8.

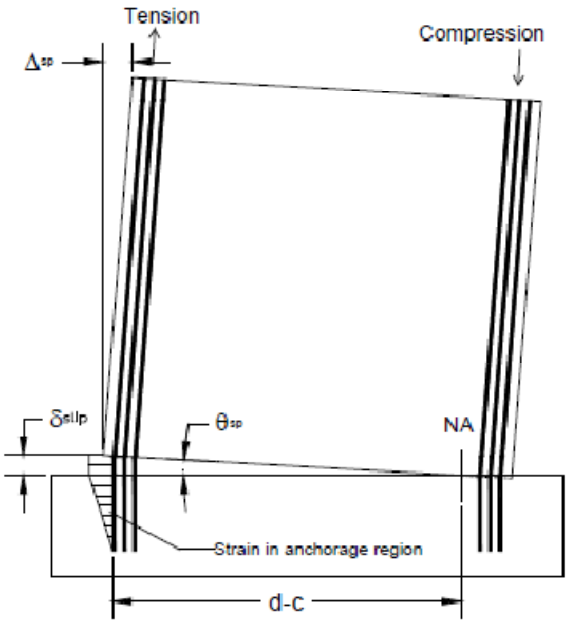

Figure 3.8 strain penetration deformation

By using the analytical procedure presented above, the measured lateral deformation of the three rectangular walls was decomposed into flexural, shear and strain penetration components. Few longitudinal bars along the wall length were welded with small studs to measure the slip in the longitudinal reinforcement due to strain penetration effect. Complete details about the instrumentation plan, types of instruments used and the location of instruments can be found in Johnson (2007). Figure 3.9 shows decomposition of first story displacement into three components for all the three walls. From the figure, it can be seen that for RWN and RWC, shear and flexural deformation in the plastic hinge region was nearly same. However, in case of RWS, shear deformations were higher than flexural deformations in the plastic hinge regions. Figure 3.10 shows the decomposition of the top displacement into three components for the three rectangular walls. As expected with the slender walls, the flexural component was significant in total displacement. However, it is worthwhile to note that strain penetration deformation contributed towards nearly 8-10% of the total top displacement. Hence, it is important to capture the strain penetration effects to accurately predict the concrete wall behavior. Figure 3.11 presents the hysteresis behavior of observed shear deformation in the first story of RWN and RWC.

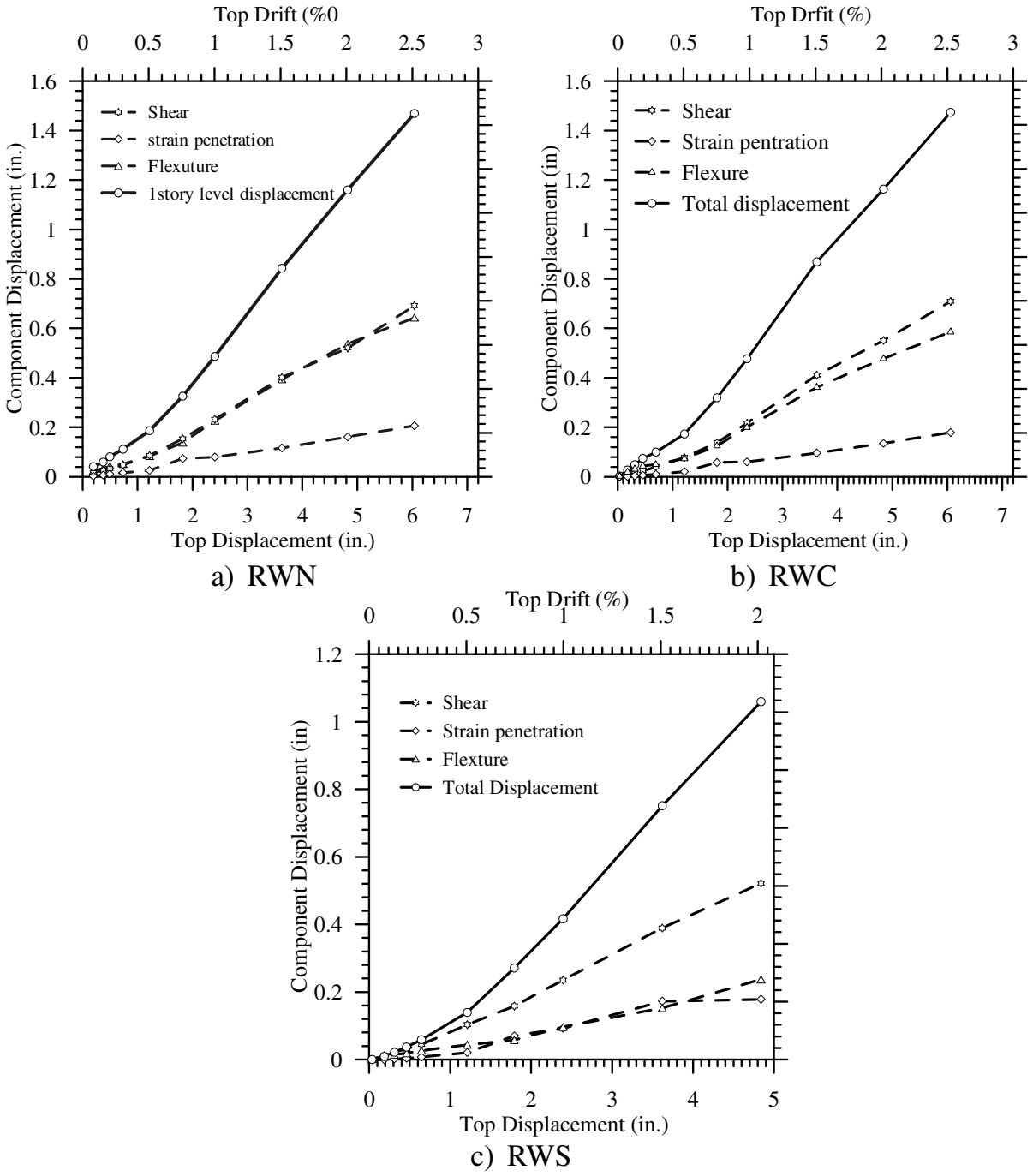

Figure 3.9 Deformation components for RWN, RWC and RWS at first story level

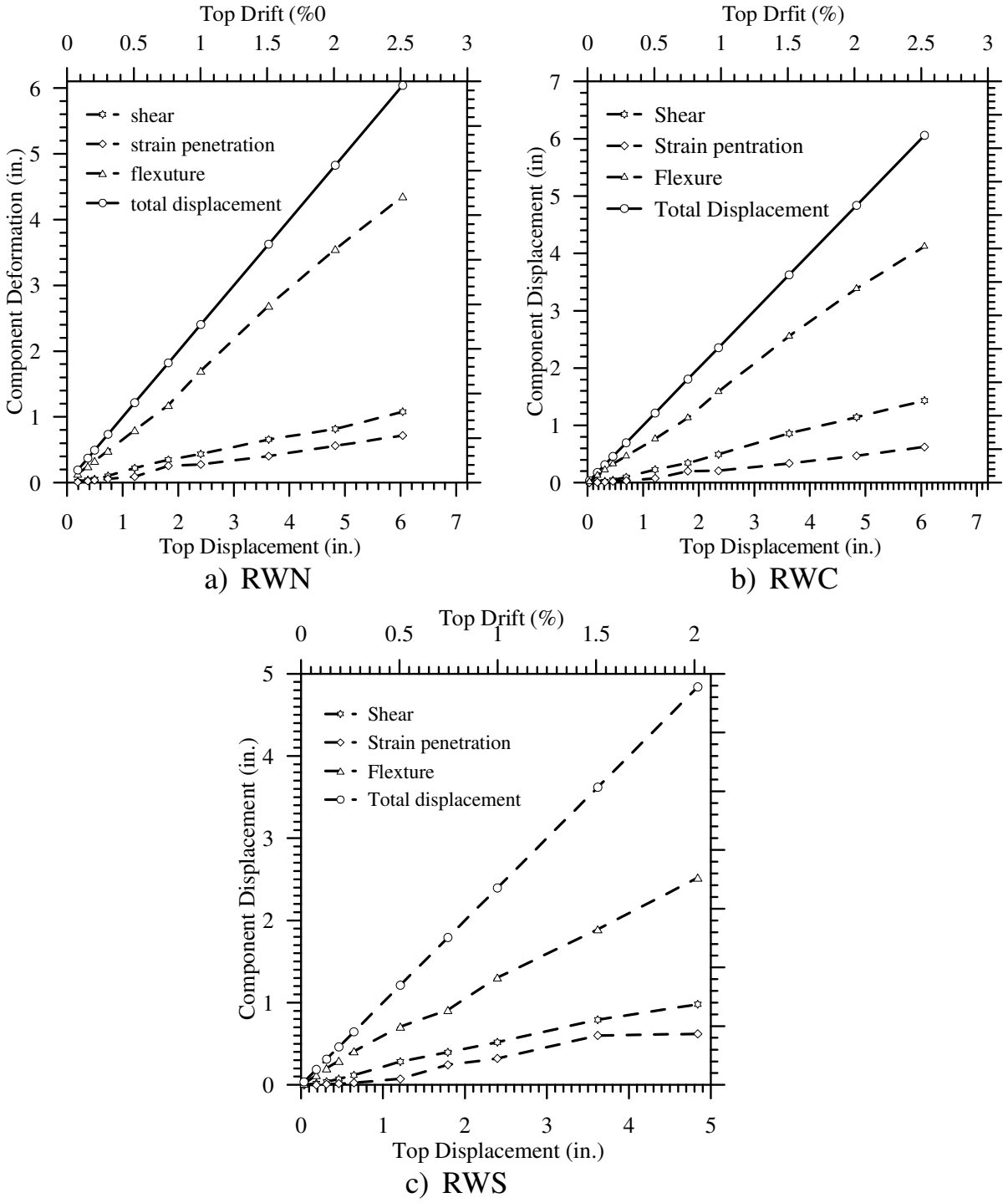

Figure 3.10 Deformation components of top displacement for RWN, RWC and RWS

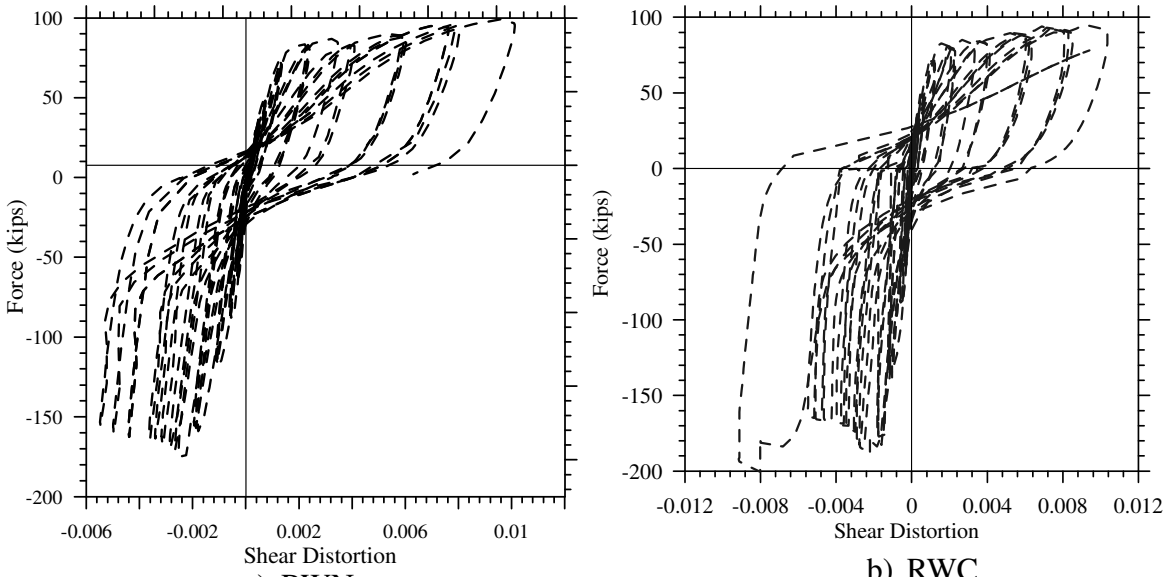

Figure 3.11 First story cyclic shear hysteresis response of RWN and RWC

3.3 OpenSees Models

The lateral load behavior of the three rectangular walls was analytically investigated using fiber based beam-column elements available in OpenSees (OpenSees 2007). The walls were modeled using nonlinear forced-based beam-column elements. Described below are the details of the analytical models developed for the three rectangular walls, which include information on how various anchorage details of the test specimens were modeled.

The base block of each wall was rigidly connected to the strong floor. Lateral movement and rotation of the base block with respect to the strong floor were monitored during testing. Since these measurements were found to be negligible, the base block was modeled with a node (i.e. node 1 in Figure 3.12) in the analytical model and its degrees of freedom were restrained in all the directions. Furthermore, since adequate anchorage was provided for the longitudinal reinforcement in the foundation, the longitudinal bars were assumed to experience no slip in the foundation due to anchorage condition. However, slipping of the bars along a portion of a fully anchored bar should be expected due to strain

penetration (Zhao and Sritharan, 2007), which was accounted for in the analytical model as detailed below.

3.3.1 Model for RWN

In order to capture the overall and local responses of the wall accurately, the analysis model should satisfactorily capture the individual deformation components due to flexure, shear and strain penetration. In this section, the analytical model developed for RWN is described. Figure 3.12 shows a schematic of the fiber-based OpenSees model developed for RWN, which consists of five force-based beam-column elements along the height of the wall. Force-based beam-column elements were preferred over the displacement-based beam-column elements for the model because the force-based beam-column element captures the plastic hinge region and the spread of plasticity along the length of a member more accurately than a displacement based beam-column element. Consequently, the force-based element was expected to capture the flexural response more accurately than a displacement-based element.

Previous research has shown that sufficiently anchored longitudinal reinforcement of the flexural members experiences slip along a portion of the bar embedment due to strain penetration along the longitudinal reinforcing bars anchored into a connecting concrete member. It was also demonstrated by Sritharan et al. (2000) and Zhao & Sritharan (2007) that ignoring the strain penetration effects in analytical models will significantly affect the prediction of the local response parameters. Consequently, as recommended by Zhao & Sritharan (2007) (see Appendix A) a zero-length fiber-based element was used at the interface between the wall and foundation to account for the strain penetration effects. This zero length interface element had the same cross section as the rectangular wall (i.e. cross section-1 for RWN, shown in Figure 3.12). The steel fibers of this zero length section were modeled using the strain penetration material model, which relates the stress in a fully anchored reinforcement with the total slip of the bar at the interface.

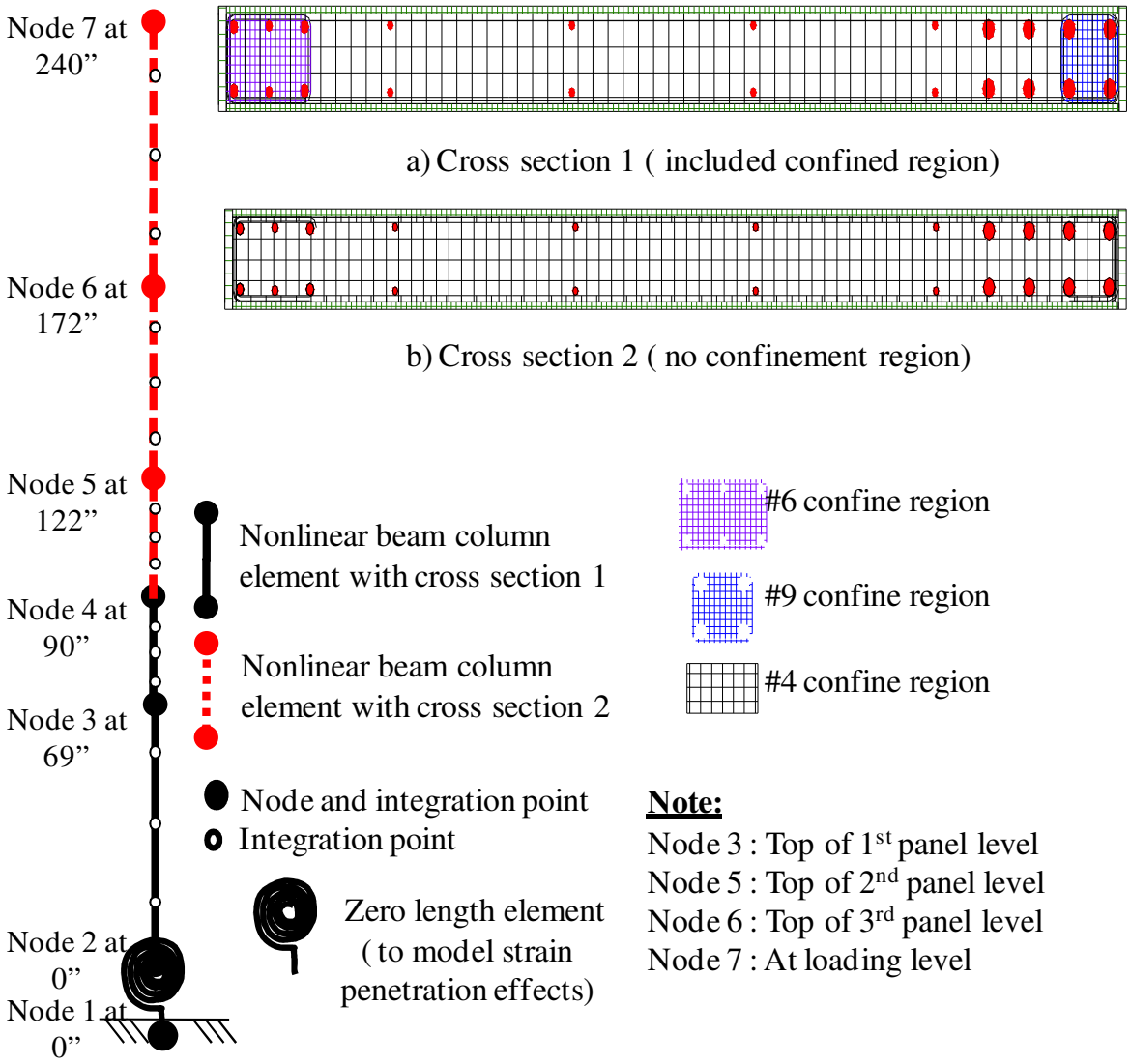

Figure 3.12 Schematic of the nonlinear fiber-based OpenSees model for RWN

Based on the experimental observations and data from RWN, some modifications to the suggested values by Zhao and Sritharan (2007) for the model parameters such as slip at yield were incorporated. A preliminary analysis was carried out with the suggested slip values at the yield stress, which were 0.01373 in. for #5 bar, 0.01541 for #5 bar, 0.01680 for #6 bar and 0.02196 in. for #9 bar respectively. However, after examining the response of the wall and comparing the experimental and analytical slip values and their contributions, the slip at yield stress for #6, #5 and #4 rebars was increased by a factor of 1.5, while the yield slip for #9 bars was increased by a factor of 6. The increase in the yield slip value for #9 bars

was high and is suspected to be due to the use of 1.875 in. clear spacing between bars and the associated congestion of the reinforcing bars in the boundary element to match the capacity of T-wall in flange in tension direction.

Except for the second panel, a single force-based beam-column element (i.e. nonlinearBeamColumn in OpenSees) with five integration points along its length modeled each panel of RWN. The location of integration points followed the Gauss-Lobotto scheme. For example, in an element with five integration points, the integration points are located at both ends of the element (-1.0 and 1.0 in an isoparametric formulation), at the center of the element (0.0 in an isoparametric formulation) and at points located at a distance of 0.17267 times the length of the element from both ends (-0.65465367, 0, 0.65465367) of the element. The second panel was modeled with two force-based elements since the boundary elements were extended 21 in. into the second panel, changing the cross section details at 90 in. from the base of the wall. A fiber section was used to represent the cross section of the wall. The details of the fiber sections used for the nonlinear beam-column elements are shown in Figure 3.12. The wall cross sections in the confined and unconfined regions were discretized using fibers approximately 0.2 in. x 0.2 in. The confined and unconfined concrete fibers were modeled to follow the modified Chang and Mander confinement model described in Waugh et al. (2009) (i.e., *Concrete07* in OpenSees).

The unconfined concrete strength for the wall specimen was obtained from testing of ten 4 in. x 8 in. cylinders at the end of testing of RWN. The average concrete strength for RWN was 7870 psi for bottom two panels and 6880 psi for the remainder of the wall. The concrete strength was different between the top two and bottom two panels because the wall was cast in two different stages. The concrete tensile strength was taken as $6\sqrt{f_c'}$ (psi) in both cases. However, the tensile strength in the No. 6 boundary region of the first panel was reduced to $3\sqrt{f_c'}$ (psi), to account for the effects of pre-existed shrinkage cracks in the region near the wall base. The concrete young's modulus was approximated to $57000\sqrt{f_c'(psi)}$ (psi). The confined concrete properties in the boundary regions were obtained using the confined concrete model proposed by Mander et al. (1988) based on the details of the transverse reinforcement.

All longitudinal reinforcement (i.e. #4, #5, #6 and #9 bars) was modeled using the *ReinforcingSteel* material model available in OpenSees. This model has the ability to closely follow the strain response of Grade 60 mild steel reinforcement, especially under cyclic loading.

Table 3.1 Measured properties of reinforcement used in the RWN model

Bar size (dia (in.))	Yield Strength (ksi)	Elastic Modulus (ksi)	Tangent at initial strain hardening (ksi)	Strain hardening strain (in/in)	Ultimate strength (ksi)	Strain at ultimate strength (in/in)
#9 (1.125 in.)	66.74	26546	775	0.0086	90.0	0.10
#6 (0.75 in.)	71.00	28249	800	0.0096	96.5	0.10
#5 (0.625 in.)	71.03	28560	875	0.0095	97.5	0.10
#4 (0.5 in.)	58.00	22282	-	-	90.0	0.10
#3 (0.375 in.)	66.00*	29000*	-	-	-	0.12
#2 (0.25 in.)	79.34	29000*	-		96.3	0.12

* assumed

The #4 reinforcing bar was modeled using the modified Menegotto-Pinto model (i.e., *Steel02* in OpenSees) because the uniaxial testing of #4 rebar did not exhibit any yield plateau. Furthermore, the strain demand in #4 bars was never reported to exceed 0.035 in/in. Figure 3.13 compares the modeled stress-strain response of #4, #5, #6, and #9 bars with the experimental stress-strain behavior obtained from monotonic pull tests. The reinforcement properties used for the OpenSees model of RWN are shown in Table 3.1.

Significant contribution of shear deformations towards the lateral deformation of walls and the existence of shear-flexural coupling in the plastic hinge regions was demonstrated by previous research on flexural dominant rectangular concrete walls with aspect ratios greater than 2.0 (Thomsen & Wallace 1995). These phenomena were also observed in the experimental response of the RWN (Johnson, 2007). Therefore, it follows that to accurately capture the lateral load behavior, it is necessary to account for the shear deformations along the height of the wall.

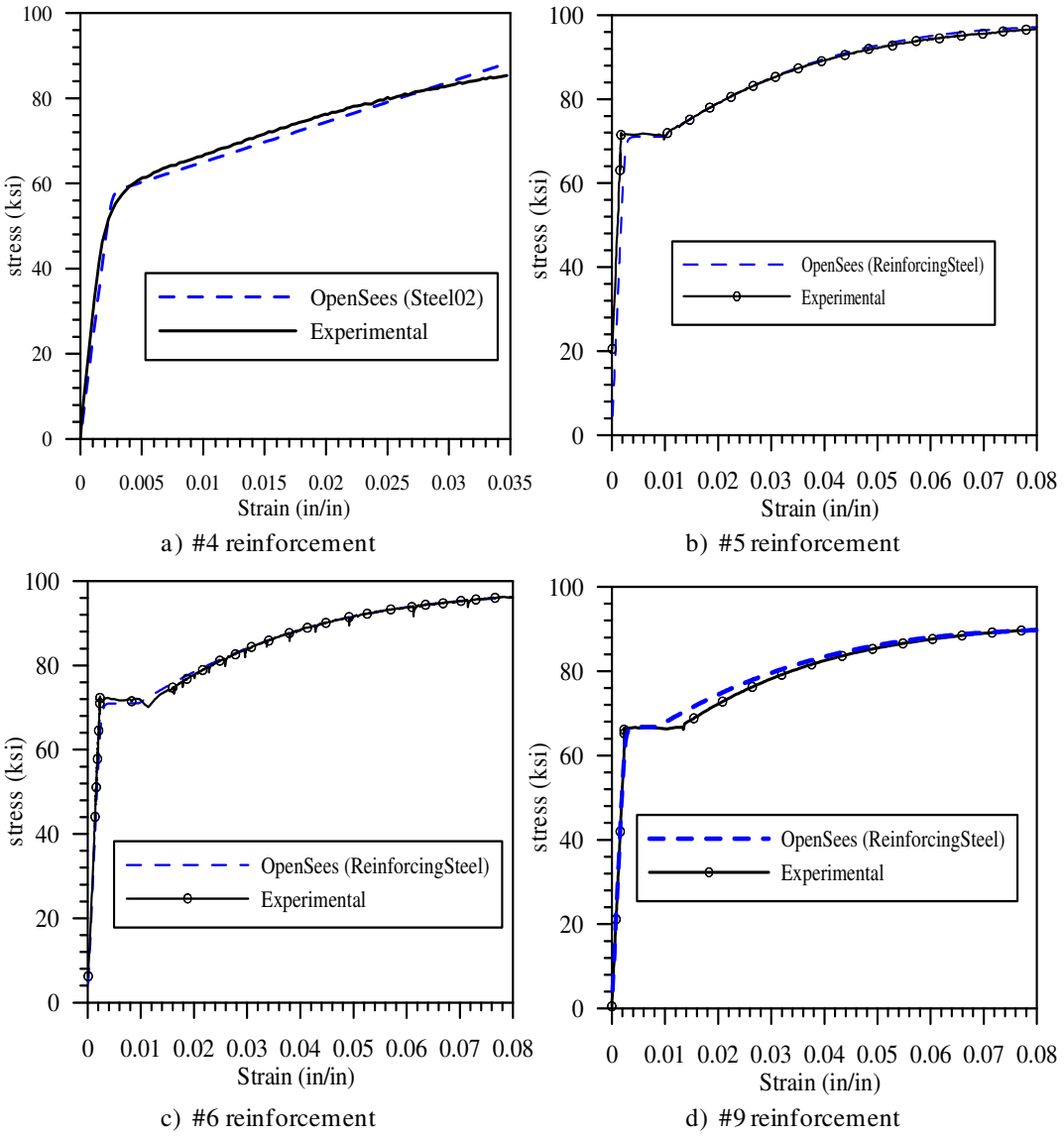

Figure 3.13 Comparison of experimental and theoretical stress-strain responses of RWN longitudinal reinforcement under monotonic loading

The force-based beam-column element in OpenSees accounts only the flexural response while ignoring the effects of shear mechanism and possible interaction between flexure and shear mechanisms. Although, there are several formulations recommended in literature to account for the shear deformations in the force-based beam-column elements (Petrangeli, 1999 and Martinelli, 2008) no such technique was available in OpenSees to account for the effects of shear deformation. Therefore the shear deformations in RWN were accounted by aggregating a uniaxial material behavior (i.e. *Pinching4* in OpenSees) over the flexural

response of the nonlinear beam-column element. Although, the section aggregation method helps in accounting for the shear deformation, it doesn't account for the effects of flexure-shear interaction. The experimentally observed shear force-distortion relationship of RWN was used to arrive at the model parameters for the *Pinching4* model. Also, with the *Pinching4* material model, the observed degradation of shear stiffness could not be captured and thus the shear degradation is ignored in the model.

3.3.2 Model for RWC

In this section, the analytical model developed for the rectangular wall with couplers near the foundation interface is described. The overall modeling of RWC followed that of the RWN, but it incorporated a sixth force-based beam-column element. This new beam-column element was used to model the region containing the mechanical couplers. Figure 3.14 presents the schematic of the OpenSees model developed for RWC. It was anticipated that the presence of couplers would modify the strain distribution in the bottom region of the wall. A challenge associated with this modeling was that, the length and the area of the couplers varied based on the size of the rebar. Since the response that subjected the #5 and #6 longitudinal bars in tension experienced severe nonlinearity, the length of this beam-column element representing the coupler region was taken as the average length of the #5 and #6 bar couplers. The lengths and cross sectional areas of the couplers used in RWC are presented in Table 3.2. Concrete and longitudinal reinforcement fibers in RWC were modeled as in RWN, while the couplers were modeled with their increased cross sectional area, but with the stress-strain model same as the corresponding longitudinal reinforcing bar. During construction of the test specimen, no confinement hoops were placed within the coupler region as this would not have permitted any cover to the hoop reinforcement. The concrete fibers in the coupler region were therefore, modeled as unconfined concrete. Because the couplers were kept above the wall-to-foundation interface in the specimen, reinforcement fibers in the zero-length section at the wall-to-foundation interface were modeled using the reinforcing bar area instead of couplers area. The strain penetration effect and the shear deformations were included in the same manner as it was done in RWN model.

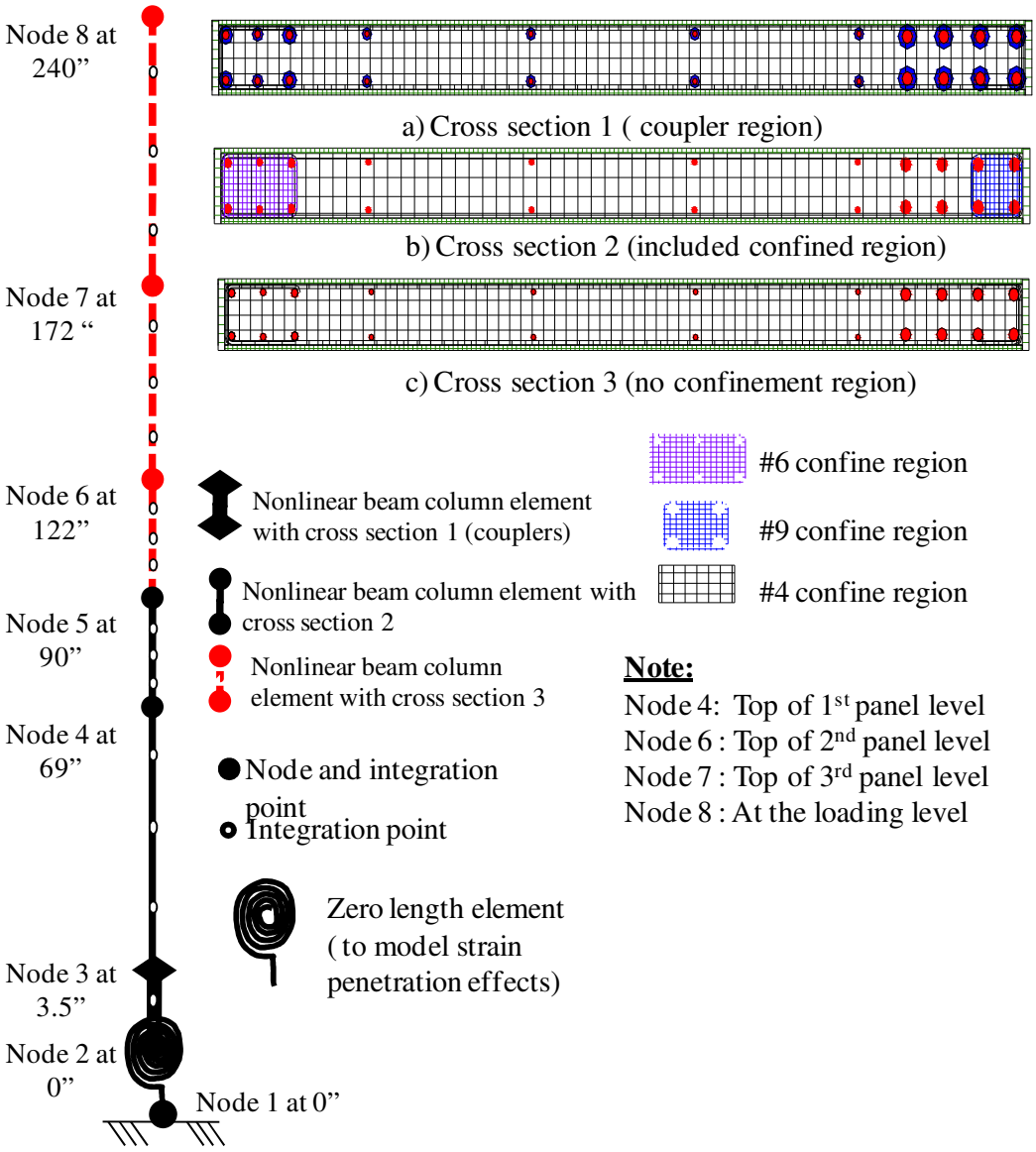

Figure 3.14 Schematic of the nonlinear fiber-based OpenSees model for RWC

As with RWN, the unconfined concrete strength of the wall specimen was obtained from testing of ten 4 in. x 8 in. cylinders at the end of testing of RWC. The average concrete strength of RWC was 7500 psi for bottom two panels and 9100 psi for the top two panels. The concrete strength was different between the top and bottom halves of the wall due to same reason as RWN. The concrete tensile strength was taken as $6\sqrt{f_c'}$ (psi) in the both cases. However, as with RWN, the tensile strength in the No. 6 boundary region of the first

story was reduced to $3\sqrt{f_c'}$ (psi), to account for the effects of pre-existed shrinkage cracks in the bottom panel. The concrete young's modulus was approximated to $57000\sqrt{f_c'(psi)}$ (psi). The confined concrete properties in the boundary regions were obtained using the confined concrete model proposed by Mander et al. (1988) based on the details of the transverse reinforcement. The longitudinal reinforcement was modeled with same material properties as in RWN.

Table 3.2 Length and cross section area details of the couplers in RWC

Bar Size (dia)	Coupler length (in.)	Coupler dia (in.)	Coupler Area (in^2)
#4 (0.5 in.)	2.75	0.99	1.125
#5 (0.625 in.)	3.00	0.99	1.125
#6 (0.75 in.)	4.00	1.50	1.77
#9 (1.125 in.)	5.00	2.0	3.14

3.3.3 Model for RWS

In this section, the analytical model developed for the rectangular wall with traditional lap splices near the wall base (i.e., in the plastic hinge region), RWS is described. The overall modeling of RWS was done as for RWN, except for introducing five more force-based beam- column elements. These new beam-column elements were used to model the region containing the traditional lap splices. Figure 3.15 presents the schematic of the OpenSees model developed for RWS. It was anticipated that the presence of lap splices in the plastic hinge region would influence the strain distribution in the spliced region. It was also anticipated that along the length of the splice, the effective bar area will be larger than that of one bar in the middle region of the splice because of the conservatism built into the estimation of code based lap splice length as used in RWS. A review of relevant literature indicated that structures with lap splices have been typically modeled with a single rebar effectively representing the lap splice. This is because it is generally accepted that the

strength of a spliced bar is almost the same as that of a single embedded bar (Cho and Pincheira, 2006).

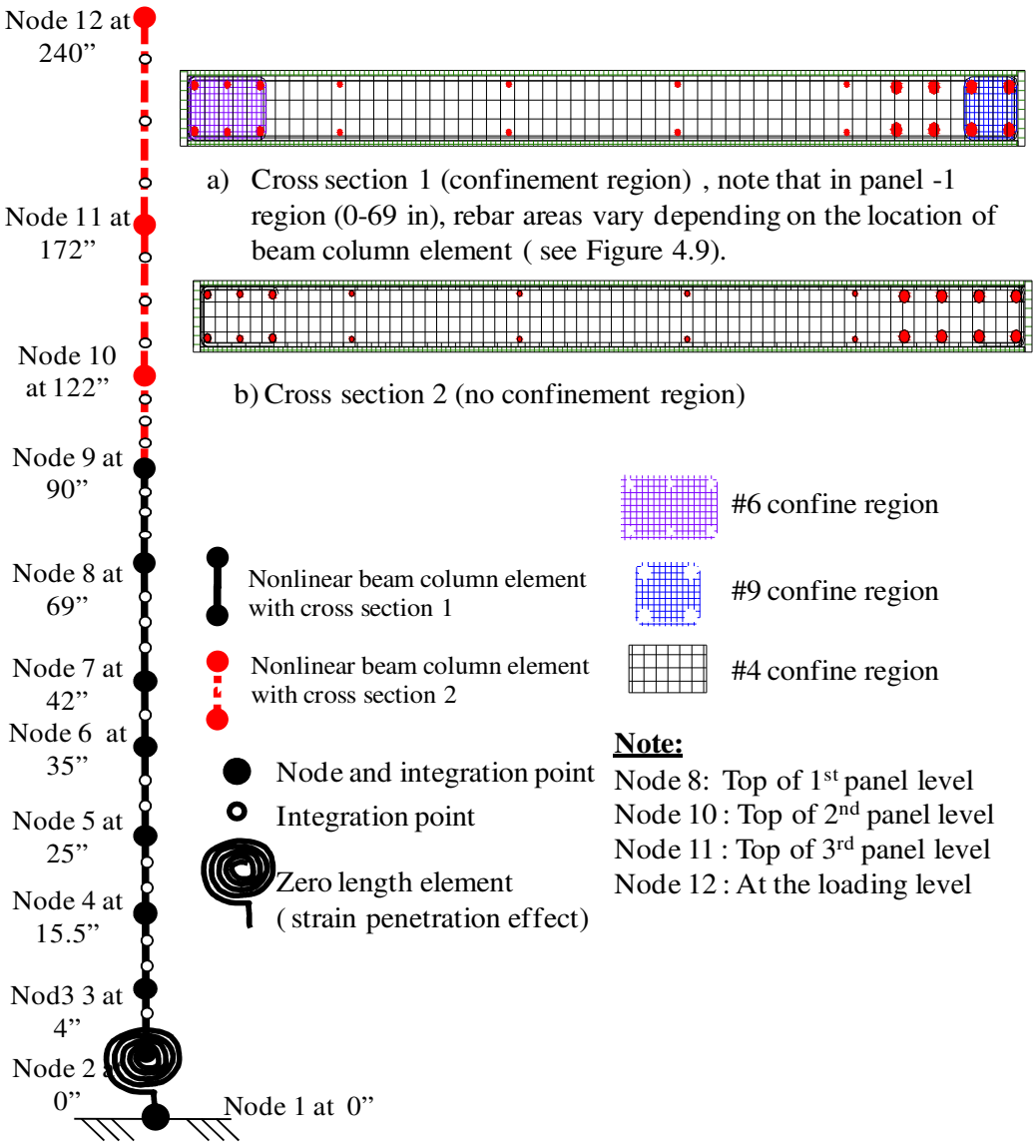

Figure 3.15 Schematic of the nonlinear fiber-based OpenSees model of RWS

Using this approach, a preliminary analysis of RWS with the lap-splice represented by a single rebar located at the center of the lap splice was conducted. A comparison of the response from the analysis with experimental response did not support this approach (see results in Figure 3.30, presented in Section 4.4.3.1). Consequently, in the RWS model, the

lap splice region was modeled using six nonlinear beam-column elements, with effective reinforcing bar areas varying from one bar area to two bar area depending upon the location of the beam-column element. Figure 3.16 shows the assumed effective bar area over the splice length in the RWS model for different bar sizes, which were obtained based on assumed bond strength of $10\sqrt{f_c'(psi)}$ along the splice region. The strain penetration effect and the shear deformation in this model were handled in the same manner as in the RWN model. During the experiment, slip between the longitudinal bars (predominantly in #6 and #5 bars) in lap splice region was observed. Since there are neither specific experimental studies nor analytical models found in the literature to model the slip within the spliced region, the potential slip of bars in the spliced region was not modeled.

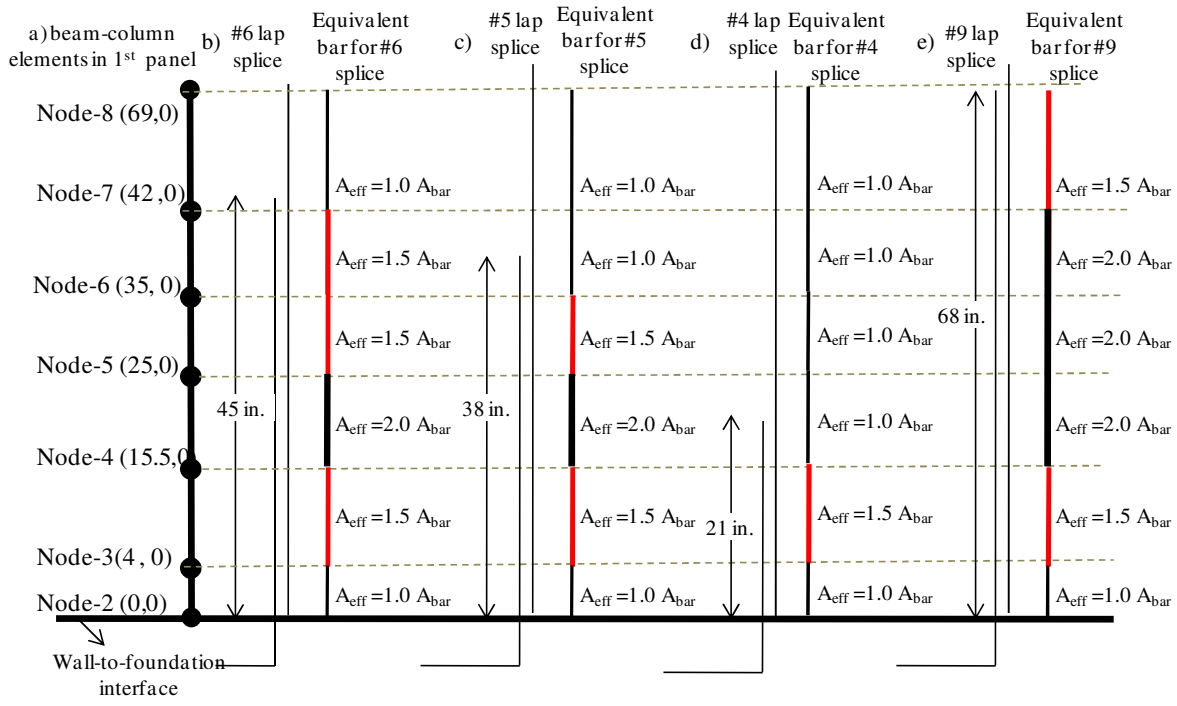

Figure 3.16 Schematic of the effective bar area used over the lap splice length of #4, #5, #6 and #9 in the RWS model

Again, the unconfined concrete strength for the wall specimen was obtained from testing of ten 4 in. x 8 in. cylinders at the end of testing of RWS. The average concrete strength for RWS was 8110 psi for bottom two panels and 6580 psi for the top two panels.

The concrete strength was different between the top two and bottom two panels for the same reason as RWN and RWC. The concrete tensile strength was taken as $6\sqrt{f_c'}$ (psi) for the entire wall. The concrete young's modulus was approximated to $57000\sqrt{f_c'(psi)}$ (psi). The confined concrete properties in the boundary regions were obtained using the confined concrete model proposed by Mander et al. (1988) based on the appropriate details of the transverse reinforcement. The longitudinal reinforcement was modeled as with the RWN model using the same material properties.

3.4 Comparison of Results

3.4.1 RWN

In this section, the OpenSees analytical model and experimentally observed responses of RWN are compared and appropriate comments are made. In addition to the global response, accuracy of the local responses is examined, including the force-displacement response of RWN at different panel levels. Also a comparison of experimental and calculated contribution of various deformation components to the lateral displacement at first panel level and top of wall is presented

3.4.1.1 Cyclic Response

The measured and calculated cyclic responses of RWN when subjected to the loading protocol in Figure 3.5 are shown in Figure 3.17. As seen in this figure, the OpenSees simulation accurately captured the force-displacement response of RWN for the loading direction that subjected the #6 and #5 longitudinal bars in tension. The unloading stiffness, reloading stiffness, and residual displacements were all well simulated by the analysis model in this direction. In the opposite direction, that subjected the #9 bars in tension, the analytical response closely matched the experimental response up to about 2.4 in. of lateral displacement, which was the peak lateral displacement for the majority of testing. However, the agreement is not as good as that observed for the other direction. The calculated peak values were within 3% of the experimental values for up to 2.4 in. (i.e., 1% drift) of lateral displacement in the #9 bars in tension direction. At 4.8 in. lateral displacement, for #9 bars in

tension, the analytical model overestimated the lateral force resistance by 7.9%. The over estimation of the load and the underestimation of the residual displacements are due to disregarding of the shear degradation in the OpenSees model, which is further discussed in the next section. The initial stiffness in the both directions was captured with good accuracy.

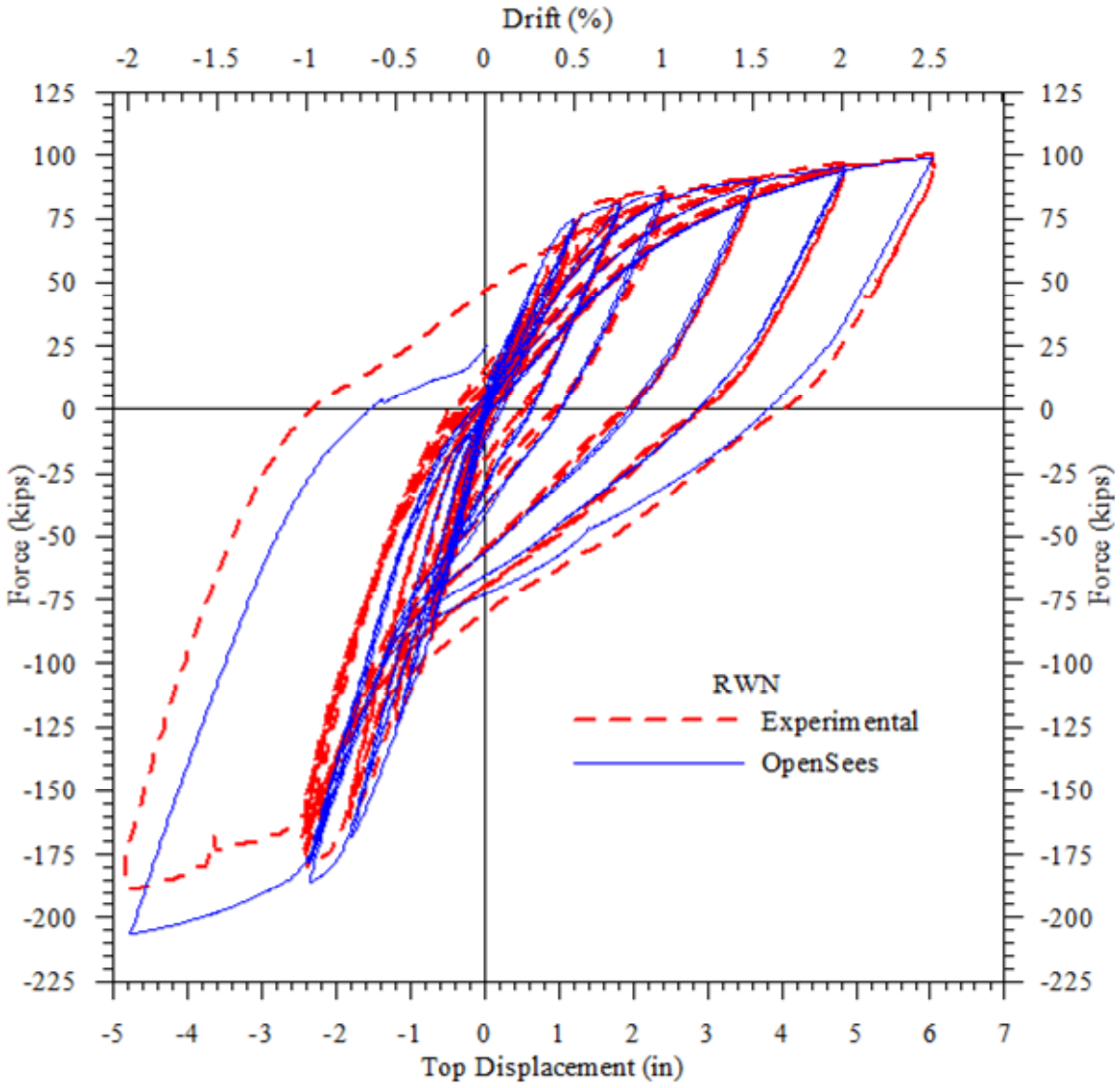

Figure 3.17 Comparison of measured and calculated force-displacement responses of RWN

3.4.1.2 Response at top of First Panel

To ensure that the OpenSees model adequately captured the different deformation components accurately, the responses at different panel levels were also examined. It was

expected that the first panel response would be heavily influenced by the contribution of shear deformation, due to the reduction of shear stiffness caused by the flexural damage and yielding of the longitudinal reinforcement within the first panel. Thus, the comparison of lateral load response at the first panel level provides an opportunity to examine the modeling accuracy of the shear deformation. The calculated and measured force-displacement responses at the first panel level are shown in Figure 3.18a. The OpenSees model did not capture the first panel response in both loading directions as accurately as it did at the top of the wall. It is seen that the analytical model over predicted the total lateral displacement for the direction that subjected the #6 bars in tension and under predicted the lateral displacement for the #9 bars in tension. However, the analytical model estimated the initial stiffness and the post yield stiffness of the first story level with good accuracy.

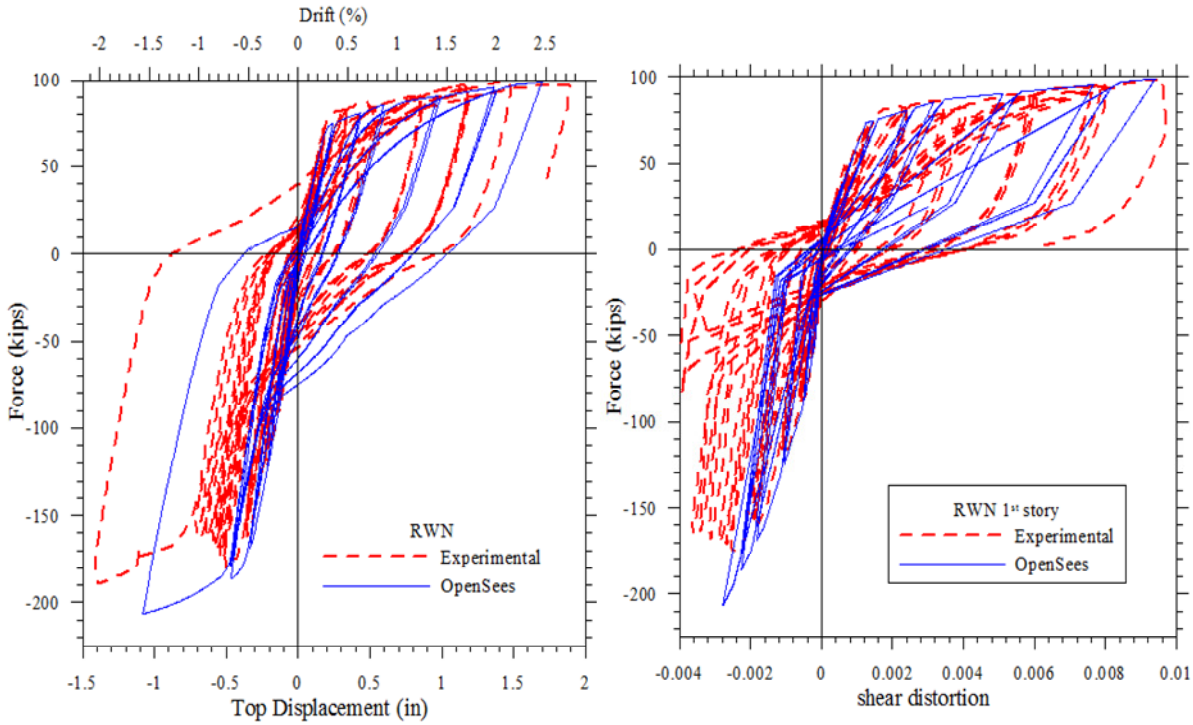

a) force-displacement response at top of 1st panel b) 1st panel force-shear distortion response

Figure 3.18 Overall and the shear distortion responses of RWN at the first panel level

The under prediction of the lateral displacement response in the #9 bars in tension direction was expected as the *pinching4* model used for capturing the shear response did not account for possible strength degradation and softening of the structure expected due to repeated loading to the same lateral displacement of 2.4 in. (i.e. -1% drift) in #9 bars in

tension direction. This can be clearly seen in Figure 3.18b, which compares the theoretical and experimental shear distortions of the first panel in RWN. The increase in the shear distortion (from -0.002 rad. to -0.0038 rad.) due to the repeated loading to -1% drift was expected due to significant damage observed in the first panel of RWN during testing. Large inclined shear cracks were developed during the +1.5%, +2.0% loading cycles in the #6 bars in tension direction due to yielding of longitudinal reinforcement. The wall was heavily cracked at +2% drift with minor spalling of cover concrete. Figure 3.19 shows the damage state of the first panel of RWN as the drift in the #6 direction changes from 1% to 2.5 % while a constant drift of -1% was maintained in #9 in tension direction. The level of shear cracking shown in Figure 3.13 at different drift levels supports the measured increase in shear distortion in the first panel in #9 bars in tension direction.

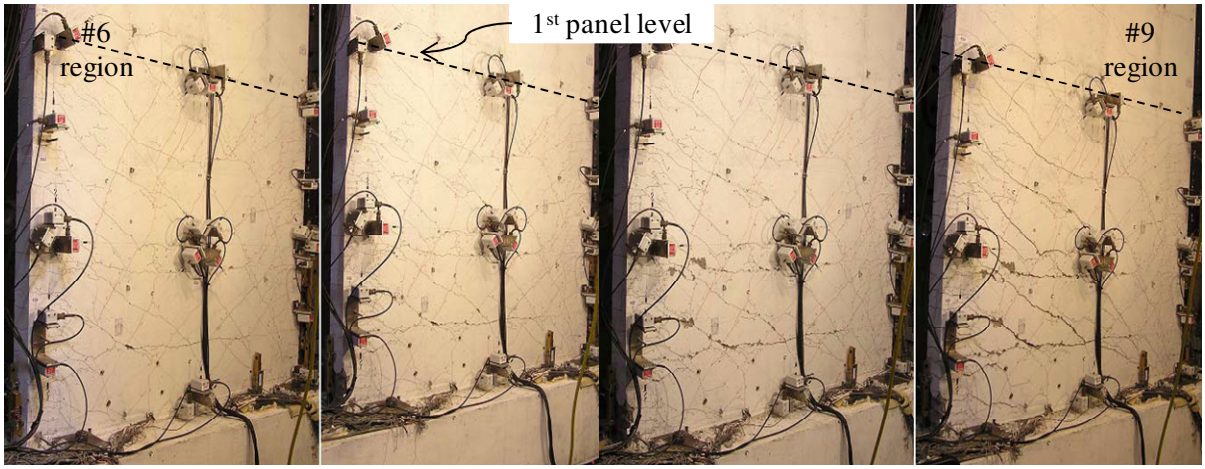

a) at 1% drift b) at 1.5% drift c) at 2% drift d) at 2.5% drift

Figure 3.19 Extent of shear cracking observed at different drift levels within the first panel of RWN

3.4.1.3 Response at top of Second Panel

The lateral load response of RWN at the top of second panel was also compared to the measured experimental response and is shown in Figure 3.20. The OpenSees model captured the force-displacement behavior at the second panel level with good accuracy in the #6 bars in tension direction. The stiffness of the loading, unloading, reloading paths and

residual displacements all are well captured by the model in the #6 bars in tension direction. The initial stiffnesses in both directions were also captured accurately by the OpenSees model. However, the residual displacements in the #9 in tension directions were under predicted as observed for the response at the top of the wall. This observation again reinforces that the discrepancy seen in the total response of RWN in Figure 3.17 is largely due to the shear distortion error encountered in the first panel of the wall.

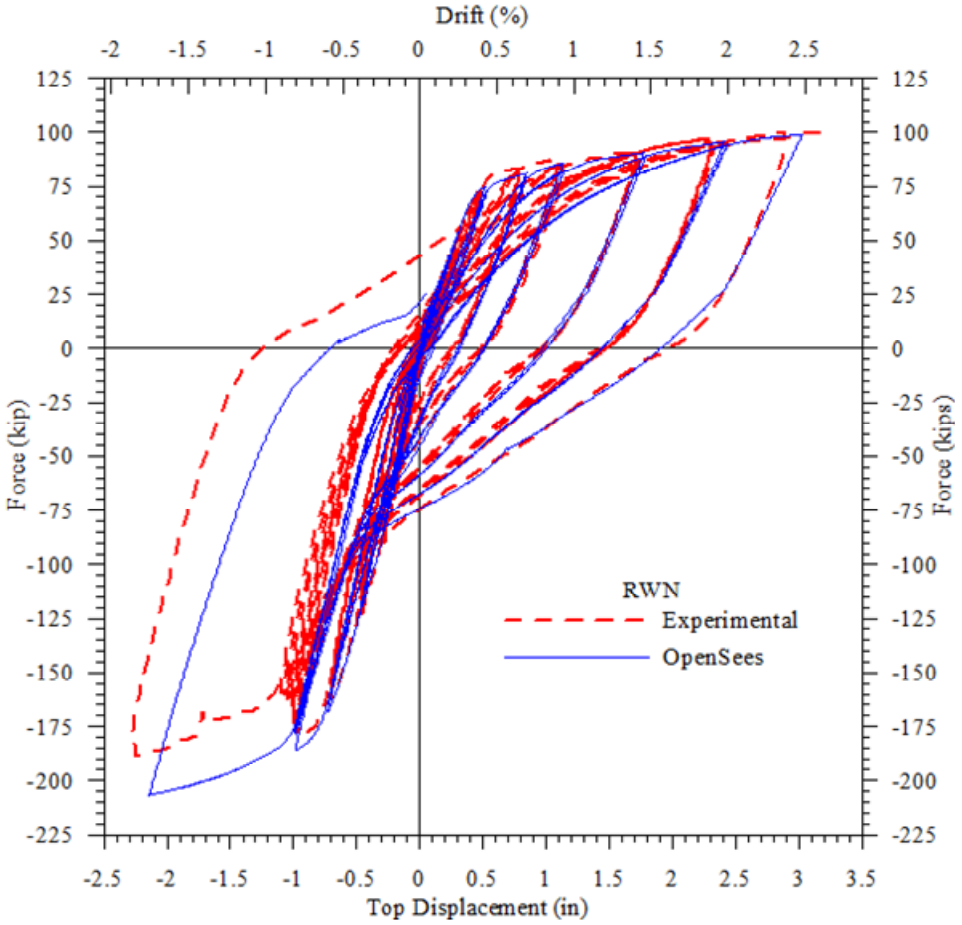

Figure 3.20 Comparison of the measured and calculated force-displacement responses of RWN at the top of the second panel

3.4.1.4 Comparison of Deformation Components

Calculated and experimental values of various deformation component responses of RWN at the first panel level and the top of the wall during the peak displacements are compared and appropriate comments are presented. Since the #6 and #5 bars in tension

direction response was of significant interest, the comparisons are presented for that loading direction only.

The comparison between the calculated and measured values of various deformation components of RWN at the first panel level and the top of the wall are shown in Figure 3.21 and Figure 3.22 respectively. It can be seen from Figure 3.21 and Figure 3.22 that the analytical model over predicted the localized flexural deformation in the first panel, while accurately predicting the overall flexural deformation of RWN. The shear deformation and the deformation due to strain penetration in the first panel and at the top of RWN were well captured by the model.

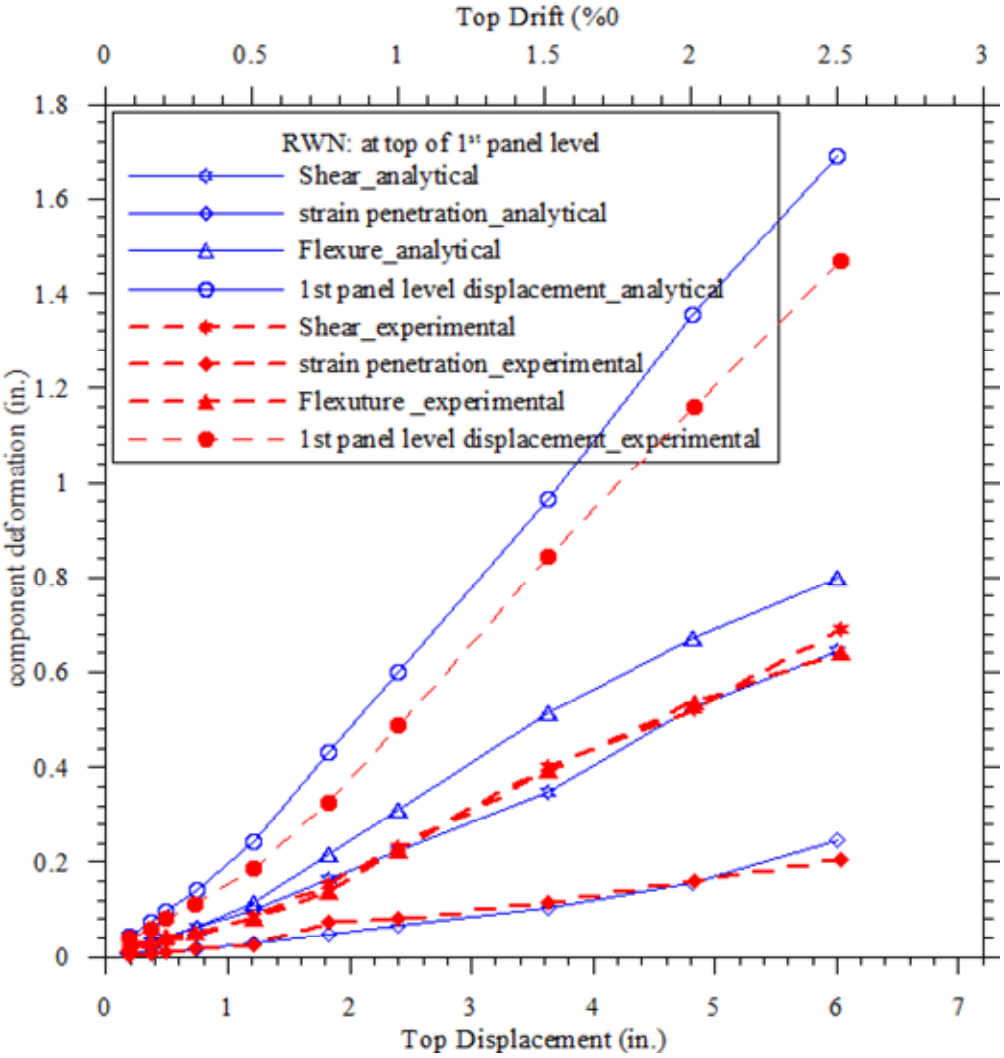

Figure 3.21 Comparison between calculated and experimental deformation component responses at the first panel level of RWN

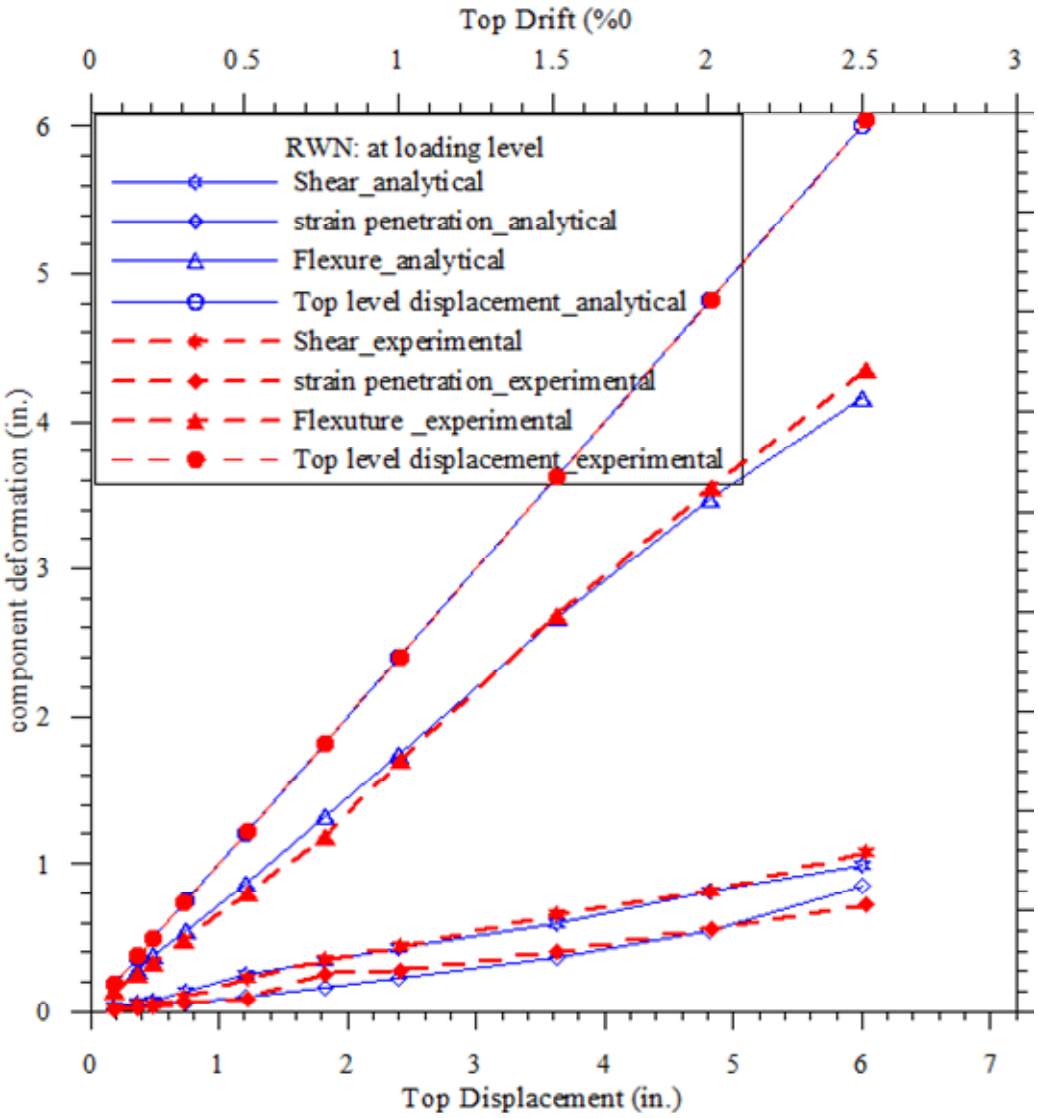

Figure 3.22 Comparison between calculated and experimental deformation component responses at the top of RWN

3.4.2 RWC

In this section, the OpenSees analytical model and experimentally observed responses of RWC are compared and appropriate comments are made. In addition to the global response, accuracy of the local responses is examined, including the force-displacement response of RWC at different panel levels.

3.4.2.1 Cyclic Response

The measured and calculated cyclic responses of RWC when subjected to the loading protocol in Figure 3.5 are shown in Figure 3.23. As seen in this figure, the OpenSees simulation accurately captured the force-displacement response of RWC for the loading direction that subjected the #6 and #5 longitudinal bars in tension.

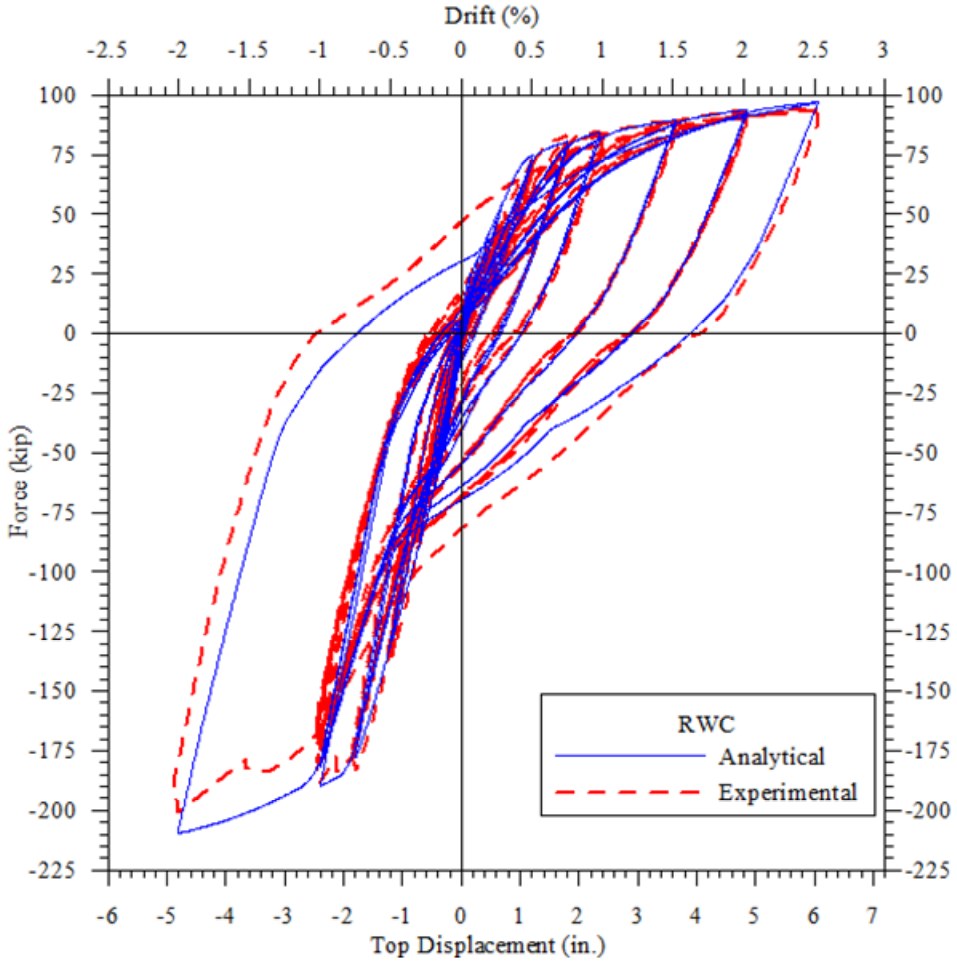

Figure 3.23 Comparison of measured and calculated force-displacement responses of RWC

The unloading stiffness, reloading stiffness, and residual displacements were all well simulated by the analysis model up to a lateral displacement of 6.0 in. (i.e., +2.5% drift) in this direction. In the opposite direction, that subjected the #9 bars in tension, the analytical response accurately captured the experimental response up to a lateral displacement of 2.4 in. (i.e. -1% drift) and the calculated peak values were within 3% of the experimental values. At

-2% drift, the analytical model overestimated the load by 5.0%. The over estimation of the load and the underestimation of the residual displacements are due to disregarding of the shear degradation in the OpenSees model, which is further discussed in the next section. The initial stiffness in the both directions was captured with good accuracy.

3.4.2.2 Response at top of First Panel

To ensure that the OpenSees model adequately captured the different deformation components accurately, the responses at different panel levels were examined. As explained in section 3.4.1.2, the comparison of lateral load response at first panel level provides an opportunity to further examine the modeling accuracy, including that of shear. The calculated and measured force-displacement responses at the first panel level are shown in Figure 3.24a.

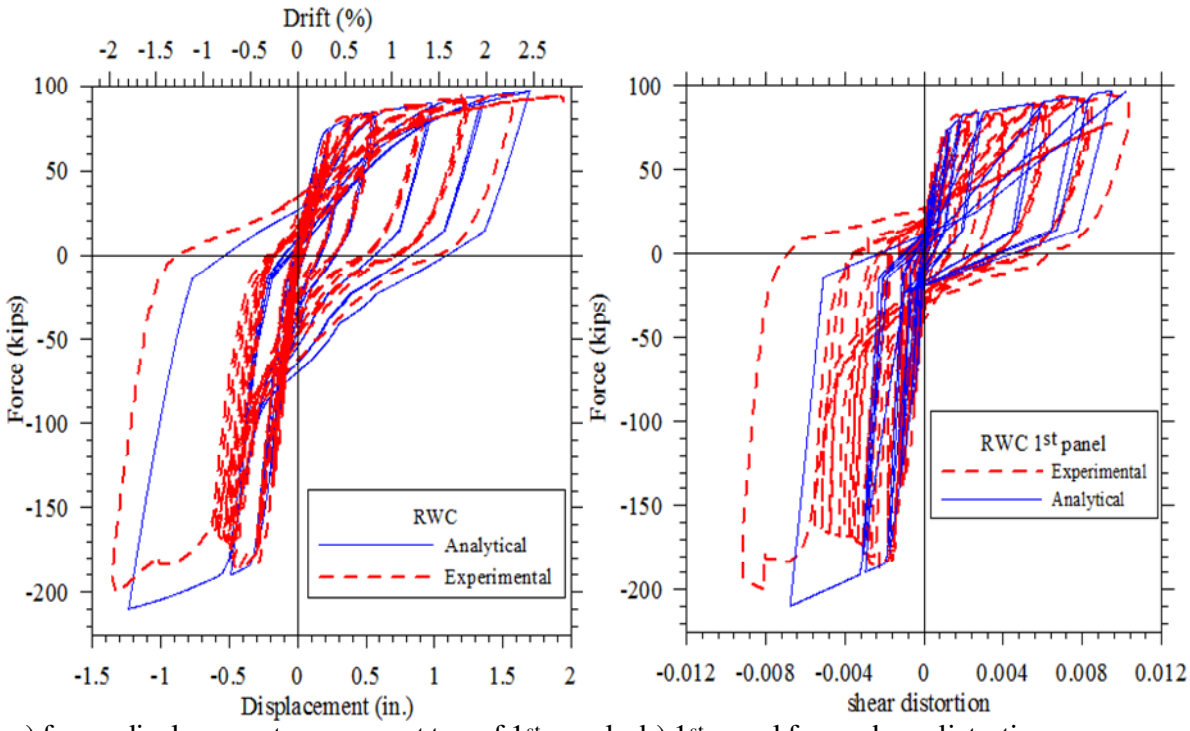

a) force-displacement response at top of 1st panel b) 1st panel force-shear distortion response

Figure 3.24 Overall and the shear distortion responses of RWC at the first panel level

As observed previously with RWN, the OpenSees model did not capture the first panel response in both loading directions as accurately as it did at the top of the wall. It can

be seen that the analytical model over predicted the total lateral displacement in the #6 bars in tension, which was observed previously in RWN. The strength degradation and the increase in the first panel level displacement at -1% drift were not well captured by the analytical model. The unloading stiffness and reloading stiffness were well captured up to a drift of 0.75% in the #6 bars in tension direction. However, the analytical model estimated the initial stiffness and the post yield stiffness of the first panel level with good accuracy. The over prediction of the strength and not capturing the strength degradation at 2.4 in. lateral displacement (i.e., -1% drift) in the #9 bars in tension direction was expected as the *pinching4* model used for capturing the shear response did not account for the strength degradation and softening of the structure expected due to repeated loading to the same lateral displacement of 2.4 in. (i.e. -1% drift) in #9 bars in tension direction. It can be seen in Figure 3.24b, which compares the theoretical and experimental shear distortions of the first panel in RWC. The increase in the shear distortion with the repeated loading to -1% drift was expected based on significant damage observed in the first panel of RWC. Similar to RWN, large inclined shear cracks were developed during the +1.5%, +2.0% loading cycles in the #6 bars in tension direction due to yielding of longitudinal reinforcement. Figure 3.25 shows the damage state of the first panel of RWC at different drift levels.

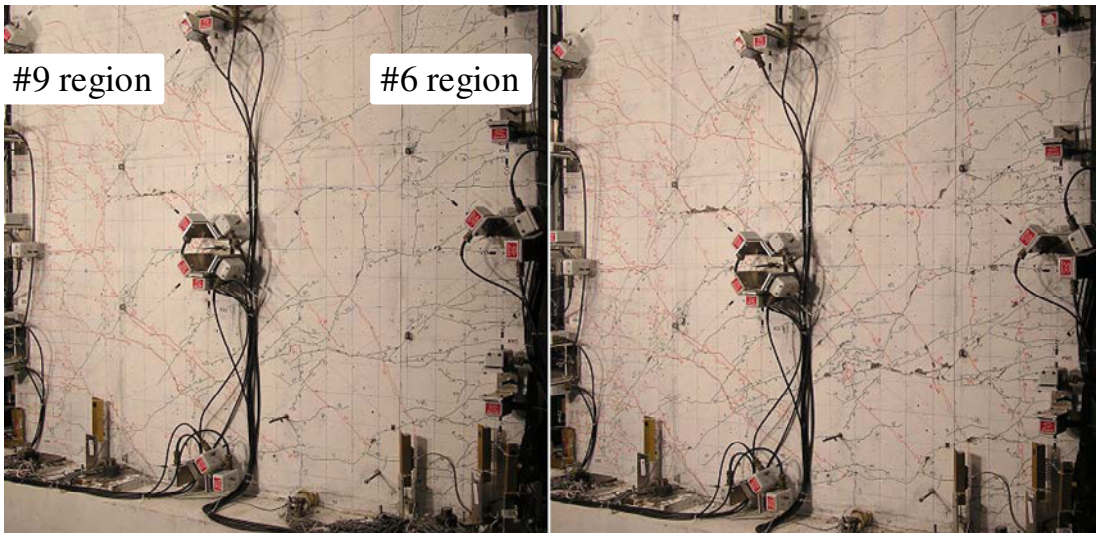

a) at +1 % Drift b) at +1.5 % Drift

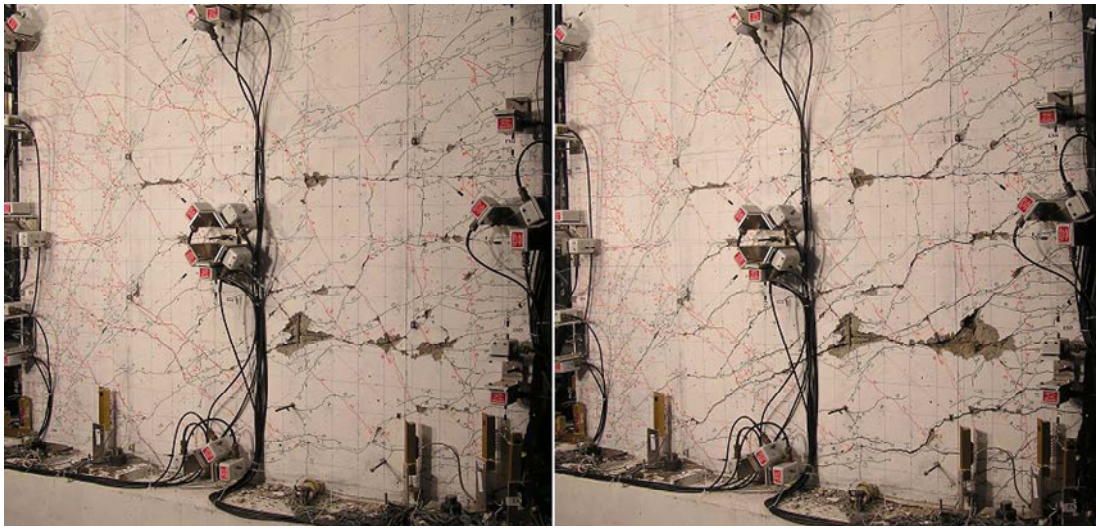

c) at +2.0 % Drift d) at +2.5 % Drift

Figure 3.25 Extent of shear cracking observed at different drift levels within the first panel of RWC

3.4.2.3 Response at top of Second Panel

The lateral load response of RWC at the top of second panel was also compared to the measured experimental response and is shown in Figure 3.26. The OpenSees model captured the force-displacement behavior at second panel level with good accuracy up to 1.5% drift in the #6 bars in tension direction. The stiffness of the loading, unloading, reloading paths and residual displacements were all well captured by the model in the #6 bars in tension

direction. The initial stiffnesses in both directions were also captured accurately by the OpenSees model. However, the residual displacements in the #9 in tension direction were under predicted as observed for the response at the top of the wall, which was also observed in RWN. This further reinforces the discrepancy in capturing the shear distortion by the *pinching 4* model.

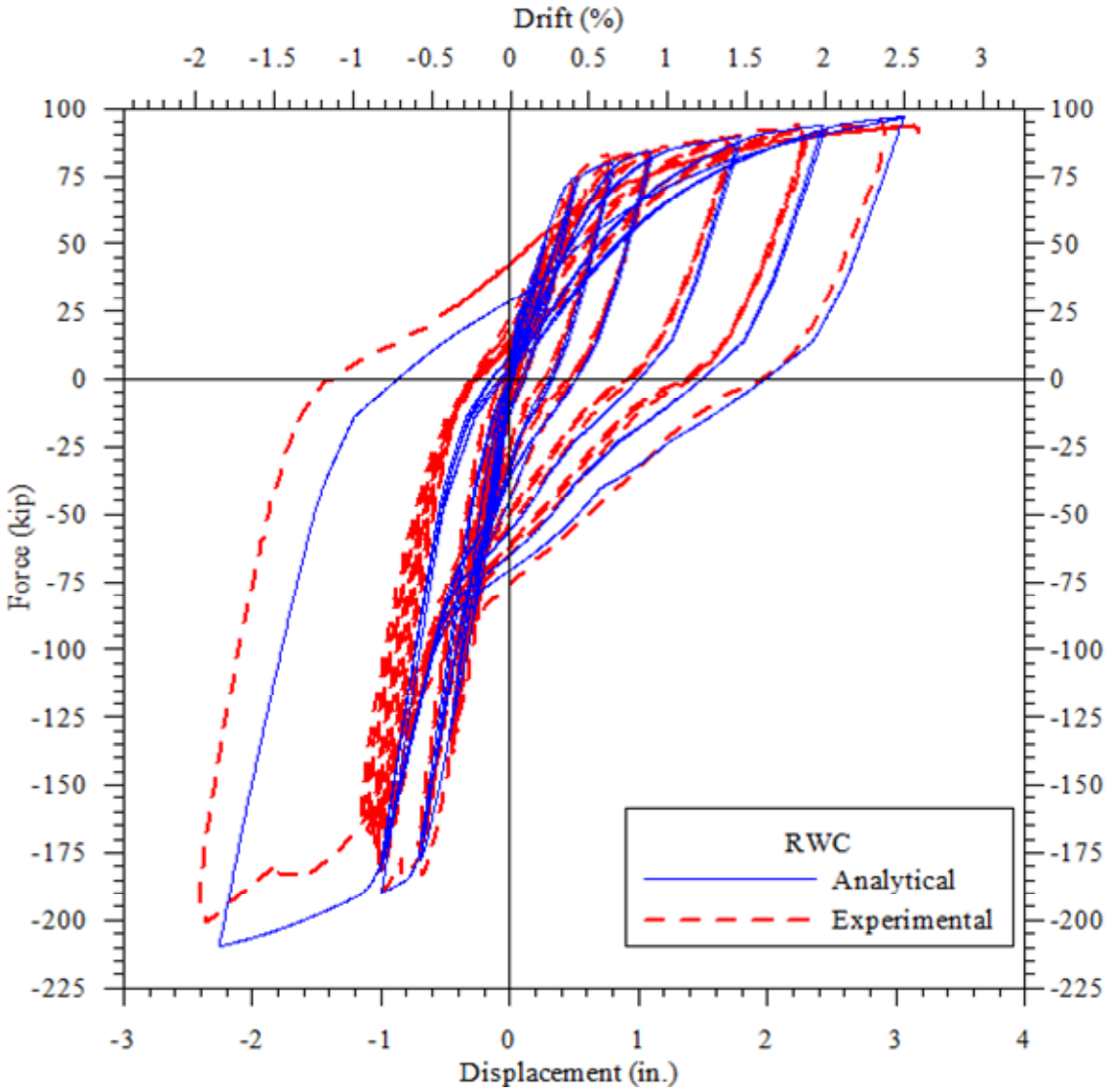

Figure 3.26 Comparison of the measured and calculated force-displacement responses of RWC at the top of the second panel

3.4.2.4 Comparison of Deformation Components

Calculated and experimental values of various deformation component responses of RWC at the first panel level and the top of the wall during the peak displacements are compared and appropriate comments are presented. Similar to RWN, the comparisons are presented only in the #6 bars in tension direction.

The comparison between the calculated and measured values of deformation components of RWC at the first panel level and the top of the wall are shown in Figure 3.27 and Figure 3.28 respectively. As observed in RWN, the flexural deformations in the first panel of RWC were

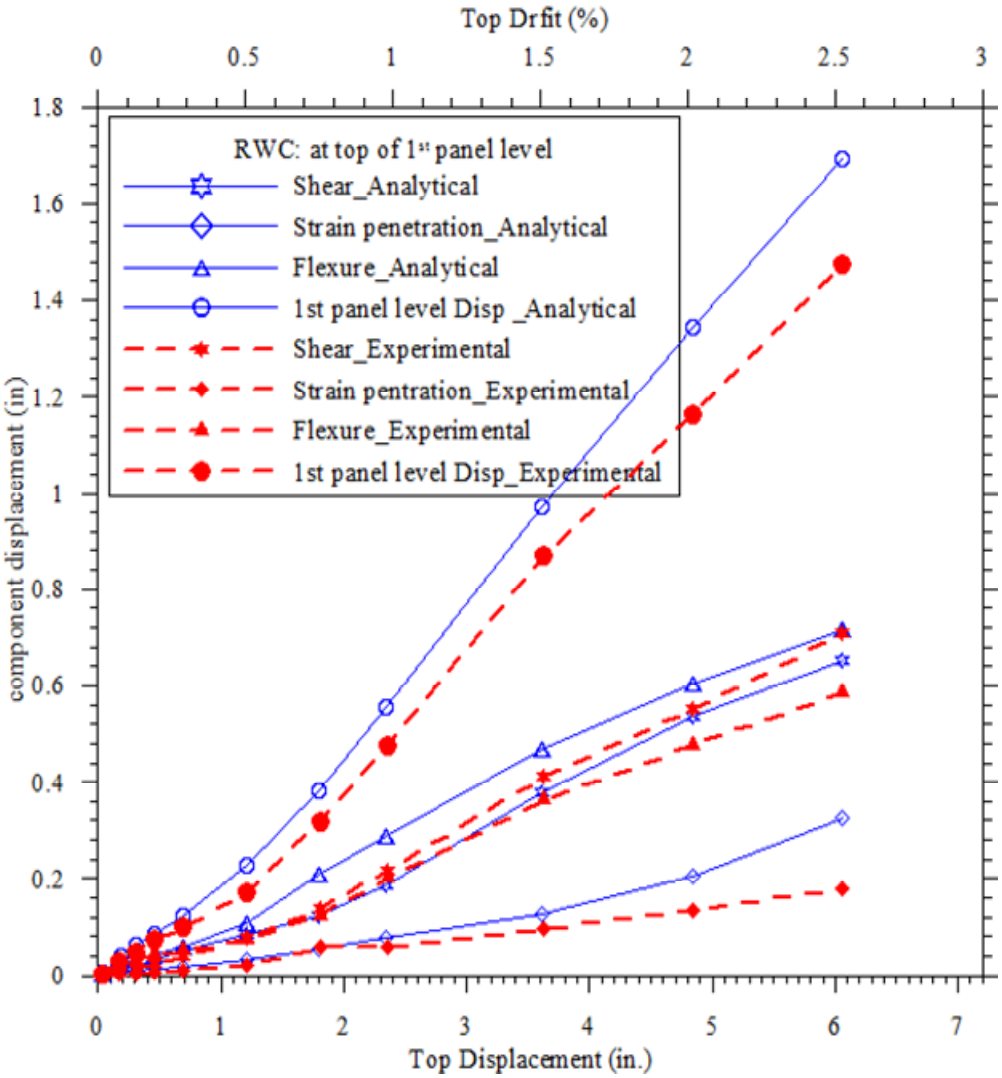

Figure 3.27 Comparison between calculated and experimental deformation component responses at the first panel level of RWC

overpredicted by the model. The deformation due strain penetration was well captured by the model up to a top displacement of 2.4 in. (i.e. 1% drift). The total flexure deformation at the top of wall was well captured by the OpenSees model and can be seen in Figure 3.28. The shear deformation and deformation due to strain penetration were well captured by the model up to a top displacement of 2.4 in. (i.e. 1% drift). However, beyond 1% drift, the shear deformations and strain penetration deformations were under predicted and over predicted respectively. Consequently the prediction of overall response of RWC was not affected by the inaccurate shear and strain penetration deformations.

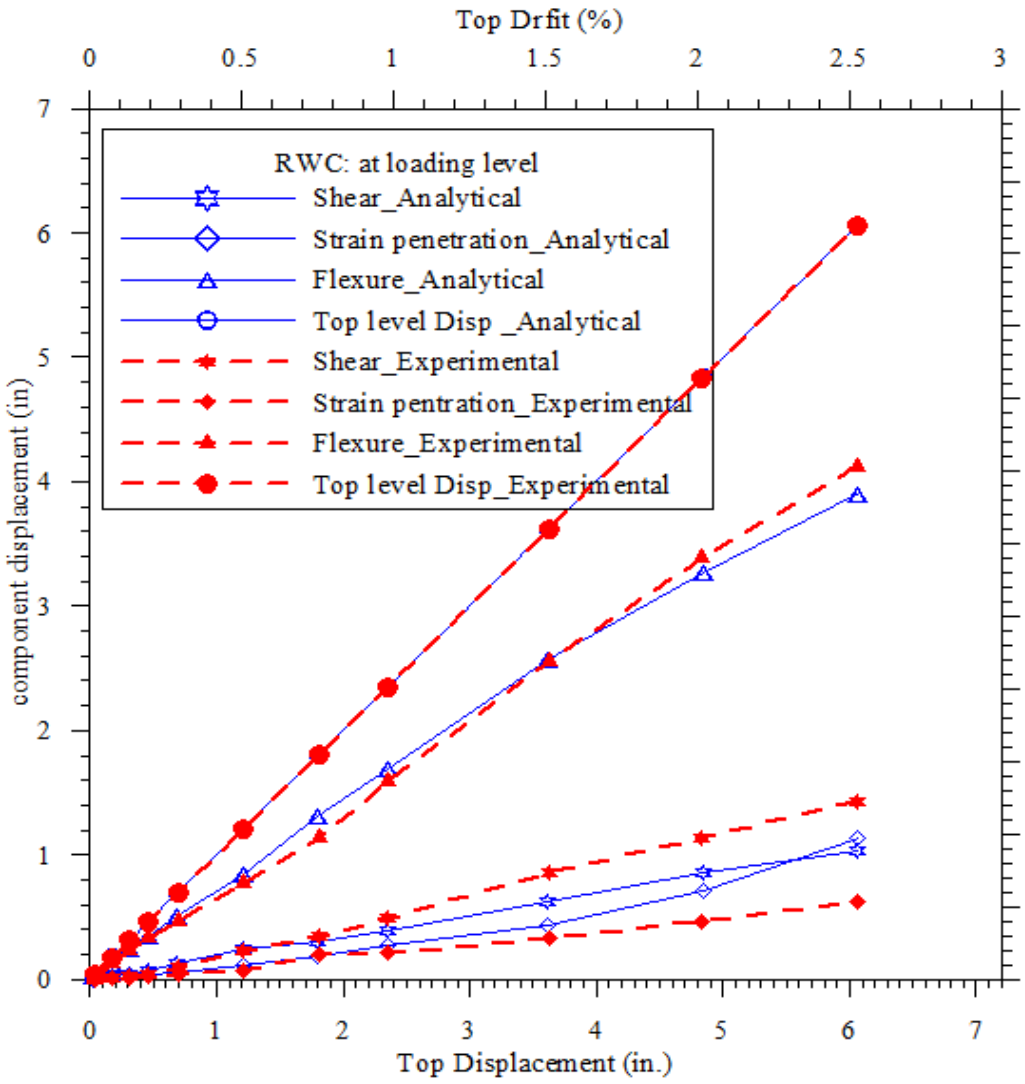

Figure 3.28 Comparison between calculated and experimental deformation component responses at the top of RWC

3.4.3 RWS

In this section, the OpenSees analytical model and experimentally observed responses of RWS are compared and appropriate comments are made. In addition to the global response, accuracy of the local responses is examined, including the force-displacement response of RWS at different panel levels.

3.4.3.1 Cyclic Response

The measured and calculated cyclic responses of RWS subjected to the loading protocol in Figure 3.5 are shown in Figure 3.29. Figure 3.30 shows the comparison of measured response of RWS with the calculated response obtained by representing the traditional lap splice with a single bar.

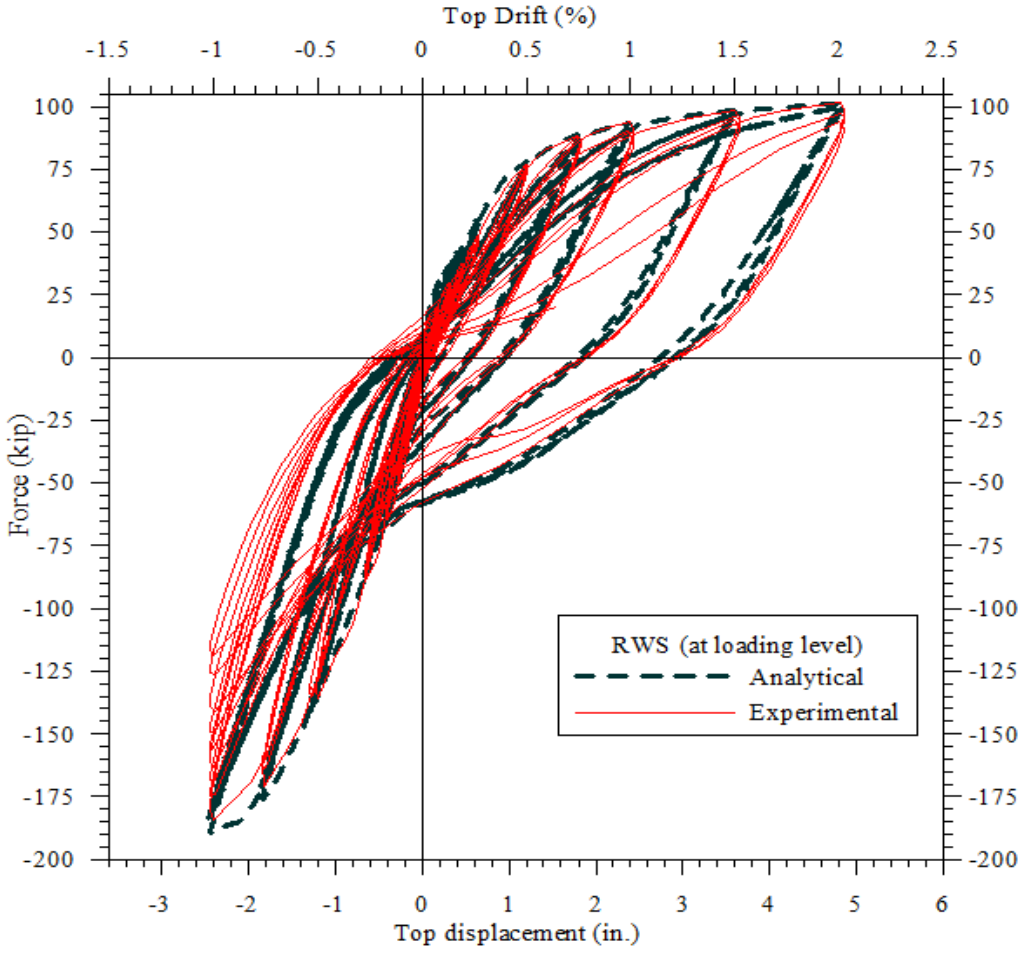

Figure 3.29 Comparison of the measured and calculated force-displacement responses of RWS

This figure shows that replacing the bars in a lap splice with a single bar area didn't captured the strength of RWS and thus supports that a varying effective bar area along the lap splice length should be used to represent a lap splice region.

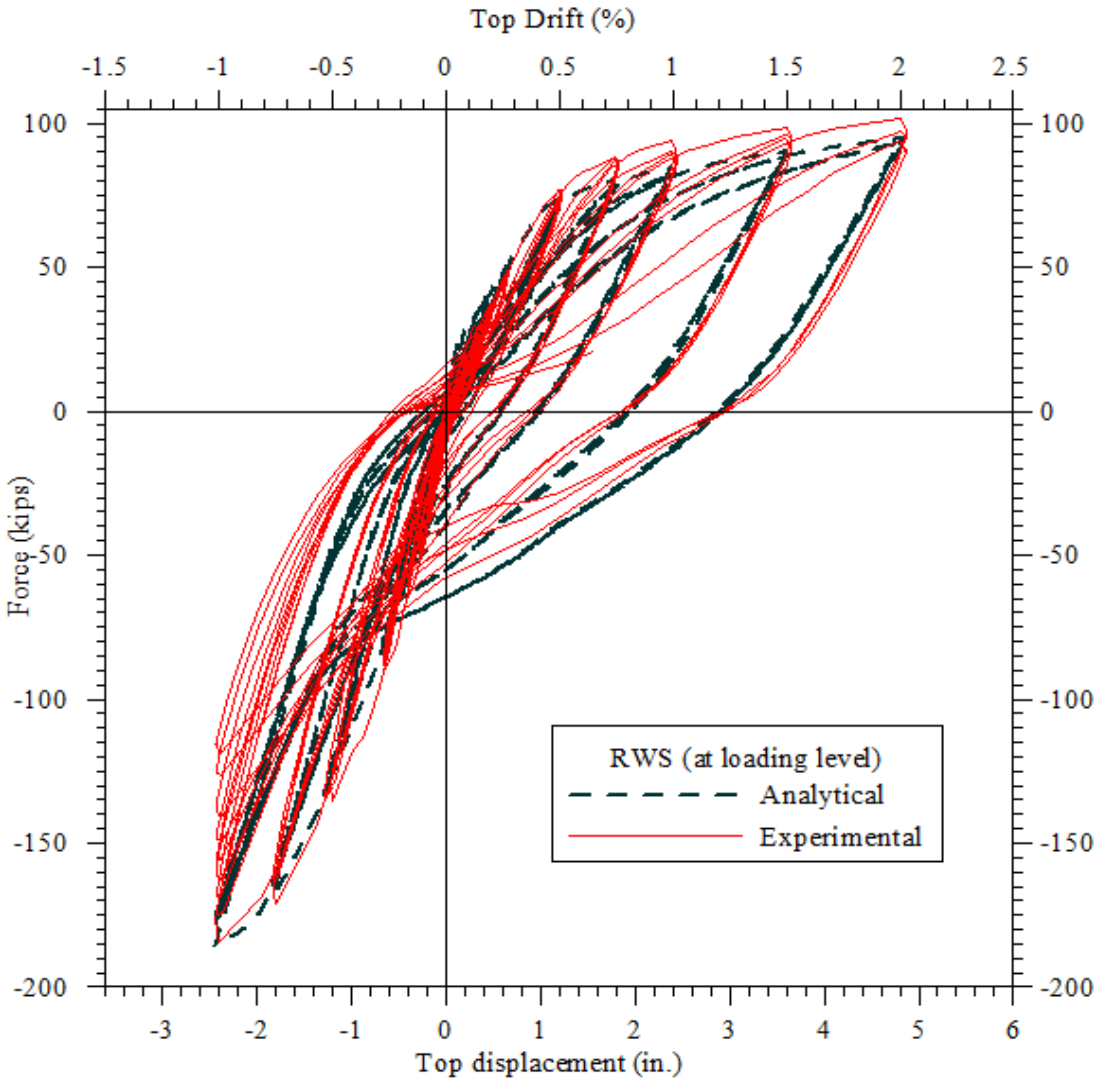

Figure 3.30 Comparison between the measured response of RWS and calculated force-displacement response using single bar assumption for lap splice

As shown in Figure 3.29, the OpenSees simulation using equivalent effective bar area for lap splices accurately captured the force-displacement response of RWC for the loading direction that subjected the #6 and #5 longitudinal bars in tension. The unloading stiffness, reloading stiffness, and residual displacements were well simulated by the analysis model in this direction. In the direction that subjected #9 bars in tension, the analytical response is

closely matched with the experimental response. The calculated peak values were within 3% of the experimental values for up to a lateral displacement of 2.4 in. (i.e. -1% drift) in #9 bars in tension. The strength degradation observed at -1% drift was not captured by the OpenSees model. The strength degradation in the experimental response was observed due to the slip of longitudinal bars in lap splices (see Figure 3.32d) and the shear stiffness degradation due to repeated cyclic loading at the lateral displacement of 2.4 in. (i.e. -1% drift) in the #9 bars under tension direction. As noted before (in section 3.3.3), the model did not account for the local bar slip in the lap splice region. Also, as observed before with RWN and RWC, *Pinching 4* model did not capture the shear stiffness degradation. However, the initial stiffness in the both directions was captured with good accuracy.

3.4.3.2 Response at the top of First Panel

To ensure that the OpenSees model adequately captured the different deformation components accurately, the responses at different panel levels were also examined. As explained in section 3.4.1.2, the comparison of lateral displacement at first panel level provides an opportunity to examine the modeling accuracy of the shear deformation. The calculated and measured force-displacement responses at the first panel level are shown in Figure 3.31a. Similar to observations made in RWN, the OpenSees model did not capture the first panel response as accurately as it did at the top of the wall in both directions. The analytical model over predicted the displacement response in the #6 bars in tension direction. As observed in the previous walls (RWN and RWC) analyses, the analytical model didn't captured the strength degradation at 2.4 in. displacement in the #9 bars in tension direction (i.e., -1% drift). The analytical model captured the unloading and reloading stiffnesses for the #6 bars in tension direction, the initial and the post yield stiffnesses of the first panel with good accuracy.

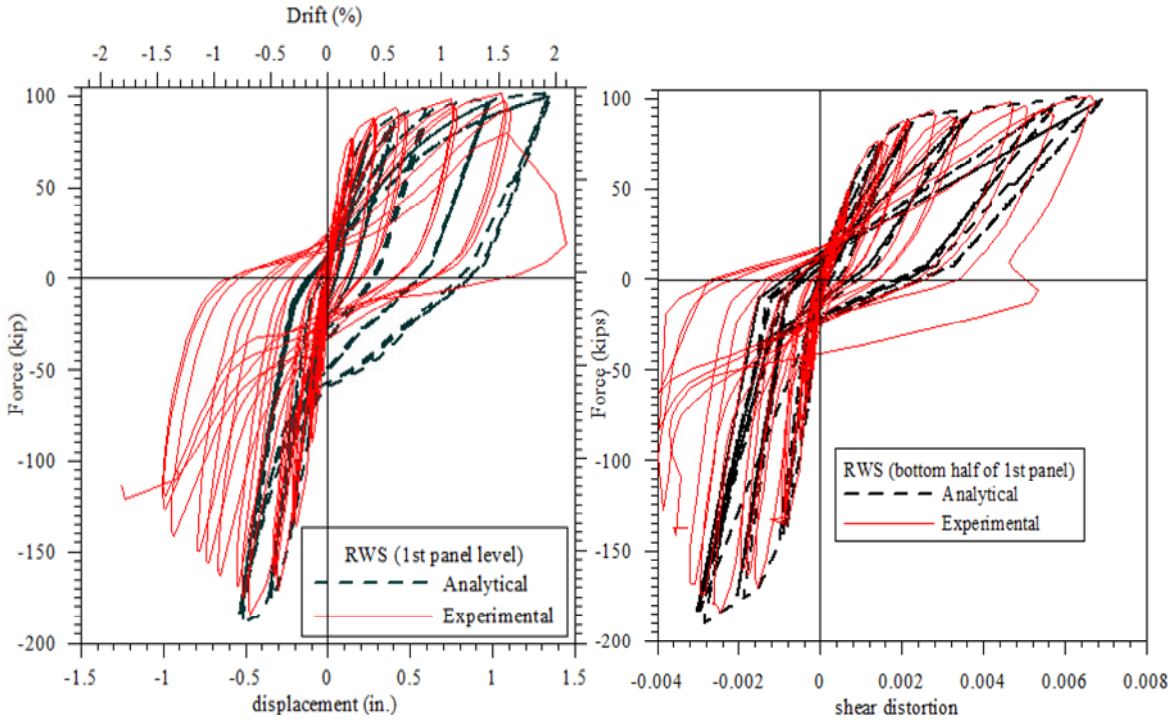

a) force-displacement response at top of 1st panel

b) force-shear distortion response of bottom half of 1st panel

Figure 3.31 Overall and the shear distortion responses of RWS at the first panel level

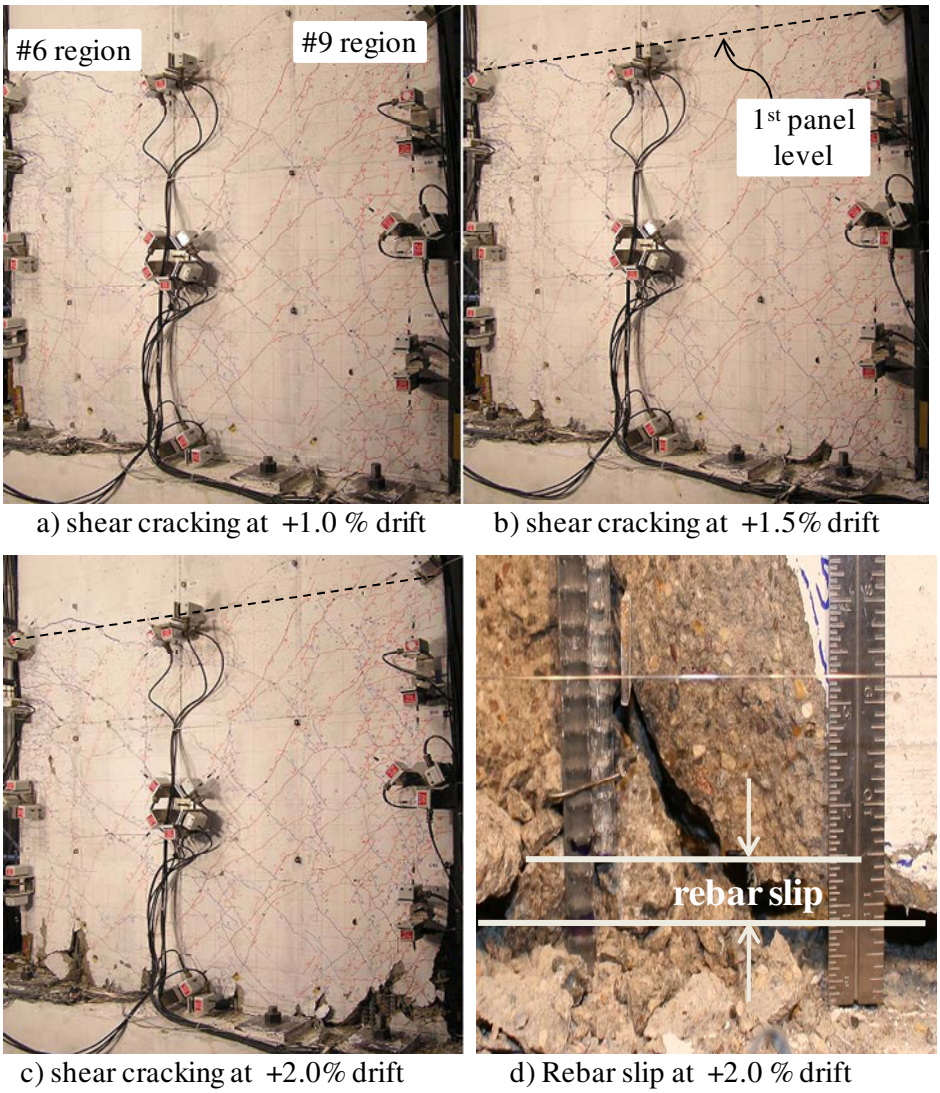

a) shear cracking at +1.0 % drift

b) shear cracking at +1.5% drift

c) shear cracking at +2.0% drift

d) Rebar slip at +2.0 % drift

Figure 3.32 Extent of shear cracking observed at different drift levels in the first panel of RWS and the observed rebar slip at 2%

The over prediction of the strength and not capturing the strength degradation at 1% drift in the #9 bars in tension direction was expected, as the local bar slip in the splice region was not modeled. This can be seen in the Figure 3.31b, which compares the predicted and experimental shear distortions in the bottom half of the first panel of RWS. Figure 3.32 shows the damage to the first panel of the wall at different drift levels and the observed bar slip in the lap splice region at 2% drift.

3.4.3.3 Response at the top of Second Panel

The lateral load response of RWS at the top of second panel level was also compared to the measured experimental response and is shown in Figure 3.33. The OpenSees model captured the force-displacement behavior at the second panel level with good accuracy in the #6 bars in tension direction. The stiffness of the loading, unloading paths and residual displacements were all well captured by the model in the #6 bars in tension direction. The initial stiffnesses in both directions were also captured accurately by the OpenSees model. The pinching of the force-displacement loops at 1.5% and 2.0% drifts were not well captured by the analytical model. However, this was expected because the RWS model did not account for the bar slip occurred in the lap splice region.

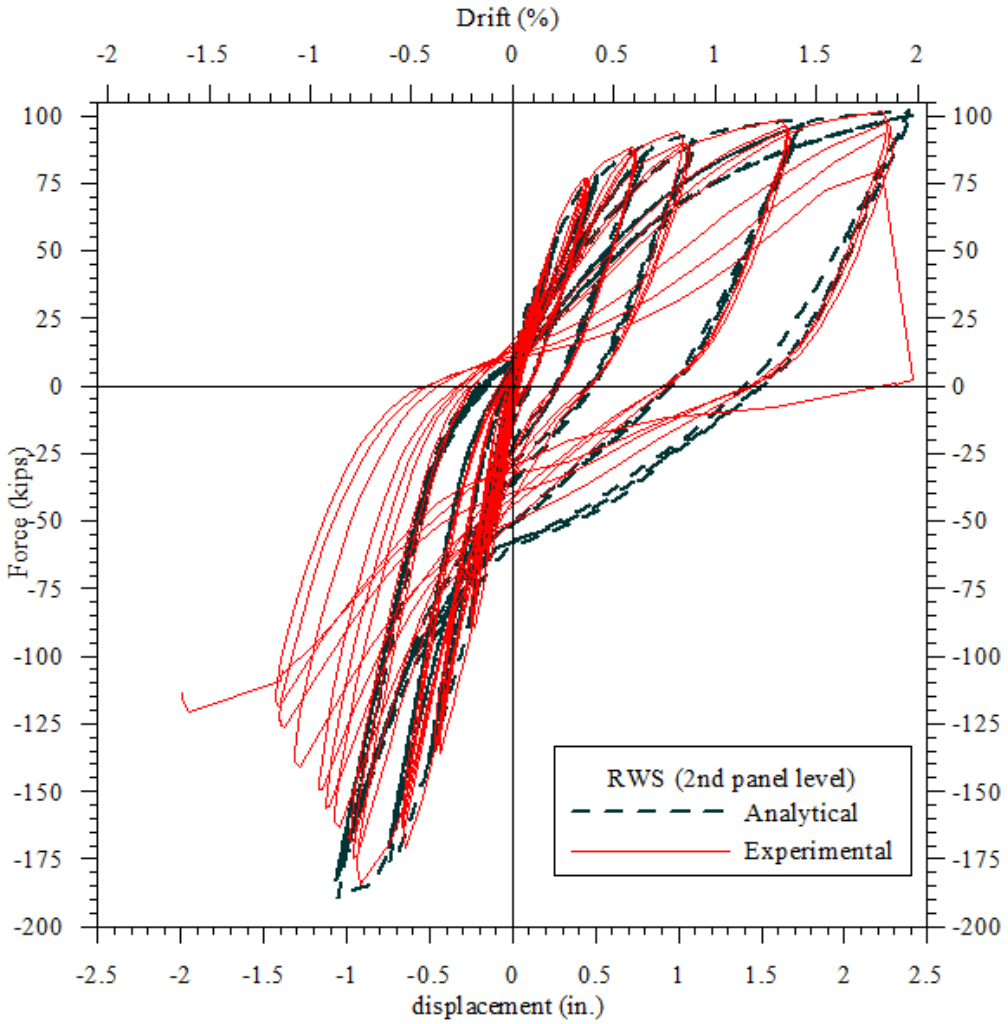

Figure 3.33 Comparison of the measured and calculated force-displacement responses of RWS at the top of the second panel

3.4.3.4 Comparison of Components of Deformation

The comparison between the calculated and measured values of deformation components of RWS at the first panel level and the top of the wall are shown in Figure 3.34 and Figure 3.35 respectively. OpenSees Simulation overestimated the deformations due to flexure and strain penetration at the first panel level in RWS. However, the flexure deformation at the top the wall was well captured by the analytical model. The deformation due to strain penetration was overestimated by nearly 300%. At the top of the wall, the summation of the experimentally obtained deformation components (flexure, shear and strain penetration deformations) did not match the measured displacement at the top of the wall. This was expected as local bar slip in the splice region was observed during the experimental testing of RWS (see Figure 3.32d). This local slip contributed to the additional rotation at the wall base and in turn to the lateral displacement of the wall. The instrumentation used for capturing the different deformation components, did not capture the deformation due to bar slip in splice regions. However, the analytical model overestimated the strain penetration deformation, which compensated the deformation due to the rebar slip in the splice regions. Consequently, the RWS model accurately captured the observed force-displacement response (see Figure 3.29).

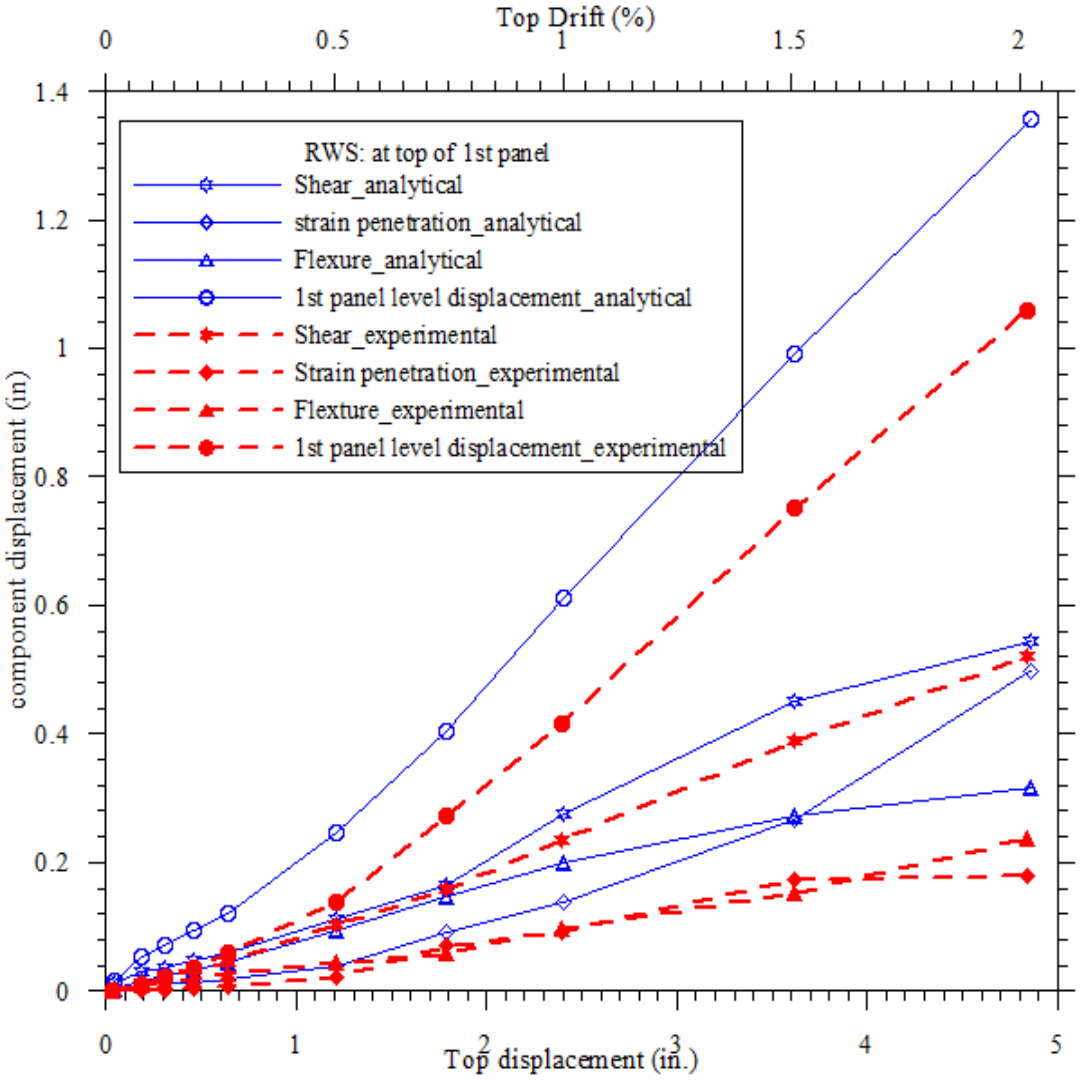

Figure 3.34 Comparison between calculated and experimental deformation component responses at the first panel level of RWS

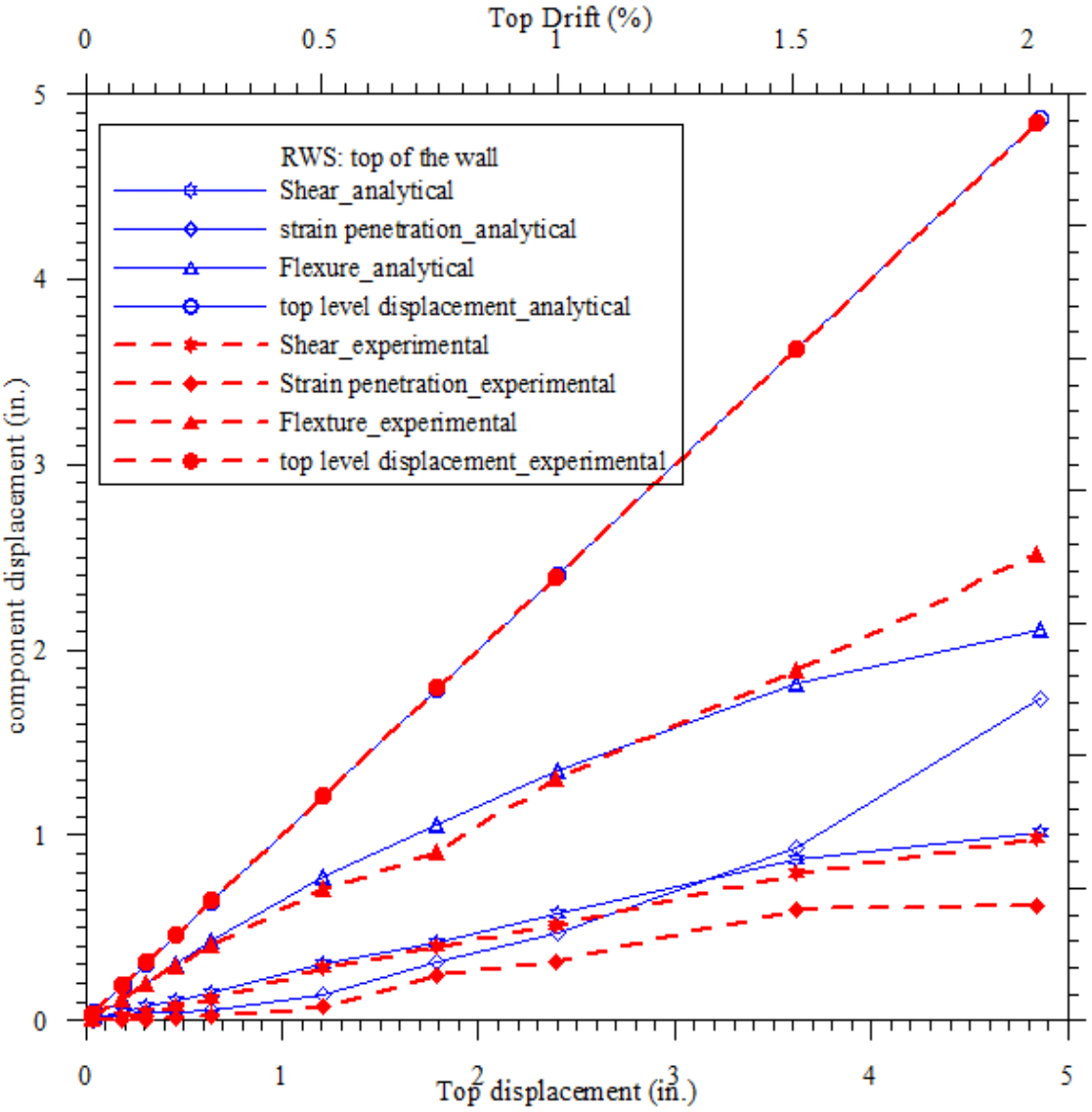

Figure 3.35 Comparison between calculated and experimental deformation component responses at the top of RWS

CHAPTER 4

EXPERIMENTAL AND ANALYTICAL INVESTIGATION OF A PREWEC SYSTEM AND COMPONENTS

Over the past decade, researchers have demonstrated experimentally the viability of using precast structures combined with unbonded post-tensioning (UPT) in seismic regions. During this period, several precast moment resisting frame and wall systems were developed. The UPT precast wall systems developed to date include single wall, hybrid wall and jointed wall systems. The precast frame systems have been successfully implemented in buildings in seismic regions, but the adoption of precast wall systems has been limited.

The unbonded post-tensioned single precast walls do not have adequate capability to dissipate the energy imparted to the building during a seismic event. Consequently, the walls will experience large seismic displacements, leading to damage to non-structural elements. The jointed wall system uses special connectors to increase the energy dissipation capacity of the system. But, it has considerably less moment resisting capacity (about 30%) than an equivalent traditional reinforced concrete wall, affecting the cost-effectiveness of the system. These disadvantages have significantly compromised their practical applications, despite their proven superior performance in terms of self centering capability and minimum structural damage during a seismic event. By addressing these concerns, a new cost-effective precast wall system, known as Precast Wall with End Columns (PreWEC) system, has been introduced by Aaleti and Sritharan (2007). Lateral load behavior of this system has been previously investigated analytically (Aaleti and Sritharan 2007), pending an experimental validation to confirm its performance. Also, the use of PreWEC system for real world applications in seismic regions requires the experimental validation of the system's performance under lateral loads and satisfying the requirements set forth by ACI 318 (ACI 318, 2005). Chapter 21 of ACI 318 (ACI 318, 2008) specifies that "a reinforced concrete structural system not satisfying the requirements of this chapter shall be permitted if it is demonstrated by experimental evidence and analysis that the proposed system will have

strength and toughness equal to or exceeding those provided by a comparable monolithic reinforced concrete structure satisfying this chapter."

The minimum experimental evidence needed to achieve the code-validation of PreWEC system is specified in ACI ITG-5.1 (2007) for "special" reinforced concrete (RC) shear walls. As part of the study presented in this thesis, a large-scale test of a PreWEC system and the associated components was conducted at the National Center for Research on Earthquake Engineering (NCREE) in Taiwan. This was a part of a collaborative research project between the United States, Taiwan and New Zealand, with support from the National Science Foundation in the U.S, the National Science Council of Taiwan and the Tertiary Education Commission in New Zealand. A PreWEC test specimen was subjected to in-plane cyclic displacements to validate its performance under cyclic lateral loads. The design and experimental testing of the PreWEC system and its components are discussed in this chapter. Additionally, a simplified analytical method used to predict the PreWEC system behavior and a finite element model that is suitable to characterizing the behavior of the special connectors used in the system are presented herein. Also a design methodology for PreWEC systems is presented.

4.1 PreWEC System Concept

The Precast wall with end column (PreWEC) system, as shown in Figure 4.1, consists of a single precast concrete wall and two end columns constructed from steel, concrete or a composite material (e.g. concrete filled tubes). The wall and columns in this system are anchored to the foundation using unbonded post-tensioning and joined together using special energy dissipating connectors. The post-tensioning tendons can be distributed along the length of the wall or concentrated at the center. By leaving the tendons unbonded, the tendons develop constant strain along the length of the tendon, eliminating the development of large localized strains. This approach allows the wall system to undergo large lateral displacements without the prestressing tendons exceeding their yield strain and/or premature fracture of strands. Leaving the tendons unbonded also eliminates the development of large bond stresses in surrounding concrete and the associated local damage to concrete. When the PreWEC system is subjected to a lateral load, the wall and end

columns rock individually with the opening of mainly a single crack at the base of the wall and columns. The post-tensioned steel in the system is designed to remain elastic when subjected to events up to design-level earthquakes. As a result, the post-tensioning provides the necessary restoring force to recenter the PreWEC system when the applied lateral force is removed, minimizing the residual displacements. When subjected to lateral loads, special, replaceable connectors placed between the wall and end columns experience relative vertical displacements due to the gap opening at the base of the wall system. This results in connectors enduring large inelastic deformations and providing the necessary energy dissipation for the system.

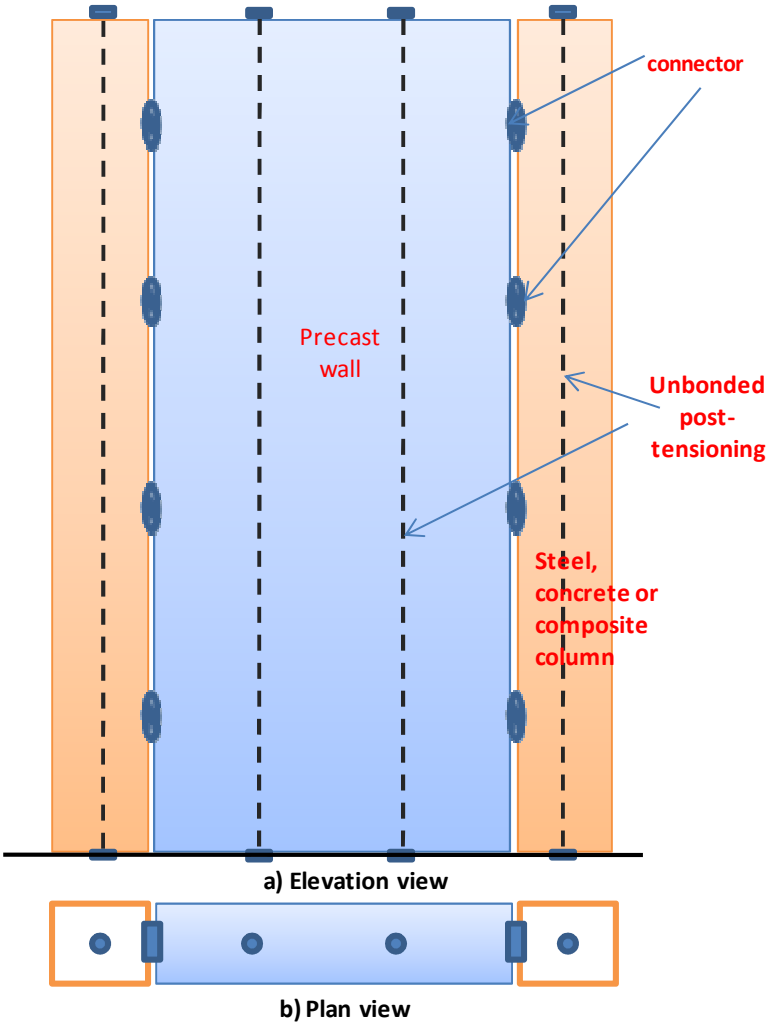

Figure 4.1 Sketch of the PreWEC concept

4.2 Test Unit

A PreWEC system for testing was designed following the basic guidelines in ACI ITG-5.2 (2009) and ACI 318 (2008) (ACI 318 2008). It was designed to match or exceed the moment resisting capacity of RWN, the cast-in-place reinforced concrete wall with continuous longitudinal reinforcement, (see Figure 3.1) tested as part of the PreNEESR project. RWN was designed to comply with the current design practices and included Grade 50 (f_y =60 ksi) mild steel longitudinal reinforcement continuing from the foundation to all the way to the wall top without any splices. The cross-section details of the RWN and its performance under lateral loads are presented in Chapter 3. The prototype design of the PreWEC system involved the following tasks.

- Arriving at the required post-tensioning steel area to anchor the precast wall and columns to the foundation;
- Development of a low-cost connector;
- Designing the confinement reinforcement boundary elements to sustain large compressive strains;
- Designing the required shear reinforcement to resist the design base shear; and
- Quantification of the number of connectors required to provide energy dissipation without affecting the self-centering nature of the system.

The post-tensioning steel was designed to yield between 2% to 2.5% lateral drift in accordance with ITG 5.2 guidelines (ACI ITG 5.2, 2009). The amounts of post-tensioning steel and the number of connectors were designed so that the PreWEC specimen would match the lateral load capacity of RWN in #6 bars in tension direction. Confinement reinforcement was designed to sustain a maximum expected compressive strain based on an equation proposed by Aaleti and Sritharan (2009).

In order to design a cost effective and easily replaceable connector for the wall system an extensive analytical investigation was conducted before the final design was validated through experimental testing. Based upon the analytical investigation, an oval shaped connector, or O-connector, made from grade A50 steel was found to provide the most

efficient design. The designed O-connector can provide the necessary energy dissipation primarily experiencing inelastic strains in the connector leg regions (Figure 4.2b).

The cross-section of the PreWEC system at the base are shown in Figure 4.3, while the cross section and reinforcement details of the precast wall panel are depicted in Figure 4.4 and Figure 4.5, respectively. The PreWEC system was designed with a 72 in. (1828.8 mm) long, 6 in. (152.4 mm) thick precast wall, connected to a pair of 8 in. by 6 in. (203.2 mm by 152.4 mm) concrete filled steel tube (CFT) end columns as shown in Figure 4.3. The thickness of the steel tube was 0.25 in. (6.5 mm). The total PreWEC system length was kept to 90 inches so it would match the length of RWN. The PreWEC system height was 258 in. (6.553 m), same as that of RWN. Since the prestressing tendons contribute towards the base moment resistance of the PreWEC system, the longitudinal reinforcement in the wall panel was designed to satisfy the ACI 318 (ACI 318, 2005) minimum longitudinal steel ratio requirements. The longitudinal reinforcement was terminated within the wall panel as seen in Figure 4.4. The boundary elements, or confinement regions, were provided in the bottom corners of the precast wall by means of Grade 40 (f_y = 40 ksi), #3 (d_b=9.5 mm) hoops spaced at 2 in. (50.8 mm) over the bottom 72 in. (1828.8 mm) height of the wall. Though there are no specific guidelines available for determining the height of the boundary elements in literature, it was decided to follow the ACI design code provisions recommended for reinforced concrete walls for detailing the precast wall. The single crack opening at the base of the wall causes the concentration of the curvatures at the wall-foundation interface leading to the decrease in the length of plastic hinge region. In addition to the confinement reinforcement, a 0.61 m (2-ft) long, 6.4 mm thick (0.25 in.) thick steel channel was attached to the bottom of the wall near the toe regions to minimize the spalling of the concrete in these regions (see Figure 4.4). The precast wall and each end column were designed to be anchored to the foundation using 12, 15.2 mm (0.6 in.) diameter post-tensioning strands with a total area of 1680 mm^2 (2.604 in^2) and 3, 15.2 mm (0.6 in.) diameter post-tensioning strands with a total area of 420 mm^2 (0.651 in^2), respectively. In accordance with shear design provisions of ACI 318-05, shear reinforcement in the wall panel was provided with #3 (d_b=9.53 mm) bars at 7.5 in. (190 mm c/c) spacing. However, due to the unavailability of

grade 60 #3 reinforcement in Taiwan, grade 40 #3 bars at 6 in. (150 mm c/c) spacing were used as the shear reinforcement.

In order to design a suitable connector a target force-displacement envelope was derived based on the dimensions and expected maximum lateral drift of the PreWEC system. This design envelope, shown in Figure 4.2a, was used to develop suitable dimensions for the O-connector, shown in Figure 4.2b. Subsequently, from this information, it was determined that six pairs of O-connectors at each end of the wall were required to connect the wall and the end columns. The connector also had the ability to undergo large relative displacements in excess of 2 inches, before experiencing failure. The O-connectors were made by cutting an oval shape plate from a standard Grade 50 (f_y =50 ksi) steel plate, making it very economical.

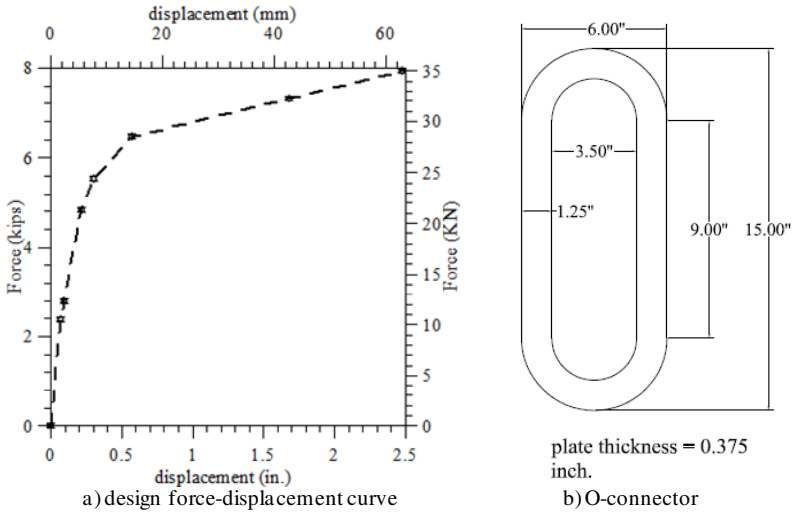

a) design force-displacement curve

b) O-connector

Figure 4.2 Target force-displacement envelope and the dimensions of the O-connector

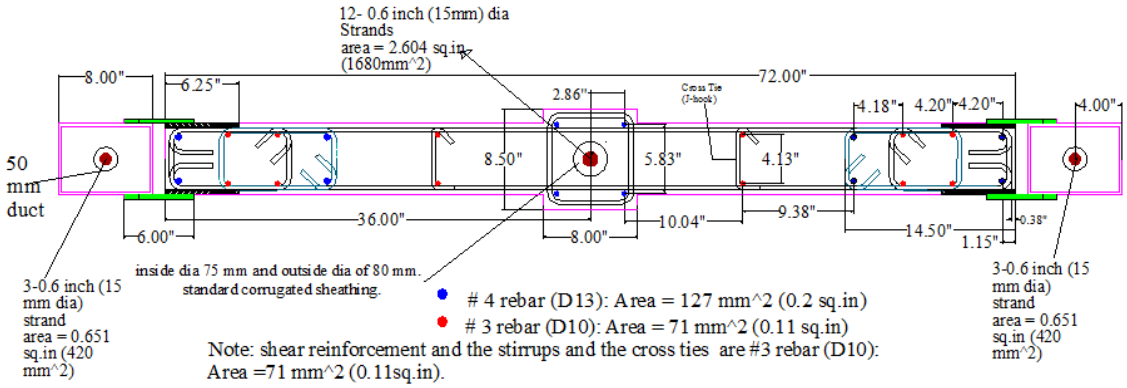

Figure 4.3 Cross section details of the PreWEC test specimen at the base

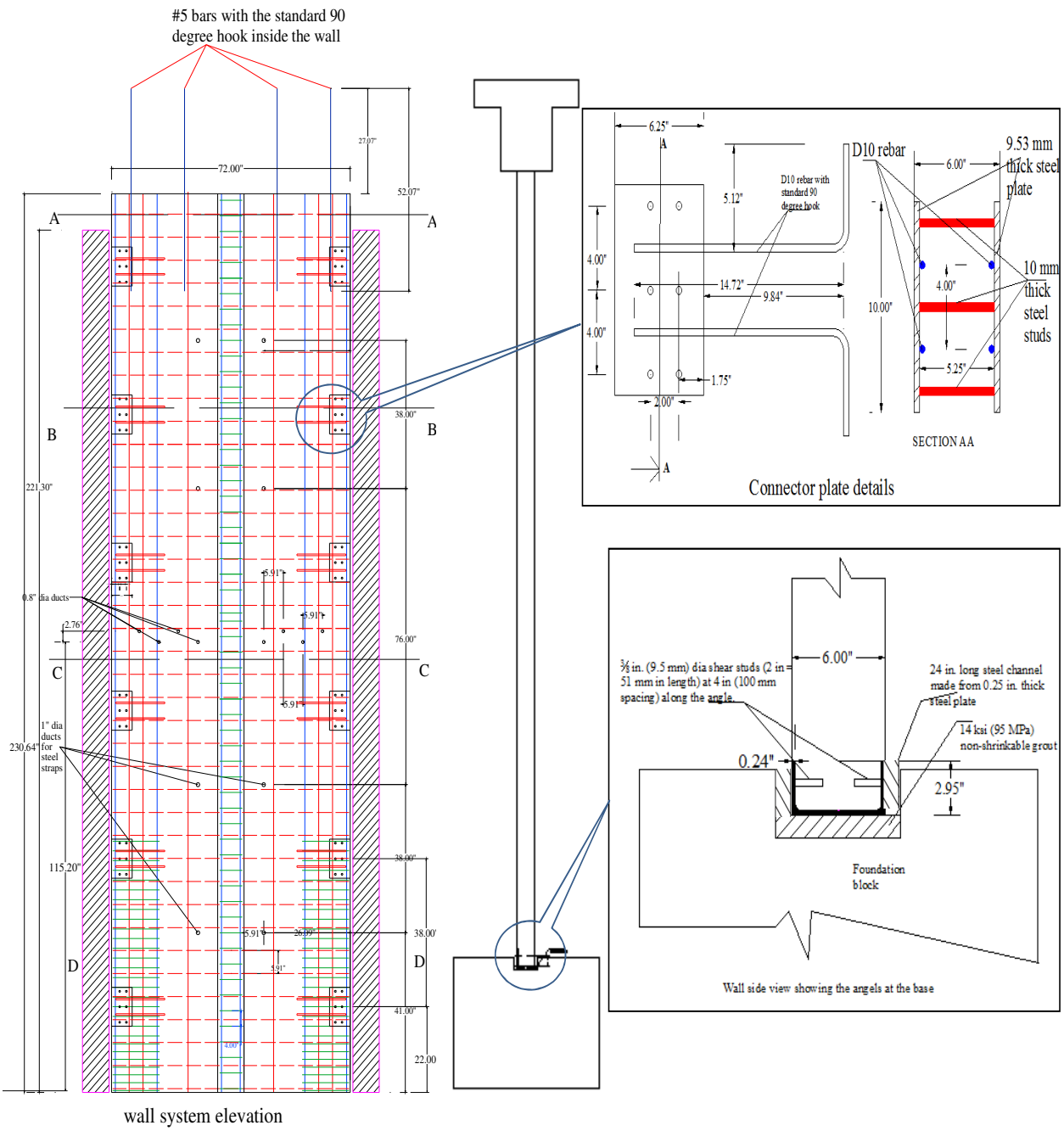

Figure 4.4 Reinforcement details of the PreWEC test specimen

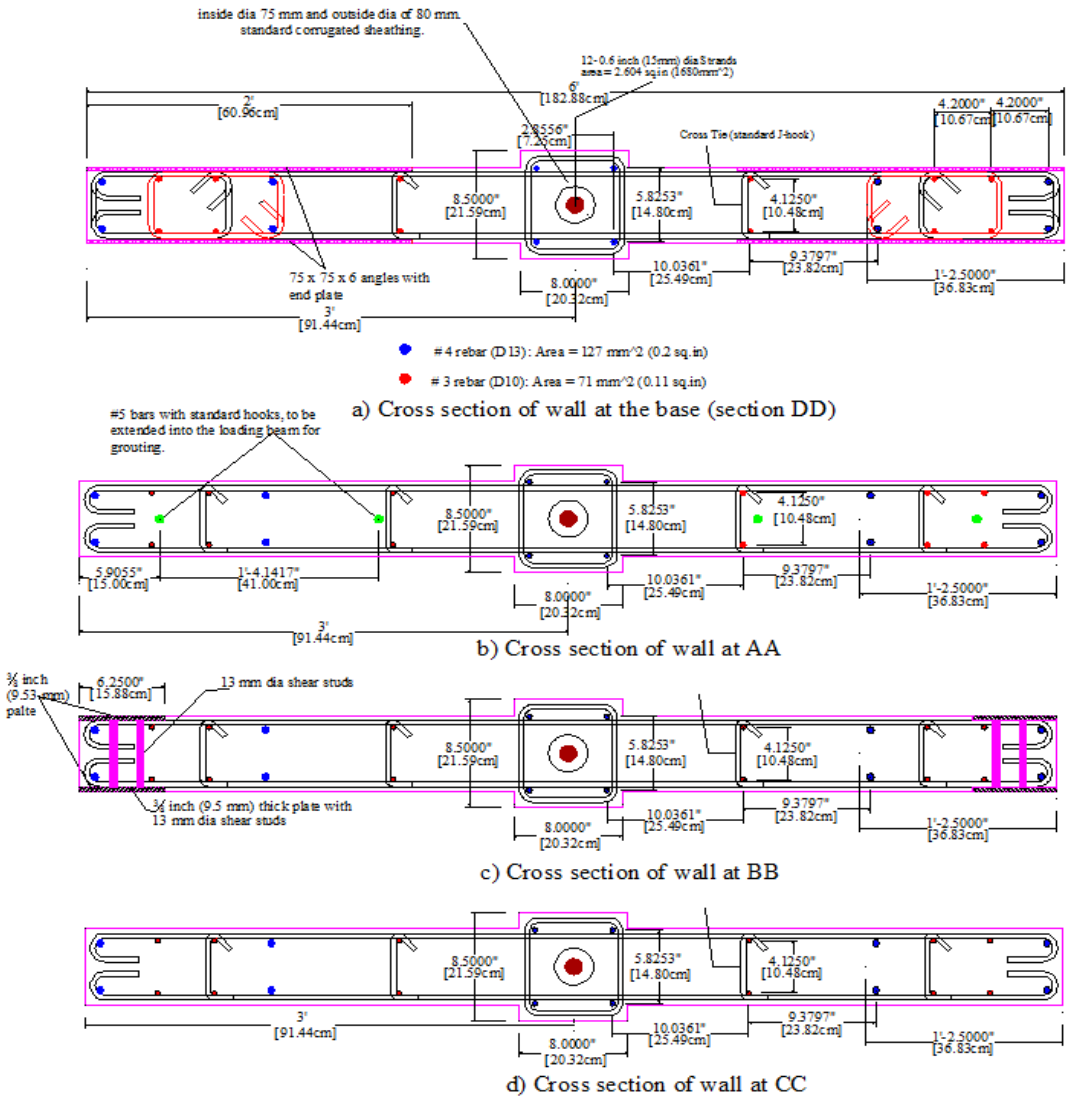

Figure 4.5 Cross section details of the wall panel at different elevations

4.3 Connector Testing

As previously observed during testing of the PRESSS jointed wall system (Priestley et al. 1999), establishing the contribution of the connectors through component testing was identified as a critical step in quantifying the expected lateral load behavior of the wall system. Consequently, experimental tests were performed on sets of O-connectors at Iowa State University and National Center for Research for Earthquake Engineering (NCREE), Taiwan. The tests at Iowa State University (ISU) included three uniaxial tensile tests to characterize the material behavior through the coupon tests and quantifying the connector

response via reverse cyclic testing of two sets of O-connectors. In addition, three further sets of O-connectors were subjected to reverse cyclic loading and another set were subjected to a derived seismic displacement history at NCREE. Also, uniaxial tension coupon tests were performed to characterize the material behavior of the connectors tested at NCREE.

4.3.1 ISU Tests

4.3.1.1 Uniaxial Tension

Three tensile test coupons were manufactured and tested in accordance with ASTM standards for tension testing of metallic materials. The coupons were laser cut from 3/8-in thick grade A50 steel plate used for making the O-connectors. The dimensions of the test coupons are shown in Figure 4.6, while Table 4.1 provides the actual dimensions of the coupons measured prior to testing. The coupons were subjected to direct tension using a uniaxial MTS fatigue machine. In addition to the load output from the MTS machine, an extensometer (gage length = 2 in.) and two strain gauges, one on each face of the coupon, were used to record strains. The stress-strain curves determined from the three uniaxial tests and a close-up of the initial portion of the stress-strain curves are shown in Figure 4.7.

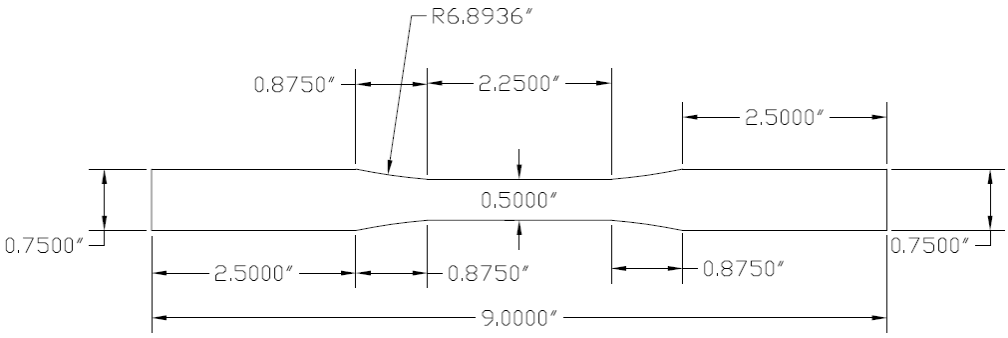

Figure 4.6 Dimensions chosen for test coupon for the uniaxial tensile tests

Table 4.1 Measured dimensions of the tension test coupons

	Width (in)	Thickness (in)
Specimen1	0.509	0.375
Specimen2	0.510	0.375
Specimen3	0.510	0.376

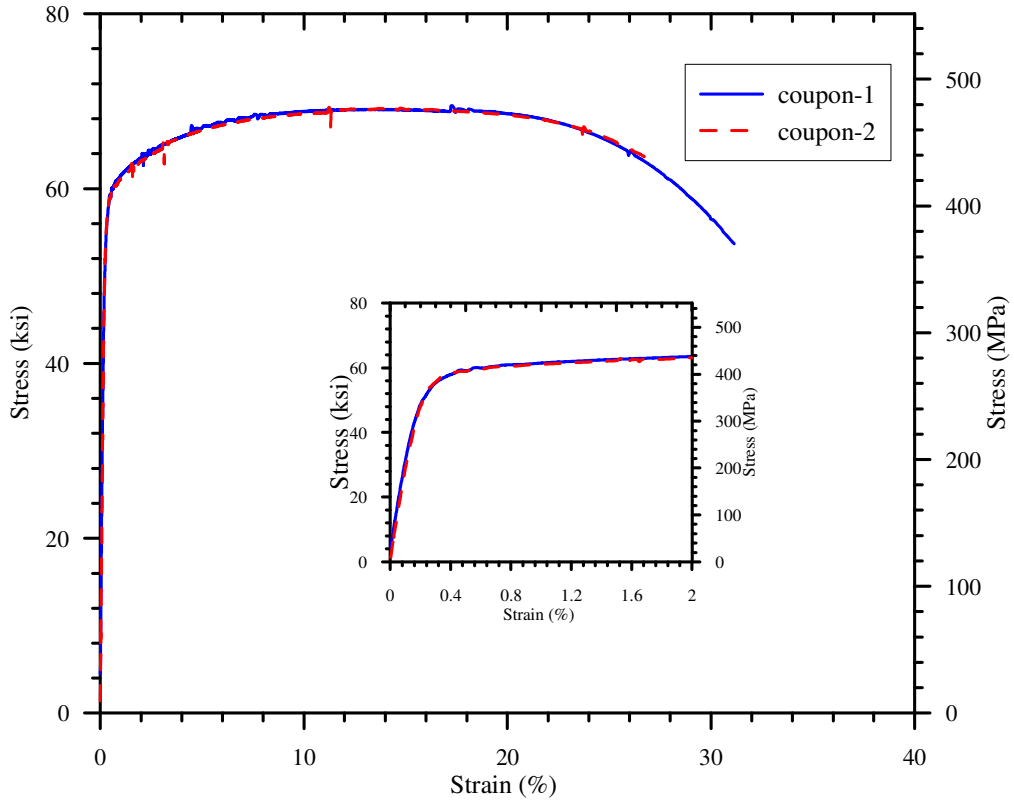

Figure 4.7 Measured stress-strain response of ISU O-connector coupons under uniaxial tension

4.3.1.2 Cyclic Testing

Two cyclic tests were performed on O-connectors to failure at ISU; each set consisted of four connectors to ensure deformation of the connectors as they would undergo in a PreWEC system. The first cyclic connector test was completed prior to the PreWEC system test, while the second test was completed after the system test. The first test was used to verify the assumed force-displacement response of the connector that was used in design of the PreWEC test specimen. The O-connectors were cut from a 3/8 inch thick grade A50 steel plate, using the laser cutting technique to minimize the residual stresses induced during the fabrication process. The dimensions of the connector used for the first test are shown in Figure 4.8.

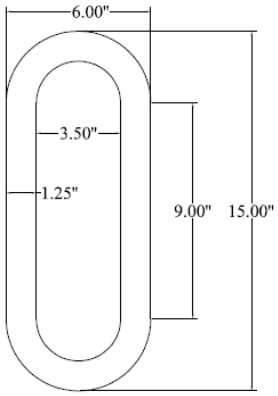

Figure 4.8 Dimensions of the ISU O-connector

Test setup

A test setup was designed using steel tubes and steel plates to apply the desired loading to the O-connectors using a MTS uniaxial testing machine, as shown in Figure 4.9. The test setup consisted of a U-frame made by welding 0.25 in. thick, 4 inch square tubular sections and an H-section made from 1 inch thick steel plates. The columns and the wall in the PreWEC system are represented by the legs of the U-frame and the H-section respectively. Thick steel stubs were welded to the sides of the square tubes to guide the H-section to move vertically during loading without experiencing any out-of-plane movement.

In order to apply a direct shear force to the O-connector without subjecting it to any eccentric loading, four O-connectors were tested together in aforementioned test setup. Additionally, this arrangement provided a more accurate average of the connector's response allowing for variations in the manufacturing process thus producing a more broad validation than relying on testing a single connector. O-connectors were welded to the 4 inch square tube sections on one side and to the H-section on the other side (see Figure 4.9). The test setup was placed in the MTS uniaxial testing frame and gripped at each end with the standard friction grips. The loads were applied to the O-connectors using the MTS machine in a displacement controlled mode. The U-frame of the setup was moved up and down, resulting in a relative displacement between the two legs of the O-connector thus emulating the relative displacements expected for the connectors in the actual PreWEC system.

Strain gauges and LVDTs were used to measure the critical strains and connector displacements. The LVDT data was also used to monitor any slip at the friction grips (at both ends of the test setup) during the loading process.

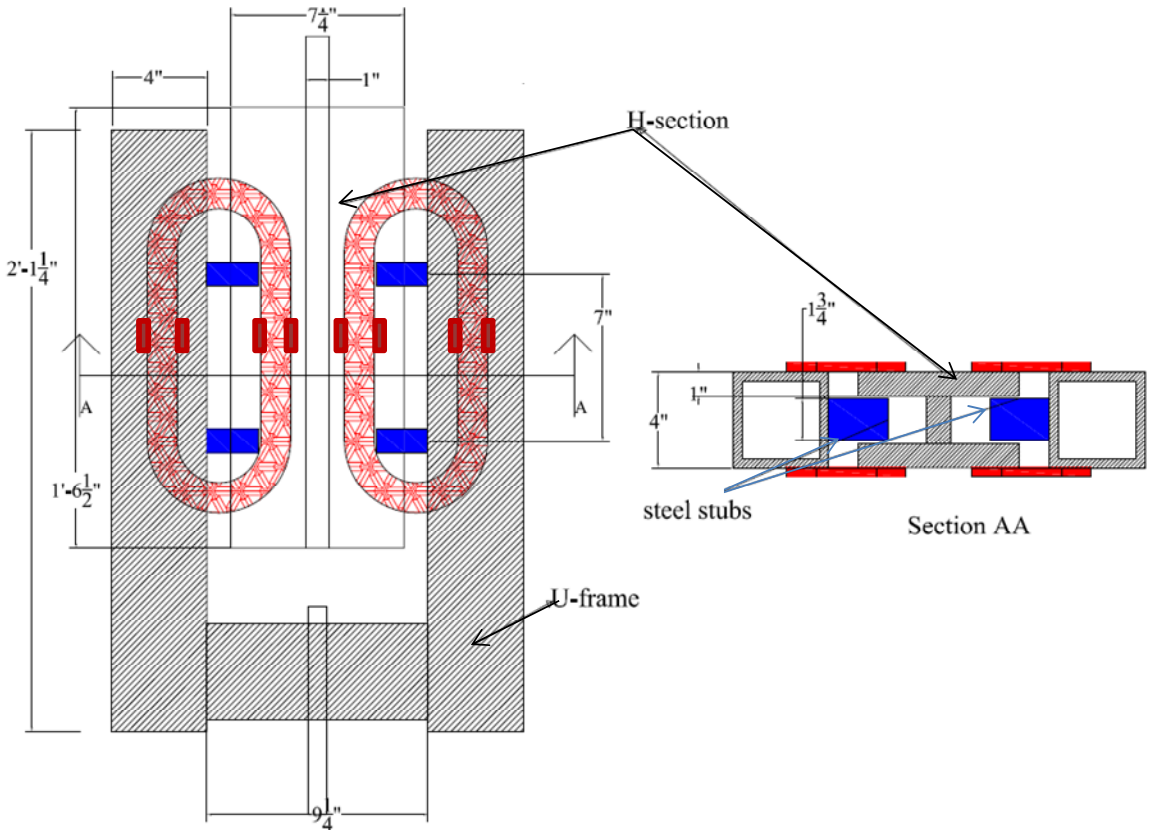

Figure 4.9 Setup used for testing the O-connectors under cyclic loading

Cyclic Test 1 (O-ISU-1)

O-connectors were welded to the U-frame and H-section of the test setup using a 2 inch (50.8 mm) long weld on both sides of the connectors. The O-connectors were then subjected to gradually increasing cyclic displacements as shown in Figure 4.10. The selected loading protocol was to simulate the expected displacement history of the connectors when the PreWEC test specimen is subjected to reverse cyclic loading (Aaleti and Sritharan 2007). During the cyclic tests, the connectors were subjected to a maximum peak displacement of 2

inches (50.8 mm) in the negative direction and 0.5 inches (12.7 mm) in the positive direction. The displacement in the positive direction were capped at 0.5 inches (12.7 mm), as the connectors in the PreWEC system would experience unsymmetrical displacements and this value represented a conservative maximum negative displacement. The connectors were cycled three times at each displacement level to ensure the stability of the force-displacement response.

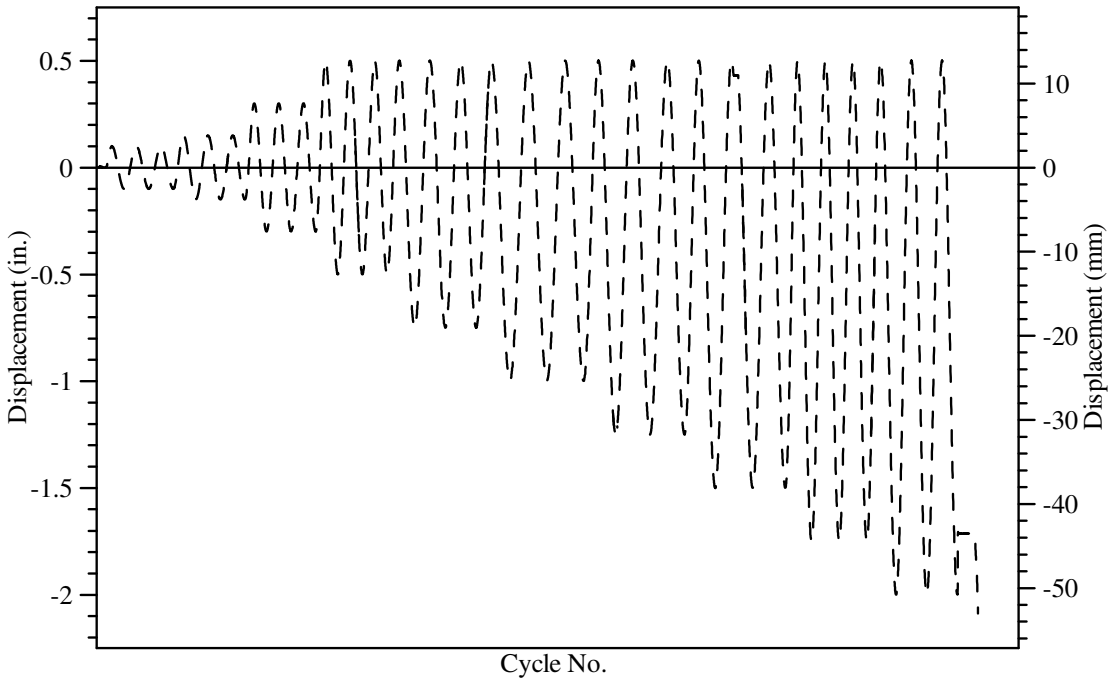

Figure 4.10 Displacement history used for testing the O-ISU-1 Connector

The connector displacement was measured using LVDTs, but no strains were recorded as this test was intended to verify the assumed force-displacement response of the O-connector in the design of the PreWEC test specimen. The average force-displacement hysteresis response established for a single O-connector is shown in the Figure 4.11. It was found that the O-connectors behaved as predicted by the finite element model for the most part. The finite element prediction of the O-connector cyclic behavior is presented elsewhere in Henry et al. (2009). The connectors provided stable hysteresis loops with significant energy dissipation upto 1 in. displacement. However, as expected, the O-Connectors began to experience out-of-plane buckling during the displacement cycle to 1.25 inch (31.75 mm). The out-of-plane bucking became more prominent during large displacement cycles (see

Figure 4.11), causing significant strength degradation. This observed behavior warranted the development of a retrofit measure for the connector to prevent the out-of-plane buckling. No cracking or fracture to the connectors was observed at the end of the test.

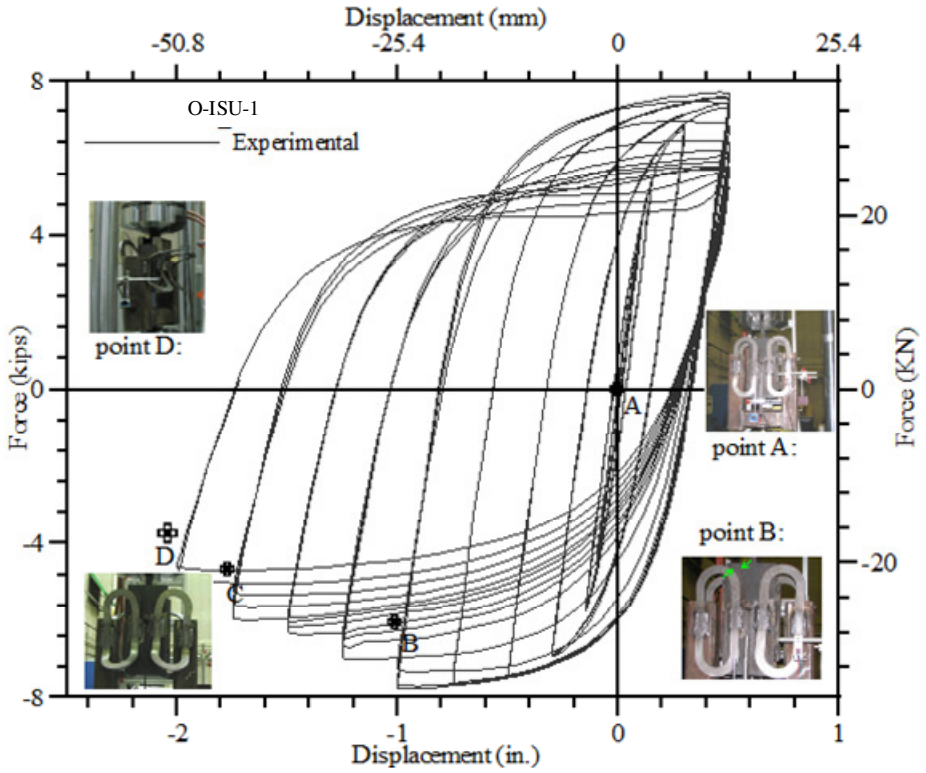

Figure 4.11 Measured force-displacement response of the O-ISU-1 connector

Cyclic Test 2 (O-ISU-2)

Similar to the first set of O-connectors, the second set of connectors were welded to the test frame using 1.75 inch long welds. Instead of the loading protocol used for O-ISU-1, the second set of O-connectors were subjected to the displacement history that the O-connectors experienced during large-scale testing of the PreWEC system. As a result, the displacement path for this test was established using the measured connector displacements obtained during the PreWEC system (see details in Section 4.6.4). Figure 4.12 shows the displacement history used for the second test, which subjected the connectors to a maximum peak displacement of 2.25 inches (50.8 mm) in the negative direction and 0.6 inches (15.24mm) in the positive direction. As with the first test, the connectors were subjected to

three cycles at each displacement level to observe the stability of the force-displacement response.

To prevent the observed buckling of the connector in O-ISU-1, a restrainer was added by means of a 3/8 thick steel plate welded to the square tubes, as shown in Figure 4.13. For this test, in addition to the LVDT measurements, strain gauges were used to record the strains in the critical regions of a connector at different displacements. The strain gauges were located at 21 mm from the weld end on compression and tension faces of both legs of the O-connector (See Figure 4.15), as these locations were determined to be the most critical based on a 3D finite element analysis of connector response (Henry et al. 2009). The average force-displacement hysteresis response established for one O-connector and the measured strains are shown in Figure 4.14 and Figure 4.15 respectively. From Figure 4.14, it can be seen that the O-connectors behaved as expected with stable hysteresis loops and dependable energy dissipation. The addition of restrainer plates prevented the out-of-plane buckling of the connectors and thus they sustained large vertical displacements without experiencing any strength degradation until reaching a displacement of 2.5 in. During the displacement cycle to 2.75 inch, one of the four O-.Connectors experienced fracture at the edge of the weld. It caused in stability in the test setup and thus the test was aborted for safety reasons.. Overall, the force-displacement capacity of the O-connector was more than the required design strength. The connector in the PreWEC system test experienced only 2.1 inches displacement at 3.5% lateral drift, which is much less than the displacement capacity of the O-connector.

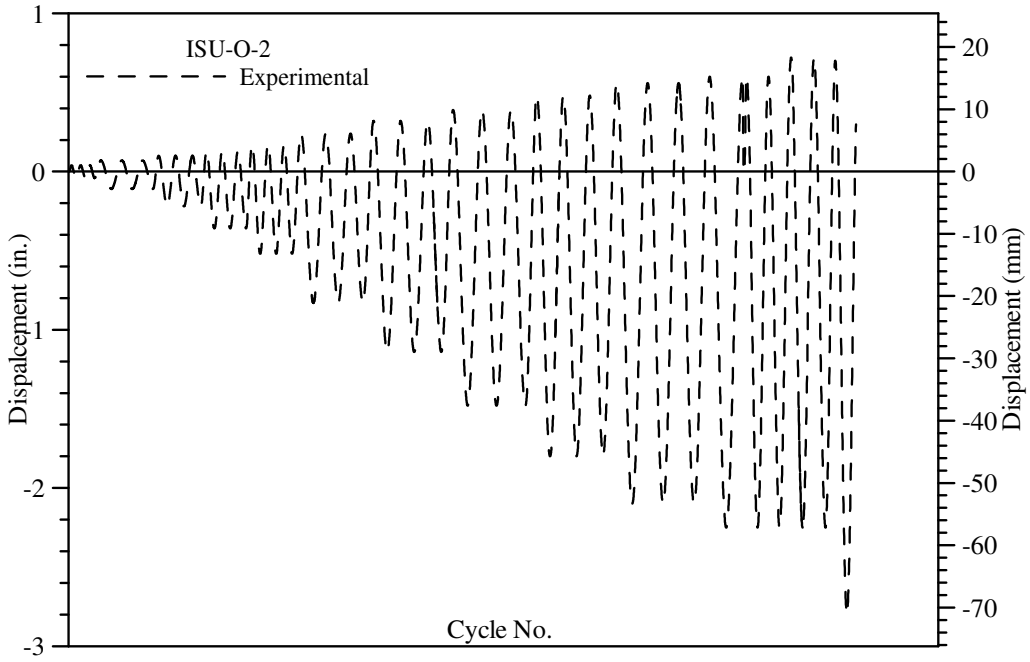

Figure 4.12 Displacement history used for testing the O_ISU-2 Connector

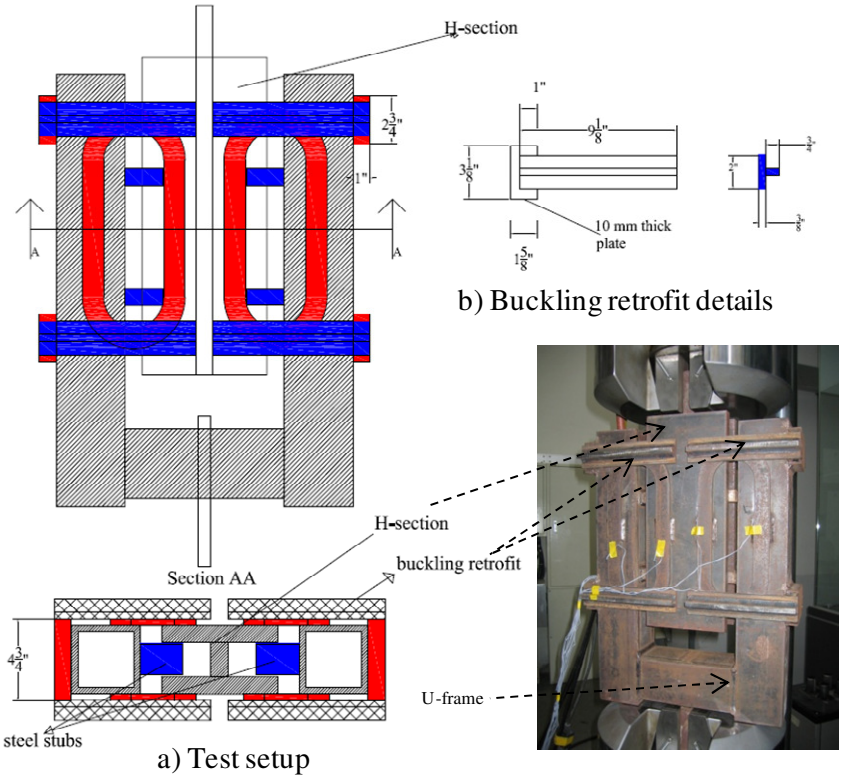

Figure 4.13 Test setup with buckling restraint

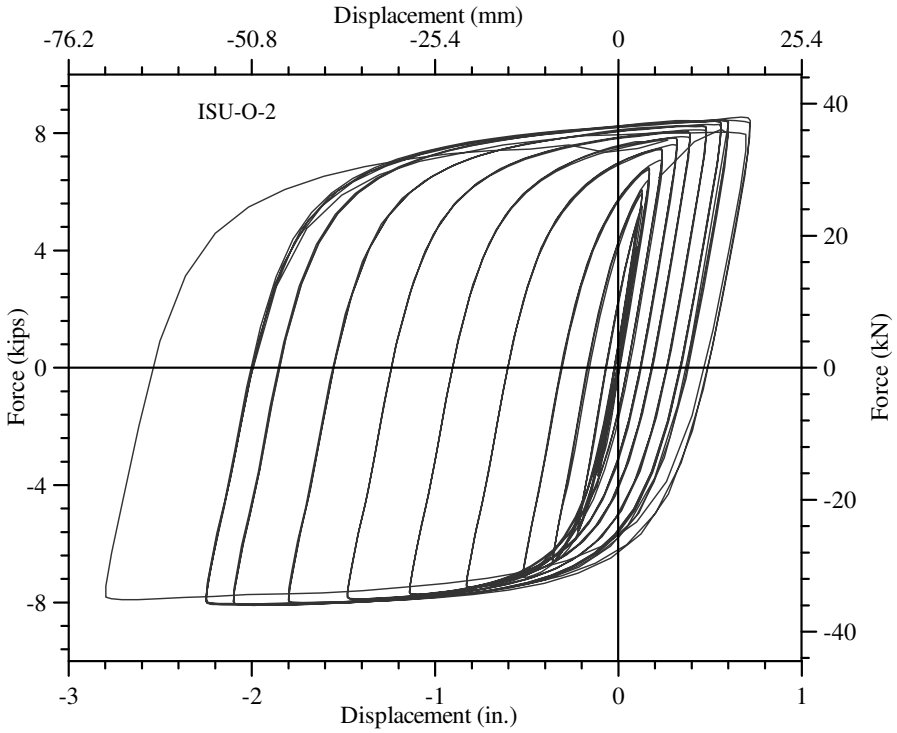

Figure 4.14 Measured average force-displacement response of a O-ISU-2 connector

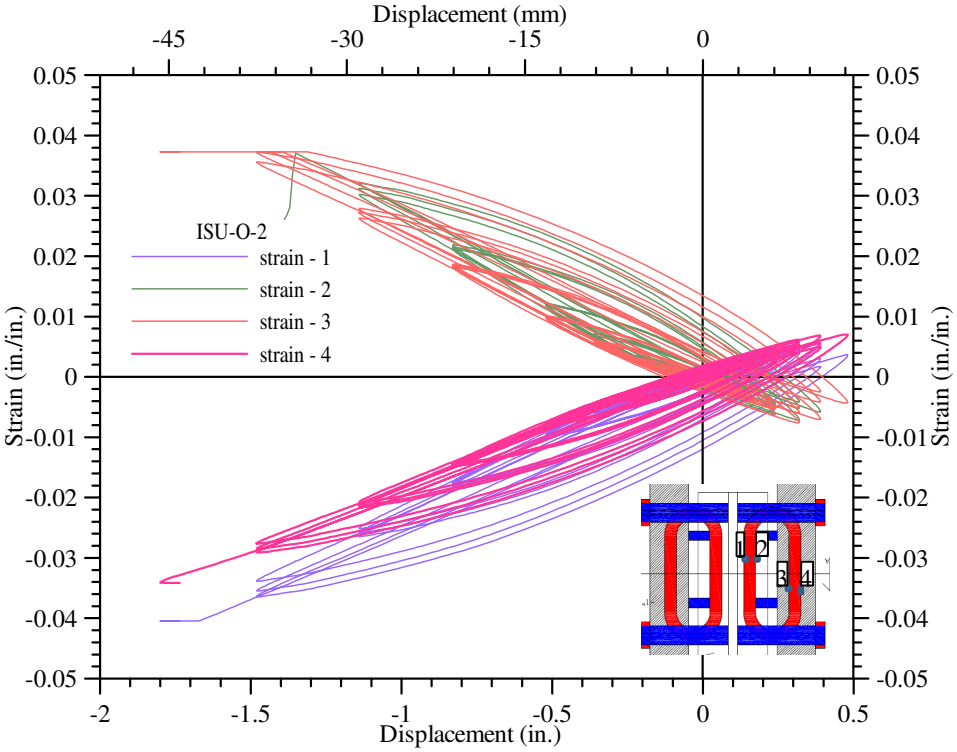

Figure 4.15 Measured strains of the O-ISU-2 connector

4.3.2 NCREE Tests

4.3.2.1 Uniaxial Tension Testing

Three tensile test coupons were cut from the same material used for the connectors and tested according to ASTM standards in a similar fashion as described above. The stress strain behavior determined from the material tests is shown in Figure 4.16. The yield strength, modulus of elasticity, and the failure stress and strain values are shown in Table 4.2. It should be noted that the material used in the Taiwan connector testing has a definite yield plateau, when compared with the material tested at ISU. The first three specimens represent the material behavior of the connectors used in the large scale PreWEC system testing. The last specimen presents the average material behavior of the connectors used in the cyclic testing (NCREE tests 1 to 3) done prior to the wall system testing.

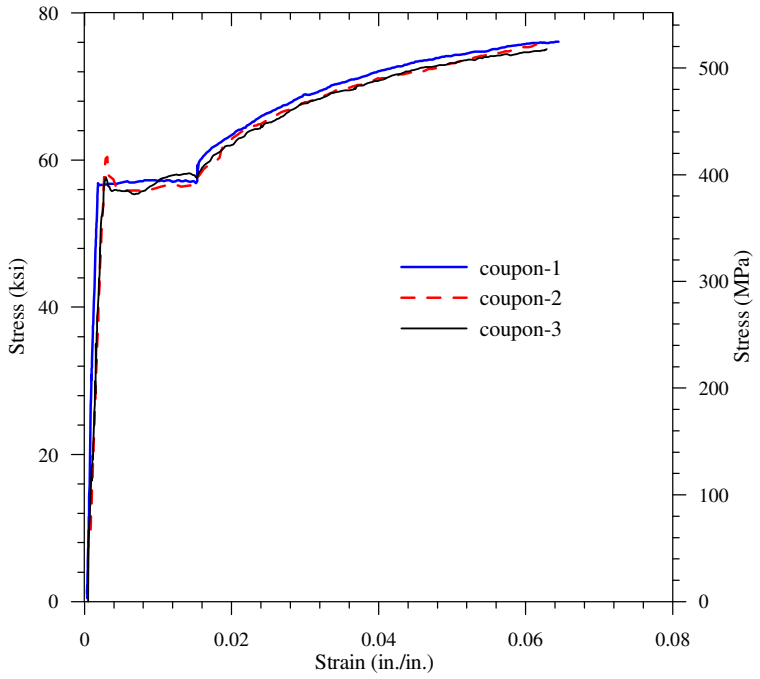

Figure 4.16 Measured stress-strain response of NCREE O-connector coupons under uniaxial tension

Table 4.2 Summary of uniaxial tensile coupon tests for the NCREE connectors

	Thickness(in.)	Avg. Young's modulus (ksi)	Failure strain (in. /in.)	Yield stress (ksi)	Failure stress (ksi)
Specimen-1	0.395	31075.38	0.28	56.56	76.43
Specimen-2	0.392	31075.38	0.25	59.47	76.29
Specimen-3	0.393	31075.38	0.24	58.16	76.14
Specimen-4	0.395	29524.14	0.23	55.55	76.43

4.3.2.2 Cyclic Tests

Further cyclic tests on O-connectors were performed to failure at NCREE in Taiwan; similar the cyclic tests at ISU, each set consisted of four connectors. The additional testing was required to confirm the O-connector behavior prior to the large-scale PreWEC test. The steel material available at in Taiwan was different from the material used in the ISU tests and also the laser cutting technique was not easily available for the connector fabrication. The O-connectors were cut from a 0.395 in. (10 mm) thick grade A50 steel plate. Three of the tests were completed prior to the large-scale PreWEC test, while the fourth test was performed using connectors manufactured from the same batch as those used during the large scale testing of the PreWEC system. It was also found that, due to a fabrication error, the O-connectors tested at NCREE were one inch shorter in length compared to the connectors tested at ISU. The dimensions of the connectors tested at NCREE are shown in Figure 4.17.

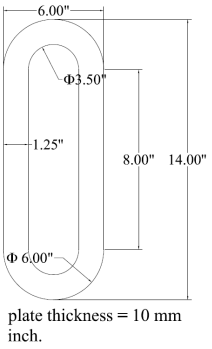

Figure 4.17 Dimensions of the NCREE O-connector

The same test setup as used for the ISU tests was used for testing the O-connectors at NCREE, Taiwan. The connectors were welded to the test frame with a 2.5-3.0 inch long weld

for all of the cyclic tests. Strain gauges and LVDTs were used to measure the critical strains and connector displacements respectively. MTS machine displacement readings along with the LVDT readings were used to monitor possible slip at the friction grips during the loading process.

Cyclic Test 1 (O-NCREE-1)

This test, a duplication of the O-ISU-1 cyclic test with the NCREE O-connector, was conducted to quantify the influence of different material properties and dimensions on the expected force-displacement behavior of the connector. The test was also intended to verify the necessity of the buckling retrofit to prevent the out-of-plane buckling of the connector at large displacements. The connectors were subjected to same displacement history as the O-ISU-1 connector (see Figure 4.10) except few extra smaller displacement cycles were added at the end of the test.

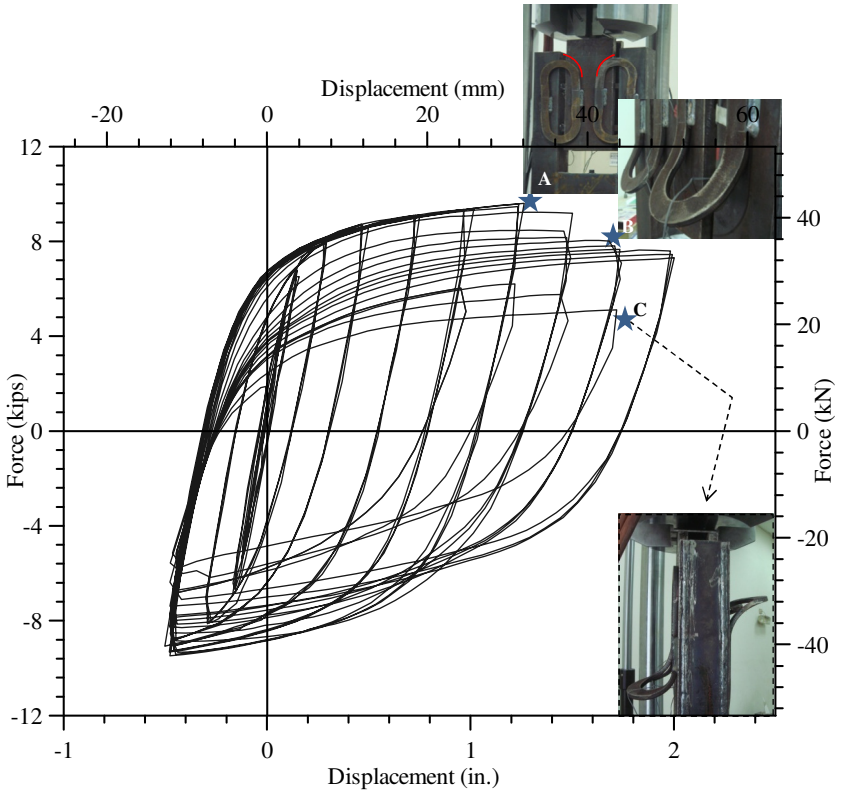

Figure 4.18 Measured force-displacement response of the O-NCREE-1 connector

The connector displacement was measured using the LVDTs along with the MTS machine displacement reading. Comparison of LVDT readings to the MTS readings showed only minor variation indicating no slip at the ends of the test setup. The force-displacement hysteresis response of a single O-connector is shown in Figure 4.18. Similar to the O-ISU-1 test, out-of-plane buckling of the connectors initiated during the 1.5 inch displacement cycle. This was later than the observed behavior in O-ISU-1 test, where out-of-plane buckling initiated on the 1.25 inch cycle. From Figure 4.18, it can be seen that the O-connectors behaved as predicted by the finite element model (Henry et al. 2009) upto 1.25 inches of displacement with good force-displacement behavior. The connector legs experienced large inelastic strains under cyclic displacements and thus provided sufficient energy dissipation with stable hysteresis loops. Figure 4.19(c) shows the striations formed along the connector leg due to yielding. Four strain gauges were mounted on the connectors at 20.6 mm (0.8 in.) from the weld ends as shown in Figure 4.19b. Figure 4.19a shows the variation of strain as a function of the displacement. The out-of-plane bucking became more prominent during large displacement cycles (see Figure 4.18), causing significant strength degradation (nearly 20%).

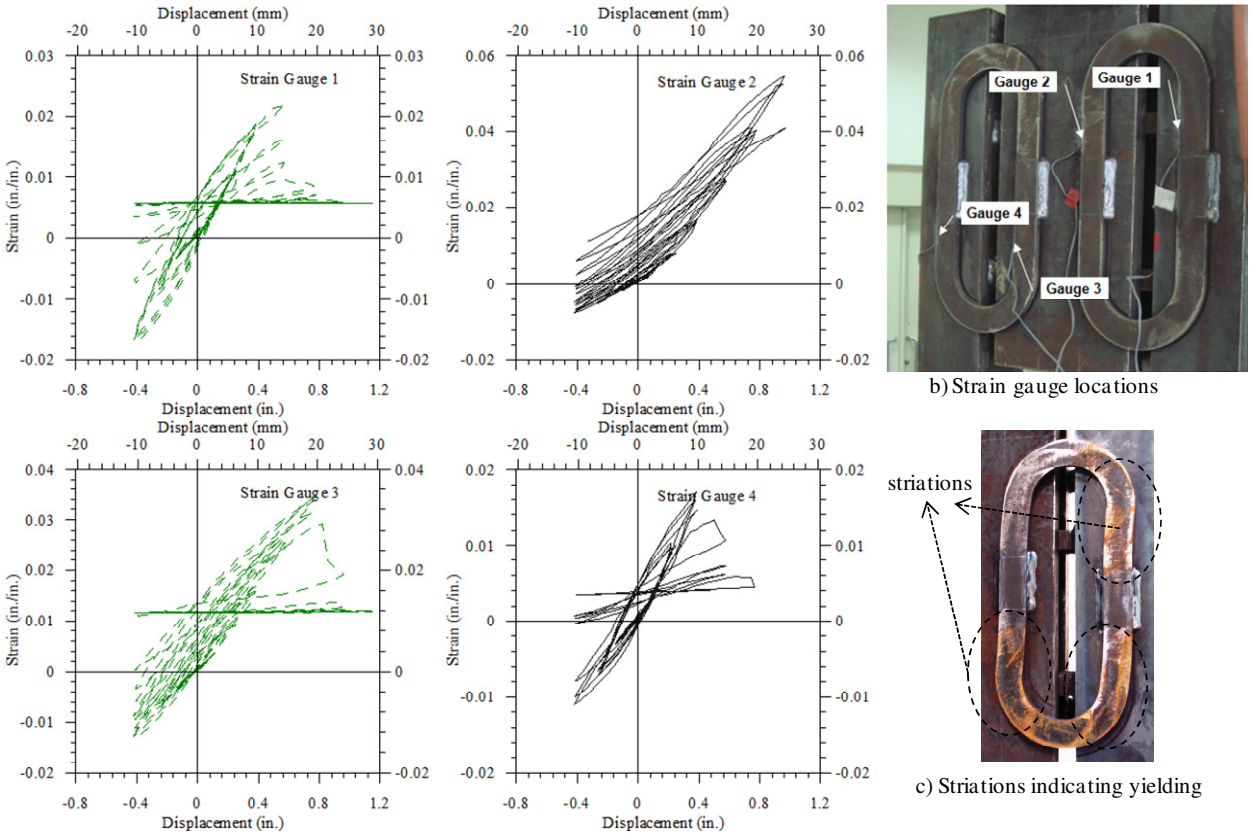

Figure 4.19 Measured strain readings, strain gauge locations and yield pattern for O-NCREE-1 connector

Overall, the force-displacement behavior of the connector was similar to the assumed design envelope. The connector's capacity was increased by nearly 25% when compared with that of the connectors tested at ISU due to different material properties and decrease in the overall length of the connector by one inch. The out-of-plane buckling was delayed slightly when compared with that of the ISU connectors. However, local buckling eventually occurred causing strength degradation and solidifying the need for a retrofit.

Cyclic Test 2 and 3 (O-NCREE-2 and O-NCREE-3)

A further two cyclic tests (O-NCREE-2 and O-NCREE-3) were completed with O-connectors fashioned with a T-shaped steel plate restraint to prevent the out-of-plane buckling of the O-connector (see Figure 4.13). The connectors were subjected to the same displacement history as in the Test 1 (O-NCREE-1).

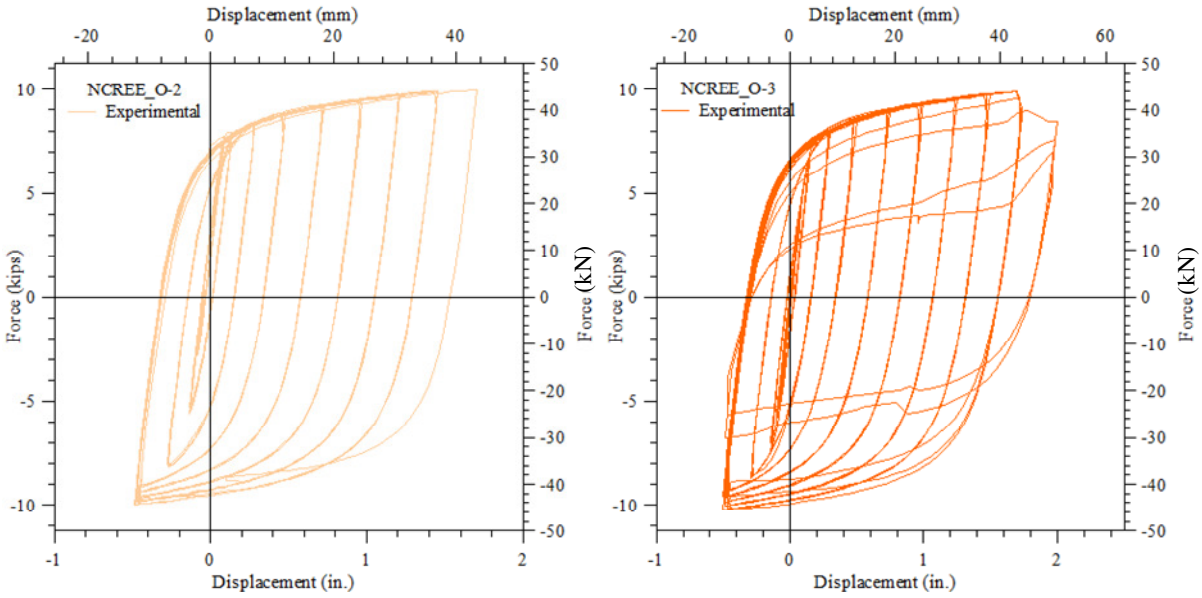

a) O_NCREE-2 response

b) O_NCREE-3 response

Figure 4.20 Measured force-displacement response of the O-NCREE-2 and O-NCREE-3 connectors

As with the previous tests, the displacement and critical strains were measured using LVDTs and strain gauges respectively. The strain gauges were located at 20.5 mm (0.8 in.) from the ends of the 3 inch weld (see Figure 4.19 b). The force-displacement responses obtained from Tests 2 and 3 on the buckling retrofit O-connectors are shown in Figure 4.20a and Figure 4.20b respectively. The O-connectors in both tests behaved as predicted by the finite element model (Henry et al. 2009) with no occurrence of out-of-plane buckling. The connectors showed a stable force-displacement behavior, with good energy dissipation up to 1.75 in. (44 mm) displacement. The strain variation at the critical section in Tests 2 and 3 is shown in Figures 4.22a and 4.22b respectively.

During the O-NCREE-2 test, one of the connectors experienced partial fracture during the unloading cycle of 1.75 in. (44 mm) displacement. However, it did not affect the capacity of the connector. At the end of the 2nd cycle at 1.75 in. (44 mm) of displacement, further connectors began to fracture (see Figure 4.21a), causing a significant drop in the strength. The test was terminated after the 3rd cycle at 1.75 in. (44 mm) displacement due to unstable rotation of the specimen. During the O-NCREE-3 test, a slight tear began to open on one of the connectors during the unloading cycle of 1.75 in. (44 mm) of displacement.

However, it did not affect the capacity of the connector. At the end of the 3rd cycle at 1.75 inch displacement, one of the connector fractured, causing a significant drop in the strength. Three out of four connectors were fractured partially during the 2nd and 3rd cycles of 2 in. (50.8 mm) displacement (see Figure 4.21b), causing instability of the test setup and subsequent termination of the test.

In summary, the O-connectors fashioned with the buckling retrofit performed well, displaying no out-of-plane buckling and providing good energy dissipation. The connectors tested at NCREE had 25% more capacity than those tested at ISU. This strength increase is attributed to the variation in the material stress-strain behavior and the change in the connector length.

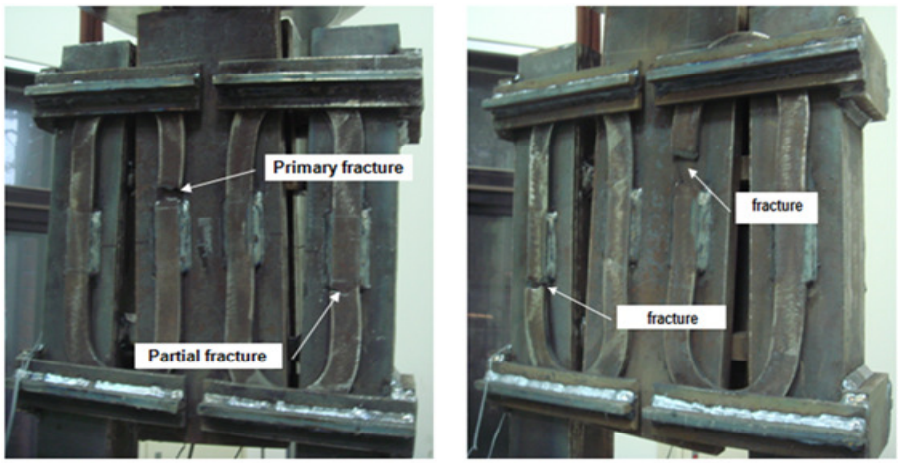

a) O_NCREE-2 b) O_NCREE-3

Figure 4.21 Condition of the O-connectors at the end of the Tests 2 and 3

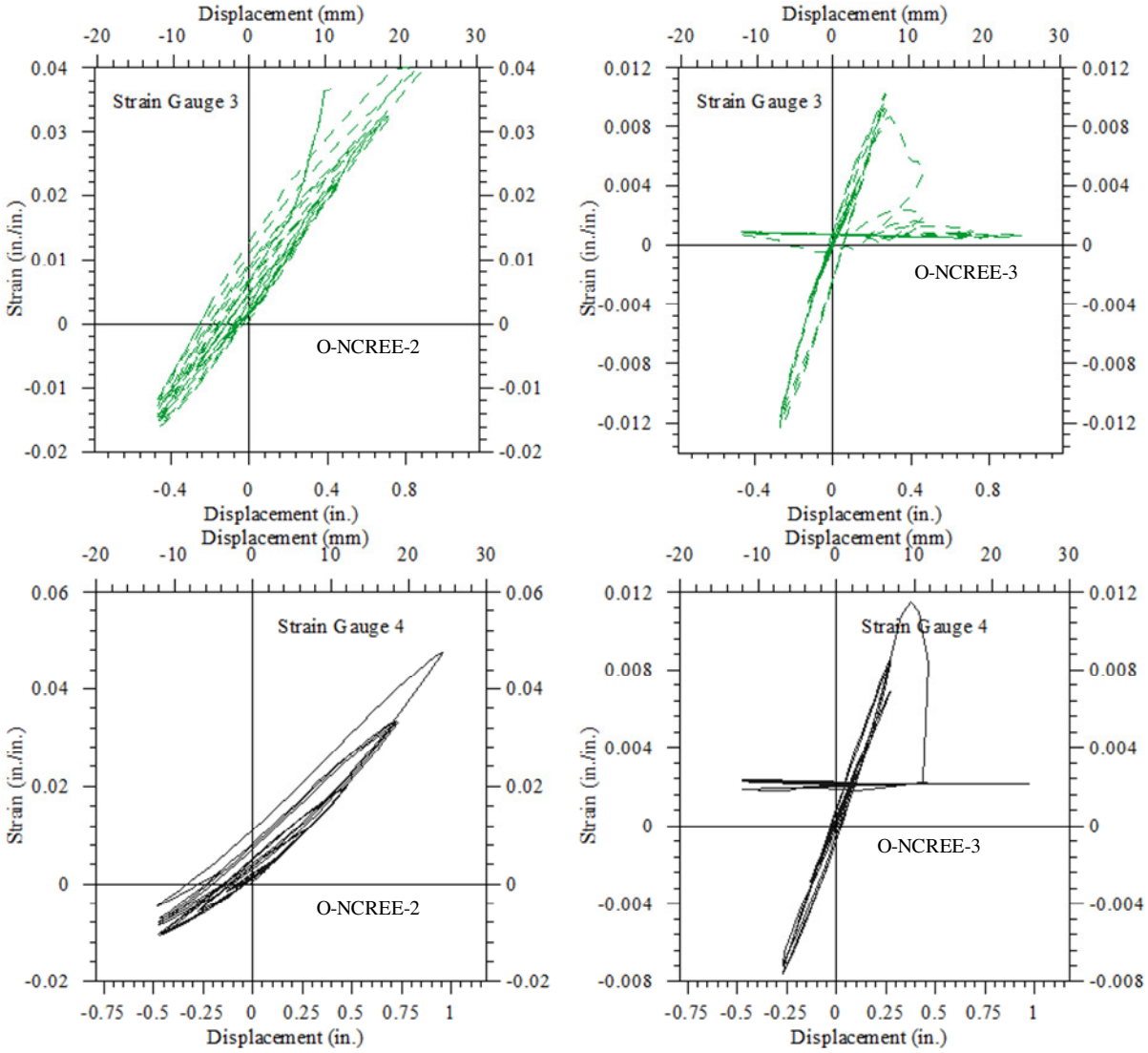

a) O-NCREE-2 strains

b) O-NCREE-3 strains

Figure 4.22 Measured strain readings for O-NCREE-2 and O-NCREE-3 connectors

Cyclic Test 4 (O-NCREE-4)

The satisfactory performance of O-connectors under incremental cyclic displacement history was evident from the cyclic tests completed at ISU and NCREE. However, the response of the connector to a randomized displacement history which can be expected during an earthquake needed to be investigated. Therefore, an additional test was conducted using a set of four connectors and the same test setup as described before subjecting the

connectors to a random displacement history. The displacement history, shown in Figure 4.23, was derived using the displacement history experienced by a UFP connector in the PRESSS test building (Thomas and Sritharan, 2004). The PRESSS building was subjected to a pseudo dynamic loading derived from different ground motion levels. Consequently, the displacement history of a UFP connector from the PRESSS building represents multiple earthquake hazard levels and was therefore chosen to evaluate the performance of the O-connector. The peak displacement in the displacement history from the PRESSS test building was scaled to match the peak displacement experienced by the O-connectors in the large-scale PreWEC system test.

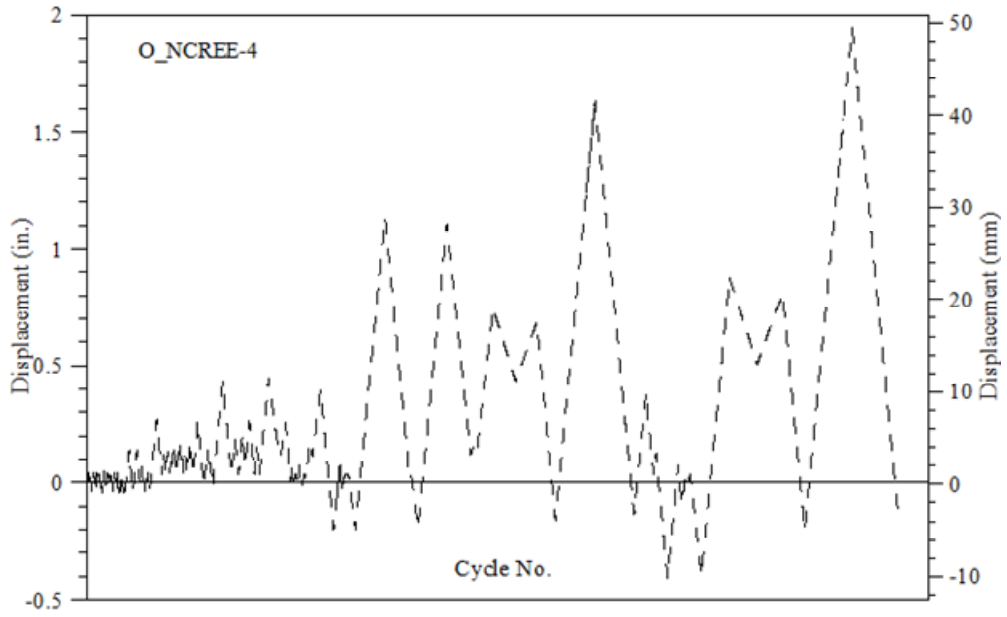

Figure 4.23 Displacement history used in the Test 4 on the O-connector at NCREE

The relative vertical displacement and the strains at the critical locations on the connectors were measured as before. The connector force-displacement response to the applied displacement history is shown in Figure 4.24. The O-connector performed similar to previous tests. The connectors did not fracture at the end of the applied displacement history, verifying the good performance of the O-connector.

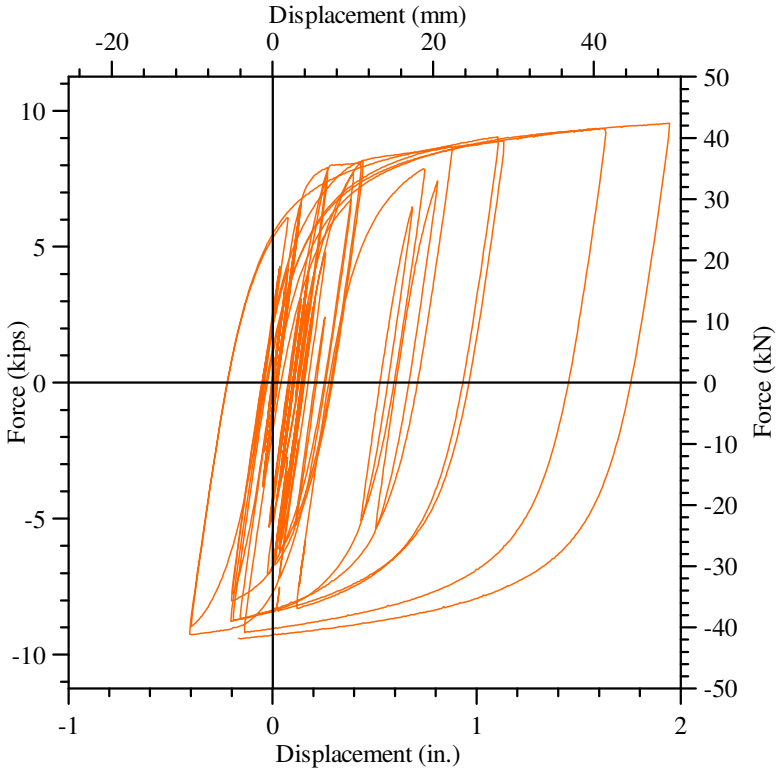

Figure 4.24 Measured force-displacement response of the O-NCREE-4 connector

4.4 PreWEC-1Test Setup

This section discusses the test setup and the loading protocol used for the experimental investigation of PreWEC-1 at NCREE in Taiwan. A schematic of the test setup is shown in Figure 4.26. A 12 ft (3.66 m) long, 4.8 ft (1.44 m) wide precast foundation block with block outs at the bottom and a pocket on the top was cast at precast plant. The foundation block was brought into the final position on the test floor and was post-tensioned to the strong floor using eight two-inch diameter high strength threaded bars to prevent sliding from occurring during the lateral load testing. The precast wall panel and the CFT columns were erected on a concrete foundation block. A T-shaped beam was placed on the wall to connect the actuator. The erection process of the PreWEC-1 is shown in Figure 4.25. As required by ACI ITG-5.1 (2007) and ACI ITG-5.2 documents (2009), a 1.5 in. (37 mm) thick Pagel® V 1A/40 grout, a high strength steel fiber reinforced grout with a specified compressive strength of 14 ksi (98 MPa) at 14 days, was placed at the interface between the foundation and wall to obtain uniform contact between the PreWEC system elements and the foundation (see Figure 4.27a). The prestressing tendons in the wall and column were anchored at the top of the loading beam (Figure 4.27b) and column and in the foundation beam at the bottom. All of the post-tensioning strands (12, 0.6 in. dia.) in the precast wall panel were pulled simultaneously using a VSL post-tensioning system to introduce uniform compression in the wall panel and prevent variation of strand stresses. However, the strands in the columns were post-tensioned one after the other until all strands reached similar stresses and the desired total prestressing was reached. The prestressing forces were monitored using load cells placed at top of the columns. Based on the O-connector's measured force-displacement behavior from the experimental investigation at NCREE (presented in Section 4.3.2.2), five pairs of O-connectors with restrainers (Figure 4.27c) were used at each side of the wall. The dimensions of the O-connectors used in the test are shown in Figure 4.17.

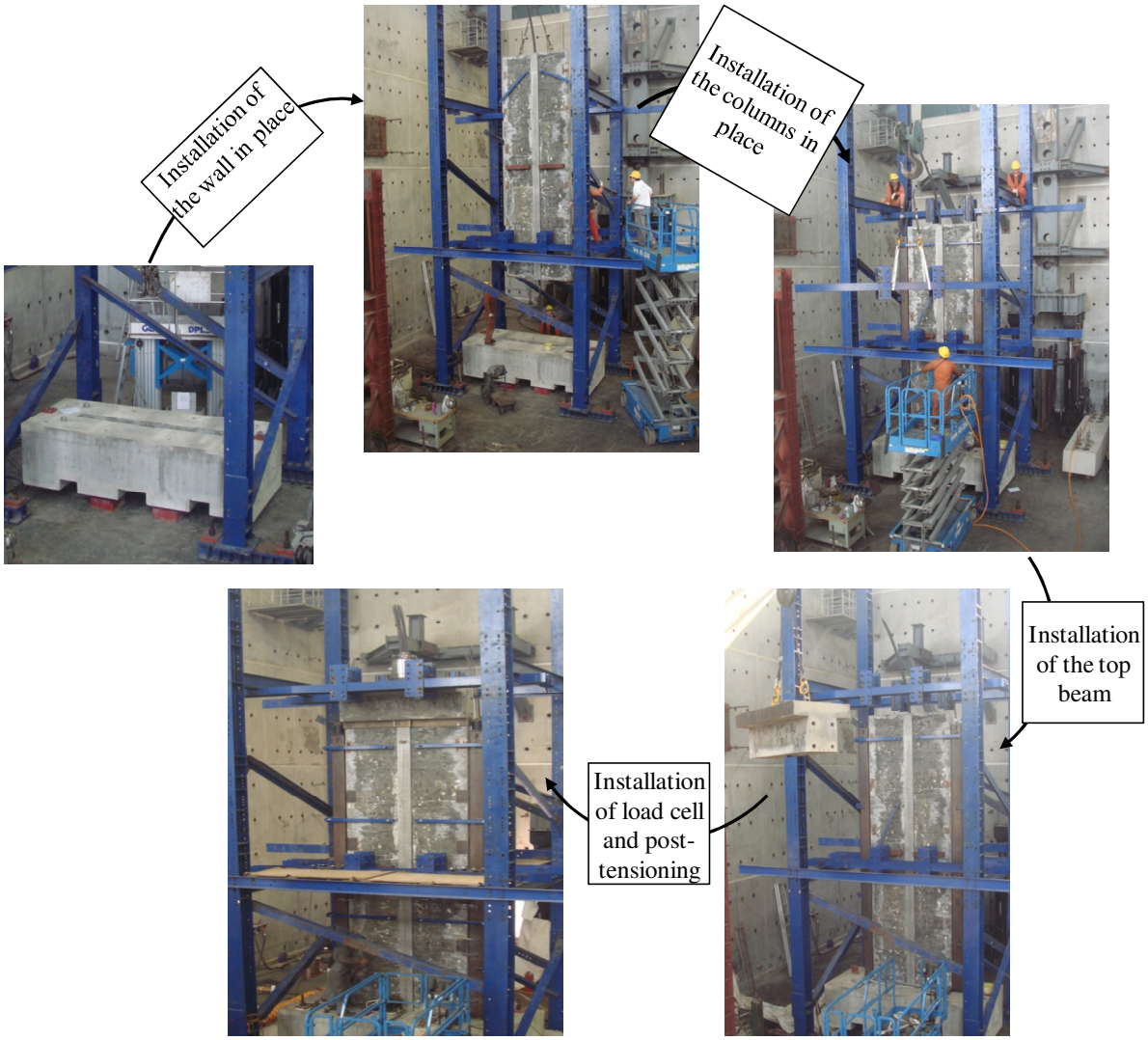

Figure 4.25 PreWEC -1 erecting process

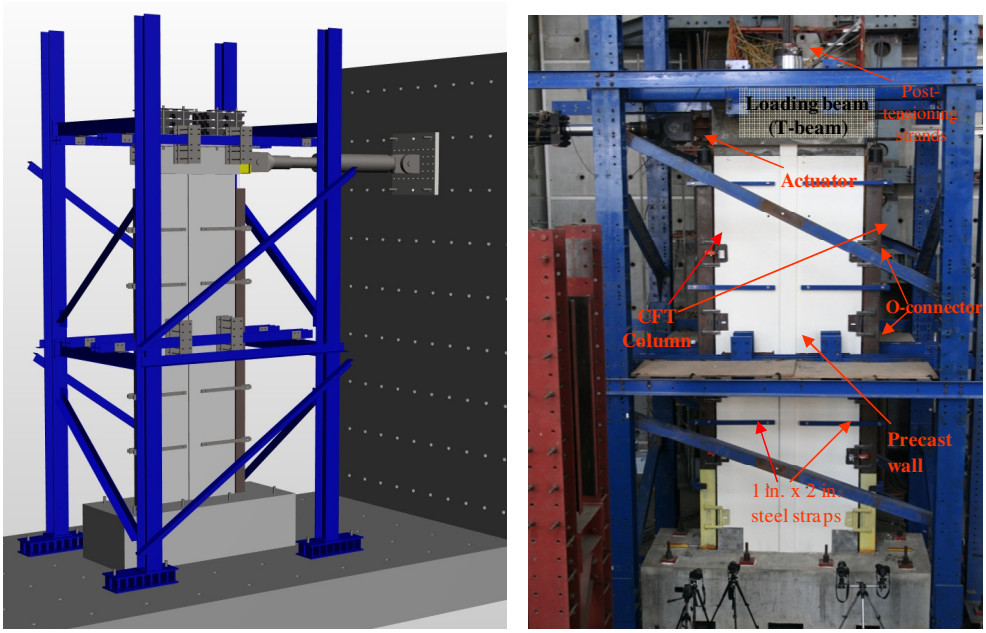

a) Schematic view

b) A picture of PreWEC-1

Figure 4.26 The test setup used for the PreWEC system testing

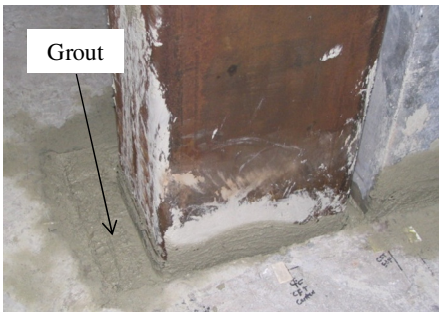

a) Pagel V 1A/40 grout at column-foundation interface

b) Post-tensioning anchor of the wall panel

c) A view of an installed O-connector with restrainer near the base of the wall

d) Steel Struts

Figure 4.27 Close-up of the PreWEC-1 system at different locations

In a typical building, walls are restrained from out-of plane movement by the floor elements. Therefore, to simulate this condition, the test setup included an out-of-plane restraint at the top and at mid-height of the wall, which was constructed by using rollers supported on steel beams (see Figure 4.28). This arrangement was to prevent twisting and unexpected buckling of the wall during lateral load testing. The out-of-plane supports were used in erecting the wall in the vertical position and a gap of 1/8 to 1/4 inch (3 to 6 mm) was left between the rollers and the wall during testing to allow small movements as the wall displaced laterally. This arrangement was used to avoid the lateral forces being transmitted to the support frame. The support frame was anchored to the strong floor using high strength threaded bars. Additionally, the wall and the column elements were tied together at four places using 1 in. thick by 2 in. wide (25 mm by 50 mm) steel struts in the horizontal direction. These steel struts were connected to the columns and wall by means of a hinge mechanism to ensure that wall and columns would undergo the same amount of lateral movement without influencing their individual uplift behavior.

The wall system was subjected to reverse cyclic lateral loading using a ± 220 kip (± 1000 KN) capacity hydraulic actuator, mounted to a reaction wall at 20 ft (6.1 m) above the wall-to-foundation interface. The actuator was connected to a T-shaped precast loading beam located at top of the wall. The interface between the loading beam and the precast wall panel was grouted using a high early strength cement grout (5 ksi) to create a uniform contact between the elements. Similar to the previously tested cast-in-place concrete walls, the wall system was not subjected to any external gravity load.

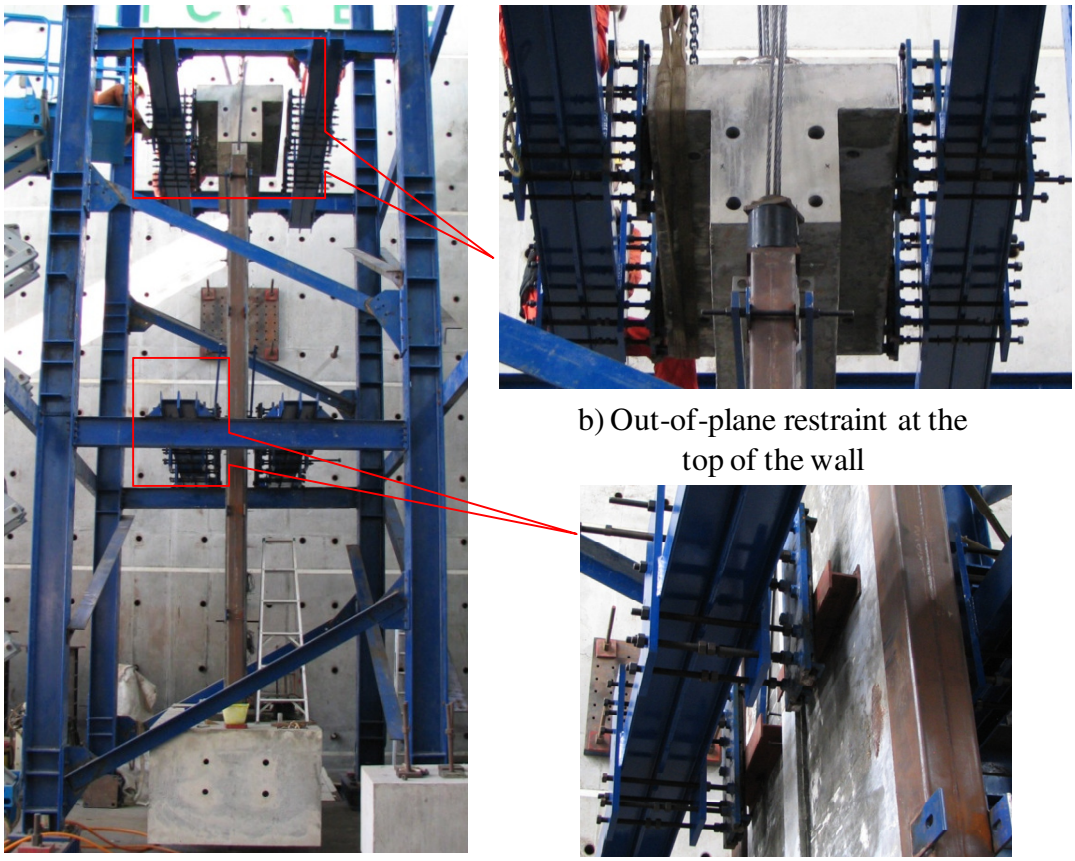

b) Out-of-plane restraint at the top of the wall

a) Side view of PreWEC-1

c) Mid height out-of-plane restraint

Figure 4.28 Out-of-plane restraints added at the top and mid height of PreWEC-1.

4.5 Instrumentation

The following section details the various instruments used to measure the performance of the PreWEC system during testing. Several types of instruments were used including load cells (LC), linear variable differential transducer (LVDTs), string potentiometers (string pots), rotation meters and strain gauges. Figure 4.29 shows the locations and designations of the displacement gauges and the load cells. A 600 kip load cell (shown as LCwall in Figure 4.29) and two 110 kip load cells (shown as LCcol_S and LCcol_N in Figure 4.29) were placed at the top to measure the forces in the post-tensioning steel of the wall panel and the south and north columns respectively. LVDTs and string potentiometers (string pots) were used to measure the in-plane global displacements (denoted as SPL25, SPL50 and SPL75 in Figure 4.29) over the height of the test unit, as well as the

relative deformations within the wall. The arrangement of the instrumentation at the base of the wall is shown in Figure 4.29.

LVDTs were attached vertically at the wall-foundation interface in order to measure the uplift of the wall and columns with respect to the foundation block (see Figure 4.30). LVDTs were also used to monitor any unintentional uplift or horizontal slip of the foundation block (not shown in Figure 4.29) that was intended to be rigidly connected to the laboratory strong floor. Two temposonic displacement gauges (denoted as SPLTOP1 and SPLTOP2 in Figure 4.29) were attached to the specimen at the loading level to measure the overall lateral displacement of the system relative to a steel reference frame erected independently of the steel lateral support frame. Rotation devices (RWB, RCS, RCN and RWT in Figure 4.29) were mounted near the bottom of the wall, bottom of the columns, and at the top of the wall to measure the rotations. Any possible slip at the wall-loading beam interface and uplift of the loading beam were monitored using two LVDTs (LBS and LBUT) mounted to the wall panel at 1 in. (25 mm) from the top T-beam and wall interface.

LVDTs were used to measure the relative displacements between the wall and columns at two different connector levels for each column at the location of connectors as shown in Figure 4.31. The bottom story of the wall was instrumented with string pots in an X-configuration to measure the relative deformation contributions by flexural and shear actions.

A number of embedded concrete and steel strain gauges were used to measure the strain demands in the longitudinal reinforcement, shear reinforcement, confinement hoops and the confined concrete in the compression regions. Figure 4.32 to Figure 4.34 show the locations of the various strain gauges. Strain gauges were also placed on Concrete Filled Tube (CFT) columns, bottom steel struts and the O-connectors to measure the strain demand experienced during testing.

During the test, the data from all instruments were recorded using a computer based data acquisition system. The data acquisition speed was varied depending on the target displacement. All channels were read and recorded each time the data was to be saved.

However, due to unforeseen reasons, the data from string potentiometers and rotation meters was not recorded upto a lateral drift of ±1%.

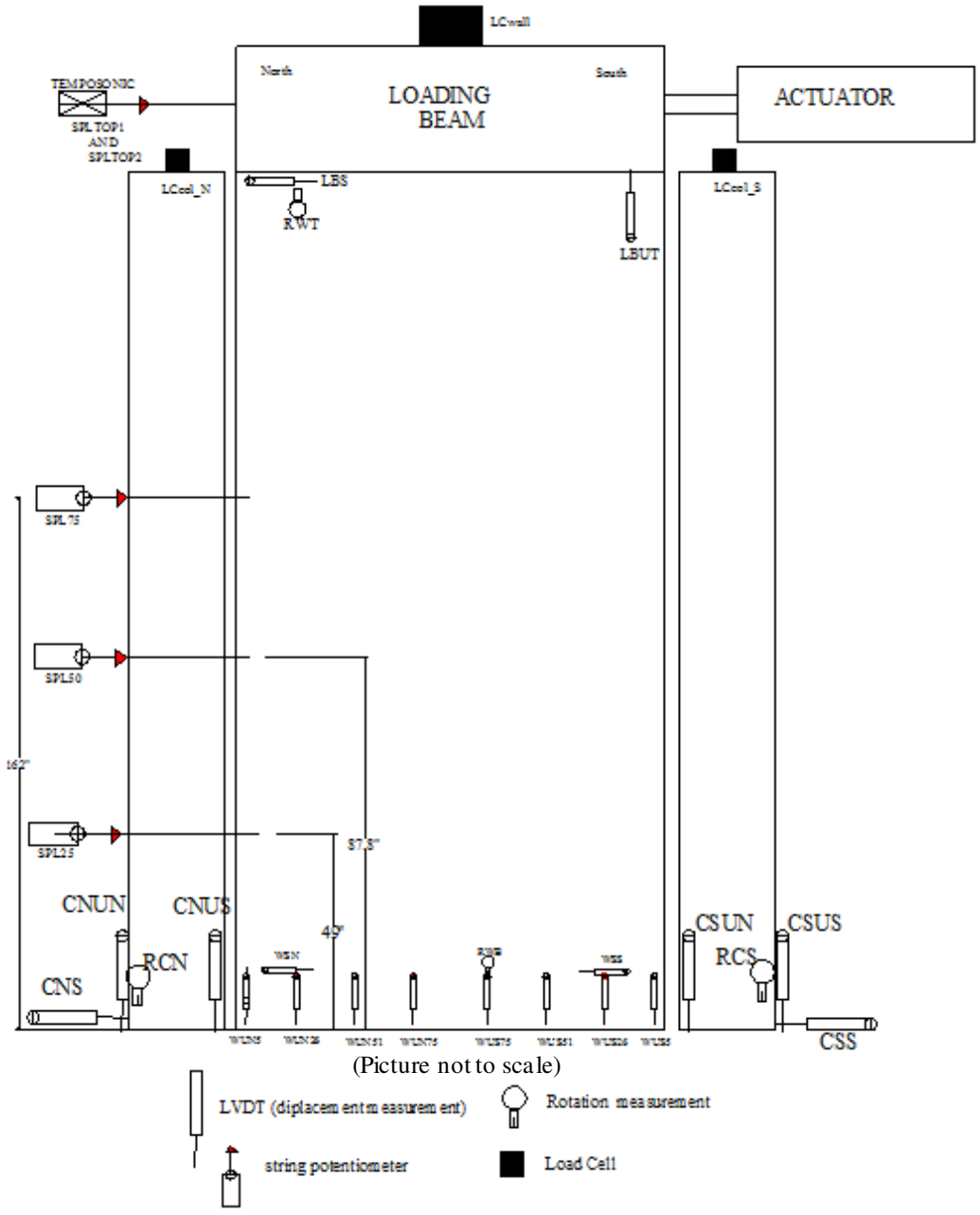

Figure 4.29 A schematic of PreWEC-1 showing load cell and displacement gauge locations

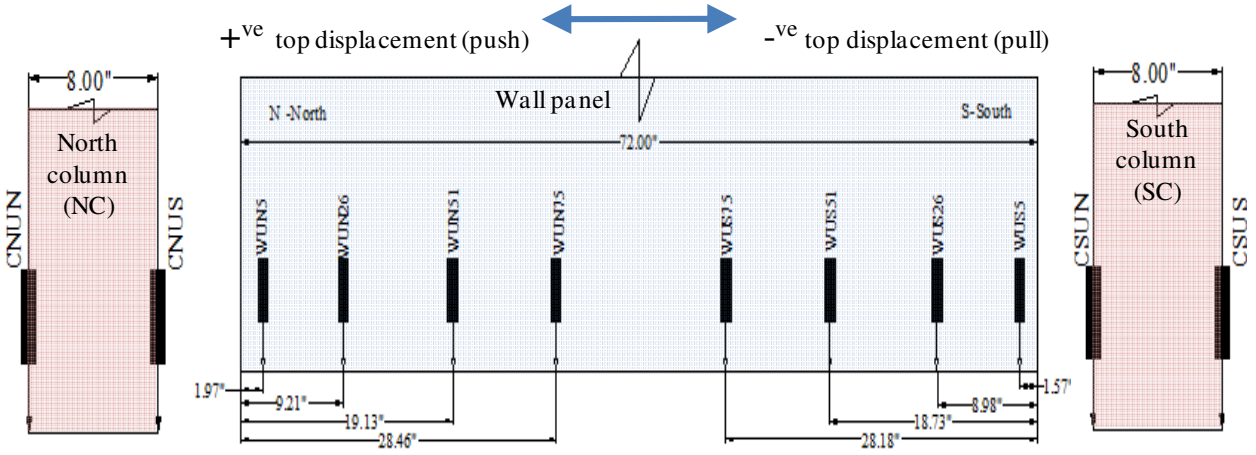

Figure 4.30 Locations of the displacement transducers along the wall and column ends

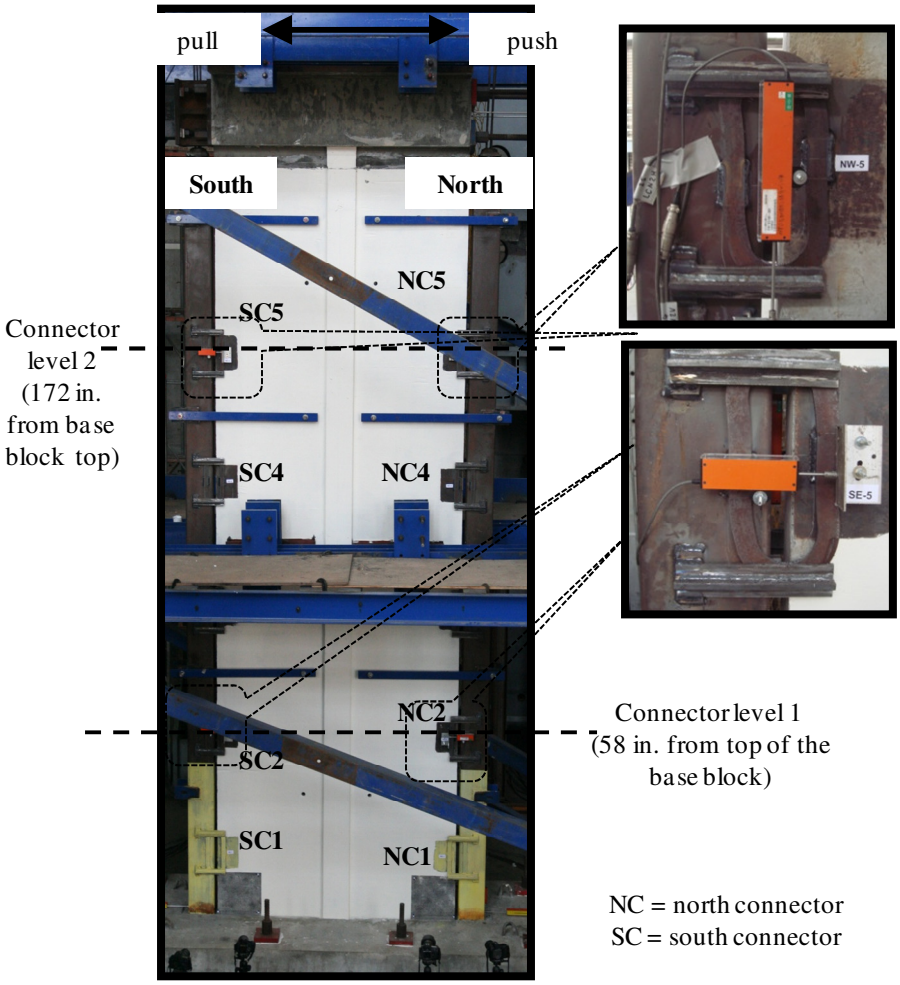

Figure 4.31 Locations of LVDTs used to measure the displacement demands on the O-connector

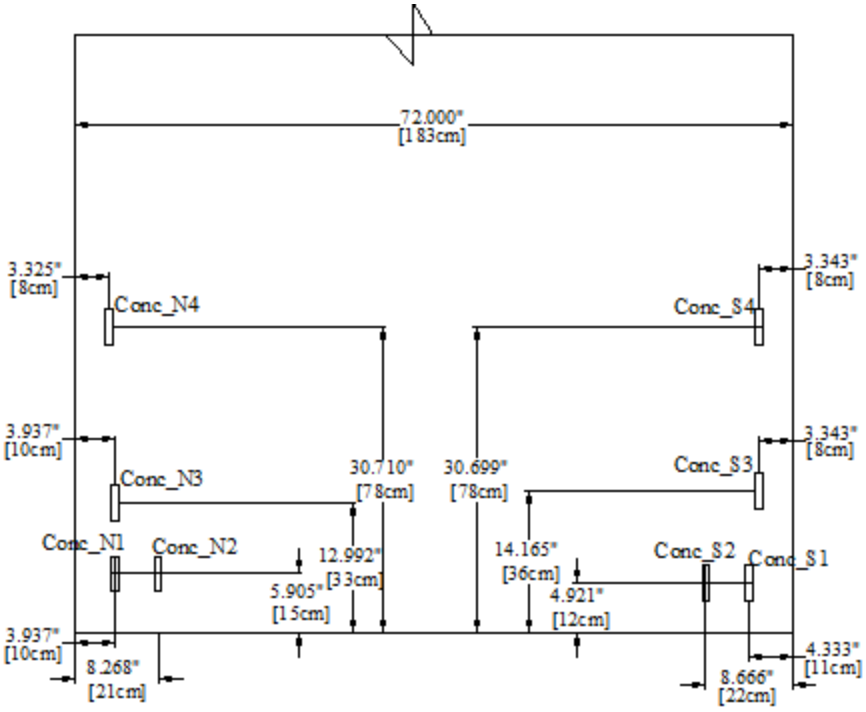

Figure 4.32 Locations of the embedded concrete gauges in the wall panel boundary regions (concrete gauge type: PML-60-2L, gauge factor: 2.09)

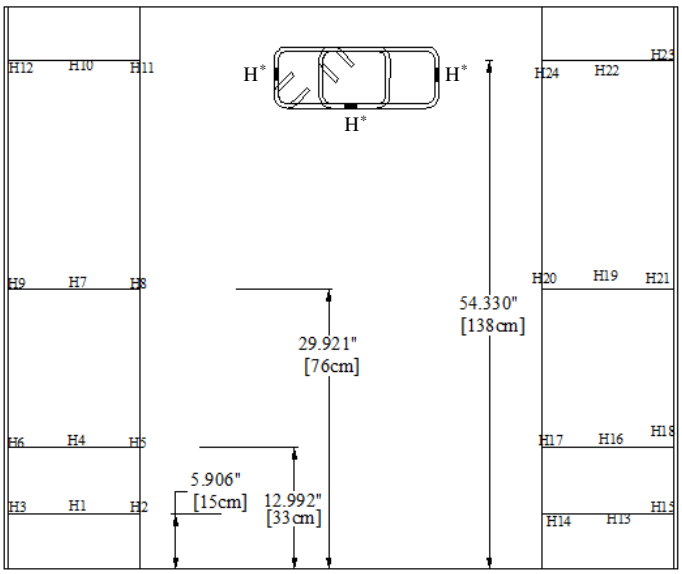

Figure 4.33 Locations of the hoop gauges in the wall panel boundary regions

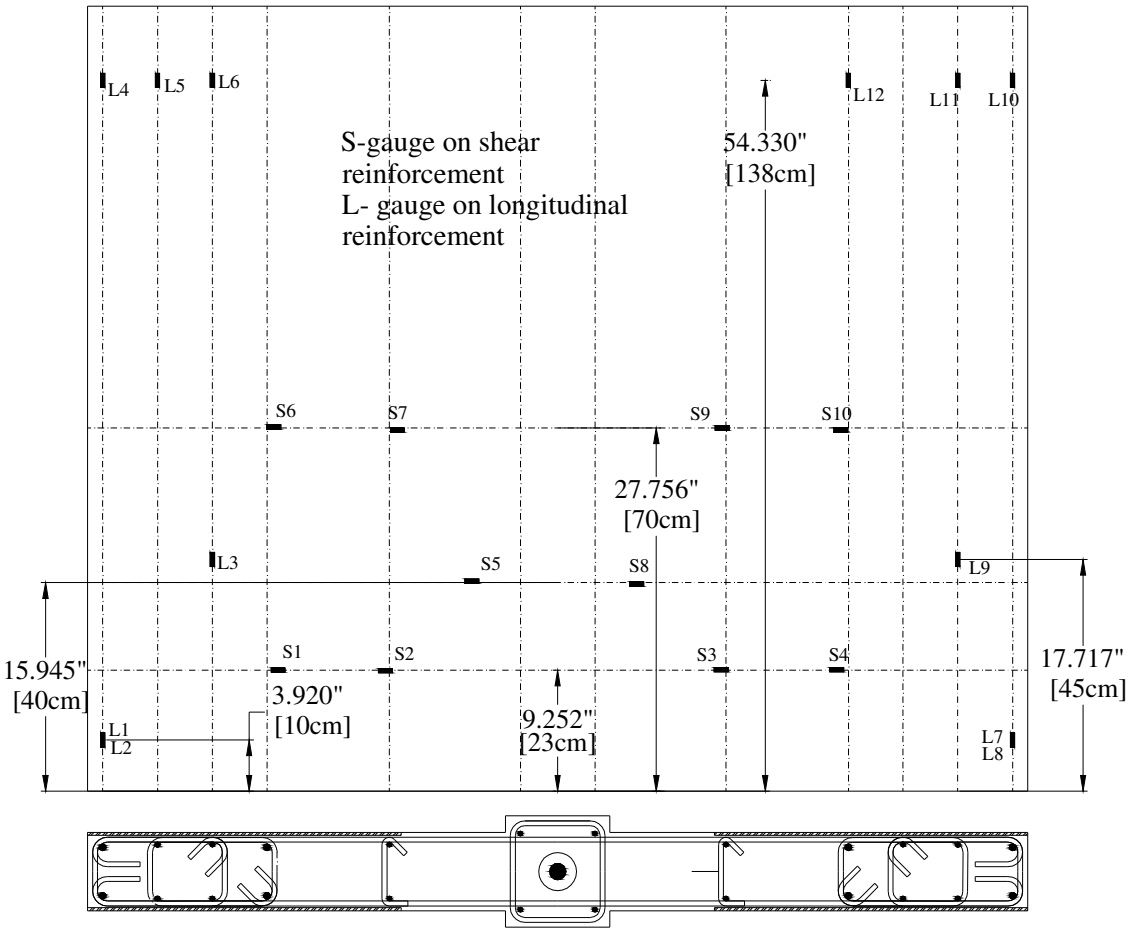

Figure 4.34 Locations of the strain gauges mounted to the longitudinal and shear reinforcement of the wall panel

4.5 Load Protocol

To simulate the seismic effects the wall was subjected to a pseudo-static reverse cyclic lateral load by the actuator. The cyclic displacement history applied to the wall system is shown in Figure 4.35. For the first four cycles of loading, up to the decompression point of the wall system, the load was applied under a force-controlled mode. Then, the load was applied under displacement control mode. The displacement targets for the testing were chosen based on the load protocol guidelines recommended by ACI ITG 5.1 document (ACI ITG 5.1 2007) on validating testing of special precast concrete walls for seismic regions. The wall system was subjected to a maximum lateral drift of ±3.5%, with three full reversed

cycles at each target drift up to 3%. Three load cycles were used at each target displacement to ensure the stability of the force-displacement response at that displacement. During testing, the applied lateral displacement to the wall system was controlled using an external temposonic displacement gages located at the loading height (i.e., 20 ft (6.1 m) from the base of the wall).

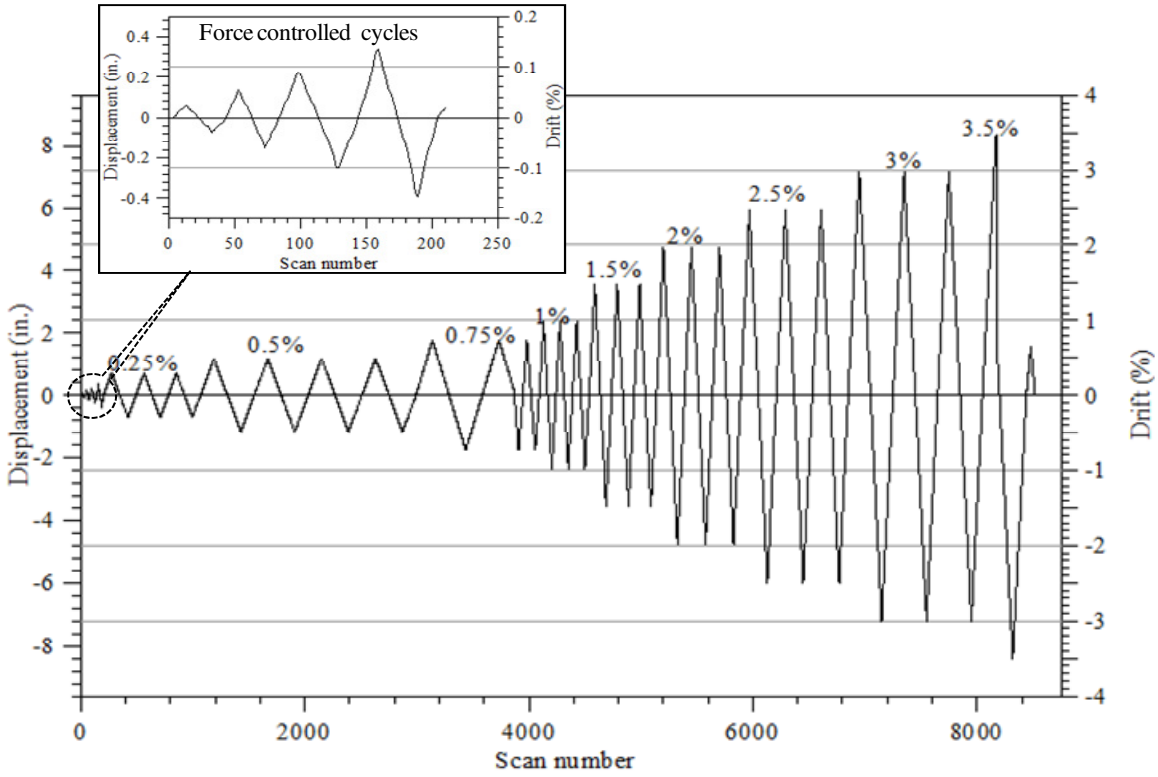

Figure 4.35 The cyclic displacement history used for the PreWEC system testing.

4.6 Experimental Observations and Results

This section presents the observations and detailed experimental results from the PreWEC-1 testing. The results include global lateral response of the wall system, connector deformations at different heights, post-tensioning stress variations, wall uplifts, information about the wall panel contact lengths and strain gauge responses.

4.6.1 Test Observations

PreWEC-1 performed very well with negligible damage to the wall panel and no damage to end columns. The damage to the wall was limited to spalling of cover concrete

over a 10 in. (25 cm) depth at the bottom corners. The channel placed at the bottom of the wall experienced some bending and its impact on the response of the overall system behavior needed to be further investigated in future tests. The O-connectors behaved as expected providing sufficient shear transfer and energy dissipation during the reverse cyclic testing. The O-connectors experienced progressive fracture started at lateral drift ± 3% and eventually failing during 3.5% drift cycles. Even after the connector was fractured, it was able to transmit the forces as the connector ends came into full contact with each other. Consequently, the force-displacement behavior of the PreWEC-1 was not affected by the fracture of connectors. Figure 4.36 shows the damage state of the PreWEC specimen and RWN at 3% drift.

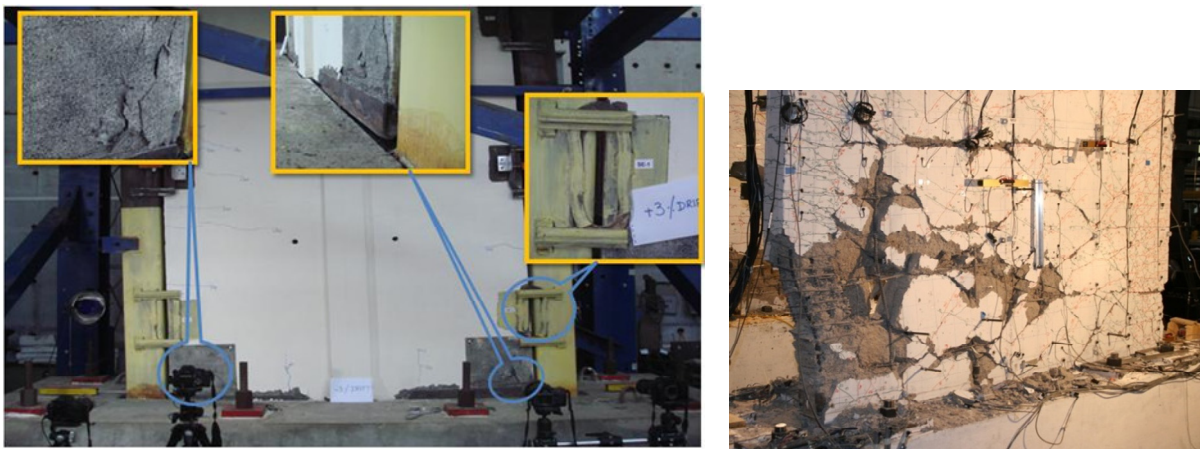

a) PreWEC condition at 3% drift

b) RWN condition at 3% drift

Figure 4.36 Condition of the PreWEC system and RWN at 3% drift

4.6.2 Lateral Load response

The lateral load response of PreWEC-1 system is presented by plotting the base shear as a function of the lateral drift, as shown in Figure 4.37a. The cyclic force-displacement hysteretic response of PreWEC-1 was stable. There was no significant strength degradation between the successive cycles imposed at any drift. The PreWEC test unit performed exceptionally well compared to the traditional reinforced concrete walls. The base shear capacity of the PreWEC-1 in the push and pull directions was 115.67 kips (514.2 kN) and -119.3 kips (530.3 kN) respectively. The base shear capacity of the PreWEC system is nearly 12%-15% more than that of the reference cast-in-place concrete wall (RWN) (see Figure

4.37b). Note that the force-displacement response included in Figure 4.37b for RWN assumes that the boundary elements at both ends of the wall contained #5 and #6 longitudinal bars, resulting in identical response for the positive and negative displacement directions.

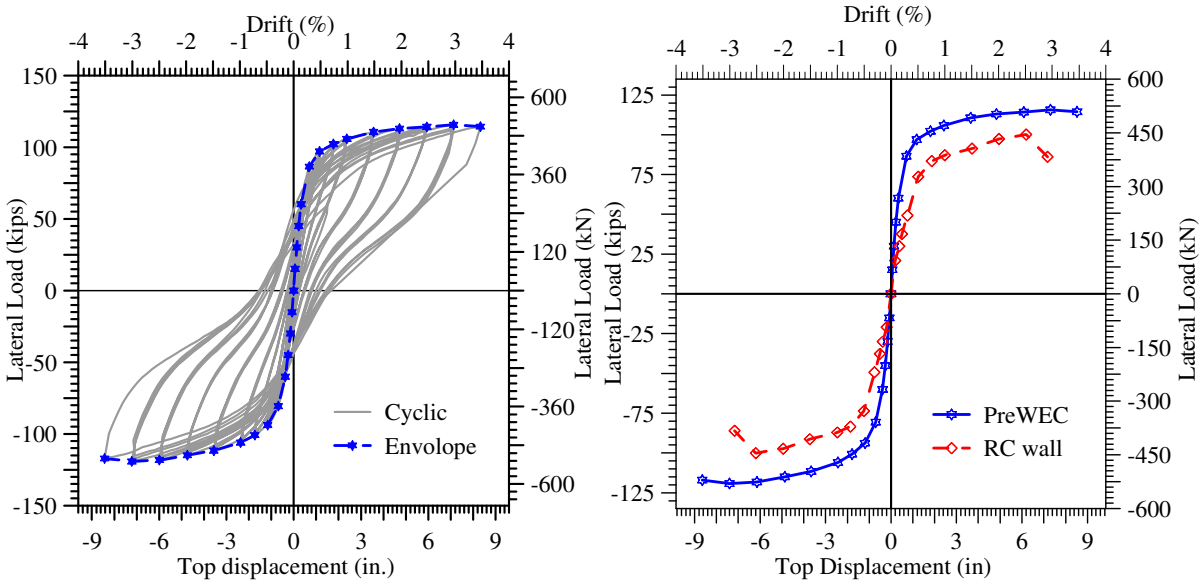

a) PreWEC-1 response

b) Comparison of PreWEC-1 and RWN response envelopes

Figure 4.37 Measured force-displacement response of PreWEC-1

4.6.3 Prestressing steel response

The post-tensioning tendon in the wall panel was at a stress of $0.67f_{pu}$ at the beginning of the test, resulting in a total prestress force of 454.157 kips (2019.18 kN) acting at the center of the wall. The prestressing steel in the north and south column were at a stress level of $0.662f_{pu}$ and $0.677f_{pu}$ after losses, anchoring the columns to the foundations with a force of 112.07 kips (498.3 kN) and 114.68 kips (509.9 kN) respectively.

Figure 4.38 shows the variation of post-tensioning tendon forces in the wall panel and the north and south columns as a function of lateral drift. Figure 4.38a shows that the increase in the wall post-tensioning force is linearly proportional to the top displacement until yielding of the tendon occurred. The post-tensioning tendon in the wall panel experienced yielding after a lateral drift of 2% was exceeded, resulting in small loss of initial prestress force and a reduction to the reloading stiffness of the system. The prestress loss in the wall panel was nearly 8.5% after unloading from the ±3% drift. Prestress losses of 4 to

5% were observed in the column post-tensioning steel at 1% drift, as shown in Figure 4.38b and Figure 4.38c. This observation indicates a possibility of overstressing one of the three strands in the columns, leading to yielding before 2% drift. However, this did not affect the overall behavior of the wall system, as the contribution of the columns to the lateral strength of the system is not significant.

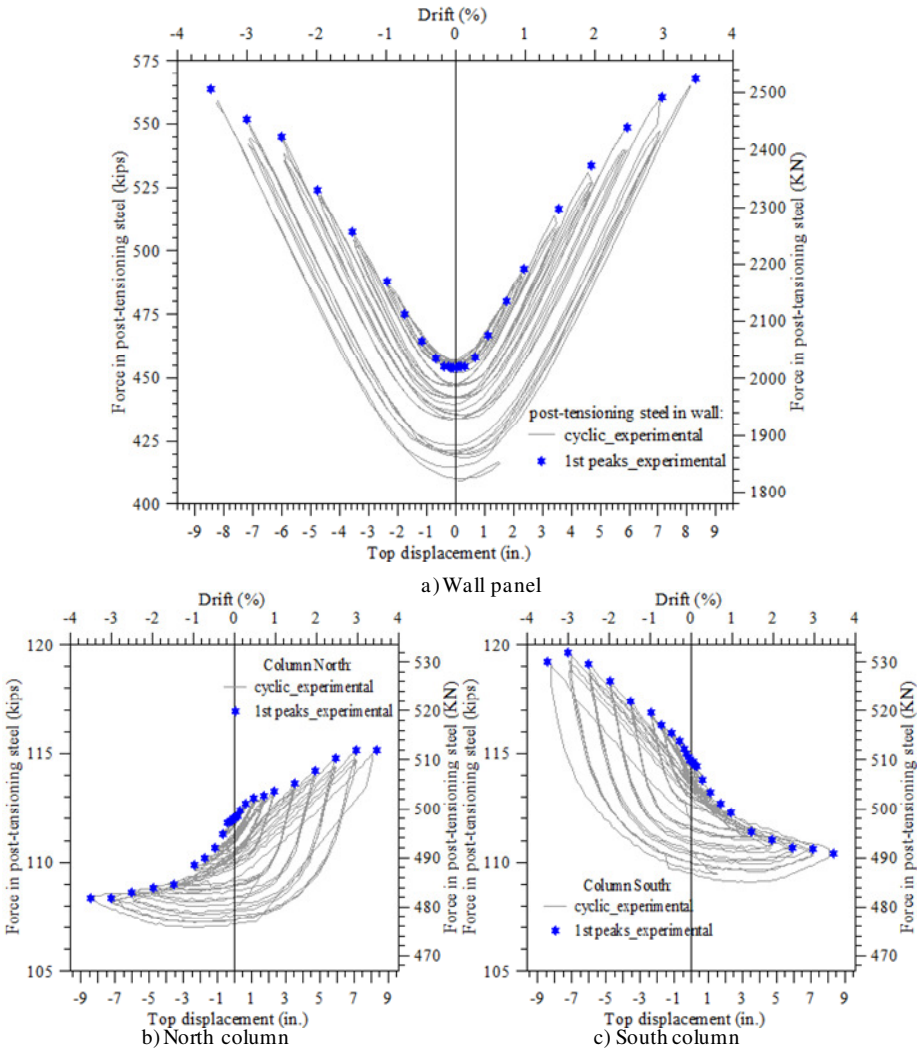

Figure 4.38 Variation of forces in the post-tensioning tendon in the wall panel and the north and south columns

4.6.4 Wall panel and Column Uplift

As expected, the flexural deformation of the wall system was concentrated at the wall-to-foundation interface. Displacement transducers (LVDTs) were placed at the wall and column bases as shown in Figure 4.30. The cyclic displacements and displacement at first peaks measured by these LVDT's and are shown in Figure 4.39 and Figure 4.40 for the wall and end columns respectively. Figure 4.39 shows that the maximum uplift occurred at the end of the wall (WUN5 and WUS5) was 2 in. (50mm) which is same as the maximum displacement demand on the O-connector. Additionally, the profiles of the uplift along the wall length for various drift levels in the push and pull direction are presented in Figure 4.41 and Figure 4.42. The contact length for the wall panel was estimated based on the uplift along wall length and Figure 4.43 shows its variation with top lateral displacement of the wall. It is clear from the Figure 4.43 that the contact length rapidly decreases at the beginning of the loading. The variation of the contact length is not significant after 0.5% drift. This supports the previous observations made by Aaleti and Sritharan (2009) in case of jointed wall systems.

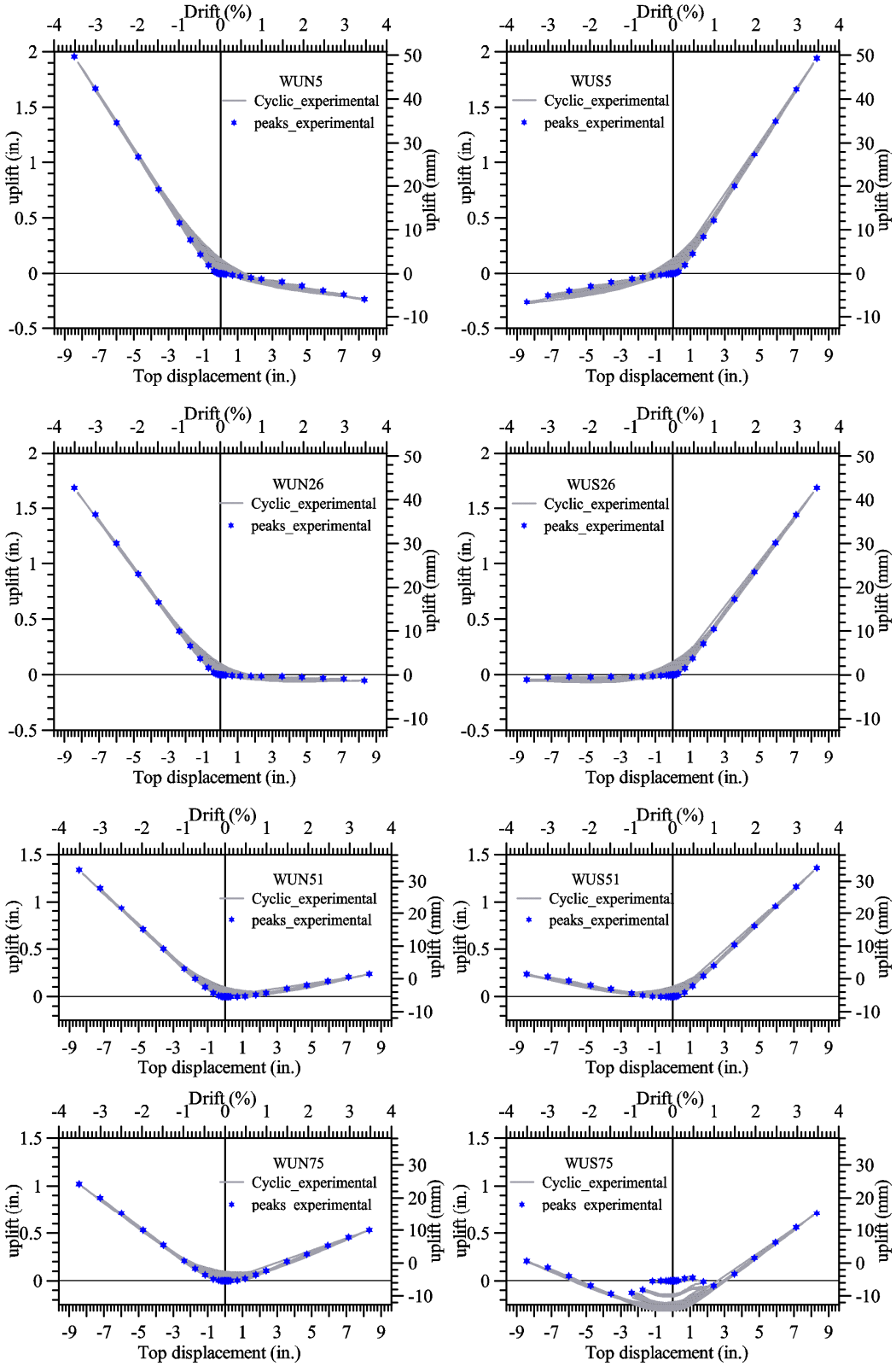

Figure 4.39 Variation of wall panel uplifts along the length with lateral drift

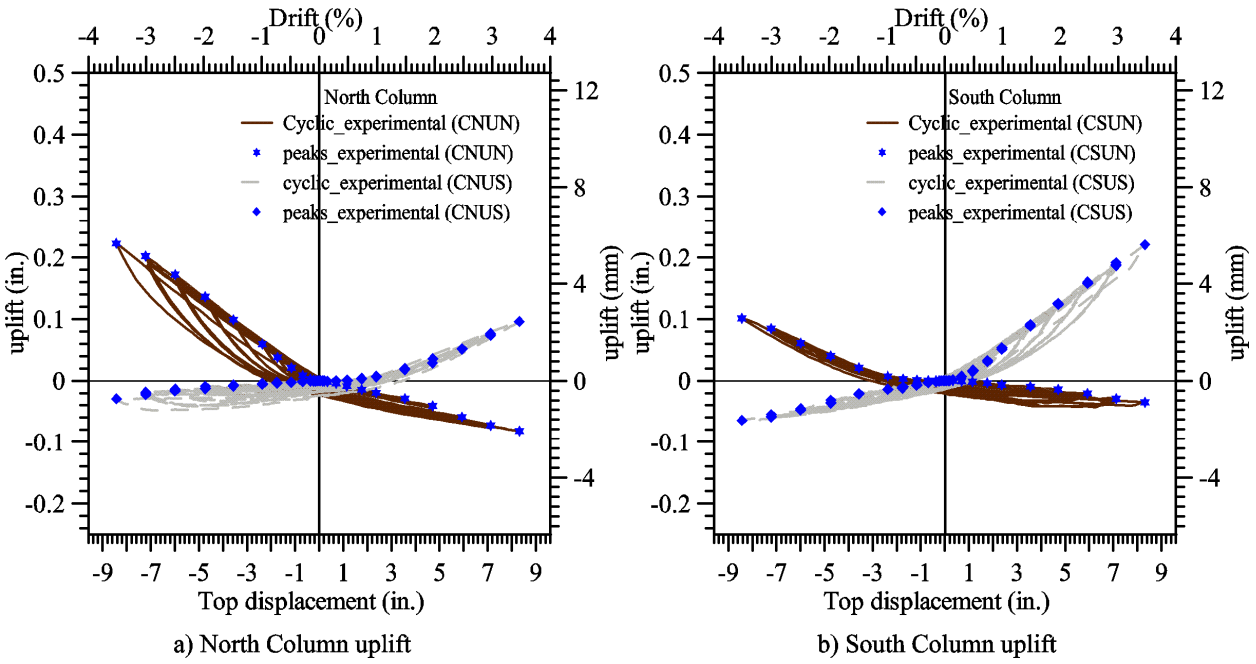

Figure 4.40 End column uplifts on north and south faces as a function of lateral drift

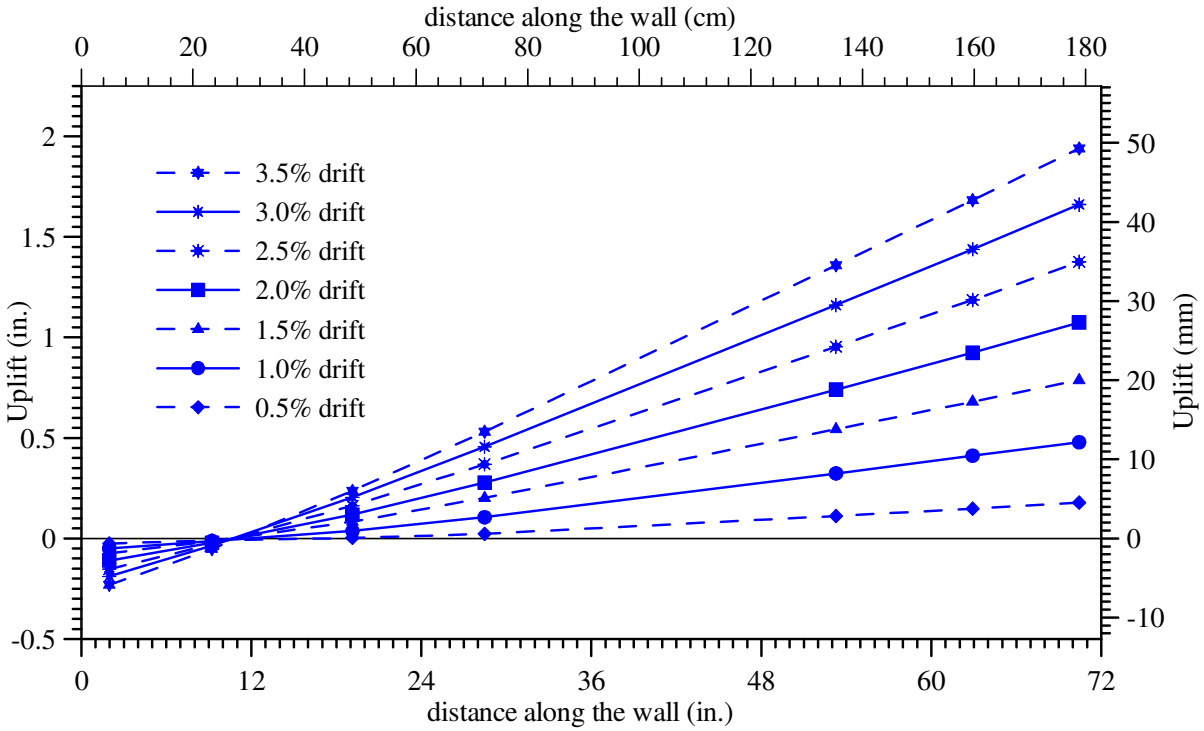

Figure 4.41 The uplift along the wall length at various drift levels in the positive direction of loading

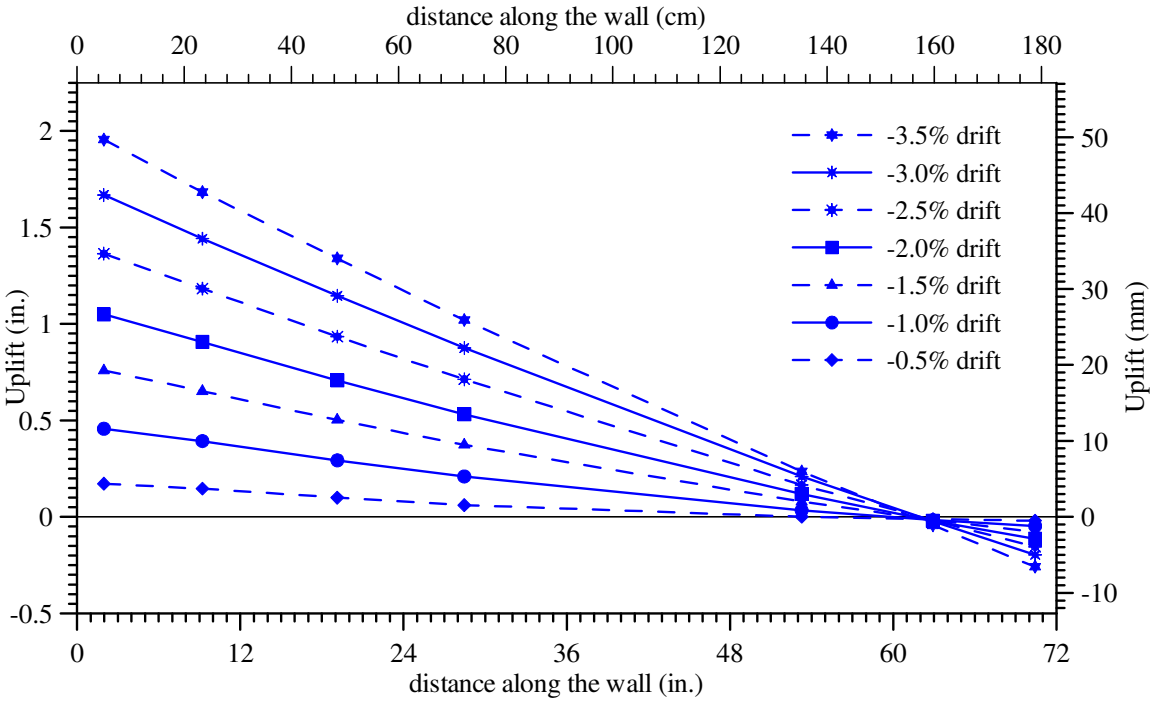

Figure 4.42 The uplift along the wall length at various drift levels in the negative direction of loading

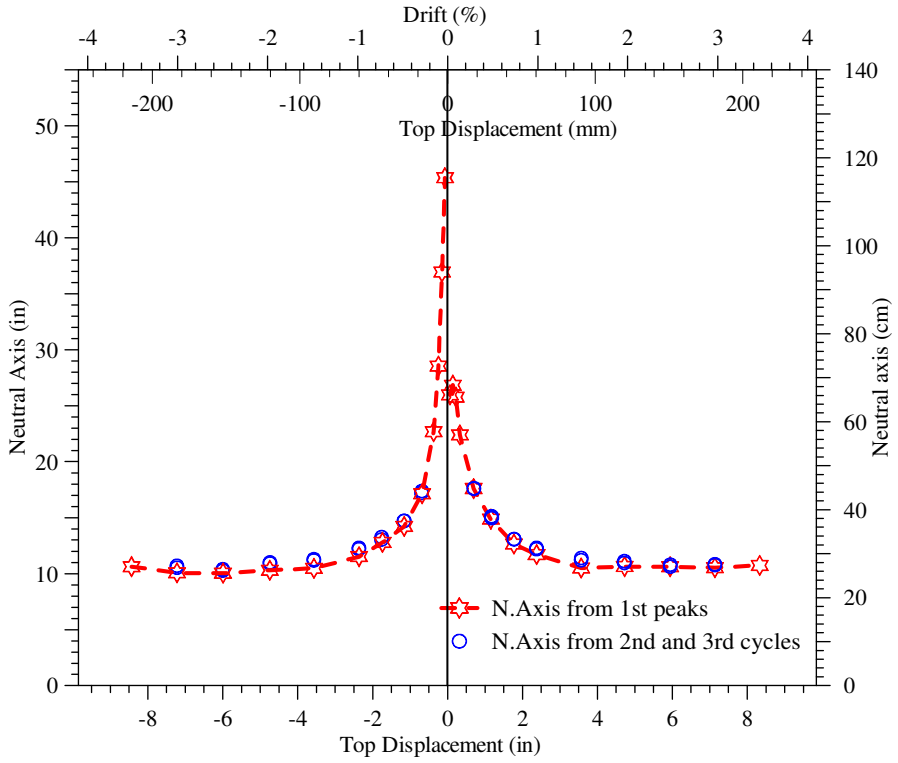

Figure 4.43 Variation of the wall panel contact length with lateral drift

4.6.5 Connector Response

The O-connectors performed as expected with a stable response until cracking occurred in the critical regions of the connectors during the third 3% drift cycle. The condition of the bottom most connectors (north and south side) at various drift levels is shown in Figure 4.44. As shown in Figure 4.45, three of the connectors at the top of the wall system underwent a progressive fracture starting at ± 3.0% drift with eventual failure occurring during 3.5% drift cycles. It is important to note that even after fracture, the connectors were able to transfer forces when ends of the connectors came in contact with each together. As a result, the wall system showed almost no strength degradation due to the fracture of the connectors, which can be observed in the system force-displacement response in Figure 4.37a.

On both sides of the wall panel the vertical and horizontal deformations that the O-connectors experienced along the vertical joint were measured using two LVDTs near the bottom connector located at 58 in. (1.47 m) from top of the base block and at the top most connector located at 172 in. (1.83 m) from top of the base block. Figure 4.31 shows the locations of the LVDTs used for measuring vertical and horizontal displacement demands experienced by the O-connectors. The horizontal LVDTs were used to monitor the horizontal separation between the wall and the column along the vertical joint during testing, while the vertical LVDTS measured the connector displacement demands. Figure 4.47 and Figure 4.48 depict the data obtained from the vertical displacement transducers, which shows that the vertical displacement demand imposed on the connectors was almost linearly proportional to the top lateral displacement. Additionally, Figure 4.46 shows a time history plot for one of the bottom connector, which together with Figure 4.47 and Figure 4.48 , indicate that the O-connectors underwent a maximum positive displacement of 2.1 inches (53.4 mm) and a maximum negative displacement of 0.55 inches (13.97 mm) in the direction parallel to the side face of the wall panel. The maximum negative displacement does not match with the maximum uplift estimated for the columns (see Figure 4.40), implying that the compression at the wall toe should be taken into consideration when estimating the connector displacement. The maximum value of wall compression (obtained from uplift measurements of LVDTs WUS5 and WUN5) was found to be 0.27 in. (6.86 mm), which when added to the

maximum column uplift of 0.24 in. (6.1 mm) nearly matches with the maximum measured negative displacement of 0.55 in. (13.97 mm). The horizontal LVDTs measured a horizontal movement of 0.09 in. (2.2 mm) and 0.17 in. (4.38 mm) between the wall panel and the end columns at bottom and top connector level respectively, which did not seem to have influence the connector behavior.

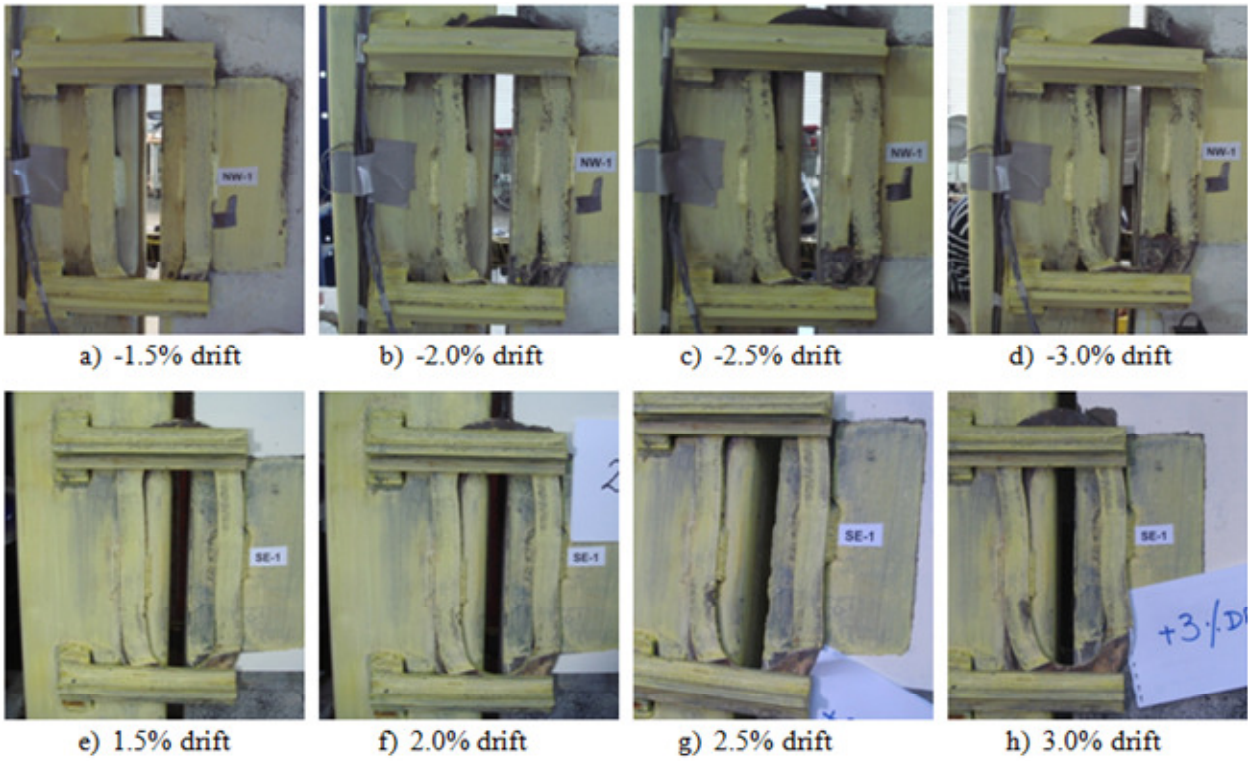

Figure 4.44 Condition of the bottom O-connector at various drift levels.

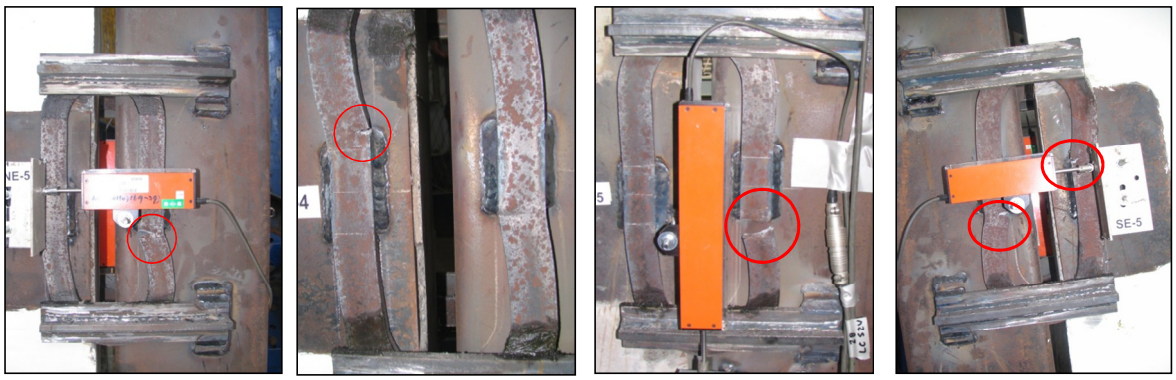

a) Crack initiation at critical regions of connector at 3% drift

b) Fractured connectors at 3.5% drift

Figure 4.45 Progressive fracture of a top O-connector observed during the 3% and 3.5% drift

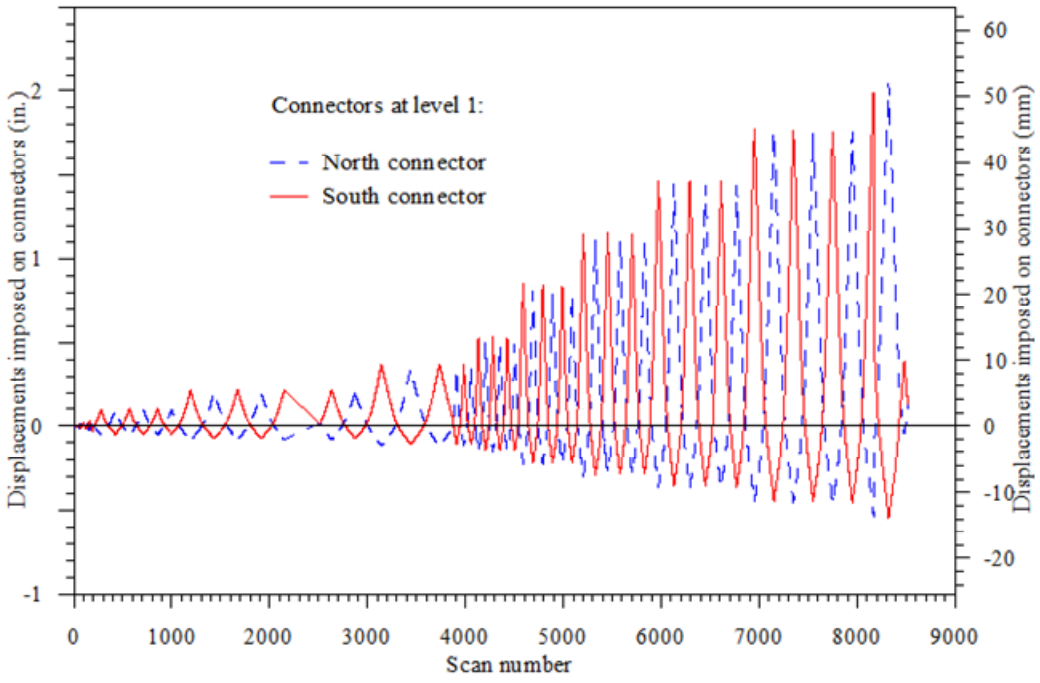

Figure 4.46 Vertical displacement demand recorded for the connector near the base in the direction parallel to the wall side face as a function of scan number

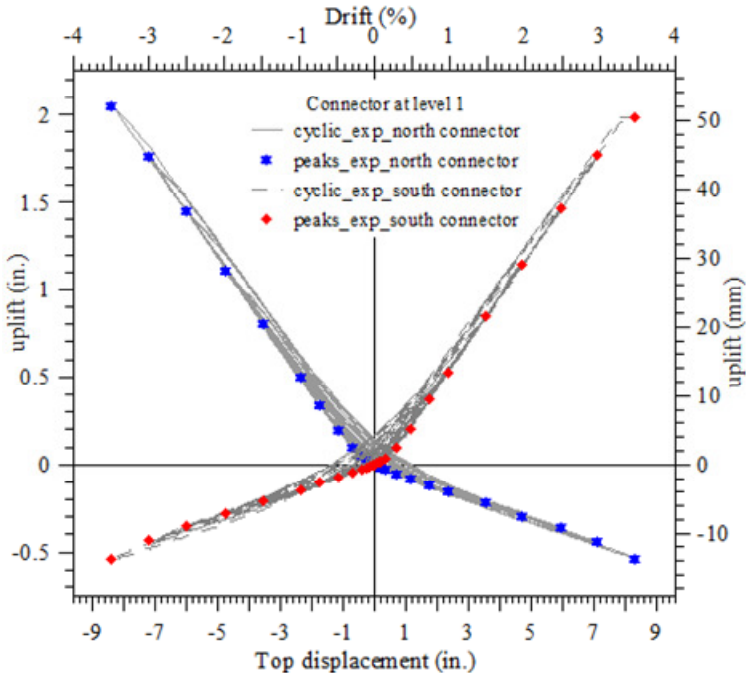

Figure 4.47 Vertical displacement demand recorded for the connector near the base in the direction parallel to the wall side face

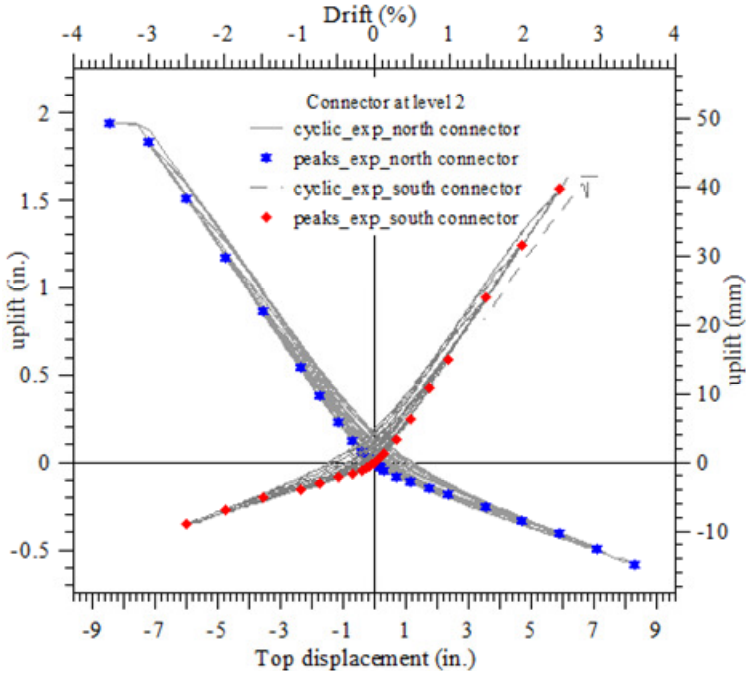

Figure 4.48 Vertical displacement demand recorded for the connector near the top in the direction parallel to the wall side face

4.6.6 Strain in the Horizontal Straps

The wall panel was secured with three pairs of 1-in. thick, 2-in. wide Grade 60 steel plates, with an objective of providing resistance if the wall panel was to move away from the columns in the direction parallel to the direction of loading. Gauges mounted on the outside surfaces of the straps monitored the strain demands, which did not exceed 160 με. This corresponds to a maximum force of 4.64 kips (19.6 kN) in each strap.

4.6.7 Strain in the Confinement Reinforcement

Strain gauges were mounted to the confinement reinforcement placed at the wall ends to estimate the required confinement steel area and the height over which confinement is needed. The details of the hoop strain gauges locations are provided in Section 4.3.

Figure 4.49 and Figure 4.50 show that the hoop strains of gauges located at 5.9 in. and 13 in. above the wall base. Figure 4.49 indicates that the strains imposed on the confinement reinforcement did not cause yielding of this reinforcement. This finding is consistent with the test observations in that no damage to the confinement reinforcement or significant spalling of cover concrete in this region was observed during the test. The strain demand on the hoop reinforcement at 13 in. (see Figure 4.50) indicates that the hoop reinforcement did not experience yielding. This observation implies that the amount of confinement reinforcement required at this level could be reduced

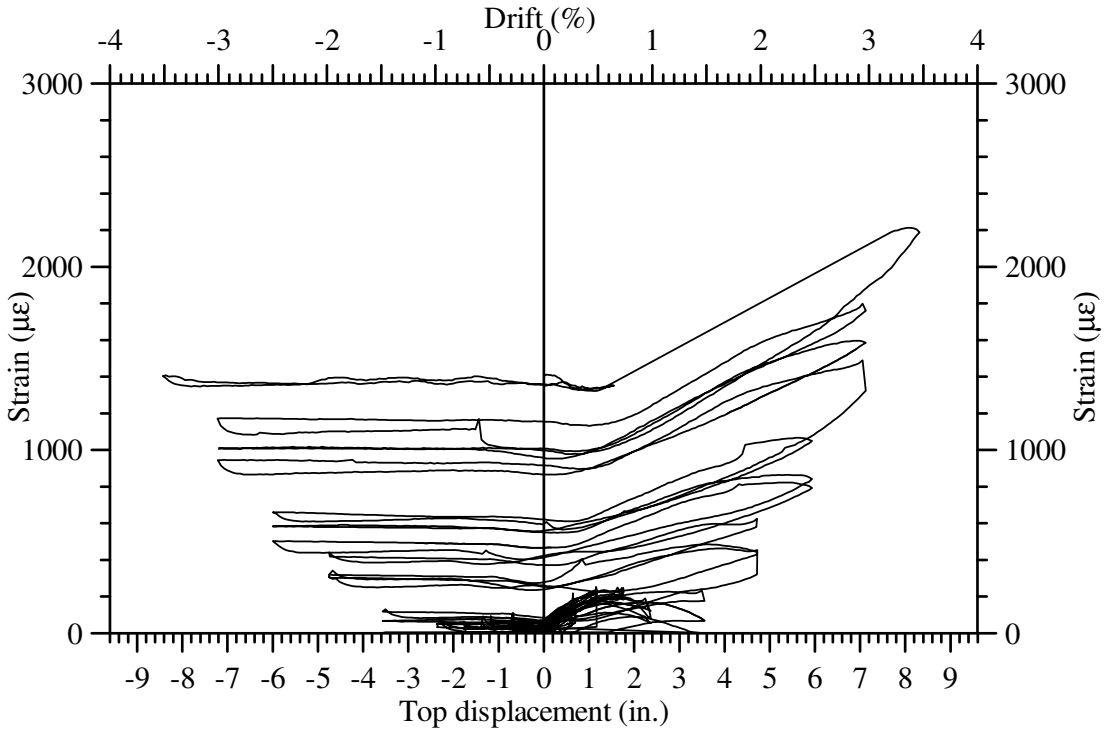

Figure 4.49 Variation of strains recorded by a confinement hoop gauge (H_1) located at 5.9 in. from the base of the wall panel .

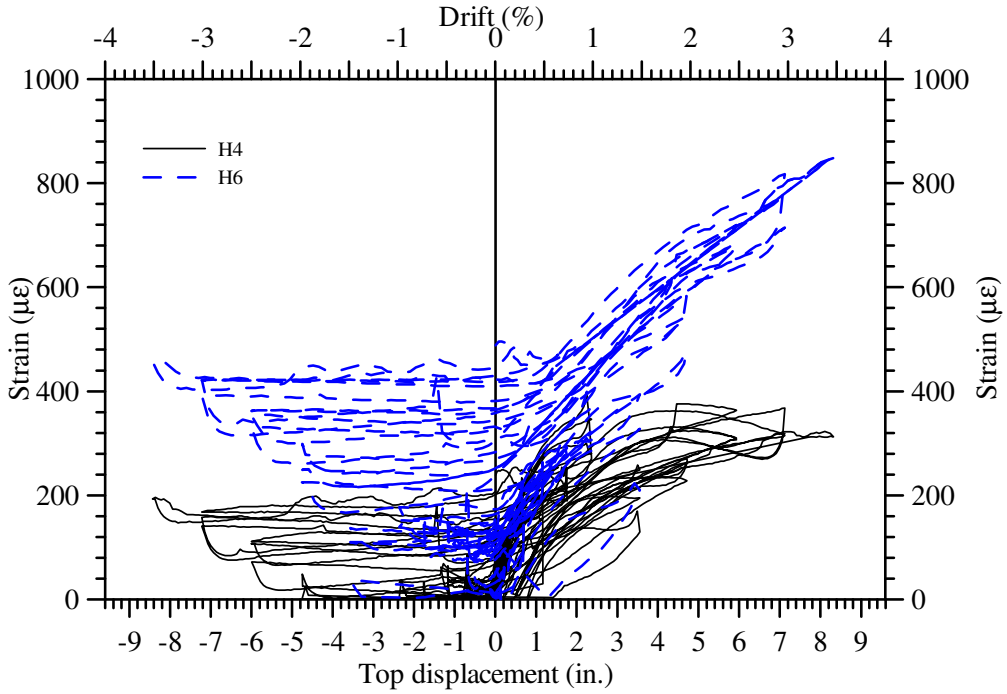

Figure 4.50 Variation of strains recorded by a confinement hoop gauges (H_4 and H_6) located at 13 in. from the base of the wall panel

4.6.8 Confined Concrete Strains

Concrete strain gauges were placed in the confined concrete regions of the wall panel at different levels along the wall height to estimate the strain demand in the concrete. The distribution of the gauges along the height of the wall provides an estimate for the required height of the confinement region. The location and the distribution of the concrete gauges in the wall panel are shown in Figure 4.32.

Figure 4.51 shows the strain demand in the confined concrete at 5 to 6 in. (12.6 cm to 15.1 cm) from the base of the wall. The strain demand at 15 in. (38 cm) and 33 in. (83.8 cm) along the height of the wall in the north and south confined regions is shown in Figure 4.52. This figure indicates that the concrete strain demand at 15 in. (38 cm) above the base of the wall was less than 0.003 in./in. up to 3% lateral drift. The strain demand at 33 inches (83.8 cm) from the wall base is around 0.0012 in./in (see Conc_N4 and Conc_S4 in Figure 4.52) indicating no need for confinement reinforcement in this region.

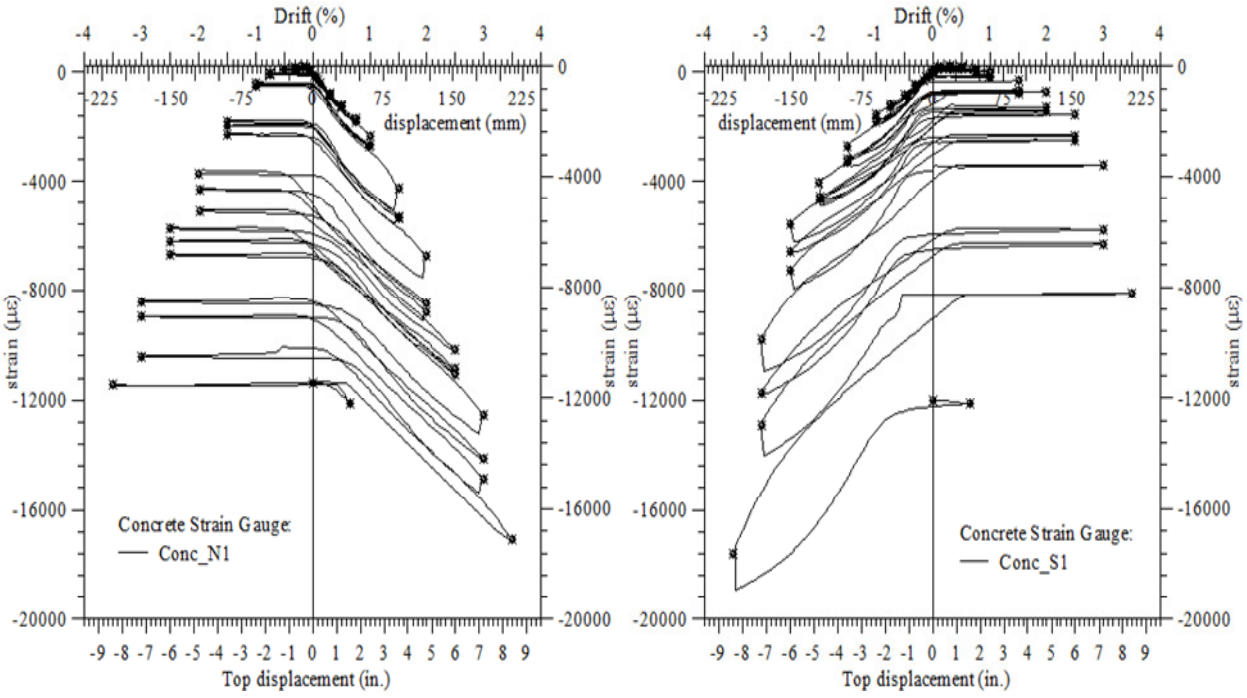

Figure 4.51 Recorded confinement strain demand in wall toe regions at 5 in. to 6 in. from wall panel base as a function of top displacement

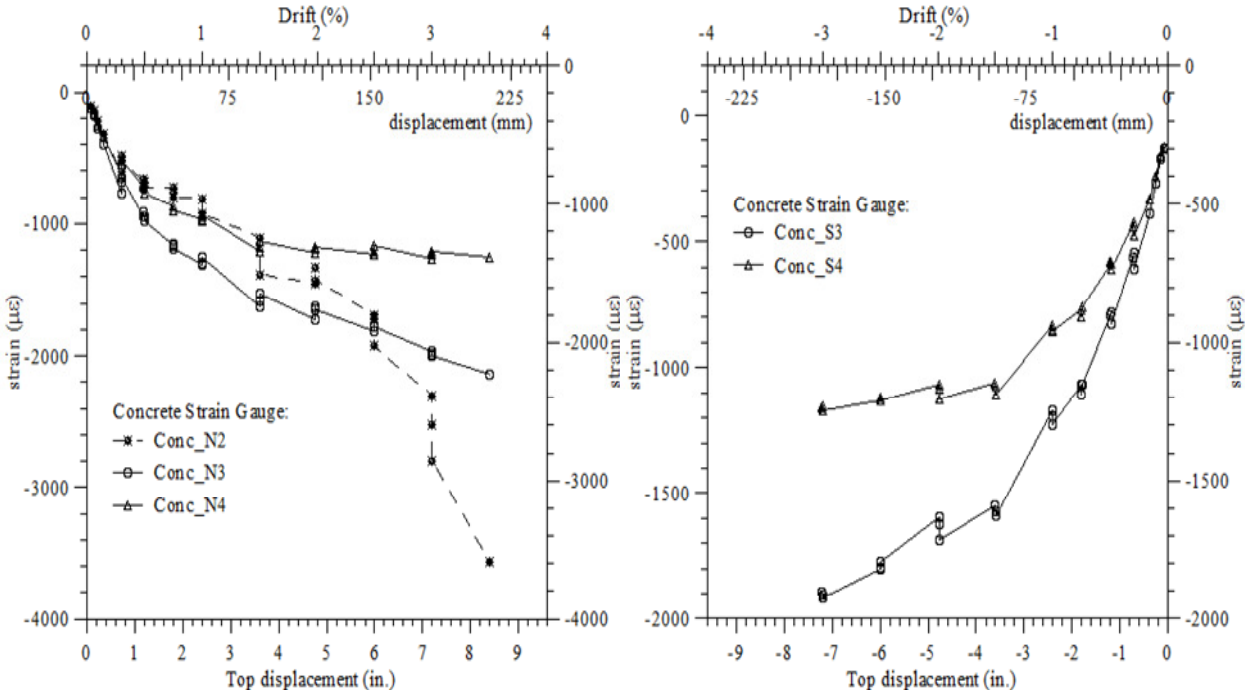

Figure 4.52 Recorded confinement strain demand at 15 and 33 inches from the wall base as a function of top displacement

4.6.9 Energy dissipation capacity

Using the force-displacement response recorded during the test, the amount of energy dissipated by the PreWEC-1 system was quantified in terms of equivalent viscous damping using Eqn(4.1). The majority of the energy dissipation for the wall system was provided by inelastic deformation experienced by the O-connectors. Figure 4.53 shows an example of the experimental hysteresis loop obtained for PreWEC-1 system at +2% drift, which was used in estimating the equivalent viscous damping.

$$\varsigma_{eq} = \frac{2}{\pi}\frac{A_{loop}}{A_{rect}} \tag{4.1}$$

where, A_{loop} is the area enclosed by a hysteresis loop at a given drift, and

A_{rect} is the area of the rectangle circumscribing the hysteresis loop.

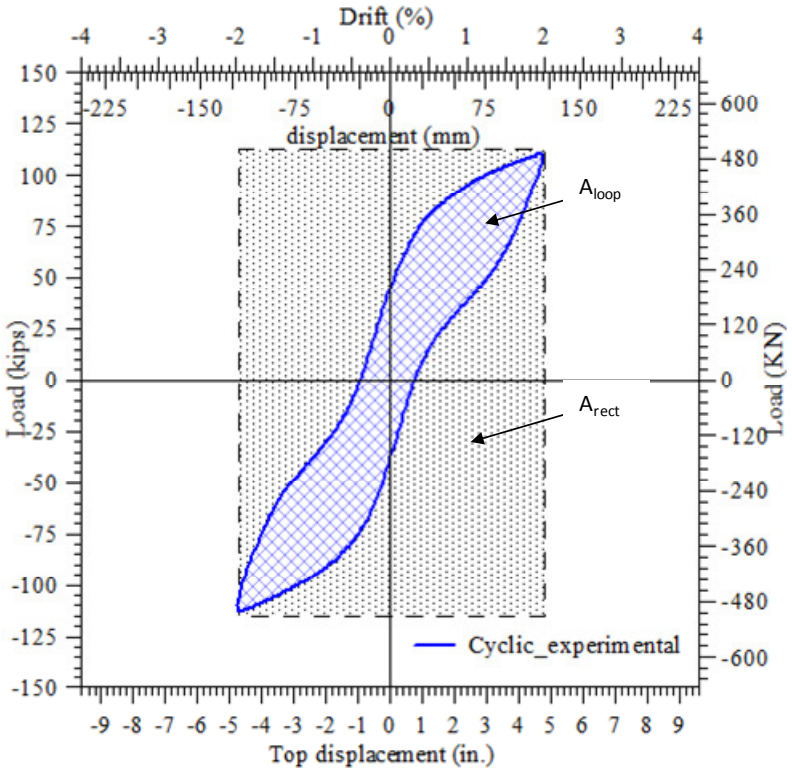

Figure 4.53 Hysteresis loop of the PreWEC system at 2% drift

ACI ITG 5.1 document on validation testing of unbonded precast wall systems uses a relative energy dissipation ratio (β) to characterize the energy dissipation capability of special unbonded precast wall systems. The ratio β is defined as the ratio between the energy dissipated by the specimen during the loading cycle at a particular drift level (i.e., A_{loop}), and the energy that would be dissipated by an equivalent elasto-plastic system. Accordingly β is defined by Eqn. (4.2).

$$\beta = \frac{A_{loop}}{A_{rect}} \tag{4.2}$$

Figure 4.54 shows the calculated values for the equivalent viscous damping and the relative energy dissipation ratio of PreWEC-1 for drifts ranging between 0.25% and 3.5%. As can be seen, PreWEC specimen exhibited excellent relative energy dissipation ratios throughout the test, with β values ranging from 5% at low drift levels to nearly 27% at 3.0% drift. It is worth mentioning that a β value of 12.5% is specified in the ACI-ITG 5.1 document (ACI ITG 5.1

2007) as the minimum acceptable value behavior of unbonded post-tensioned precast wall systems for seismic loading. In terms of equivalent viscous damping, PreWEC-1 exhibited 3 to 17% of damping.

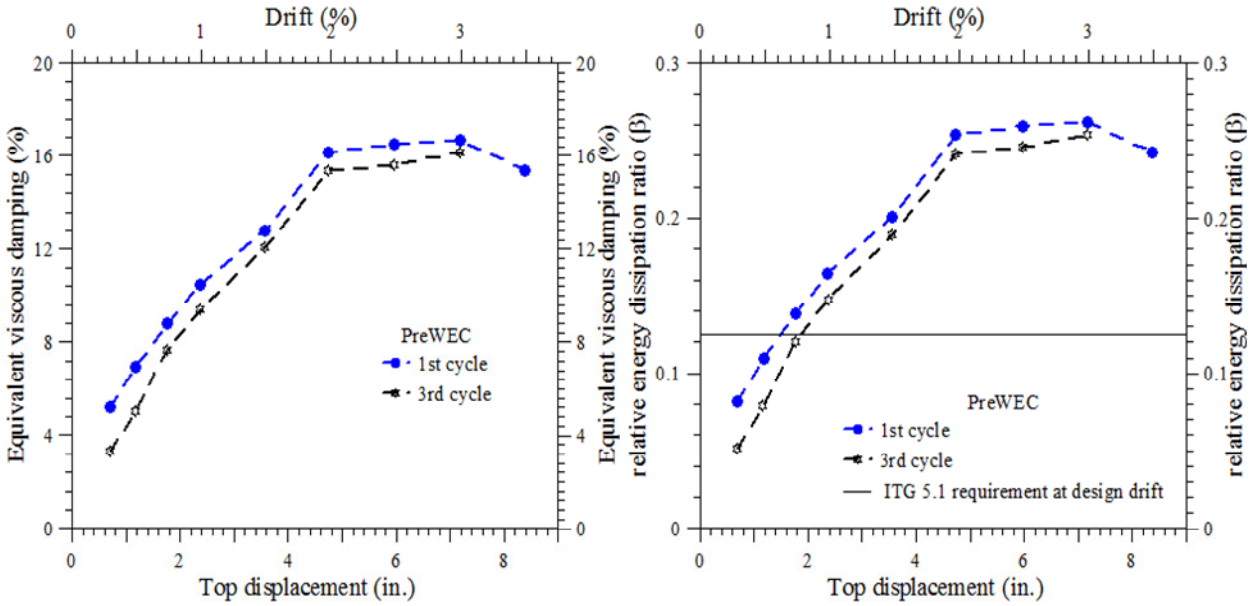

a) Equivalent viscous damping b) Relative energy dissipation ratio

Figure 4.54 Measured equivalent viscous damping and relative energy dissipation ratio for PreWEC-1

4.6.10 Code Validation of PreWEC-1 Behavior

This section examines the PreWEC-1 performance against the acceptance criteria established for special unbonded pos-tensioned precast walls, ACI-ITG 5.1 (2007). The PreWEC system can be deemed to have performed satisfactorily when all of the following criteria of ITG-5.1document are met for both directions of in-plane response, making the application of this system viable in construction practice.

Criteria-1*: "In cycling up to the drift level given by Sec.7.4 through 7.6, fracture of reinforcement or coupling elements, or other significant strength degradation, shall not occur. For a given direction, peak lateral strength during any cycle of testing to increasing displacement shall not be less than 0.8 times* E_{max} *for that direction."*

From the experimental response and observations presented in Section 4.6.2 Lateral Load response, it is clear that the lateral force did not decrease as the lateral drift increased. The maximum drift level required by ITG for the PreWEC specimen is calculated using section 7.4 of ITG 5.1 document and is equal to 3%. As presented in Section 4.6.5 Connector Response, coupling elements (O-connectors) began to fracture only at 3% drift, which is same as the maximum drift level required by ITG 5.1.

Criteria-2: *"For cycling at the given drift level for which acceptance is sought in accordance with Sec.7.4, 7.5 or 7.6, as applicable, the parameters describing the third complete cycle shall have satisfied the following:*

1. the relative energy dissipation ratio shall be not less than 1/8; and

2. the secant stiffness between drift ratios of -1/10 and +1/10 of the maximum applied drift shall be not less than 0.10 times the stiffness for the initial drift ratio specified in Sec. 7.3.

3. the force in any vertical unbonded tendon in any wall shall not exceed 0.95 times the measured yield strength of the prestressing steel of that tendon at 1% elongation.

4. the maximum relative displacement between the base of a wall and the adjacent foundation (shear-slip) shall not exceed 0.06 in (1.5 mm)."

From Figure 4.54, it can be clearly seen that the relative energy dissipation ratio of the PreWEC system for the 3rd complete cycle is greater than 0.125 for drifts greater than 0.75%. Thus, the PreWEC-1 system satisfied this requirement. Figure 4.55 shows the secant stiffness between drift ratios of -1/10 and +1/10 of the maximum applied drifts of 2% and 3%, which are 0.21 and 0.11 times the initial stiffness of the PreWEC system. The measured force of the post-tensioning tendons in the wall panel at 2% design drift is less than 95% of the measured yield force of the prestressing steel (see Figure 4.38). The measured maximum relative displacement between the base of a wall and the adjacent foundation (shear-slip) was 0.044 in. (1.13 mm), which is less than the acceptable value of 0.06 in. (1.5 mm).

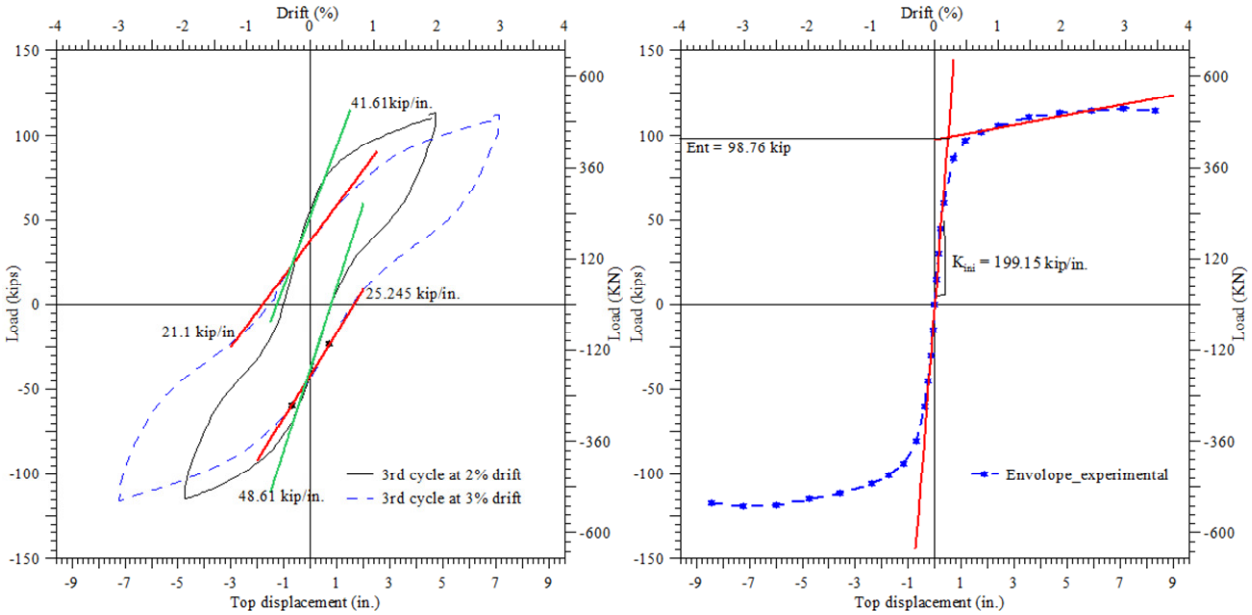

a) Secant stiffness b) Initial stiffness

Figure 4.55 Secant stiffness and initial stiffness at 2% and 3% drifts for the PreWEC-1

In summary, the PreWEC-1 satisfied the requirements of the ITG 5.1 document for good performance. However, ITG 5.1 requires at least two specimens are to be tested to validate the performance requirements. So, in order to implement the PreWEC system in practice, another test should be conducted.

4.7 Analytical Investigation

4.7.1 O-connector

This section presents an analytical investigation that was undertaken to theoretically characterize the force-displacement response envelope of the O-connector. The fiber based beam-column element available in OpenSees (OpenSees 2007) was used for this purpose. Taking advantage of the symmetry, only the top half portion of the O-connector was modeled as shown in Figure 4.56. The O-connector was modeled using 2-D nonlinear forced-based beam-column elements located along the center line. The circular portion of the connector was discretized into twelve segments as shown in Figure 4.56. The weld at the center of the connector was assumed to act as a rigid connection and thus modeled with a node restrained in all degrees of freedom direction. A single force-based beam-column element with 4 integration points was used to model the vertical legs of the connector, whereas, the circular portion of the connector was modeled using twelve force-based beam-column elements with three integration points for each element. The location of integration points followed the Gauss-Lobotto scheme. For example, in an element with four integration points, the integration points are located at both ends of the element (-1.0 and 1.0 in an isoparametric formulation), and at points located at a distance of 0.2764 times the length of the element from both ends (-0.4472, 0.4472) of the element.

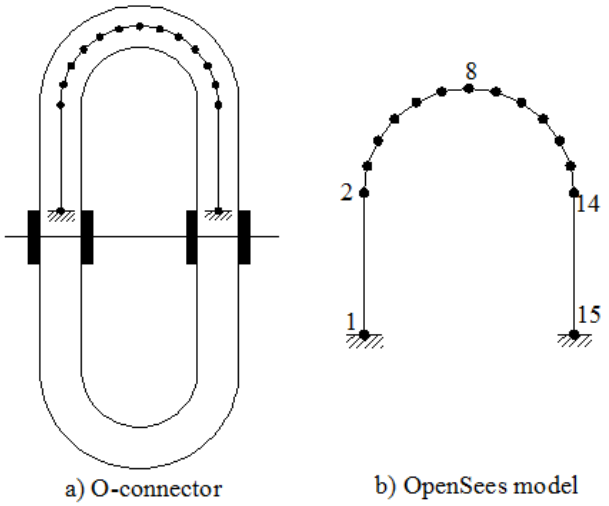

Figure 4.56 A fiber based beam-column model of the O-connector.

A fiber section was used to represent the cross section of the connector. The connector cross section was discretized using fibers with approximate cross section of 0.025 in. x 0.05 in. The stress-strain behavior of the connector material was modeled using a bilinear curve (i.e., *Steel02* in OpenSees). The O-connector was monotonically loaded by applying the measured maximum peak displacement from the O-connector test to node 15 in the vertical direction.

The measured envelope responses of the NCREE and ISU O-connectors and that calculated for the OpenSEES model are shown in Figure 4.57 and Figure 4.58 respectively. From the figures, it is clear that the OpenSEES model underpredicted the strength of the O-connector tested at NCREE by an average of 15%. The initial stiffness of the ISU O-connector was overestimated by the analytical model. In conclusion, a simple beam-column element can be used to estimate the force-displacement characteristics of the O-connector.

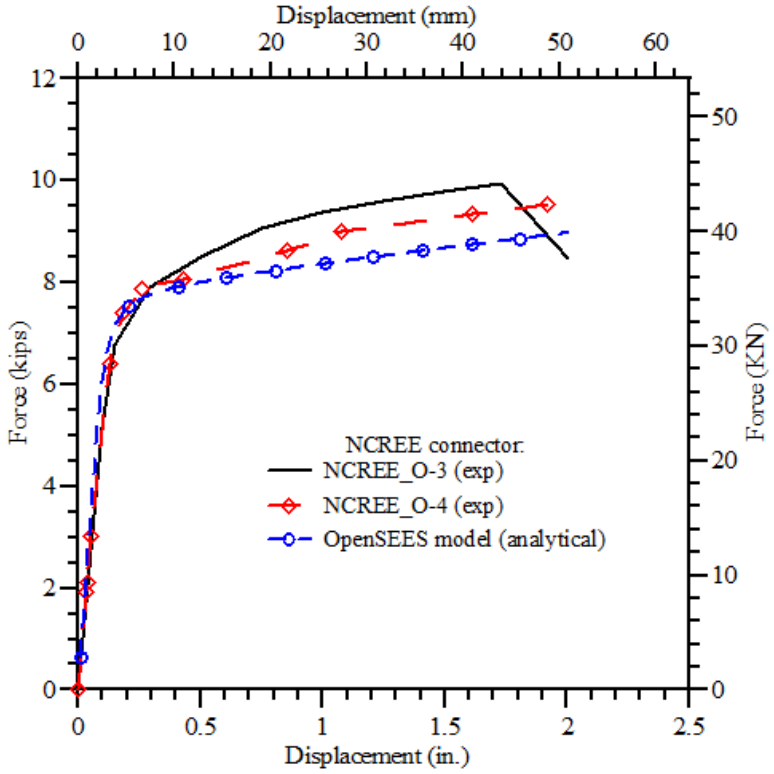

Figure 4.57 Comparison of the experimental and calculated force-displacement response of the O-connector tested at NCREE.

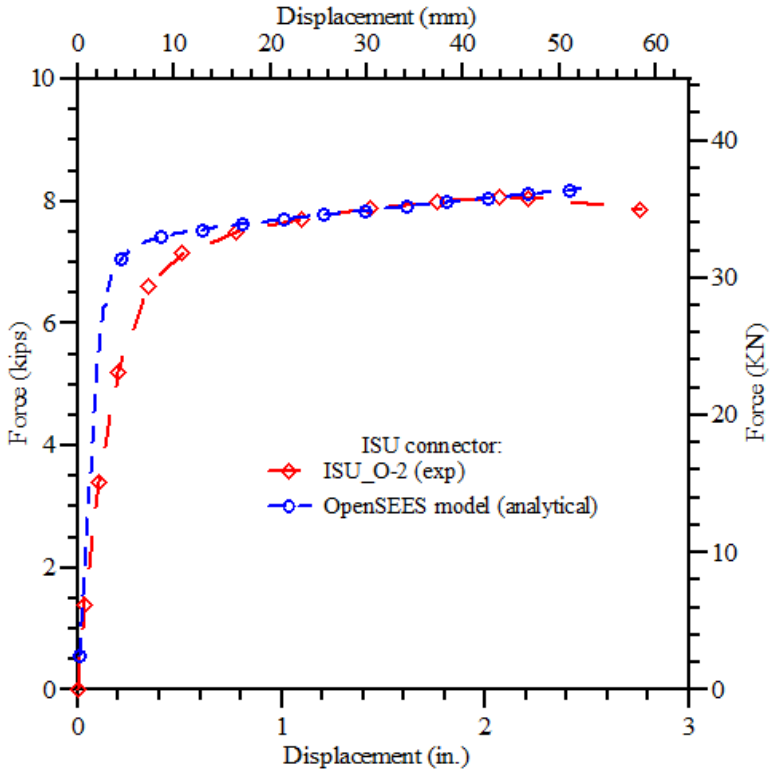

Figure 4.58 Comparison of the experimental and calculated force-displacement response of the O-connector tested at ISU.

4.7.2 PreWEC System

The conventional section analysis cannot be applied to PreWEC system because of the nonexistence of strain compatibility condition between the unbonded post-tensioning steel and concrete at the section level. Therefore, to analyze a PreWEC wall system, a non-iterative procedure is presented in this section by establishing a relationship between the neutral axis depth and the base rotation for the wall panel and the columns. This relationship is based on the neutral axis depth estimated at a base rotation of 2% and is found from an iterative procedure involving the force equilibrium and geometric compatibility conditions. Similar to other unbonded precast wall systems (Aaleti and Sritharan, 2009), the following assumptions are made in the analysis procedure:

1. The wall panel and the columns are provided with adequate out-of-plane bracing, preventing them from experiencing torsional and out-of-plane deformations.

2. The dimensions and material properties of the wall panel, columns and connectors are known.
3. The fiber grout pad located at the interface between the wall panel and the foundation does not experience any strength degradation.
4. Wall panel and the columns will undergo the same lateral deformation at every floor level due to the rigid floor assumption.
5. The wall panel base has adequate friction resistance, such that it will not undergo any relative lateral movement at the base with respect to the foundation.
6. The connectors and the post-tension steel anchors remain fully effective for the entire analysis.
7. All vertical joints in a PreWEC wall system have the same number of connectors.

Presented below are descriptions of the different steps of the proposed analysis procedure. It is expected that the analysis of wall system be performed in the following order: 1) wall panel; 2) leading column; and 3) the trailing column.

Step 1: Define Dimensions, Reinforcement Details, and Material Properties

The following variables are defined in this step.

System Dimensions

h_w = height of the wall system,

t_w = thickness of wall,

L_s= total length of the wall system,

l_w = length of wall.

l_{col} = width of column

t_{col} = depth of column

Post-tensioning Steel

Wall panel:

A_{pt} = area of a post-tensioning tendon,

$n_{pt,w}$ = number of post-tensioning tendons in wall,

$h_{u,w}$ = unbonded length of the post-tensioning tendon in wall,

$x_{pt,i}$ = location of the i^{th} post-tension tendon from the rocking edge of the wall,

E_p = modulus of elasticity of the post-tensioning tendon,

$f_{pi,w}$ = initial stress in the post-tensioning tendon in the wall,

f_{py} = yield strength of the post-tensioning tendon, and

$A_{p,w}$ (= $n_{pt,w}\, A_{pt}$) = total area of post-tensioning steel in wall.

Columns:

$n_{pt,\,col}$ = number of post-tensioning tendons in column,

$x_{pt,col}$ = location of the post-tensioning steel from the rocking edge of the column. Note that in a PreWEC system, the post-tensioning steel in columns is located at the center of the columns. Thus, $x_{pt,col} = 0.5 l_{col}$.

$A_{p,col}$ (= $n_{pt,col}\, A_{pt}$) = total area of post-tensioning steel in each column, and

$f_{pi,col}$ = initial stress in the post-tensioning steel in each column.

Confinement Details

A_s = area of confinement steel (which may be taken as $0.5(A_{sx}+A_{sy})$,

A_{sx} = area of confinement steel in the x-direction,

A_{sy} = area of confinement steel in the y-direction,

s = spacing of the confinement reinforcement,

l_{cr} = length of confinement area, and

f_y = yield strength of the mild steel reinforcement.

Concrete Properties

$f_c^{'}$ = compressive strength of unconfined concrete,

$f_g^{'}$ = compressive strength of grout,

$f'_{cc,w}$ = confined concrete strength in wall panel (from Mander's confinement model),

$f'_{cc,col}$ = confined concrete strength in end columns (from Mander's confinement model),

ε_{cc}= concrete strain at $f'_{cc,w}$,

ε_{cu} = strain capacity of confined concrete in wall panel, and

γ_c = concrete density.

Connector Details:

n_{con} = number of connectors per joint,

F_{con} = downward connector force acting on the wall at a given displacement,

F'_{con} = upward connector force acting on the wall at a given displacement, and

Δ_{con} = deformation of the connector parallel to the vertical face of wall.

(Use a reliable force-displacement response of the O-connector to determine the values of F_{con} *and* F'_{con} for a given Δ_{con}, see Figure 4.57.)

Step 2: Decompression point

In this step, the decompression point is established, which defines the beginning of a gap opening at the wall panel base and corresponds to the condition that makes the stress in the extreme concrete fiber furthest from the rocking edge of the wall reaching a value of zero. Assuming a linear strain distribution at the critical section due to the moment induced by the decompression force (F_{dec}), the following equations are used to determine the corresponding moment resistance. The decompression moment capacities of the wall ($M_{dec,w}$) and columns ($M_{dec,col}$) are calculated from the elastic flexural formula $\sigma = \frac{Mc}{I}$ and substituting the values for the neutral axis depth (c) and the moment of inertia (I):

$$M_{dec} = \frac{\sigma I}{c}$$

where σ = stress in the wall panel or columns due to the initial prestress force (F_{pi}) and the

total gravity load (P_D) and I = moment of inertia of wall panel or columns based on the gross section properties. Hence,

$$\sigma_w = \frac{P_{D,w} + \sum_{1}^{n_{pt,w}} f_{pi,w} A_{pt}}{l_w t_w} \text{ and } \sigma_{col} = \frac{P_{D,col} + \sum_{1}^{n_{pt,col}} f_{pi,col} A_{pt}}{l_{col} t_{col}} \tag{4.3}$$

$$I_w = \frac{1}{12} t_w l_w^3 \text{ and } I_{col} = \frac{1}{12} t_{col} l_{col}^3 \tag{4.4}$$

$$c_w = \frac{l_w}{2} \text{ and } c_{col} = \frac{l_{col}}{2} \tag{4.5}$$

Hence, the decompression moment capacity of the wall system (M_{dec}) is given by

$$M_{dec} = M_{dec,w} + \sum M_{dec,col} = \frac{1}{6} l_w \left[P_{D,w} + \sum_{1}^{n_{pt,w}} f_{pi,w} A_{pt} \right] + \frac{1}{3} l_{col} \left[P_{D,col} + \sum_{1}^{n_{pt,col}} f_{pi,col} A_{pt} \right] \tag{4.6}$$

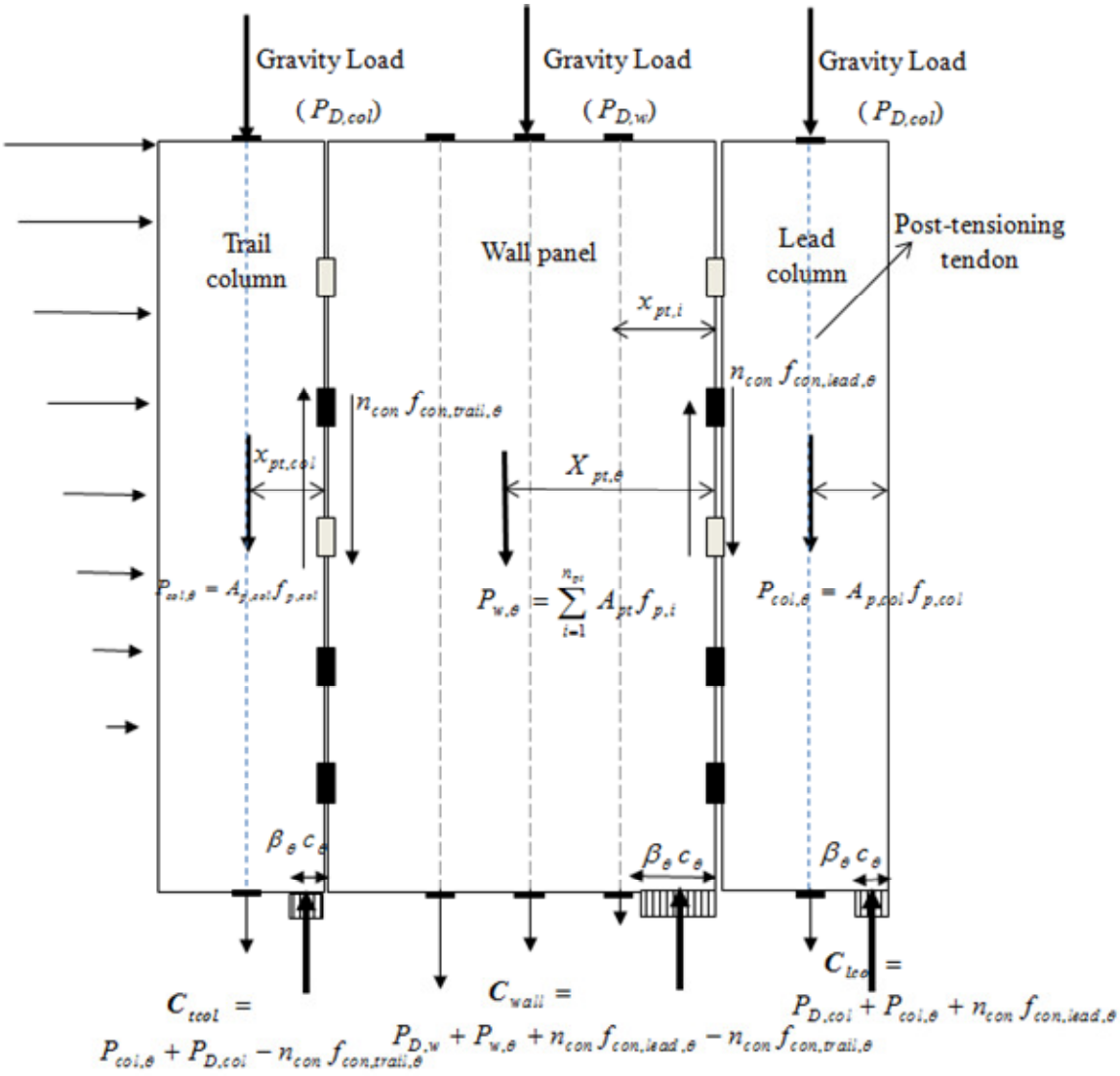

Figure 4.59 Various forces acting on a PreWEC system at base rotation θ.

Step 3: Neutral Axis Depth at 2% Base Rotation

The neutral axis depth that satisfies the vertical direction force equilibrium at the wall system base is found for wall panel and each column through an iteration process with an assumed neutral axis depth as the initial value. The following sub-steps are used in this process.

Estimating the n.axis depth for wall panel:

1. *Assume a neutral axis depth (c) for the wall panel*

2. *Determine the total gravity load on wall ($P_{D,w}$)*

$$P_{D,w} = \gamma\, l_w t_w h_w + w_{floor} l_w \tag{4.7}$$

where w_{floor} is the uniform dead load acting on the wall panel.

3. *Determine the stresses and strains in the post-tensioning tendons*

- The elongation of the i^{th} post-tensioning tendon at 2% base rotation is:

$$\Delta_{p,i} = 0.02 * (x_{pt,i} - c) \tag{4.8}$$

- The strain in this post-tensioning tendon is:

$$\varepsilon_{p,i} = \frac{\Delta_{p,i}}{h_{u,w}} + \frac{f_{pi,w}}{E_p} \tag{4.9}$$

- Determine the corresponding stress in the i^{th} post-tensioning tendon ($f_{p,i}$) from the stress-strain curve of the post-tensioning steel. The above steps should be repeated until stresses in all post-tensioning tendons in the wall panel are obtained.
- The total post-tension force in the wall is, therefore,

$$P_w = \sum_{1}^{n_{pt,w}} f_{p,i} A_{pt} \tag{4.10}$$

4. *Determine the forces in the vertical connectors*

- Estimate the deformation of the connector attached to the trailing column by equating it to the uplift at the wall panel end. Hence,

$$\Delta_{con,trail} = 0.02 * (l_w - c) \tag{4.11}$$

- Calculate the corresponding force in the vertical connector ($f_{con,trail}$) from the force-displacement response of the connector (O-connector, Figure 4.57).
- Estimate the deformation of the connector attached to the leading column by equating it to the sum of penetration of the wall panel at rocking end and the uplift of the leading column. Hence,

$$\Delta_{con,lead} = 0.02 * \left[c + l_{col} - \frac{f_{pi,col} A_{p,col} + n_{con} f_{con.lead}}{0.85\, f'_{cc,col}\, t_{col}} \right] \tag{4.12}$$

As shown in Eqn.(4.12), the deformation of the connector depends on the connector force ($f_{con,lead}$) which in turn depends on the connector deformation. Therefore, an

iteration involving the connector force is performed to arrive at the connector deformation.

- Calculate the corresponding force in the vertical connector ($f_{con,lead}$) from the force-displacement response of the connector (see an example in Figure 4.57).

5. *Determine the new neutral axis depth*

   Assuming a uniform compressive stress acting at the wall panel base over a length of βc, where c is the neutral axis depth, the resultant compressive force is obtained as follows:

$$C = (\beta c)\left(\alpha f'_{cc,w}\right) t_w \tag{4.13}$$

where α and β are the equivalent rectangular block constants and are given by

$$\alpha = \frac{2*\left(0.98 - 0.0022 f'_c\right)\ r}{r - 1 + 2^r} \text{ and } r = 1.24 + 0.01*\left(\frac{f'_c - 4.0}{0.25}\right); \beta = 0.96 \tag{4.14}$$

- Calculate the resultant compressive force from equilibrium of forces (see Figure 4.59)

$$C = P_w + P_{D,w} + n_{con} f_{con,trail} - n_{con} f_{con,lead} \tag{4.15}$$

- Calculate the neutral axis depth at the wall base

$$c = \frac{C}{\alpha\beta f'_{cc,w} t_w} \tag{4.16}$$

Iterate the above sub-steps until c calculated in Eqn.(4.16) converges to the assumed c value at the beginning.

Estimating the neutral axis depth for end columns:

1. *Assume a neutral axis depth (c) for the column*
2. *Determine the total gravity load on each column ($P_{D,col}$)*

$$P_{D,col} = \gamma\, l_{col} t_{col} h_w + w_{floor} l_{col} \tag{4.17}$$

   where w_{floor} is the uniform dead load acting on the wall panel.

3. *Determine the stresses and strains in the post-tensioning tendons*

   - The elongation of the post-tensioning tendon at 2% base rotation is:

$$\Delta_p = 0.02 * (x_{pt,col} - c) \tag{4.18}$$

- The strain in this post-tensioning tendon is:

$$\varepsilon_p = \frac{\Delta_p}{h_{u,col}} + \frac{f_{pi,col}}{E_p} \tag{4.19}$$

- Determine the corresponding stress in the post-tensioning tendon ($f_{p,col}$) from the stress-strain curve of the post-tensioning steel. The total post-tension force in the column is, therefore,

$$P_{col} = f_{p,col} A_{p,col} \tag{4.20}$$

4. *Determine the forces in the O- connectors*

   The connector forces acting along the vertical joints are calculated in the sub step 4 of the wall panel neutral axis determination.

5. *Determine the new neutral axis depth*

   Assuming a uniform compressive stress acting at the wall panel base over a length of βc, where c is the neutral axis depth, the resultant compressive force is obtained as follows:

$$C = (\beta c)\left(\alpha f_{cc,col}^{'}\right) t_{col} \tag{4.21}$$

Where α and β are the equivalent rectangular block constants and are given by

$$\alpha = \frac{2*\left(0.98 - 0.0022 f_c^{'}\right) r}{r - 1 + 2^r} \text{ and } r = 1.24 + 0.01*\left(\frac{f_c^{'} - 4.0}{0.25}\right);\ \beta = 0.96 \tag{4.22}$$

- Calculate the resultant compressive force from equilibrium of forces (see Figure 4.59)

$$C = \begin{array}{ll} P_{col} + P_{D,col} + n_{con} f_{con,lead} & \textit{for leading column} \\ P_{col} + P_{D,col} - n_{con} f_{con,trail} & \textit{for trailing column} \end{array} \tag{4.23}$$

- Calculate the neutral axis depth at the wall base

$$c = \frac{C}{\alpha \beta f_{cc,col}^{'} t_{col}} \tag{4.24}$$

Iterate the above sub-steps until c calculated in Eq. converges to the assumed c value at the beginning.

Step 4: Select a base rotation (θ)

Choose a value for θ in the range between zero and $\theta_{ultimate}$, where $\theta_{ultimate}$ may be taken as 3% or $1.5\theta_{design}$.

Step 5: Determine forces acting on the wall and columns at selected base rotation θ

1. *Determine the neutral axis depth of wall panel and end columns* ($c_{\theta,w}$ $c_{\theta,lcol}$ $c_{\theta,tcol}$) *corresponding to base rotation θ*

   From experimental data and analysis based on the monolithic beam analogy (MBA) approach on precast walls with unbonded post-tensioning, it was found that the neutral axis depth does not significantly vary beyond an interface rotation of about 0.5% as illustrated in Figure 4.60 (see Section 4.6.4 for experimental confirmation). Consistent with this observation, the neutral axis depth determined at 2% base rotation in *Step 3* is, therefore, used in the simplified analysis procedure to establish a trilinear relation between the neutral axis depth and the interface rotation at the wall base. This is demonstrated in Figure 4.60, where Point 1 corresponds to the wall length at zero percent base rotation and Points 2 and 3 are defined at base rotations of 0.1 percent and 0.5 percent, respectively. The neutral axis depth (c) at Point 3 is taken as that found at 2 percent rotation in *Step 3*, whereas the neutral axis depth is approximated 2c at Point 2.

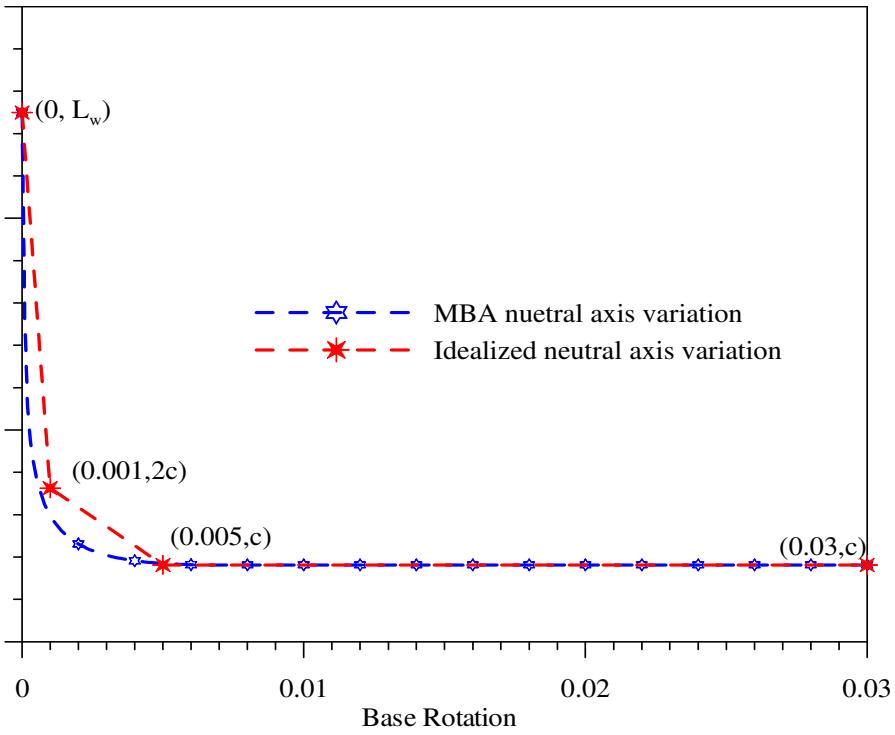

Figure 4.60 An illustration of trilinear idealization used for the neutral axis depth at the base of a wall with unbonded post-tensioning as a function of base rotation.

2. *Determine stresses and strains in the wall panel post-tensioning steel*

- The elongation of the post-tensioning tendon:

$$\Delta_{p,i} = \theta\left(x_{pt,i} - c_{\theta,w}\right) \tag{4.25}$$

- The strain in the post-tensioning tendon:

$$\varepsilon_{p,i} = \frac{\Delta_{p,i}}{h_{u,w}} + \frac{f_{pi,w}}{E_p} \tag{4.26}$$

- Determine the stress in the i^{th} post-tensioning tendon ($f_{p,i}$) from the stress-strain curve of the post-tensioning steel. The above steps should be repeated to determine the stresses in all post-tensioning tendons.
- The total post-tensioning force in the wall at the selected base rotation θ

$$P_{w,\theta} = \sum_{1}^{n_{pt}} f_{p,i} A_{pt} \tag{4.27}$$

- Calculate the location of the resultant post-tensioning force from the rocking edge using Eq. (4.28) (see Figure 4.59).

$$X_{pt,\theta} = \frac{\sum_{1}^{n_{pt}} f_{p,i} A_{pt} x_{pt,i}}{P_\theta} \tag{4.28}$$

3.*Determine the stresses and strains in the end column post-tensioning tendons*

- The elongation of the post-tensioning tendon at base rotation θ is:

$$\Delta_p = \theta * (x_{pt,col} - c_{\theta,col}) \tag{4.29}$$

Where, $c_{\theta,col} = \begin{Bmatrix} c_{\theta,lcol} & for\ lead\ column \\ c_{\theta,tcol} & for\ trail\ column \end{Bmatrix}$

- The strain in this post-tensioning tendon is:

$$\varepsilon_p = \frac{\Delta_p}{h_{u,col}} + \frac{f_{pi,col}}{E_p} \tag{4.30}$$

- Determine the corresponding stress in the post-tensioning tendon ($f_{p,col}$) from the stress-strain curve of the post-tensioning steel. The total post-tension force in the column is, therefore,

$$P_{col,\theta} = f_{p,col} A_{p,col} \tag{4.31}$$

4. *Determine the forces in the vertical connector*

- Calculate the connector deformations by using following equations

$$\Delta_{con,trail} = \theta * (l_w - c_{\theta,w}) \tag{4.32}$$

$$\Delta_{con,lead} = \theta * \left[c_{\theta,w} + l_{col} - c_{\theta,lcol} \right] \tag{4.33}$$

- Calculate the corresponding downward connector forces ($f_{con,lead,\theta}$ and $f_{con,trail,\theta}$) using an appropriate force-displacement response envelope (see an example in Figure 4.57).

5. *Calculate the resultant concrete compressive force at the wall system base*

From the equilibrium of forces in the vertical direction (see Figure 4.59),

$$C_{wall} = P_{w,\theta} + P_{D,w} + n_{con} f_{con,trail,\theta} - n_{con} f_{con,\ lead,\theta} \quad \text{for wall panel}$$

$$C_{lcol} = P_{col,\theta} + P_{D,col} + n_{con} f_{con,lead,\theta} \quad \text{for leading column} \tag{4.34}$$

$$C_{tcol} = P_{col,\theta} + P_{D,col} - n_{con} f_{con,trail,\theta} \quad \text{for trailing column}$$

Step 6: Compute the resisting moment of the wall system

For the leading column,

$$M_{lcol} = 0.5 l_{col} n_{con} f_{con,lead,\theta} + P_{col,\theta}(x_{pt,col} - 0.5 l_{col}) + C_{lcol}(0.5 l_{col} - 0.5 \beta_\theta c_{\theta,lcol})$$

For the wall panel,

$$M_{wall} = 0.5 l_w (f_{con,lead,\theta} + f_{con,trail,\theta}) + P_{w,\theta}(X_{pt,\theta} - 0.5 l_w) + C_{wall}(0.5 l_w - 0.5 \beta_\theta c_{\theta,w}) \quad (4.35)$$

For the trailing column,

$$M_{tcol} = 0.5 l_{col} n_{con} f_{con,trail,\theta} + P_{col,\theta}(x_{pt,col} - 0.5 l_{col}) + C_{tcol}(0.5 l_{col} - 0.5 \beta_\theta c_{\theta,tcol})$$

In the above equations, $0.5\beta_\theta c_{\theta,w}$ represents the distance to the resultant compression force from the rocking edge of the wall. At the decompression point, the compressive stress variation at the wall bases is expected to be triangular and hence the β_θ value is taken as 0.67 in order to locate the resultant compressive force at the appropriate location. Using Eq.(4.37), and assuming a linear variation for β_θ between the decompression point and θ of up to 0.1%, the value of β_θ is approximated for small θ values using Eq. (4.36)

$$\beta_\theta = 0.66 + 146.9\theta \text{ for } \theta \le 0.001 \quad (4.36)$$

For base rotations in the range of 0.1% and $\theta_{ultimate}$ (e.g., 3%), β_θ is obtained from Eq.(4.37), which was based on Eq. A.11 (Sritharan et al. 2007)

$$\beta_\theta = 1.0 + 0.12 \ln\left(\frac{c_{\theta,w}\theta}{0.06 h_w \varepsilon_{cu}}\right) \text{ for } 0.001 < \theta \le 0.03 \quad (4.37)$$

Repeat *Steps 4* through *6* and obtain moment resistance of the wall for all θ values.

Step 7: Compute the resisting moment of the entire wall system

The moment resistance of the wall system as a function of base rotation may be obtained by summing the resistance of the wall panel and the end columns at each selected value of θ using Eq. (4.38).

$$M_{wall\ system} = M_{lcol} + M_{wall} + M_{tcol} \tag{4.38}$$

4.8 Experimental Validation

This section presents validation for the simplified analysis procedure presented in Section 4.7.2, by comparing selected analysis results with available experimental data from PreWEC-1. The selected responses include the envelopes of the base shear capacity as a function of the top floor lateral displacement, elongation of the connectors and wall uplifts and the neutral axis depths at the wall base.

4.8.1 Base Shear Capacity

Figure 4.61 compares the base shear vs. the top lateral displacement established for PreWEC-1 with those calculated from the simplified analysis procedure. It is seen that the simplified analysis procedure provides a good estimate for the base shear vs. lateral displacement response envelope. At the top floor displacement of 7.2 inches, the calculated base shear resistance from the simplified analysis method is only 1.3% below the experimental value. At the design drift of 2%, the simplified analysis procedure underestimated the base shear resistance of the PreWEC system by 4.9%.

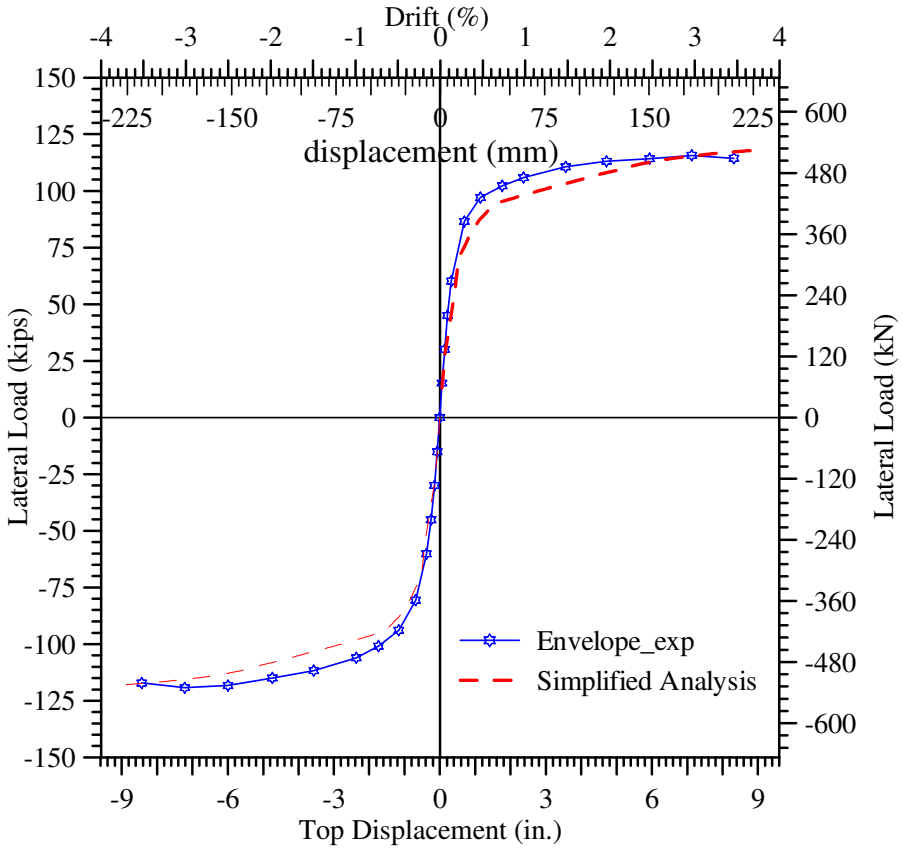

Figure 4.61 The base shear vs. top floor displacement for the PreWEC system.

4.8.2 Neutral Axis Depth

The neutral axis depths calculated using the simple analysis procedure for the PreWEC system is compared with those obtained from experimental data in Figure 4.62. It is seen from the figure that the simplified method provides a good estimate for the neutral axis depth for the wall panel. There are some differences that exist between the analytical and extracted neutral axis depths, which are largely responsible for the small underestimation of the base shear in Figure 4.61. Furthermore, Figure 4.62 confirms that the assumption of using a constant neutral axis for base rotations above a small threshold value is acceptable.

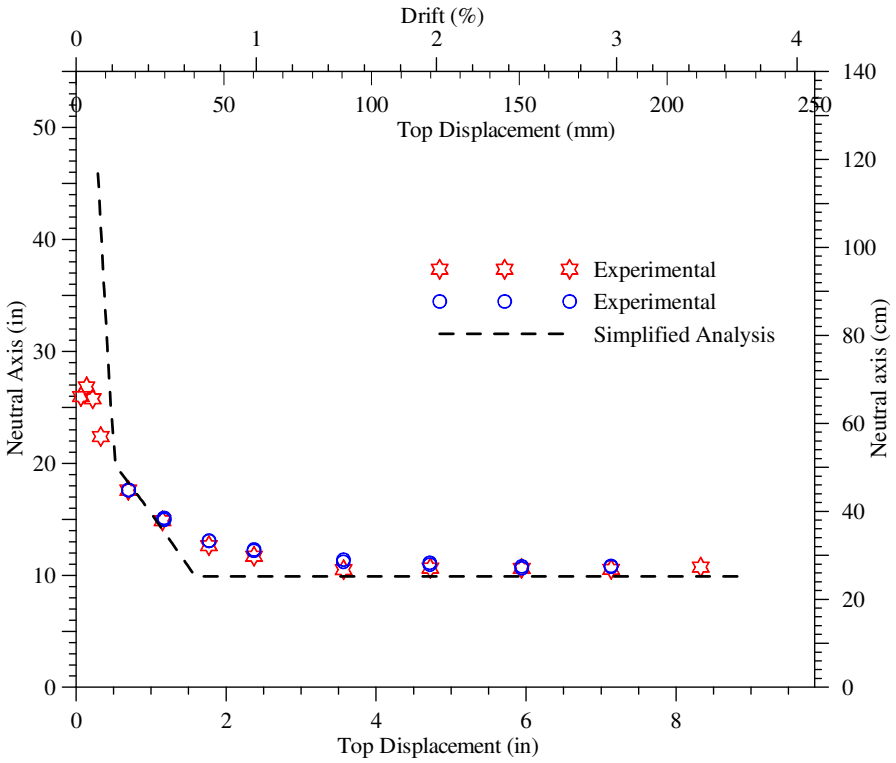

Figure 4.62 The variation of the nuetral axis depth of the wall panel with top displacement.

4.8.3 Connector displacements

Figure 4.63 compares the calculated displacement with the experimental data for both the trailing and leading connectors as a function of lateral displacement. The analysis procedure captured the connector displacement accurately.

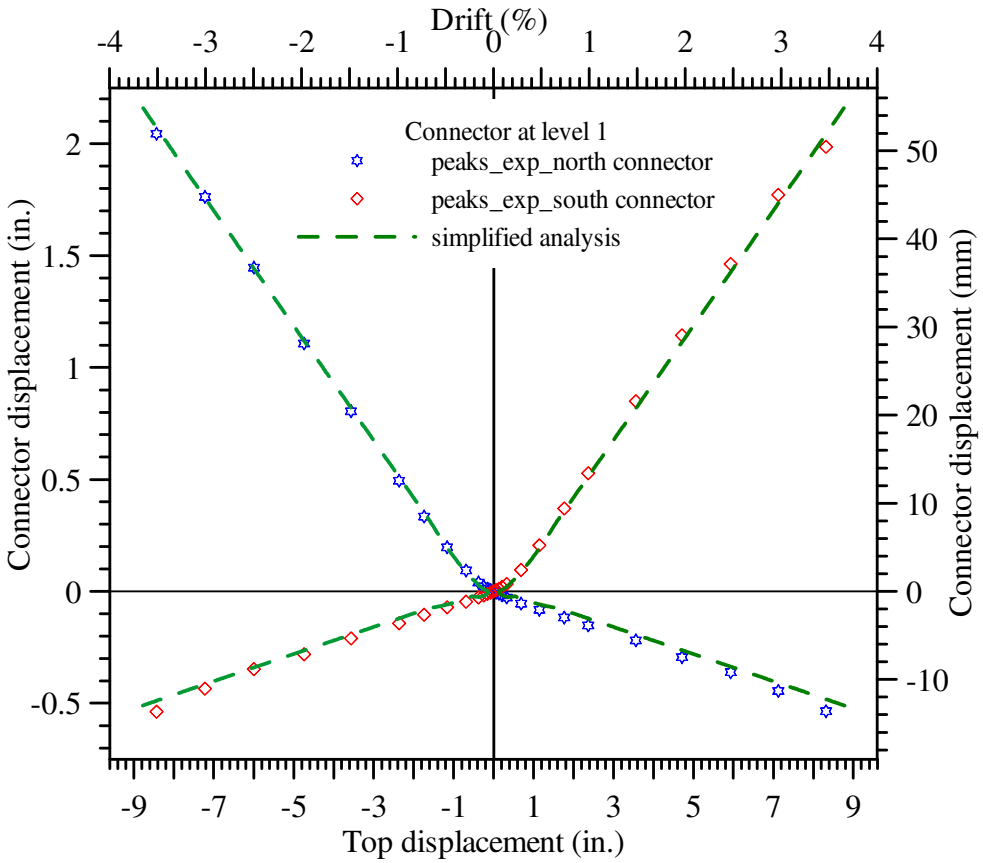

Figure 4.63 Comparison of experimental and analytical connector displacement as a function of top displacement

4.8.4 Concrete Confinement Strain

The strain data obtained from a concrete gauge (conc_N1) is compared with the analysis results in Figure 4.64, in which the analytical values were obtained using the equation proposed by Aaleti and Sritharan (2009). This concrete gauge was located in the confined concrete region at a distance of 3.94 in. from the compression wall end and at a height of 5.9 in. from the wall base. Given the simplicity used in the analysis approach, the comparison between the measured and calculated strains is remarkably good. The confined concrete strains are overestimated by the analysis. However, this is not of a serious concern for two reasons: 1) the behavior of compression toe region in the PreWEC wall system was expected to be complex and 2) the confined concrete models are inherently conservative and thus basing the confinement reinforcement on the estimated strains will provide reserve strain capacity as much as 50% above the maximum strains expected based on the theoretical

confinement models. The analysis and design methods are targeted to obtain more accurate results at a design base rotation of 2% (corresponding to a drift of slightly above 2%). It is observed in Figure 4.64 that the measured and estimated strains show good agreement at lateral displacements near the design drift.

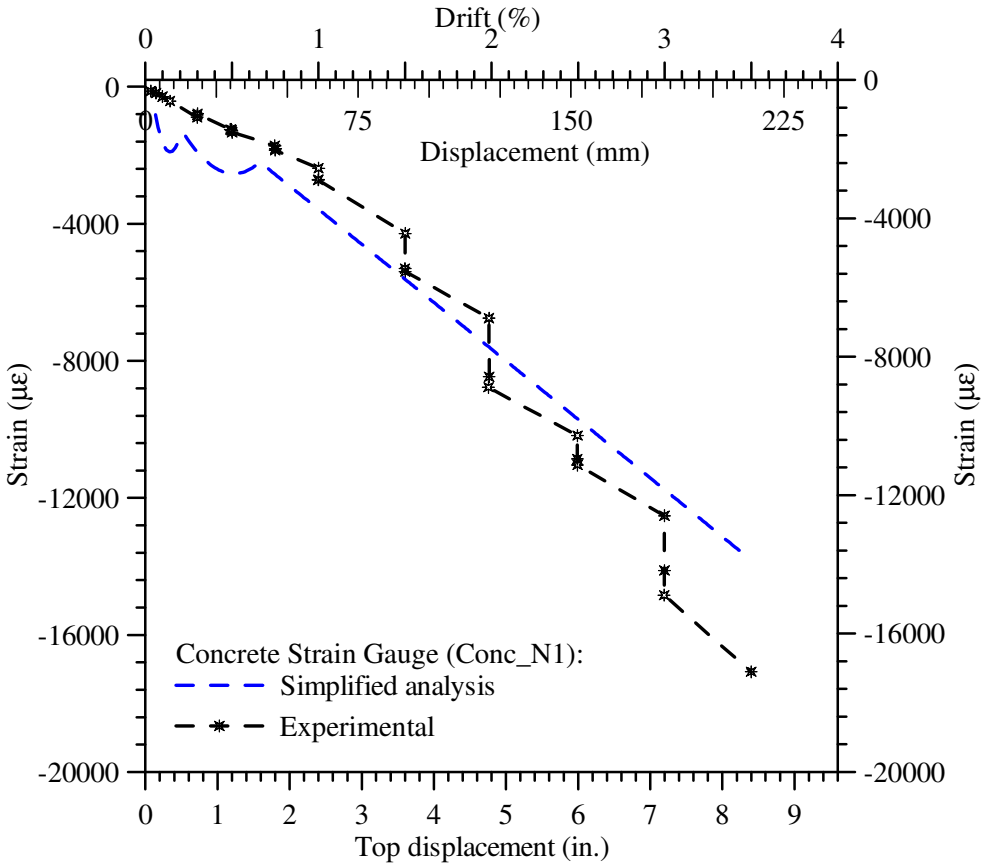

Figure 4.64 Variation of confined concrete strain with the top displacement of the PreWEC system

4.9 Design Methodology

This section presents a seismic design procedure for the PreWEC system. A design methodology was proposed by Sritharan et al. (2007) for the unbonded jointed wall systems, which was incorporated into an ACI ITG 5.2 document (ACI ITG5.2 2009) on design of unbonded post-tensioned precast walls for seismic regions. A similar approach is used while arriving at the design methodology for the PreWEC system.

4.9.1 Methodology

Similar to the jointed wall system, the lateral load resistance of a PreWEC system at a given drift depends on the geometry of the system, the amount of post-tensioning steel, the number of vertical connectors, initial prestressing force, and the force-displacement response of the vertical connector. Also, based on the experimental observations along with the analytical investigation on characterizing the lateral load behavior of PreWEC systems with O-connectors as energy dissipating devices, following observations are made.

1. The post-tensioning force in the columns does not vary significantly from the initial value during lateral loading. This is expected as the length of the column is small and thus does not cause significant elongation of the tendon. Therefore, for design purposes, it is reasonable to assume that the post-tensioning force in the columns is equal to the initial value.
2. The contribution of end columns towards the total moment capacity of the wall system is not significant. The post-tensioning provided in the columns is typically designed to keep the columns from fully uplifting from the foundation.
3. The hysteretic behavior of the PreWEC system does not match with the idealized flag-shaped hysteresis. The displacement/force corresponding to the change in unloading slope of the wall system is dependent on the cyclic behavior of the O-connector and it can be seen in Figure 4.65. The change in the unloading slope takes place at a displacement at which, the connector force is reversed and reached yield force in other direction.

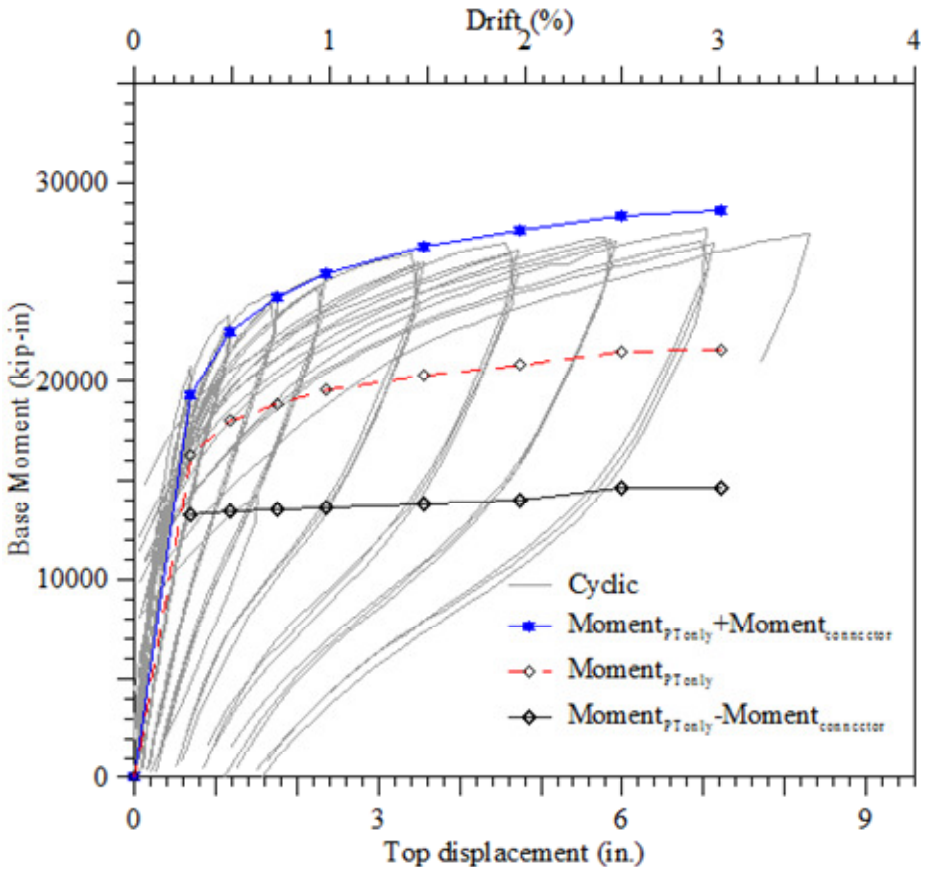

Figure 4.65 Change of unloading stiffness location for PreWEC-1

Consistent with the design methodology proposed for the jointed wall systems, the following assumptions are made for the design of PreWEC systems: 1) the wall system will undergo in-plane deformations only. Torsion and out-of-plane deformations are prevented by providing adequate out-of-plane bracing. 2) Both the vertical joints contain an equal number of identical connectors and a dependable force vs. displacement response envelope is available for the connector (e.g., see Figure 4.57). 3) The wall panel and columns undergo the same lateral displacement at the floor and roof levels due to the rigid floor assumption. 4) The strength of fiber grout that is placed between the wall base and foundation is greater than the strength of concrete in the wall panel. 5) The post-tensioning steel in the wall panel reaches the yield strain at the design drift. The corresponding rotation at the wall base is assumed to be θ_{design}, which may be taken as 2%. Alternatively, use an acceptable wall design drift to estimate a suitable value for θ_{design}.

The proposed design procedure consists of eight design steps: 1) defining the material properties and wall system dimensions; 2) defining the required design base moment resistance for the wall system, M_{design}; 3) estimating the required number of connectors, N_{con}, and the force resisted by a connector at design drift, θ_{design}; 4) estimating the area of the post-tensioning steel, A_p; 5) estimation of an initial stress for the post-tensioning steel, f_{pi}; 6) estimating the nominal moment capacity of the wall system, M_n ; 7) designing of confinement reinforcement for the boundary elements and 8) shear design.

4.9.2 Design Steps

The following seven steps are recommended for the design of the jointed wall systems.

Step 1: Material Properties and Wall Dimensions

- Select the following material properties.

  Prestressing tendon: Modulus of elasticity (E_p) and yield strength (f_{py}).

  Concrete: Unconfined concrete strength ($f_c^{'}$), elastic modulus of concrete (E_c) which may be approximated to $58{,}000\sqrt{f_c^{'}(psi)}$ or $4800\sqrt{f_c^{'}(MPa)}$, and appropriate coefficient of friction between the precast wall base and foundation (μ).

  Connector: Force vs. displacement response envelope.

- Establish the wall dimensions.

  Select the total length of the wall system (L_s) or length of a single wall (L_w), wall height (H_w), wall thickness (t_w), column length (l_{col}) and column thickness (t_{col}). The height and length of the wall system can be determined from the architectural drawings or from preliminary design calculations.

  Stanton and Nakaki (2002) suggest that H_w/L_w should be more than 2.0 to ensure flexural dominant behavior by each wall.

The following guidance may be used to determine an initial value for the wall thickness:

1. select a value in the range of $h_{story}/16$ to $h_{story}/25$, where h_{story} is the story height (Englekirk 2003);
2. ensure that the selected wall thickness should be sufficient to limit the shear stress in the wall to the permissible limit specified in the current building standard (e.g., ACI 318-08, 2008); and
3. the selected wall thickness should be sufficient to accommodate the required confinement reinforcement at the wall ends without causing any construction difficulties.

Step 2: Required Design Moment Resistance

Using a force-based design (FBD) or direct displacement-based design (DDBD) procedure, arrive at the required base moment resistance for the wall system (M_{design}). Hence, the precast wall system should be designed such that

$$\phi M_n \geq M_{design} \tag{4.39}$$

where ϕ is the flexural strength reduction factor and M_n is the nominal moment capacity of the wall system at the design drift.

Step 3: Force Resisted by the Connector

- Assuming vertical relative displacements between the wall panel and columns at both vertical joints to be $0.9L_w\theta_{design}$ and $(0.1L_w+l_{col})*\theta_{design}$, estimate the corresponding forces in the connectors (F_{con1} *and* F_{con2}) at the design drift from the force-displacement envelope curve available for the O- connector (see an example in Figure 4.57).
- For the wall systems described above, a symmetric lateral response is expected when they are subjected to symmetric cyclic loading. For such systems, the hysteretic energy dissipation can be correlated to equivalent viscous damping using Eq. 4.40.

$$\zeta_{eq} = \frac{2}{\pi}\frac{A_{loop}}{A_{rect}} \tag{4.40}$$

Where A_{loop} is the area enclosed by a symmetric hysteresis loop at the design drift and A_{rect} is the area of the rectangle circumscribing the hysteresis loop.

- The number of connectors should be determined such that a desired level of equivalent damping is incorporated in the wall system. If O- connectors, as successfully used in the PreWEC system test, are chosen, then the required number of connectors may be established from Eq. 4.41 to ensure that the wall system would have a desired level of equivalent damping. The cyclic force-displacement response of a PreWEC system is approximated to a polygon (ABCDEF) as shown in Figure 4.66a. The equation for the equivalent viscous damping of the PreWEC system is derived by using the Eq.4.40 and is presented below in Eq.4.42. Figure 4.66b presents the accuracy of the proposed equivalent viscous damping equation.

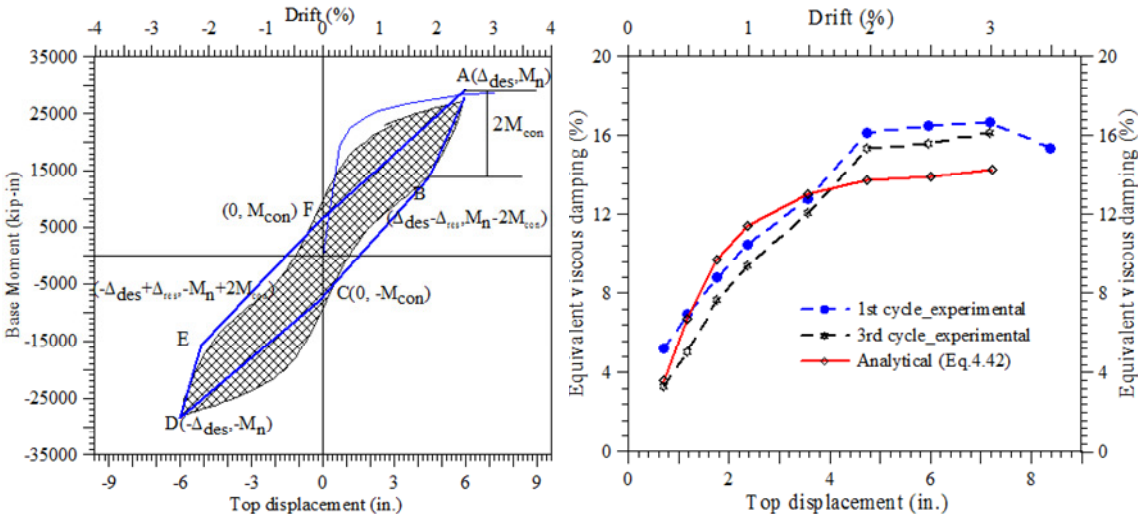

a) Approximation of cyclic response

b) Equivalent viscous damping comparison

Figure 4.66 Multi-linear approximation of the force vs. displacement hysteretic loop of PreWEC-1

$$N_{con} = \frac{\pi\left(2\Delta_{des}\zeta_{eq} + 0.5\Delta_{res}\right)M_n}{\left(4\Delta_{des} - \Delta_{res}\right)F_{con,avg}\left(L_w + l_{col}\right)} \tag{4.41}$$

$$\zeta_{eq} = \frac{2}{\pi}\frac{\left(4\Delta_{des} - \Delta_{res}\right)M_{con} - M_n\Delta_{res}}{4M_n\Delta_{des}} \tag{4.42}$$

Where, N_{con} is the number of connectors in each vertical joint between the precast wall and columns.

ζ_{eq} is the required level of equivalent viscous damping, which should be in the 15 to 20 percent range to ensure that the wall system will have adequate damping.

Δ_{des} is the design displacement of the wall system.

Δ_{res} is the displacement from the design level displacement, at which the wall system's force-displacement response has a change in slope and is given by $\Delta_{res}= 2F_{con,avg}/k_1$

k_1 is the initial stiffness of the O-connector.

$F_{con,avg}$ is the average of connector forces at the vertical joints. It is equal to $0.5*(F_{con1}+F_{con2})$.

Step 4: Required Area of the Post-tensioning Steel and Initial Stress in end columns

The area of post-tensioning steel ($A_{p,col}$) and the initial stress ($f_{pi,col}$) in the end columns is designed such that the total initial prestress force is greater than the connector force along the vertical joint. Therefore,

$$P_{D,col} + A_{p,col} f_{pi,col} = \Gamma F_{con1} n_{con}$$

Where,

Γ is a safety factor against the column uplift, whose value can be assumed to be between 1.25 to 1.5.

$f_{pi,col}$ can be assumed to be around $0.8f_{py}$

Step5: Required Area of the Post-tensioning Steel in Wall panel

The area of the required post-tensioning steel is determined based on the design moment capacity of the wall panel, $M_{design,\ wall}$. The design moment for the wall panel can be determined by Eq.4.45

$$M_{design,wall} = \frac{M_{design}}{\phi} - l_{col} F_{con,avg} - 2M_{dec,col} \qquad (4.45)$$

where, $M_{dec,col}$ is the decompression moment capacity of the end column. The decompression moment is equal to $\frac{1}{3} l_{col} \left[P_{D,col} + f_{pi,col} A_{p,col} \right]$.

- Design the area of the post-tensioning steel, $A_{p,w}$, using Eq.4.46, which uses the moment equilibrium of forces acting on the base of the wall panel (see Figure 4.59).

$$M_{design,wall} = \left(P_D + f_{py} A_{p,w}\right) * \left(\frac{L_w}{2} - \frac{P_{D,w} + f_{py} A_{p,w} + n_{con}(F_{con1} - F_{con2})}{2 * (\alpha . f_{cc}^{'}) t_w} \right) + 0.5 L_w n_{con} (F_{con1} + F_{con2}) \tag{4.46}$$

where P_D, the summation of the wall self weight and superimposed live load, is equated to ($\gamma_c L_w t_w H_w$ + W_{floor} L_w), γ_c is the unit weight of concrete, W_{floor} is the distributed superimposed live load at the base of wall from all floors, and $\alpha . f_{cc}^{'}$ approximates the expected confined concrete strength of the equivalent rectangular stress block with $f_{cc}^{'}$ representing the strength of the confined concrete. Based on the minimum confinement reinforcement requirement of ACI as detailed in *Step 8*, it is suggested that the value of $f_{cc}^{'}$ is taken as $1.35 f_c^{'}$ with a suitable value for α from Eq. 4.47. A more accurate value for $f_{cc}^{'}$ may be used after completing *Step 7*, which will optimize the amount of prestressing steel in the walls.

$$\alpha = \frac{2 * r * \left(0.98 - 0.0022 * f_c^{'}\right)}{r - 1 + 2^r} \tag{4.47a}$$

where $$r = 1.24 + 0.01 * \left(\frac{f_c^{'} - 4.0}{0.25} \right) \tag{4.47b}$$

It is noted that the effects of cover concrete were not separately accounted for in Eq. 4.46. Instead, the entire compression region is treated as a confined region to simplify the design procedure. A similar approach should be followed in conjunction with the recommended design procure. When substituting for all known variables, Eq. 4.46

will lead to a quadratic equation in A_p and the small positive root should be used as the design value for A_p.

- Once the area of the post-tensioning tendons ($A_{p,w}$) is estimated, the connector forces (F_{con1} and F_{con2}) should be revised using a better estimate for the connector deformations (Δ_{con1} and Δ_{con2}) from Eq. 4.48. With a revised values for connector forces a new value for $M_{design,wall}$ and the corresponding $A_{p,w}$ should be obtained from Eqs. 4.45 – 4.47.

$$\Delta_{con1} = \theta_{des}\left(L_w - \frac{P_D + f_{py}A_{p,w} + n_{con}(F_{con1} - F_{con2})}{(\alpha.f_{cc}^{'})t_w}\right) \tag{4.48a}$$

$$\Delta_{con2} = \theta_{des}\left(0.5l_{col} + \frac{P_D + f_{py}A_{p,w} + n_{con}(F_{con1} - F_{con2})}{(\alpha.f_{cc}^{'})t_w}\right) \tag{4.48b}$$

Step 6: Design the Initial Stress for the Post-tensioning Steel in the wall panel

- Using Eq.4.49, estimate the neutral axis depth at the base of the wall at the design drift.

$$c_{design,wall} = \frac{P_D + f_{py}A_{p,w} + n_{con}(F_{con1} - F_{con2})}{\beta*(\alpha.f_{cc}^{'})t_w} \tag{4.49}$$

where the value of β can be approximated to 0.96, which is derived from examining equivalent stress blocks for confined concrete Sritharan et al. (2007)

- Assuming that the post-tensioning tendons reach the yield limit state in the wall at the design drift, the initial stress in the post-tensioning steel is established from Eq. 4.50.

$$f_{pi} = f_{py} - \frac{\left(0.5L_w - c_{design,wall}\right)\theta_{design}E_p}{H_w} \tag{4.50}$$

Step 7: Estimate the Moment Capacity

Using the analysis procedure presented in Section 4.7.2, estimate the total base moment resistance of the PreWEC wall system and ensure that Eq. 4.39 is satisfied. Based on the examples investigated to date by the authors, the proposed design method appears to

adequately satisfy Eq. 4.39 and no further iteration was found to be necessary. However, if Eq. 4.39 is not satisfied in a design problem, it is recommended that wall dimensions be altered in order to improve the design.

Step 8: Design of Confinement Reinforcement

With the connection between the wall and foundation, strain concentrations are expected at the compressive regions of the wall toes. A realistic maximum strain demand has not been successfully established from experiments or analyses. However, using the data from the PRESSS test building and the PreWEC testing presented in this chapter and recognizing that the wall would experience the largest resultant compressive force at the base for all values of θ, Eq. 4.51 has been suggested for estimating the maximum concrete strain demand in the compressive regions of the wall toes (Sritharan et al. 2007) and a validation of this equation may be seen in Figure 4.64.

$$\varepsilon_{conc} = c_{\max,wall}\left(\frac{M_{\max,wall}}{E_c I_{gross}} + \frac{\theta_{\max}}{0.06 H_w}\right) \tag{4.51}$$

where $M_{max,wall}$ is the base moment resistance of the wall panel at the maximum expected drift, the corresponding base rotation is θ_{max}, which may be taken as $1.5*\theta_{design}$, I_{gross} is the gross moment of inertia of the wall and is equal to $\frac{t_w L_w^3}{12}$, and $c_{max,wall}$ is the neutral axis depth at the base of the leading wall at θ_{max}. The value of $c_{max,wall}$ may be established as part of the analysis of the wall system in Step 6. Following an estimate for ε_{conc} from Eq. 4.51, quantify the required amount of confinement reinforcement in the wall toes using an appropriate confinement model. If the model proposed by Mander et al. (1988) is selected, then Eq. 4.52 will be used to determine the required amount of confinement reinforcement.

$$\rho_s = \frac{(\varepsilon_{conc} - 0.004) f_{cc}^{'}}{1.4 f_{yh} \varepsilon_{su}} \tag{4.52}$$

where ρ_s is the volumetric ratio of the required confinement steel, f_{yh} and ε_{su} are, respectively, the yield strength and ultimate strain capacity of the confinement reinforcement, and $f_{cc}^{'}$ is the ultimate strength of the confined concrete. Since $f_{cc}^{'}$ is dependent on the value of ρ_s, an

iterative approach would be necessary to solve Eq. 4.52. For the first step in the iteration, $f_{cc}^{'}$ may be approximated to $1.35f_{c}^{'}$. This is because the selected confinement reinforcement should also satisfy all seismic design provisions prescribed in the current building standard for the design of transverse reinforcement in the plastic hinge region of a concrete wall. This includes the minimum hoop reinforcement requirement of ACI Eq. 21-4 (2008), which can be interpreted as demanding minimum confinement reinforcement of $0.09f_{c}^{'}/f_{y}$ in both major and minor axis directions of the wall sections. The corresponding effective confinement pressure is $0.09k_{e}f_{c}^{'}$, where k_e is the effective confinement coefficient. With a value of 0.6 for k_e, this minimum confinement pressure will provide a $f_{cc}^{'}$ value of about $1.35f_{c}^{'}$.

The confinement reinforcement should extend over a length, l_{cr}, and height, h_{cr}, near both ends of the wall at the base where the concrete strains are greater than crushing strain of the unconfined concrete, $\varepsilon_{unconfine}$. Assuming a linear strain distribution in the compression region at the base, the boundary element length can be determined using Eq.4.53.

$$l_{cr} = c_{\max,lead}\left(1-\frac{\varepsilon_{unconfine}}{\varepsilon_{conc}}\right) \tag{4.53}$$

The boundary element height, h_{cr}, which depends on the bending moment diagram along the height of the wall, can be arrived at in similar fashion as in a traditional reinforced concrete shear walls.

Step 9: Shear Design

Shear design of the wall system includes designing for the shear forces, preventing diagonal tension failure, similar to traditional reinforced concrete walls. ACI 318 (ACI 318-05, 2005) requirements for special concrete walls can be used for the shear design of the wall panel in a PreWEC system. Shear design should also eliminate potential shear slip failure along the horizontal joints between the wall panel and at the wall-foundation interface, which requires

$$\varphi_s V_{slip} \geq V_{design} \tag{4.54}$$

where ϕ_s = shear strength reduction factor, V_{slip} = shear slip resistance of the PreWEC system, and V_{design} = design base shear at wall base.

The shear slip resistance of a PreWEC system can be determined as:

$$V_{slip} = \mu \left(A_{p,w} f_p + P_D \right) \tag{4.55}$$

where, μ = friction coefficient, A_p = area of post-tensioning steel in wall, f_p = stress in the post-tensioning steel, and P_D = the summation of the wall self weight and superimposed live load.

The value of the friction coefficient depends on the interface material placed between the precast walls and foundation. Typically, if a fiber grout is used as an interface material, a value of 0.6 can be used for μ (ACI ITG 5.2-09, 2009, Soudki et al., 1995 and Hutchinson et al., 1993). Since the stress in the post-tensioning steel and the connector force increase with drift, it will be necessary to perform this check at both θ_{design} and θ_{max}.

CHAPTER 5

SHEAR MODEL

5.0 Introduction

In current day design practice researchers and designers conduct static or dynamic nonlinear analyses of structures for seismic assessment using frame elements. The nonlinearity in frame elements is typically addressed through lumped plasticity models or with distributed-inelasticity models. A fiber beam-column element could be used to model the distributed inelastic action. Also, for structural assessment and design, it is vital to quantify the overall response of reinforced concrete structures under lateral loads by capturing the deformation contributions of flexure, shear and strain penetration effects (see Section 3.4). Whilst existing fiber based modeling approaches of reinforced concrete elements may allow accurate prediction of flexural and strain penetration responses, the determination of shear response needs further developments (see Section 3.4). In recent years, a few fiber based modeling strategies were proposed to account for the shear deformation contribution (Petrangeli et al. 1999). However, they have not yet proven to neither be applicable to wide range of structural cases nor have been easily implemented in the fiber-based analysis methods. Also, these elements demand considerable additional computational power and often lead to numerical instabilities.

The experimental investigations conducted on concrete structural walls as part of this study and those conducted by others (e.g., Thomsen and Wallace 1995, Oesterle et al. 1979) have indicated that inelastic shear distortions contribute significantly towards overall deformations in the plastic hinge regions of flexural dominant concrete walls. It was also observed experimentally by various researchers (Saatcioglu et al. 1988; Saatcioglu and Ozcebe 1988, Osterle et al. 1979, Wallace et al. 2004) and as part of this study that inelastic shear response is triggered by flexural yielding, even when the member is designed to have excessive shear capacity. These observations indicate that the inelastic hysteresis of shear

deformations is unavoidable, even though the structures are designed to behave predominantly in flexural manner, which is due to the coupling between flexural and shear responses. Also, the analytical investigation of concrete structural walls presented in Chapter 3, clearly showed that the inadequate modeling of the shear hysteretic behavior affected the overall cyclic behavior of the structural wall. Therefore, to accurately predict the cyclic hysteresis behavior of the structural walls, it is essential that even if the wall is designed to have flexural dominant response the cyclic shear behavior should be captured adequately. .

Using the strut and tie modeling technique, this chapter presents a new analytical model to quantify the monotonic shear behavior of wall regions including that may experience inelastic actions. The model is then extended to capture the shear hysteresis. Finally both monotonic and cyclic models are validated using experimental data from large-scale cyclic testing of concrete walls.

5.1 Estimation of Shear Deformations

Several procedures starting from empirical formulas (Hines et al., 2004) to well-advanced methods based on modified compression filed theory (MCFT) (Vecchio and Collins 1986) were proposed by various researchers to estimate the monotonic shear deformations in reinforced concrete structures. Based on large-scale testing of bridge piers, Hines et al. (2004) proposed an empirical method which estimates the shear deformation at the top of the structure as a constant fraction of the flexural deformation. The primary shortcoming of this method is that it is not applicable for predicting inter-story shear deformations. In order to overcome this shortcoming, Brueggen (2009) suggested that the inter-story shear deformations can be satisfactorily quantified with the assumption that the shear strain is directly proportional to the curvature at that section. In other words, shear displacement is assumed to be proportional to the flexural rotation, instead of the flexural deformation. Though this method predicted the shear deformations with reasonable accuracy, the shortcoming of this method is the uncertainty in estimation of the proportionality constant. Also, this method only gives a reasonable estimate of the monotonic response, without addressing the cyclic hysteretic behavior.

Several researchers have also used the modified compression field theory (MCFT) to represent the monotonic shear response envelope or backbone curve in their models (Ozcebe and Saatcioglu 1989; Pincheira et al. 1999; Lee and Elnashai 2001; Gerin and Adebar 2004; Sezen and Chowdhury 2009). The major shortcoming of this method is that it requires carrying out an MCFT analysis of the reinforced concrete member. The MCFT analysis is complicated and requires a significant amount of computational power. However, there are some finite element programs based on MCFT (e.g., Response-2000 (2007) to conduct the analysis. In order to overcome the above mentioned shortcomings, a rational analytical procedure that is simple yet has the ability to account for the influence of flexure on the shear response is proposed using the strut-and-tie modeling concepts.

5.1.1 Strut and Tie Modeling

The strut-and-tie method of analysis is a modeling technique used to discretely represent the force paths that are established inside a structural system when subjected to external actions with a series of interconnected truss members. This modeling technique is particularly useful in depicting the force path being developed inside a structure by means of struts and ties, respectively to represent the compression and tension force paths. The model elements (truss elements) are joined at the nodes at which the actual force is concentrated and force equilibrium is achieved.

The strut-and-tie modeling technique has received renewed interest over the past decades, as it is found to be a reasonably simple rational method for analyzing and designing disturbed structural regions (D-regions) such as plastic hinge regions in structural walls. The same technique can be also used for the Bernoulli regions (B-regions), where plane section remain plane assumption is valid.

5.1.2 Model Formulation Procedure

Schlaich et al. (1987) recommended that the strut and tie model may be established based on the uncracked elastic load-path. However, in recent times researchers (MacGregor 1988, Sritharan 1998, To et al. 2009) found that the STM based on an elastic analysis is inadequate for analyzing structures at a limit state where significant inelastic strains and

progressive damage develop in structural D-regions. This is because a STM formulated using elastic theory is insufficient in capturing the redistribution of forces associated with the inelastic response of structures. To et al. (2009) proposed that a single model formulation of a structure may adopt the force path that occurred at the ultimate limit state for the structural D-regions, and the force path that developed at the serviceability limit state for the structural B-regions. To et al. (2009) have shown that this model formulation procedure using the force path at the ultimate limit state was able to capture the response of concrete beams, columns, bridge knee and T-joints, portal frames and multiple column bridge bents with reasonable accuracy. Following the recommendations of To et al. (2008), a STM model was formulated to predict the lateral load behavior of structural walls. However, to account for the yield plateau of reinforcement, when developing the model formulation procedure for the structural walls, the force path that occurred at the nominal capacity limit state was employed in this. The nominal capacity limit state defined when the strain in the extreme longitudinal reinforcement reaches 0.015 or strain in concrete in compression region reaches 0.004, whichever occurs first.

As suggested by To et al. (2008), different model element types were used in formulating the STM for the structural walls (see Figure 5.1). Flexural compression zones in B and D-regions were represented by a concrete strut and a rebar strut arranged in parallel between the nodes. Whereas, the flexural tension zone in structural B-regions and D-regions were represented by a concrete tie and a rebar tie, which was also arranged in tandem. The concrete between the boundary elements was represented by a concrete strut and a concrete tie. Shear reinforcement and distributed longitudinal reinforcement between the boundary elements were represented by a rebar strut and a rebar tie arranged along in the diagonal directions. The properties of concrete strut used in D-regions differ from that of those used in the B-regions. The detail procedure to estimate the effective material properties are presented in To et al. (2008) and are not discussed here.

As STMs are used to discretely represent the force path developed inside a reinforced concrete structure, it is logical that the "struts" and “ties" are located at the centre of the respective force path. So, the concrete tie representing the flexural tension region is located at

the tension centroid of the boundary element steel in tension estimated at the nominal capacity limit state. The width and depth of this concrete tie was taken as the boundary element length and wall thickness, respectively. Similarly the concrete strut representing the flexural compression region was located at the compression centroid at the nominal capacity. The cross-sectional area of struts, which represent the concrete flexural compression zone, was defined by the area between the neutral axis position and the extreme compression edge of the section. The area of the rebar ties and struts used to represent the longitudinal boundary element steel was equal to the area of the reinforcement in the boundary elements. The rebar ties and rebar struts were positioned at their respective centroid locations. The effective yield strength for the rebar ties were estimated based on the total tension and compression carried by the boundary element steel at the nominal capacity.

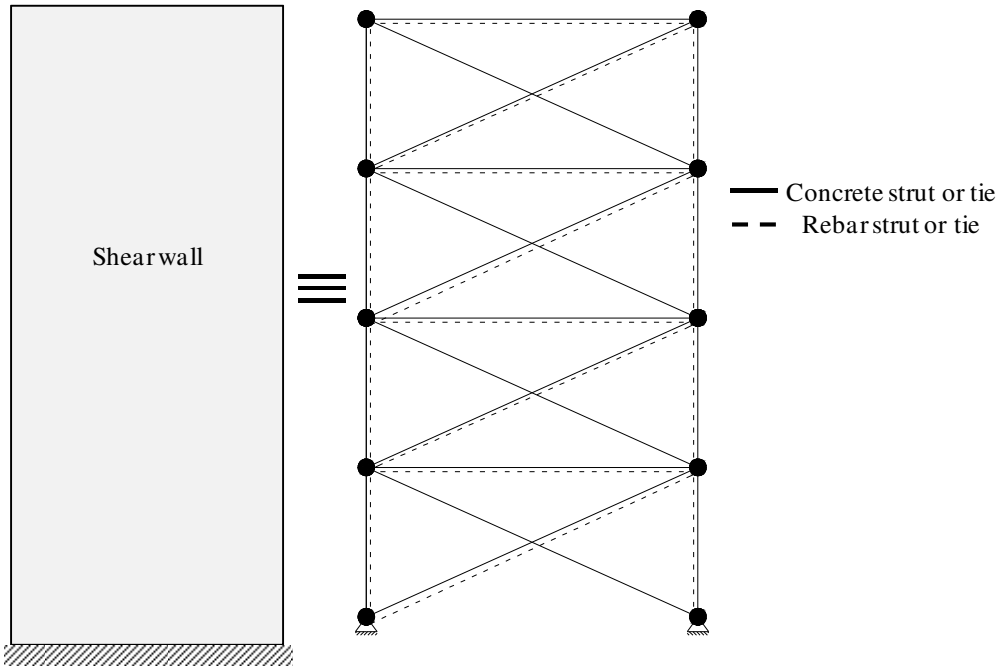

Figure 5.1 Strut and tie representation assumed for a reinforced concrete shear wall

The diagonal elements in the model were positioned such that the angle between the diagonal concrete struts and the member longitudinal axis between 31^{o} and 59^{o} as recommended by CEB-FIP (1978). The width of the diagonal concrete strut and ties was

chosen as shown in Figure 5.2. The area of the diagonal rebar strut and tie (see Figure 5.3) is given by $A_{dia} = \frac{0.5A_y}{\sin\theta}$, where A_y is the distributed longitudinal steel and θ is the inclination of the diagonal strut. Area of the horizontal rebar strut, A_h, is equal to $\left(A_x - 2A_{dia}\cos\theta\right)$ where A_x is the total area of the shear reinforcement over the height of the panel. The width of the horizontal concrete strut was equal to the shear reinforcement spacing.

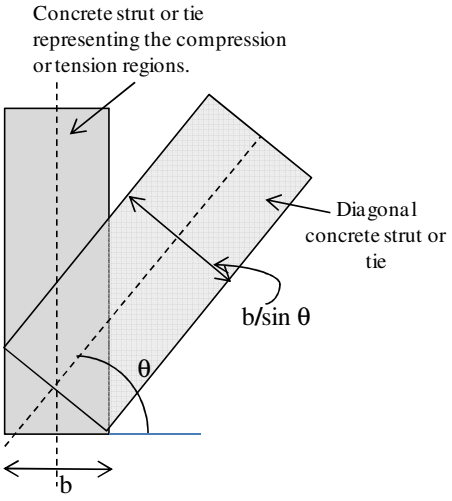

Figure 5.2 Estimation of the diagonal strut and tie widths

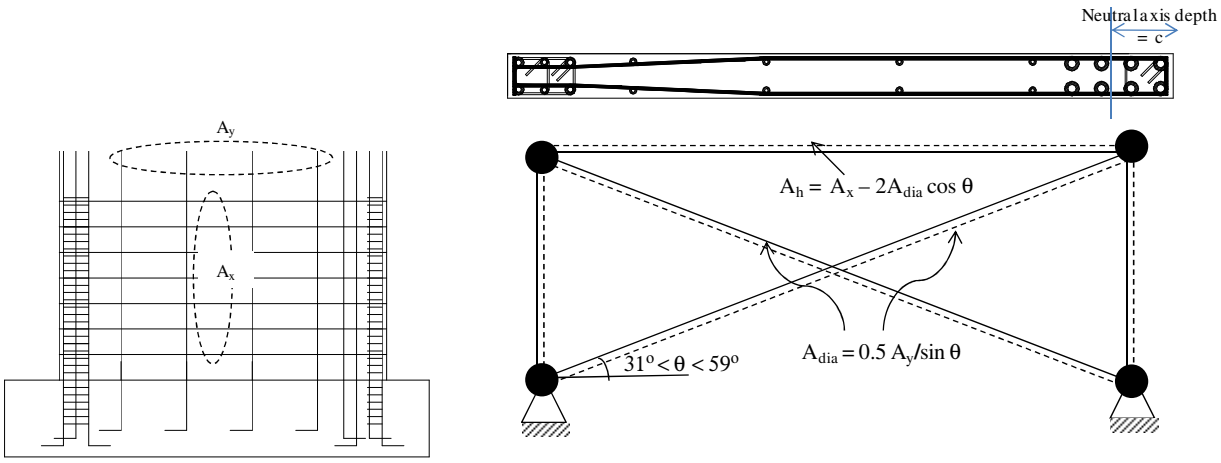

Figure 5.3 Estimation of the area of the diagonal and horizontal rebar strut and tie

5.1.3 Estimation of Shear Deformation

Once the strut and tie model was formulated, lateral load was applied at the appropriate node and the displacements of all the nodes were quantified. Using the analytical method presented in Chapter 3 (see Section 3.2.3), estimation of the shear deformations can be obtained using the nodal displacements. The steps used to to estimate the shear deformations at a given level of concrete wall are summarized below.

Step 1: the moment-curvature analysis was performed for the wall cross section using the measured concrete and steel material properties.

Step 2: the neutral axis depth and centroid of the steel tension force at the nominal capacity was estimated for the given wall cross-section.

Step 3: effective concrete and steel properties based on the calculated concrete compression force and steel tension force were estimated using the recommendations by To et al. (2009).

Step 4: area of the diagonal struts and ties for both concrete and rebar was estimated.

Step 5: the loads (shear, axial) were applied at appropriate node of the STM and the nodal displacements were quantified.

Step 6: the shear deformations were estimated from the nodal displacements using the procedure described in Section 3.2.3.

5.1.4 Validation of STM procedure

This section illustrates the application of STM procedure to arrive at the shear force vs. shear deformation response at first story level of two rectangular structural walls. The wall specimen, RWN, tested as part of this study and wall specimen RW2 (see Section 2.1.2.10), tested by Thomsen and Wallace (1995) are used to demonstrate the applicability of the STM procedure to predict the shear deformations. The cross-section details of RWN and RW2 are presented in detail in Chapter 3 (Section 3.1) and Chapter 2 (Section 2.1.2.10), respectively. The moment-curvature analysis of each wall section was conducted using a zero length element in OpenSEES with measured material properties. The moment-curvature response for RWN and RW2 are shown in Figure 5.4.

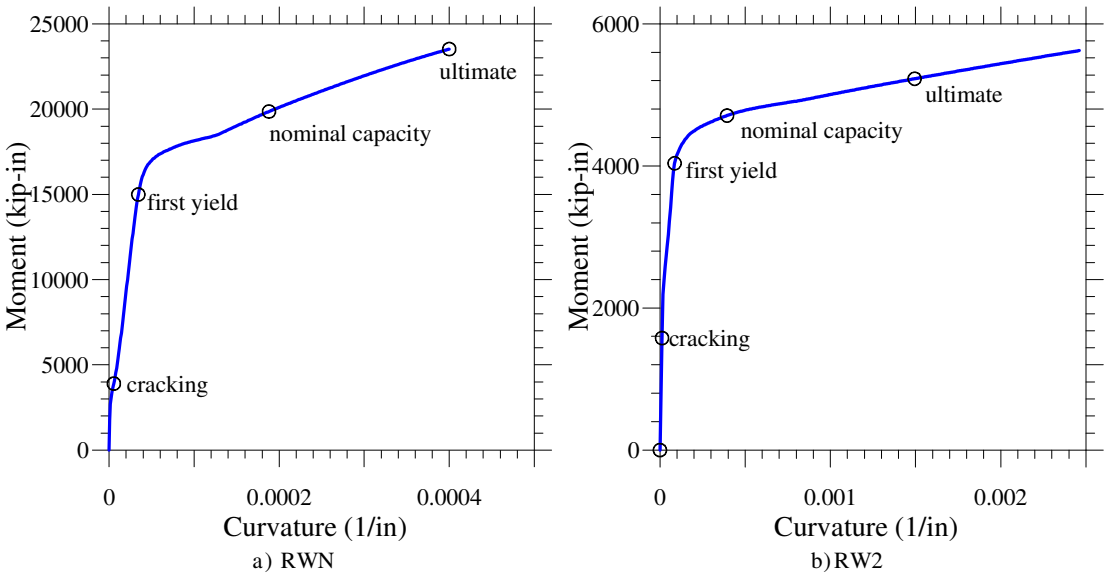

Figure 5.4 Calculated moment-curvature responses of RWN and RW2

The required parameters for the STM formulation such as the neutral axis length, location of the tension force and the material properties at the nominal capacity limit state are estimated as explained in previous section and are presented below for RWN and RW2.

For RWN:

- the length of the boundary element on tension side (#6 side of RWN) = the length of the concrete strut in flexural tension = 11.2 in.;
- area of longitudinal reinforcement in #6 side boundary element = four #6 bars + two #5 bars = 4 (0.44 in^2) +2 (0.31 in^2) = 2.38 in^2
- length of the neutral axis depth at nominal capacity limit state = 5.5845 in.; therefore, the length of the concrete strut in flexural compression = neutral axis depth = 5.5845 in.;
- area of longitudinal reinforcement in #9 side boundary element = eight #9 bars = 8 in^2;
- distance between the centroid of boundary element tension force and compression forces = 81.6 in.;
- thickness of all the concrete strut and ties = wall thickness = 6 in.;
- width of the diagonal concrete strut = 5.5845/sinθ = 8.648 in.;

- width of the diagonal concrete tie = 11.2/sinθ = 17.35 in.;
- width of the horizontal concrete strut = shear reinforcement spacing = 7.5 in.;
- area of the distributed longitudinal steel (A_y) = eight #4 bars = 8 (0.2 in^2) = 1.6 in^2;
- area of the distributed longitudinal steel (A_x) = twenty #3 bars = 20 (0.11 in2) = 2.2 in^2;
- area of diagonal rebar strut and tie (A_{dia}) = 1.24 in^2; area of horizontal rebar tie/strut (A_h) = 0.3078 in^2;
- concrete compression strength = 0.72 f_c' = 0.72*(7.861 ksi) = 5.66 ksi;
- concrete tension strength = 0.05 f_c' = 0.393 ksi;
- yield strength of rebar tie = 64.9 ksi;
- yield strength if rebar strut in compression region = 66.74 ksi;

For RW2:

- the length of the boundary element on tension side = the length of the concrete strut in flexural tension = 6.02 in.;
- area of longitudinal reinforcement in the boundary element = eight #3 bars = 8(0.11 in^2) = 0.88 in^2;
- length of the neutral axis depth at nominal capacity limit state = 6.09 in.;
- length of the concrete strut in flexural compression = neutral axis depth = 6.09 in.;
- distance between the centroid of boundary element tension force and compression forces = 40.53 in.;
- thickness of all the concrete strut and ties = wall thickness = 4 in.;
- width of the diagonal concrete strut = 6.09/sinθ = 9.065 in.;
- width of the diagonal concrete tie = 6.02/sinθ = 9.05 in.;
- width of the horizontal concrete strut = shear reinforcement spacing = 7.52 in.;
- area of the distributed longitudinal steel (A_y) = eight #2 bars = 0.4 in^2;
- area of the distributed longitudinal steel (A_x) = ten #2 bars = 0.5 in^2;
- area of diagonal rebar strut and tie (A_{dia}) = 0.295 in^2;
- area of horizontal rebar tie/strut (A_h) = 0.05 in^2;
- concrete compression strength = 0.63 f_c' = 0.63*(8.331 ksi) = 5.25 ksi;
- concrete tension strength = 0.05 f_c' = 0.416 ksi;

- yield strength of rebar tie = 63.0 ksi;
- yield strength if rebar strut in compression region = 63.0 ksi;

Figure 5.5 shows the strut and tie model for the first story of RWN and RW2. The STM model was developed using the truss elements in OpenSEES and analysis was conducted at four limit states shown Figure 5.4. The concrete and steel properties were modeled using *concrete 03* and *steel 02* material models available in OpenSEES. Using the nodal displacements the shear deformations were estimated using the procedure described in Chapter 3 (see Section 3.2.3). The comparison between the experimental and calculated shear deformations at the first story level for RWN and RW2 are presented in Figure 5.6. It can be seen from Figure 5.6, that the shear deformations of structural walls were captured with acceptable accuracy by the simple STMs.

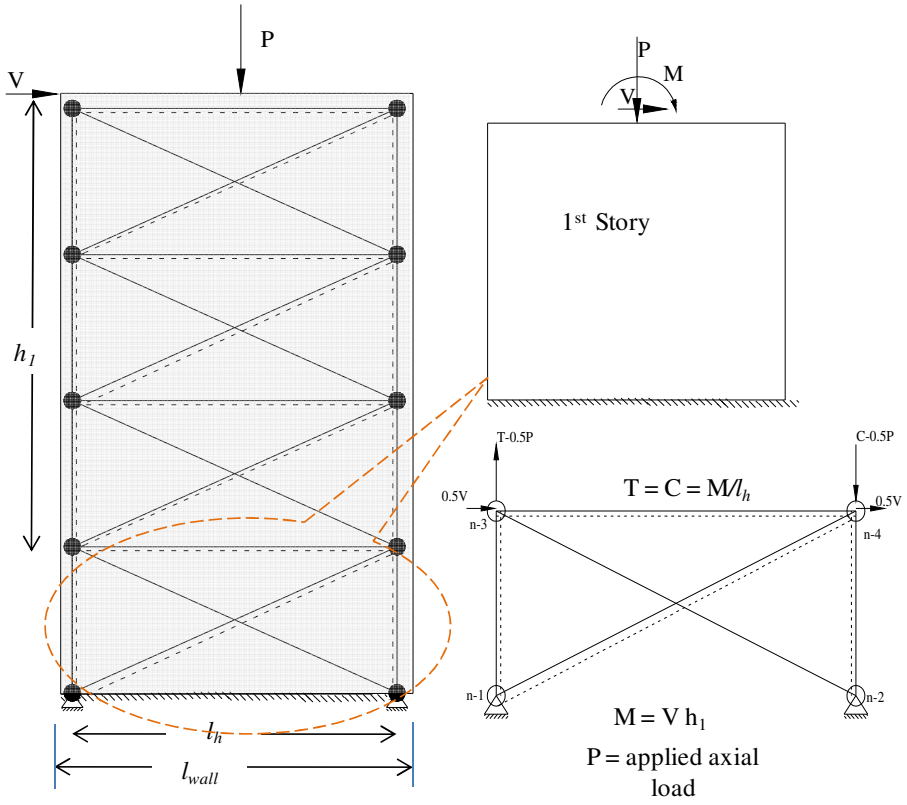

Figure 5.5 Strut and tie model for the first story of RW2 and RWN

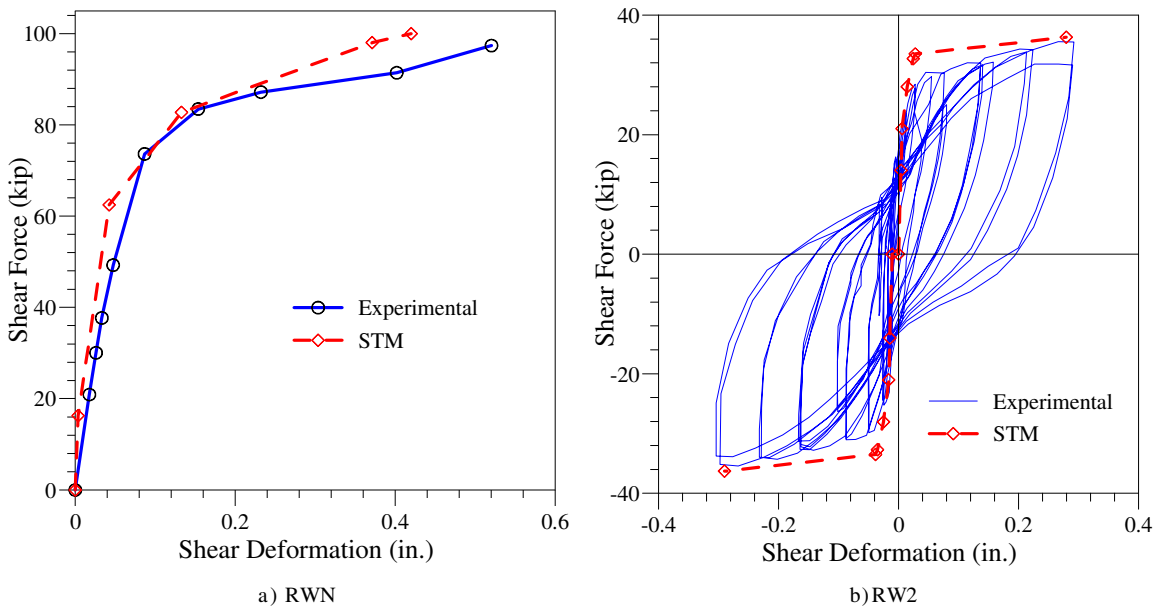

Figure 5.6 Comparison of experimental and calculated first story shear force vs. shear displacement response envelope for RWN and RW2

5.2 Shear Model Description

Considering the success of the strut-and-tie approach in modeling the concrete structural shear wall to capture the shear deformations, this section proposes a shear model suitable for OpenSEES in two parts. The first defines an envelope for the shear force vs. shear deformation response under monotonic loading. The second part presents the unloading and reloading branches so that the hysteretic behavior for the shear model can be established incorporating the strength and stiffness degradation.

5.2.1 Monotonic response envelope

A multi-linear envelope is proposed to represent the monotonic response envelope of shear deformation response of concrete structural walls. The points at which the segments of the curve meet are referred to as breakpoints. The breakpoints were chosen to represent certain damage limit states, which were cracking of concrete, first yield or yielding of the extreme longitudinal reinforcement, nominal moment capacity, defined by steel strain reaching 0.015 or concrete strain reaching 0.004, ultimate limit state which was defined by fracture strain of longitudinal reinforcement (steel strain of 0.06) or crushing of concrete in

confined regions. The monotonic envelope is estimated using strut-and-tie modeling approach outlined in previous section.

5.2.2 Nomenclature used for cyclic shear model definition

V_{cr}^{+} = load corresponding to the cracking limit state in positive direction.

V_{cr}^{-} = load corresponding to the cracking limit state in negative direction.

Δ_{cr}^{+} = deformation corresponding to the cracking limit state in positive direction.

Δ_{cr}^{-} = deformation corresponding to the cracking limit state in negative direction.

k_{ucr}^{+} = uncracked stiffness in positive direction and is equal to $\frac{V_{cr}^{+}}{\Delta_{cr}^{+}}$

k_{ucr}^{-} = uncracked stiffness in negative direction and is equal to $\frac{V_{cr}^{-}}{\Delta_{cr}^{-}}$

V_{y}^{+} = load corresponsding to the yielding limit state in positive direction.

V_{y}^{-} = load corresponsding to the yielding limit state in negative direction

Δ_{y}^{+} = deformation corresponding to the yielding limit state in positive direction.

Δ_{y}^{-} = deformation corresponding to the yielding limit state in negative direction.

k_{y}^{+} = yield stiffness in the positive direction and is equal to $\frac{V_{y}^{+}}{\Delta_{y}^{+}}$

k_{y}^{-} = yield stiffness in the negative direction and is equal to $\frac{V_{y}^{-}}{\Delta_{y}^{-}}$

$\Delta_{un}^{+}, \Delta_{un}^{-}$ = unloading deformations in positive and negative directions, respectively.

V_{un}^{+}, V_{un}^{-} = load corresponding to the unloading points in positive and negative directions, respectively.

μ = ductility at a unloading point in a given direction and is equal to $\frac{\Delta_{un}}{\Delta_y}$ in the given direction.

Δ_{his}^{+} = maximum deformation experienced by the structural member in positive direction in a shear deformation history.

Δ_{his}^{-} = maximum deformation experienced by the structural member in negative direction in a shear deformation history.

V_{his}^{+} = lateral load corresponding to Δ_{his}^{+}.

V_{his}^{-} = lateral load corresponding to Δ_{his}^{-}.

$k_{sec,his}$ = secant stiffness at the maximum deformation in a given loading direction in an applied deformation history.

5.2.3 Hysteretic Rules

Based on the cyclic shear models that exist in literature (e.g., Ozcebe and Saatcioglu 1989; Cheng et al. 1993) and the observations from cyclic shear force vs. shear deformation behavior of reinforced concrete walls tested as part of this study (RWN), the hysteretic rules shown in Figure 5.7 were established and are described below in detail.

loading branches

Similar to the shear model proposed by Ozcebe and Saatcioglu (1987), the initial loading of hysteretic response follows the primary curve until unloading starts. The first loading in the opposite direction is directed towards the cracking load in the opposite direction, i.e. to a point (Δ_{cr}, V_{cr}). If the member has not been loaded beyond the cracking

load in one direction, the initial loading in that direction aims at the cracking load even if the member experienced inelastic deformations previously in the opposite direction.

Unloading branches

(1) If unloading starts below the cracking load, irrespective of the previous cyclic shear deformation history (e.g., D_1E_1, B_1C_1), the unloading follows a straight line from the load reversal point to a point on zero load axis. The slope of this straight line is equal to the cracking stiffness in the direction of loading and mathematically shown in Eq. (5.1)

$$V_\Delta = \begin{cases} k_{ucr}^{+}\Delta \text{ for } \Delta \geq 0 \text{ where } k_{ucr}^{+} = \dfrac{\mathrm{V}_{cr}^{+}}{\Delta_{cr}^{+}} \\ k_{ucr}^{-}\Delta \text{ for } \Delta \leq 0 \text{ where } k_{ucr}^{-} = \dfrac{\mathrm{V}_{cr}^{-}}{\Delta_{cr}^{-}} \end{cases} \tag{5.1}$$

(2) If unloading begins between the cracking and yield limit states, and the yield load in the direction of loading has not been exceeded during previous cycles, unloading follows a straight line from the load reversal point to a point on zero load axis (e.g., AB). The slope of this line varies in the loading direction between uncracked stiffness and secant stiffness. A variation between these two limits is proposed as a function of displacement as presented in Eq. (5.3)

$$V_\Delta = \begin{cases} k_{\text{int}}\left[\Delta - \Delta_{un}^{+}\right] + \mathrm{V}_{un}^{+} \text{ for } \Delta \geq 0 \\ k_{\text{int}}\left[\Delta - \Delta_{un}^{-}\right] + \mathrm{V}_{un}^{-} \text{ for } \Delta \leq 0 \end{cases} \tag{5.2}$$

$$k_{\text{int}} = \begin{cases} k_{ucr}^{+}\left[\dfrac{\Delta_{cr}^{+}}{\Delta_{un}^{+}}\right] + k_{\text{sec}}^{+} \text{ for } \Delta \geq 0 \text{ where } k_{\text{sec}}^{+} = \dfrac{\mathrm{V}_{un}^{+}}{\Delta_{un}^{+}} \\ k_{ucr}^{-}\left[\dfrac{\Delta_{cr}^{-}}{\Delta_{un}^{-}}\right] + k_{\text{sec}}^{-} \text{ for } \Delta \leq 0 \text{ where } k_{\text{sec}}^{-} = \dfrac{\mathrm{V}_{un}^{-}}{\Delta_{un}^{-}} \end{cases} \tag{5.3}$$

If the yield load in the direction of loading has been exceeded at least once in the loading direction, then the unloading follows a bilinear curve to a point on zero load axis (e.g., YZ – ZA_1). In this case, the hysteresis model unloads from the unloading point with a stiffness of

k_1 given by Eq. (5.4) curve over a force equal to V_{uN1} (e.g., YZ), which is given by Eq. (5.5) and Eq. (5.6). Unloading continues for remainder of the load to a point on a zero load axis with a stiffness of k_2 (e.g., ZA_1) given by Eq. (5.7).

$$k_1 = \begin{cases} k_{ucr}^{+}\left[1-0.02\dfrac{\Delta_{un}^{+}}{\Delta_{y}^{+}}\right] & \text{for +ve direction loading} \\ k_{ucr}^{-}\left[1-0.02\dfrac{\Delta_{un}^{-}}{\Delta_{y}^{-}}\right] & \text{for -ve direction loading} \end{cases} \tag{5.4}$$

Depending on the loading direction,

$$V_{uN1} = \Psi_{\Delta} V_{cr}^{+} \text{ or } \Psi_{\Delta} V_{cr}^{-} \tag{5.5}$$

$$\Psi_{\Delta} = \begin{cases} 0.5+\dfrac{1}{6}(\mu-1) & \text{for } 1 \le \mu \le 4 \\ 1 & \text{for } \mu \ge 4 \end{cases} \tag{5.6}$$

$$k_2 = \begin{cases} k_{y}^{+}\left[1-0.025\dfrac{\Delta_{un}^{+}}{\Delta_{y}^{+}}\right] & \textit{for +ve direction loading} \\ k_{y}^{-}\left[1-0.025\dfrac{\Delta_{un}^{-}}{\Delta-}\right] & \textit{for -ve direction loading} \end{cases} \tag{5.7}$$

(3) If the unloading starts at load higher than the yield load in the current loading direction, the unloading curve is represented by a tri-linear curve (e.g., KLNP, STUV, and DEFG). The stiffnesses of the segments in the tri-linear curve depend on the deformation ductility level at the unloading point. The first segment unloads from the unloading force and displacement with a stiffness of $k_{seg,1}$ for V_{uN1} (e.g., KL, ST, DE), with a stiffness of $k_{seg,2}$ for V_{uN2} (e.g., LN, EF, TU), and with a stiffness of $k_{seg,3}$ (e.g., UV, NP, FG) for the remaining load. The stiffness values for the segments are given by Eq. (5.8). The values of V_{uN1} and V_{uN2} are estimated using Eq. (5.5) and Eq. (5.9).

$$k_{seg,1} = k_{ucr}\left[1-0.02\mu\right]$$
$$k_{seg,2} = k_{y}\left[1-0.025\mu\right] \quad (5.8)$$
$$k_{seg,3} = 0.4k_{y}\left[1-0.07\mu\right]$$

Where, k_{ucr} and k_y are the uncracked stiffness and yield stiffness in the direction of loading. Depending on the direction of loading,

$$V_{uN2} = V_y^+ \text{ or } V_y^- \quad (5.9)$$

reloading branches

If V_{cr} is exceeded in the direction of loading, following rules describes the tri-linear reloading branch (e.g., GHIJ, VWXK, PQRS).

(1) reloading up to V_{cr} will follow a straight line passing through point (Δ_{pi}, V_{cr}), where Δ_{pi} is the displacement corresponds to the state of closing of cracks formed due to previous loading direction loading. The value of this variable depends on the maximum displacement ductility experienced by the structure in the loading direction during an applied deformation history and is given by Eq. (5.10)

$$\Delta_{pi} = \Delta_{cr}\left(1+1.5\left(\frac{\Delta_{his}}{\Delta_{y}}\right)\right) \quad (5.10)$$

(2) reloading beyond V_{cr} will follow a straight line up to the yield load (V_y) in the loading direction (e.g., WX, HI, QP) with a stiffness equal to the lowest secant stiffness ($k_{sec,his}$) experienced by the structure in the loading direction during an applied deformation history.

(3) beyond the yield point, the model reloads passing through a point (Δ_{his}, αV_{his}) until it intersects the envelope, where α is the strength degradation factor and it depends on the magnitude and number of deformation cycles. With limited availability of number of experimental data points to arrive at a variation of α with the number of cycles and deformation magnitude, the equation proposed by Ozcebe and Saatcioglu (1987) can be used.

(4) beyond the intersection of reloading branch with the envelope curve, the reloading will follow the primary curve (e.g., JK).

(5) If unloading is completed without crossing the zero load axes, reloading in the same quadrant will trace a straight line aiming at the immediately preceding peak point (e.g., MK, PK, and A1Y).

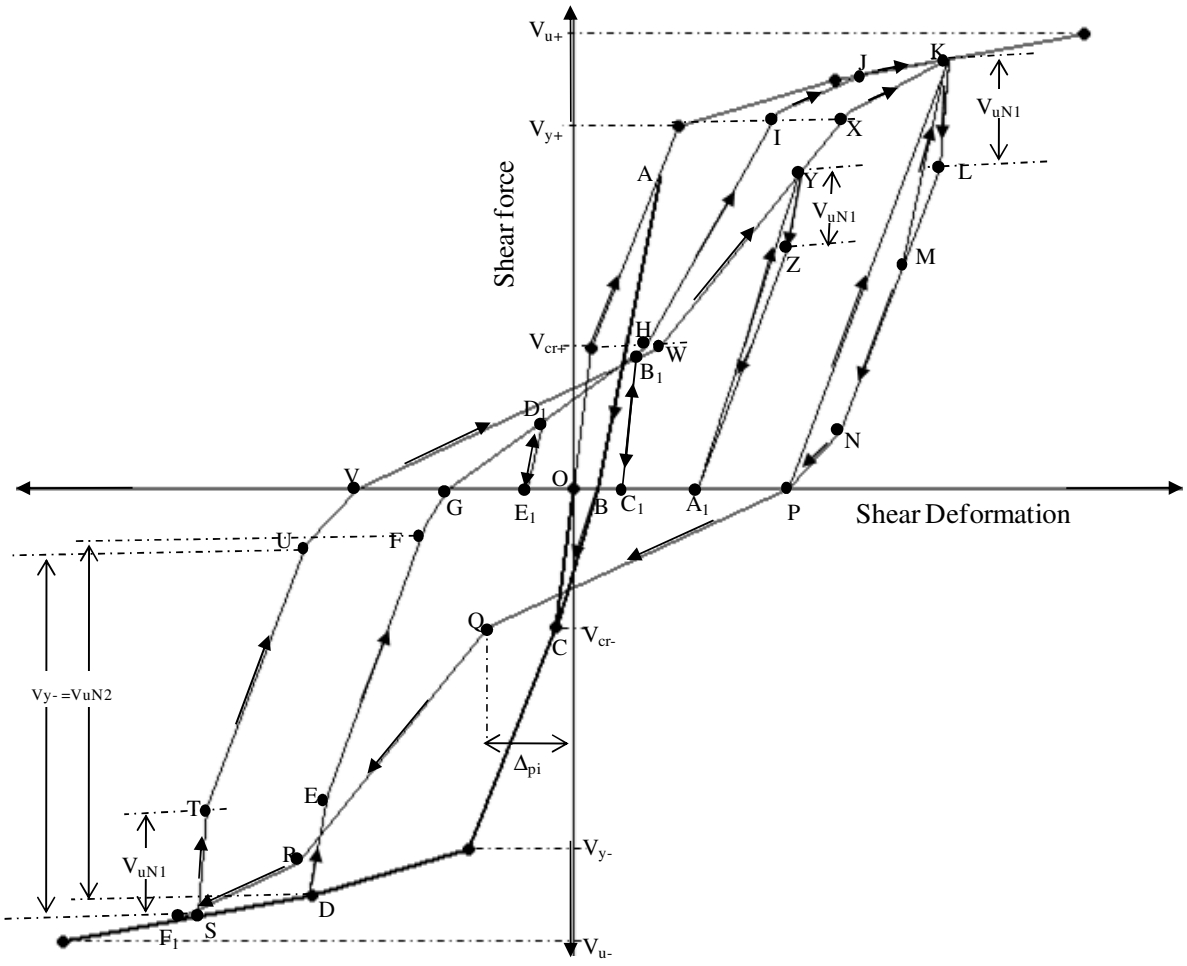

Figure 5.7 Illustration of proposed hysteretic rules of shear deformation response for concrete structural walls.

5.2.4 Model Validation

The proposed hysteretic shear model was used to predict the shear deformation behavior of rectangular walls RWN and RW2. The experimentally measured monotonic

envelope curve was used instead of the envelope curve predicted by STM to effectively validate the hysteretic rules proposed for this model. The comparison between the predicted and experimental first story shear force vs. shear deformations for RWN and RW2 are shown in Figure 5.8 and Figure 5.9, respectively. It can be seen that at large shear deformations, the proposed model captured the unloading, reloading stiffness and the residual shear deformations well for both reinforced concrete walls. The discrepancy seen in the negative loading direction (see Figure 5.9) of RW2 response is due to initial offset in the experimental data. Correcting the initial offset of shear strain was not done as the access to the individual instrument readings was not available. Overall, the proposed shear model predicted the shear hysteresis of shear walls with good accuracy.

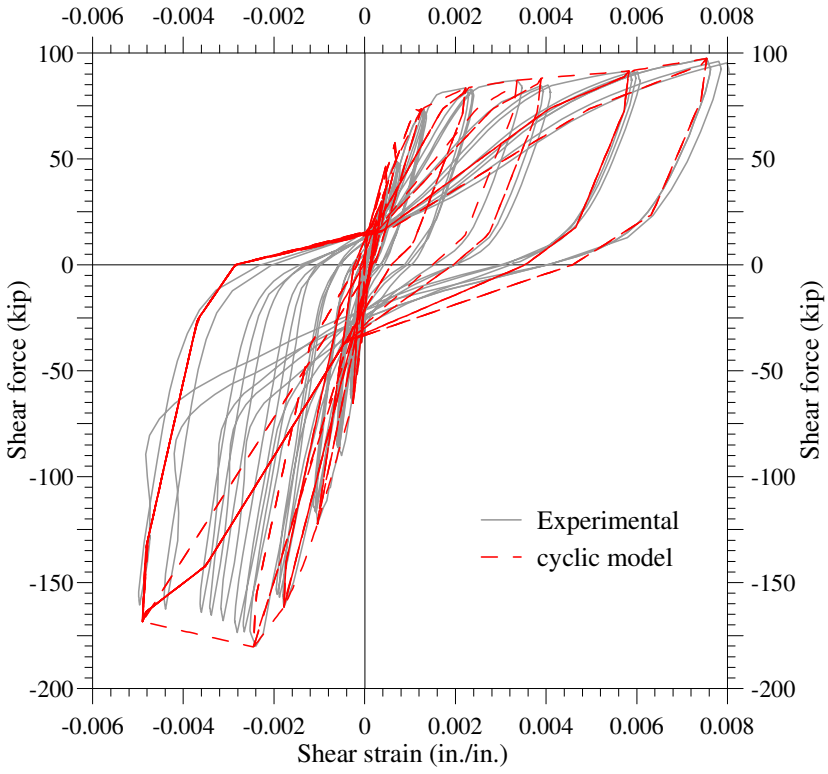

Figure 5.8 Comparison between calculated and measured first story shear force vs. shear deformation response of RWN

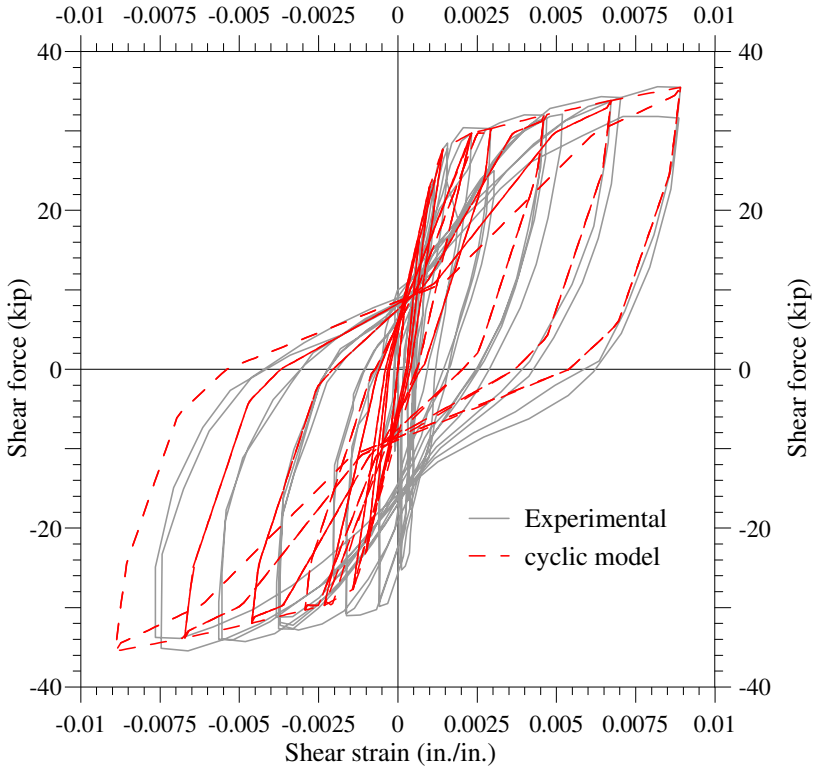

Figure 5.9 Comparison between calculated and measured first story shear force vs. shear deformation response of RW2

CHAPTER 6

SUMMARY, CONCLUSIONS AND RECOMMENDATIONS

6.1 Summary

The main focus of the study presented in the thesis was to investigate the analytical response of concrete walls connected to foundations the using the following connection details: no splices, mechanical couplers, conventional splices and unbonded post-tensioning. The experimental data for this investigation was obtained from two different testing. First, three rectangular reinforced concrete walls were designed and tested at 1/2-scale at the University of Minnesota's Multi-Axial Testing Facility as part of a PreNEESR project. Second, a 1/2-scale post-tensioned precast wall system was tested at the National Center for Research on Earthquake Engineering (NCREE), Taiwan, as part of an international collaboration. The three rectangular reinforced concrete walls, referred to as RWN, RWC and RWS, replicated the moment resistance of a prototype T-wall in the web direction and investigated the influence of the longitudinal reinforcement anchorage on the lateral load behavior of walls. RWN, RWC and RWS were, respectively, detailed with no splices, couplers and conventional code-based lap splices at the base of walls. The rectangular walls were subjected to in-plane lateral loading. The detailed experimental findings of rectangular walls are presented in Johnson (2007). This report has presented the fiber-based analysis of rectangular walls investigated as part of this project.

Until the incipient failure occurred, all rectangular walls were subjected to the same cyclic lateral load protocol that was determined based on pretest moment-curvature analyses of the `wall sections. The load protocol progressively increased the lateral displacements in a cyclic manner with full reversals and the complete details of the applied displacement histories are presented in Section 3.2. The performance of RWC was comparable to that of RWN, indicating that the mechanical couplers do not influence the wall behavior significantly. However, RWS had higher initial stiffness compared to the other two walls and exhibited relatively poor performance in comparison to the other two walls. The wall-to foundation interface crack opening observed in RWS was nearly 3 to 4 times wider than that was observed in RWN and

RWC. In RWN and RWC, the damage was extended up to 65-70 in. from the base, whereas in RWS the damage was concentrated more at the base over a shorter distance (about 25 in.), causing local buckling of the longitudinal reinforcement and thus reducing the energy dissipation capability of RWS.

The analysis of structural walls subjected to in-plane loading requires that a number of issues be addressed in the development of the analysis model. Those issues are: 1) nonlinear material behavior, including the effects of cracking and confinement of concrete as well as yielding and strain hardening of the mild steel reinforcement; 2) shear deformation of the walls; 3) interaction between the shear and flexural deformations; 4) strain penetration effects at the wall-to-foundation interface; and 5) influence of anchorage details used for the longitudinal reinforcement (e.g., couplers, lap splices etc.). The OpenSees models used for the analysis of the rectangular walls included the effects of these issues, except for the flexure-shear interaction and local slip of reinforcing bars within the lap splice, which was observed in RWS. Full descriptions of the analytical models used for the specimens were presented in Section 3.4.

The models used for the analysis in this dissertation used fiber-based beam-column elements that were available in the OpenSees analysis software. The fiber-based approach was selected because the simplification of the material model based on uniaxial behavior enabled more accurate representation of the concrete and steel reinforcement behavior in modeling the wall response. The fiber-based approach also enabled the effects of strain penetration at the wall-to-foundation interface to be included through the use of an interface element and a material model suitable for defining the local slip at the interface as a function of the stress in the longitudinal reinforcing bar, thus capturing the strain penetration effects in a rational manner. However, the fiber-based approach in OpenSees was to have two drawbacks. First, the shear distortion is handled at the element level, and thus the analysis requires that the shear deformation of the wall to be considered separately from the flexural behavior. Second, the separation of the shear and flexure behaviors makes it difficult for the shear-flexure interaction to be handled as directly as desired. The flexure-shear interaction can be modeled to a certain extent using strut-and-tie modeling technique, which was used to predict the expected shear deformation in the first story level of RWN. In addition, an improved cyclic shear model is proposed using strut and tie methodology and the test observations indicate that the shear hysteresis behavior could be captured with greater accuracy with this approach than to the

pinching model currently available in OpenSees. More details of hysteretic shear model are presented in Chapter 5.

The unbonded post-tensioned precast wall, referred to as PreWEC-1, was designed to replicate the observed experimental behavior of RWN in #6 and #5 bars in tension direction. PreWEC-1 consisted of a precast wall and two CFT columns connected together using an economical steel O-connector. PreWEC-1 performed superbly under applied cyclic lateral loads with stable response upto 3.5% lateral drift. The O-connectors experienced large inelastic strains, providing good energy dissipation capability to PreWEC-1. PreWEC-1 experienced only minor damage limited to the spalling of cover concrete in the wall toe regions. Overall, PreWEC-1 surpassed all the requirements stipulated in a performance validation document recently published for precast concrete wall systems.

The analysis of the PreWEC-1 requires addressing the issue of non existence of compatibility between the unbonded post-tensioning steel and concrete. This was addressed by incorporating an assumed trilinear variation for the wall contact length into a simplified analysis procedure. The analytical procedure predicted wall response with sufficient accuracy. More details about the PreWEC-1 performance and validation of the analytical procedure are presented in Sections 4.7 and 4.8. A simplified design procedure was developed for this new system by realizing the facts that post-tensioning force in end columns does not vary significantly under lateral load and by idealizing the cyclic force-displacement response with a multi-linear curve. More details of the design procedure are presented in Section 4.9.

6.2 Conclusions

Conclusions drawn from the research investigation presented in this dissertation are presented below.

6.2.1 Monolithic Reinforced Concrete Walls

Global Response

1. The force-based beam-column elements with fiber sections adequately captured the global cyclic force-displacement response for all the three rectangular walls. The calculated peak forces were within 5% of the experimental values while the loading,

unloading and reloading stiffnesses were simulated with good accuracy.

2. The initial stiffness of the walls was also well captured. For all three rectangular walls, the response in the direction that subjected the #6 and #5 bars in tension was better simulated than the response that subjected the #9 bars in tension. The discrepancy between the experimental and analytical results in the #9 bar in tension direction was caused primarily due to not adequately capturing the shear degradation during the repeated loading to the same lateral displacement in that loading direction. Since the best available approach was used in the analytical simulation, further improvements of the analysis of walls in OpenSees indicated integration of a new shear model.
3. The analytical models captured the flexural deformations at the top of the wall with good accuracy. The flexural component contributed 70 to 80% of the total top displacement for RWN and RWC. In RWS, the flexural contribution reduced from 70 % to 50% as the top lateral displacement increased, presumably due to increased slip of the reinforcement in the plastic hinge region.
4. The analytical model for RWN also captured the deformations due to shear and strain penetration at the top of the wall with sufficient accuracy. The deformations due to shear and strain penetration contributed 10 to 20% and 8 to 10%, respectively, to the top lateral displacement in RWN. This validates the strain penetration model proposed by Zhao and Sritharan (2007) for continuous reinforcement anchorage.
5. In RWC, for drifts higher than 1%, the analytical models overpredicted the lateral deformation due to strain penetration and under predicted the shear deformation by 30 to 50% and 10 to 27% respectively. Similarly, for RWS at lateral drift greater than 0.75%, the analytical model overpredicted the lateral deformation due to strain penetration by 30 to 170%. The over prediction of the strain penetration contribution in case of RWS did not influence the accuracy of the overall response. Because, it indirectly accounted for the deformation occurred due to rebar slip in the lap splice regions during the experimental investigation. Hence, a model similar to the strain penetration model proposed by Zhao and Sritharan (2007) with proper calibration could be used to account for the local rebar slip in the lap splice region.
6. Overall, the analytical models satisfactorily captured the total global response and flexural deformation contribution. The accuracy of the analytical simulation to predict

other modes of deformation could be further improved through introduction of an improved shear model and local slip model in lap splice regions.

Local Response

Accuracy of the analysis models cannot be sufficiently evaluated based only on the comparison of global responses. Appropriate local response parameters should also be examined. Accurate simulation of the local response is important for two reasons. First, the local response provides a better measure of damage in the structure and in performance-based design methods, which are being more frequently used. In these methods, design limits are specified using local response parameters. Second, accurate prediction of the local response is a better measure of the capability of the modeling approach. Predicting the local response accurately requires the analytical model to properly model the various lateral displacement components. Compensation of errors associated with predicting different displacement components may lead to accurate prediction of the global force-displacement of a structure; however, the local response will not be accurate.

For the rectangular walls, the various components of lateral displacement at the first panel level were examined. The analytical models for all the three walls over predicted the flexural deformation at the first panel level by 10 to 40%, depending on the top displacement. At large top lateral displacements, percentage of error was smaller. Similar to global response observations, the strain penetration component was over estimated by the analytical model in RWC and RWS.

6.2.2 PreWEC-1

1. The lateral load behavior of the PreWEC-1 under cyclic loading was excellent and its performance superseded the comparable performance of the cast-in-place reinforced concrete wall. The load carrying capacity of PreWEC-1 was 15% more than that of the reference wall, RWN. No strength degradation was observed up to a lateral drift of 3.5%, which is nearly 40% more than the comparable cast-in-place concrete wall.
2. The precast wall in PreWEC-1 experienced only minor damage limited to the spalling of cover concrete in the wall toe regions at the base. The end columns did not experience

any damage

3. The economically designed O-connectors performed exceptionally well during the component tests and during the PreWEC-1 testing. They produced a dependable stable hysteretic response during the test, contributing towards the energy dissipation capability of the PreWEC-1 system. The O-connectors produced nearly 17% viscous damping during PreWEC-1 test. The O-connectors experienced progressive fracture starting at 3% lateral drift and ultimately experiencing failure during 3.5% drift cycles. However, they continued to transfer forces when the fracture faces came in contact with each other.
4. The proposed simplified method that is comparable to the conventional section analysis method accurately predicted the monotonic response of PreWEC-1 as a function of lateral drift. The comparisons between the experimental and analytical results were satisfactory at both small and large drifts as well as at 2% drift which is commonly used as the design drift for this wall type. At all drifts, the analytical lateral resistance is within 5% of the experimental value.
5. The proposed simplified method captured the wall contact length and the displacement demand on the connectors accurately. Comparison with experimental data confirms that the trilinear approximation used for the neutral axis depth variation at the critical wall section is adequate.
6. The proposed equation for the concrete strain demand in the wall toe regions was found to satisfactorily estimate the expected compression strain demand, thereby allowing a realistic estimate of the confinement reinforcement needed in the walls.
7. The proposed equation for the equivalent viscous damping provided by the O-connectors to the damping capability of PreWEC-1 predicted the viscous damping of the PreWEC-1 system within 5 -12 % depending on the top displacement. This allows the designers to arrive at the number of special connectors based on the required damping.

6.3 Recommendations for Modeling Structural Walls

Based on the investigation in this report, the following recommendations are made for the simulation of structural walls subjected to cyclic lateral loading.

- Beam-column elements with fiber sections can accurately simulate the response of structural walls to cyclic loading and capture the contribution of various lateral deformation components of rectangular walls. The beam-column elements offer significant advantages due to their ease of use, computational efficiency, familiarity to engineering community, and ease of model construction.
- The effects of shear deformation and strain penetration should be accurately modeled in reinforced concrete walls.
- The material models selected for the analysis dictate the accuracy of hysteretic simulation of the wall behavior. The modified Chang and Mander concrete model introduced by Waugh (2008) should be used to model the concrete. Similarly the model proposed by Zhao and Sritharan (2007) is appropriate for accounting for the strain penetration effects. Also, it is important to model the influence of congestion of rebars on the strain penetration effects. The congestion of reinforcement causes the longitudinal steel to experience higher slips due to strain penetration effect.
- The response of the wall will be significantly influenced by the splice details used for the longitudinal reinforcement, especially when the splice is located within the plastic hinge region. Therefore, the splices of the wall reinforcement should be appropriately modeled to accurately capture the global and local wall responses. Conventional lap splices may be modeled as an equivalent bar with varying cross sectional area along the splice length.

6.4 Recommendations for Future Research

The investigation presented in this report has addressed several challenges associated with the analytical simulation of rectangular walls that were detailed with different anchorages for the longitudinal reinforcement. A number of issues have become apparent through the course of this investigation, which deserve further investigation as detailed below.

- More data are needed to refine the shape of the bar stress vs. loaded end slip for the bond slip material model. While the indication from this study is that the method used for capturing the strain penetration effects is appropriate, accuracy of the analysis can be improved by improving the stress vs. slip relationship.
- Since the design codes continue to permit the use of conventional lap splices in the

plastic hinge region of concrete walls, more experimental investigations are needed to understand the splicing details on overall lateral behavior of walls.

- A force based beam-column element with capability to accommodate different steel areas at integration points will be useful. This will help in modeling the lap splices effectively without reducing the element length
- A material model that has the ability to capture the local slip within the lap spliced region of the wall would be valuable.

REFERENCES

- Aaleti, S., and Sritharan, S. (2007). "A Precast Wall with End Columns (PreWEC) for Seismic Applications", Proc., 8th Pacific Conference on Earthquake Engineering, Singapore, Paper 157.
- Aaleti, S, and Sritharan S., "A simplified analysis method for characterizing unbonded post-tensioned precast wall systems," Engineering Structures, Elsevier, 2009 (in press).
- Abrams, D.P., "Laboratory Definitions of Behavior for Structural Components and Building Systems," ACI Special Publication 127, Vol. 127, No. 4, pp. 91-152, April 1991.
- ACI Committee 318, [1986] "Building Code Requirements for Structural Concrete," American Concrete Institute, Farmington Hills, Michigan, 1986.
- ACI Committee 318, (2005) "Building Code Requirements for Structural Concrete," American Concrete Institute, Farmington Hills, Michigan, 2005.
- ACI Committee 318, (2008) "Building Code Requirements for Structural Concrete," American Concrete Institute, Farmington Hills, Michigan, 2008.
- ACI Innovation Task Group 5, "Acceptance Criteria for Special Unbonded Post-Tensioned Precast Structural Walls Based on Validation Testing (ACI ITG 5.1-07) and Commentary," American concrete Institute, Farmington Hills, MI, 2007.
- ACI Innovation Task Group 5, "ITG-5.2-09 Requirements for Design of a Special Unbonded Post-Tensioned Precast Shear Wall Satisfying ACI ITG-5.1 & Commentary," American Concrete Institute, Farmington Hills, MI, 2009.
- Ali, A., and Wight, J.K., "Reinforced Concrete Structural Walls with Staggered Opening Configurations Under Reversed Cyclic Loading," Report No. UMCE 90-05, Department of Civil Engineering, University of Michigan, Ann Arbor, April 1990.
- Bolander, J., and Wright, J. (1991) "Finite Element Modeling of Shear Wall Dominate Buildings" *Journal of Structural Engineering,* Vol. 117, No. 6, pp. 1719-1739
- Brueggen, B. L. (2009) "Performance of T-shaped reinforced concrete shear walls under multi directional loading", PhD thesis, University of Minnesota, MN.

- CEB-FIP (1978) ,Model Code for Concrete Structures, CEB-FIP International Recommendation",3rdEdition,ComiteEuro-InternationalduBeton/Federation Internationale de la Precontrainte, Paris, 348 p'
- Cho, J.Y., Pincheira, A. (2006) "Inelastic Analysis of Reinforced Concrete Columns with Short Lap Splices Subjected to Reversed Cyclic Loads", *ACI Structural Journal,* V. 103, No.2, pp 280-290.
- Dazio, A. (2006) "Some Aspects of RC Walls Modeling using Fiber Elements," *Proceedings of the NEES/UCSD Workshop Analytical Model of Reinforced Concrete Walls,* San Diego, CA December, 2006.
- Dazio, A., Beyer, K., Bachmann, H., "Quasi-static cyclic tests and plastic hinge analysis of RC structural walls", Engineering Structures 31 (2009) pp.1556-1571
- Deshmukh, K., Thiagarajan, G., and Heausler, T. (2006) "Numerical Modeling of Seven Story Reinforced Model Using SAP," *NEES/UCSD Workshop on Analytical Modeling of Reinforced Concrete Walls,* San Diego, CA December 2006.
- Englekirk, R. E., *Seismic Design of Reinforced and Precast Concrete Buildings*, John Wiley & Sons, Hoboken, NJ, 2003.
- Felipe J. Perez, Stephen Pessiki, Richard Sause. "Seismic Design of Unbonded Post-Tensioned Precast Concrete Walls With Vertical Joint Connectors". PCI Journal, Vol. 49, No. 1, Jan-Feb 2004.
- Fintel, M., "Performance of Buildings with Shear Walls in Earthquakes of the Last Thirty Years", *PCI Journal,* 2002*,* Vol. 40, No. 3, pp. 62-80.
- Fischinger, M., and Isakovic, T. (2006) "NEES Blind Prediction Testing on RC Wall Building Slice, Multiple-Vertical-Line-Element Model," *Proceedings of the NEES/UCSD Workshop Analytical Model of Reinforced Concrete Walls,* San Diego, CA December, 2006.
- Gerin, M., and Adebar, P. (2004). "Accounting for shear in seismic analysis of concrete structures." Proc., 13th World Conf. on Earthquake Engineering, Vancouver, Paper No. 1747.

- Ghorbani-Renani, N. Velev, R. Tremblay, D. Palermo, B. Massicotte, and P. Léger "Modeling and Testing Influence of Scaling Effects on Inelastic Response of Shear Walls" ACI Structural Journal 2009; 106-S35, pp.358-367
- Grange, S., Mazars, J., and Koronis, P. (2006) "Seven-Story Building Slice Earthquake Blind Prediction Contest: A Simplified Model Using Multi fiber Timoshenko Beams" *Proceedings of the NEES/UCSD Workshop Analytical Model of Reinforced Concrete Walls,* San Diego, CA December, 2006.
- Henry, R. S, Aaleti, S., Sritharan, S., and Ingham, J. M., "Concept and finite element modeling of new steel shear connectors for self-centering wall systems," ASCE Journal of Engineering Mechanics, 2009 (accepted for publication).
- Hines, E.M., Restrepo, J.I., and Seible, F., 2004. "Force-Displacement Characterization of Well-Confined Bridge Piers," *ACI Structural Journal* 101 (4), pp. 537-548.
- Hutchinson, R. L., Rizkalla, S. H., Lau, M., and Heuvel, M. "Horizontal Post-Tensioned Connections for Precast Concrete Bearing Shear Walls." PCI Journal, V. 36, No. 3, Nov.-Dec., 1993, pp. 64-76.
- Johnson, B. M. "Longitudinal Reinforcement anchorage Detailing effects on RC shear wall Behavior", Master of Science Thesis, University of Minnesota, 2007, 391 pp.
- Kazushi Shimazaki "Reinforced Concrete Shear Walls with De-bonded Diagonal Reinforcements for the Damage-less Reinforced Concrete Building", Proceeding of 14th World Conference on Earthquake Engineering, October 12-17, 2008, Beijing, China.
- Kelly, T. (2006) "A Blind Prediction Test of Nonlinear Analysis Procedures for Reinforced Concrete Shear Walls," *Bulletin of the New Zealand Society for Earthquake Engineering,* Vol. 40, No. 4. pp. 142-158.
- Kelly, T. (2006) "NCEES Blind Prediction Test: Practitioner Entry From Holmes Consulting Group, New Zealand," *NEES/UCSD Workshop on Analytical Modeling of Reinforced Concrete Walls,* San Diego, CA December 2006.
- Lee, D. H., and Elnashai, A. S. (2001). "Seismic analysis of rc bridge columns with flexure–shear interaction." J. Struct. Eng., 127(5), 546–553.

- Lefas, I.D., Kotsovos, M.D. (1990), "Strength and Deformation Characteristics of Reinforced Concrete Walls under Load Reversals", ACI Structural Journal, vol. 87, no. 6, November-December 1990, pp. 716-726.
- Mander, J.B., Priestley, M.J.N., and Park, R., (1988) "Theoretical Stress-Strain Model for Confined Concrete," *Journal of Structural Engineering*, American Society of Civil Engineering, Vol. 114, No. 8, August 1988.
- Martinelli, P., and Filippou, F. (2006) *"Numerical Simulation of the Shake Table Test of a Full Scale, Seven Story Shear Wall Specimen," Proceedings of the NEES/UCSD Workshop Analytical Model of Reinforced Concrete Walls, San Diego,* CA December, 2006.
- Martinelli, L. (2008) "Modeling Shear-Flexure Interaction in Reinforced Concrete Elements Subjected to Cyclic Lateral Loading", *ACI Structural Journal,* V. 105, No. 6, pp 675-684.
- Mazzoni, S., McKenna, F., Scott, M.H., Fenves, G.L. (2006) "Open System for Earthquake Engineering Simulation," Pacific Earthquake Engineering Research Center, University of California, Berkeley, California, Ver. 1.7.4.
- Moaveni, B., He, X., Conte, J., and Restrepo, J. (2006) "System Identification of a Seven-Story Reinforced Concrete Shear Wall Building Slice Tested on the UCSD-NEES Shake Table," *NEES/UCSD Workshop on Analytical Modeling of Reinforced Concrete Walls,* San Diego, CA December 2006.
- Narina, Jung (2007), "Preliminary design of Shear Wall specimens tested with MAST", Master of Science Thesis, University of Minnesota, 2007, 257 pp.
- Oesterle, R.G., Aristizabal-Ochoa, J.D., Fiorato, A.E., Russel, H.E., and Corley, W.G., "Earthquake Resistant Structural Walls – Tests of Isolated Walls – Phase II," Report to the National Science Foundation, Construction Technology Laboratories, Portland Cement Association, Skokie, Illinois, October 1979.
- Oesterle, R.G., Fiorato, A.E., Johal, L.S., Carpenter, J.E., Russel, H.E. and Corley, W.G., "Earthquake Resistant Structural Walls – Tests of Isolated Walls," Report to the National Science Foundation, Construction Technology Laboratories, Portland Cement Association, Skokie, Illinois, November 1976.

- Open System for Earthquake Engineering Simulation (OpenSees) User Manual (1.7.5), 2007, http://opensees.berkeley.edu/.
- Orakcal, K., and Wallace, J.W. (2006) "Flexural Modeling of Reinforced Concrete Walls – Experimental Verification," *ACI Structural Journal,* Vol. 103, No. 2, pp. 196-205.
- Ozcebe, G., and Saatcioglu, M. (1989). "Hysteretic shear model for reinforced concrete members." J. Struct. Eng., 115(1), 132–148.
- Palermo, D., and Vecchio, F.J. (2004) "Compression Field Modeling of Reinforced Concrete Subjected to Reversed Loading: Verification," *ACI Structural Journal,* Vol. 101, No. 2, pp.155-164.
- Paulay, T., Priestly, M.J.N., and Synge, A.J., "Ductility in Earthquake Resisting Squat Shear Walls," Proceedings ACI Journal, American Concrete Institute, Vol. 79, No. 4, pp. 257-269, August 1982.
- Petrangeli, M.; Pinto, P. E., and Ciampi, V., "Fiber Element for Cyclic Bending and Shear of RC Structures, I: Theory," Journal of Engineering Mechanics, V. 125, No. 9, 1999, pp. 994-1001.
- Pilakoutas K, Elnashai, AS., "Cyclic behaviour of RC cantilever walls, Part I: Experimental results", ACI Structural Journal 1995; 92(3), pp.271–281.
- Pincheira, J. A., Dotiwala, F. S., and D'Souza, J. T. (1999). "Seismic analysis of older reinforced concrete columns." Earthquake Spectra, 15(2), 245–272.
- Priestley, M. J. N., Sritharan, S., Conley, J. R., Pampanin, S., "Preliminary Results and Conclusions From the PRESSS Five-Story Precast Concrete Test Building", PCI Journal, 1999, Vol. 44, No. 6, pp. 42-67.
- Rahman, A. and Restrepo, J.I., "Earthquake Resistant Precast Concrete Buildings: Seismic Performance of Cantilever Walls Prestressed using Unbonded Tendons", Research Report 2000-5, Department of Civil Engineering, University of Canterbury, Christchurch, New Zealand, 2000.
- Response-2000. (2007). "http://www.ecf.utoronto.ca/~bentz/home.shtml".Nov. 15, 2007
- Riva, P., Meda, A., and Giuriani E., "Cyclic behaviour of a full scale RC structural wall", Engineering Structures, V.25 (2003), pp. 835-845.

- Schlaich, J., Schafer, K. and Jennewin, M. (1987), "Towards a Consistent Design of Structural Concrete", PCI Journal, Vol. 32, No' 3, May-June, pp' 74-l5l'
- Sezen, H., Chowdhury, T., “Hysteretic Model for Reinforced Concrete Columns Including the Effect of Shear and Axial Load Failure”, Journal of Structural Engineering, Vol. 135, No. 2, February 1, 2009
- Shiu, K.N., Daniel, J.L., Aristizabal-Ochoa, J.D., Fiorato, A.E., and Corley, W.G., “Earthquake Resistant Structural Walls – Tests of Walls With and Without Openings,” Report to the National Science Foundation, Construction Technology Laboratories, Portland Cement Association, Skokie, Illinois, July 1981.
- Sittipunt, C., and Wood, S.L. (1993) “Finite Element Analysis of Reinforced Concrete Shear Walls,” Report to the National Science Foundation, Department of Civil Engineering, University of Illinois at Urbana-Champaign, December 1993.
- Sittipunt, C., and Wood, S.L., 1995. “Influence of Web Reinforcement on the Cyclic Response of Structural Walls,” ACI Structural Journal, 92 (6), pp. 1-12.
- Smith J. Brian, Kurama C.Y (2009) “Design of Hybrid Precast Concrete Walls for Seismic Regions”, Proceedings, 2009 Structures Congress, ASCE, Austin, TX.
- Soudki, K. A., S. H. Rizkalla, and R. W. and Daikiw. "Horizontal Connections for Precast Concrete Shear Walls Subjected to Cyclic Deformations Part 2: Prestressed Concrete." PCI Journal, V. 40, No. 5, July-Aug., 1995b, pp. 82-96.
- Sritharan, S., Priestley, N., and Seible, F. "Nonlinear Finite Element Analyses Of Concrete Bridge Joint Systems Subjected To Seismic Actions," Finite Elements in Analysis and Design. V. 36, 2000, pp. 215-233.
- Sritharan, S. "Analysis of Concrete Bridge Joints Subjected to Seismic Actions," Doctoral Dissertation, University of California, San Diego, California, 1998, 407 pp.
- Sritharan, S., Priestley, M.J.N., and Seible, F., 1996. “Seismic Response of Column/Cap Beam Tee Connections with Cap Beam Prestressing.” Structural Systems Research Report No. SSRP-96/09, Division of Structural Engineering, University of California, San Diego.
- Sritharan, S., Aaleti, S. and Thomas, D. (2007). “Seismic Analysis and Design of Precast Concrete Jointed Wall Systems”, ISU-ERI-Ames Report, Department of Civil and Construction and Environmental Engineering, Iowa State University, Ames, Iowa.

- Stanton, J. F. and Nakaki, S. D., Design Guidelines For Precast Concrete Seismic Structural Systems, PRESSS Report No. 01/03-09, UW Report No. SM 02-02, The University of Washington and The Nakaki Bashaw Group, Inc., 2002.
- Tasnimi AA (2000). "Strength and deformation of mid-rise shear walls under load reversal". Engineering Structures, Vol.22, pp.311–322.
- Taucer, Fabio F., E. Spacone, and F. C. Filippou. (1991) "A Fiber Beam-Column Element for Seismic Response Analysis of Reinforced Concrete Structures. Report No. UCB/EERC-91/17," Earthquake Engineering Research Center, College of Engineering, University of California, Berkeley.
- Thomas, D. J. "Analysis and Validation of a Seismic Design Method Proposed for Precast Jointed Wall Systems". M.S. thesis, Department of Civil, Construction and Environmental Engineering, Iowa State University, 2003.
- Thomsen, J.H., and Wallace, J.W. (1995) "Displacement-Based Design of RC Structural Walls: An Experimental Investigation of Walls with Rectangular and T-Shaped Cross-Sections," Report to the National Science Foundation, Department of Civil Engineering, Clarkson University, Potsdam, New York.
- To, N. H. T., Sritharan, S., lngham, J. M. (2009), "Strut-and-Tie Nonlinear Cyclic Analysis of Concrete Frames", Journal of Structural Engineering, Vol. 135, No. 10.
- To, N. H. T. (2005), "Nonlinear Structural analysis Using Strut-And-Tie Models", PhD thesis, Dept. of Civil and Environmental Engineering, University of Auckland, New Zealand.
- Tony Holden, Jose Restrepo, and John B. Mander. "Seismic Performance of Precast Reinforced and Prestressed Concrete Walls". ASCE structural Journal, 2003.
- Vecchio, F. J., and Collins, M. P. 1986. "The modified compression-field theory for reinforced concrete elements subjected to shear." ACI J., 83(2), 219–231.
- Wallace, J.W., 1992. "BIAX: Revision 1 – Computer Program for the Analysis of Reinforced Concrete and Reinforced Masonry Sections," Report CU/CEE-92/4, Structural Engineering, Mechanics, and Materials, Clarkson University, Potsdam, NY.

- Waugh, J., Aaleti, S., Sritharan, S., and Zhao, J., 2009. "Nonlinear Analysis of Rectangular and T-shaped Concrete Walls," ISU-ERI-Ames Report ERI-09327, Iowa State University, Ames, IA.
- Wood, L., S., Wight, K., J., Moehle, P., J., "The 1985 Chile earthquake: observations on earthquake resistant construction in Vina del Mar", Structural Research Series No. 532, University of Illinois at Urbana-Champaign, 1987-02.
- Wyllie, A., L., "Armenia Earthquake Reconnaissance Report", Earthquake Engineering Research, 1989.
- Zhang, Y.H. & Wang, Z.H. (2000), "Seismic behaviour of reinforced concrete shear walls subjected to high axial load", ACI Structural Journal, vol. 97, no. 5, pp. 739-750.
- Zhao, J., and Sritharan, S. (2007) "Modeling of Strain Penetration Effects in Fiber-Based Analysis of Reinforced Concrete Structures," *ACI Structural Journal,* Vol. 104, No. 2, pp. 133-141.